SPECTROSCOPIC INVESTIGATION OF INTERSYSTEM CROSSING, ELECTRON TRANSFER, AND ENERGY TRANSFER IN Sn(IV), Re(I), AND Ru(II) COMPLEXES IN SOLUTION

AN ABSTRACT

SUBMITTED ON THE SEVENTEENTH DAY OF DECEMBER 2014

TO THE DEPARTMENT OF CHEMISTRY

IN PARTIAL FULFILLMENT OF THE REQUIREMENT
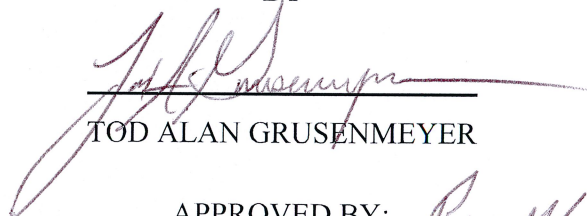
OF THE SCHOOL OF SCIENCE AND ENGINEERING

OF TULANE UNIVERSITY

FOR THE DEGREE
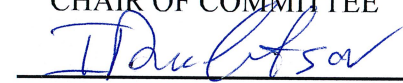
OF

DOCTOR OF PHILOSOPHY

BY

_____

TOD ALAN GRUSENMEYER
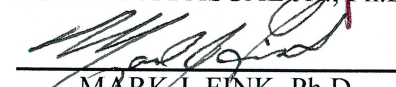
APPROVED BY: _____
RUSSELL H. SCHMEHL, Ph.D.
CHAIR OF COMMITTEE

_____
IGOR V. RUBTSOV, Ph.D.

_____
JAMES P. DONAHUE, Ph.D.

_____
ROBERT A PASCAL JR., Ph.D.

_____
MARK J. FINK, Ph.D.

ABSTRACT

The work in this dissertation has two main goals: (1) to access Sn(IV) Schiff-Base complexes as photosensitizers in photoredox reactions and (2) to use ultrafast spectroscopic techniques to understand the kinetics and reactivity governing intramolecular electron transfer, intramolecular energy transfer, and intersystem crossing.

Chapter 1 serves to provide a brief introduction to the general photochemical properties necessary to the understanding of the subsequent chapters. The applications of these principles will be discussed in relation to the presented data as necessary.

Chapter 2 focuses on the synthesis and evaluation of four, fluorescent Sn(IV) Schiff-Base complexes as photosensitizers capable of participating in photoredox reactions. Main group elements provide a potential alternative to traditional transition metal photosensitizers due to large spin orbit coupling constants (for 4th and 5th row elements), multi-electron redox behavior, and their relatively cheap cost and abundance. All four complexes absorb visible light (λ_{max} = 420 to 462 nm) and the luminescence properties are easily tunable with simple ligand modification. The complexes do not exhibit phosphorescence at room temperature or in 77 K glasses but possess long-lived triplet excited states that can be observed and followed using nanosecond transient absorption spectroscopy. The decay of the triplet excited states are dominated by triplet-triplet annihilation in acetonitrile. The lifetimes of the triplet excited states range from 500 ns – 10 ms in PMMA matrices. Further, ultrafast transient absorption measurements were used to establish the rates of intersystem crossing for these complexes. Due to the non-phosphorescent nature of the excited states, the triplet state energies for the complexes estimated via energy transfer reactions with a series of organic triplet

acceptors. Notably, photoexcited solutions of the complexes containing methyl viologen and 10-methylphenothiazine reveal the formation of methyl viologen anion radical and 10-methylphenothiazine cation radical.

Chapter 3 concentrates on the use of time-resolved transient infrared spectroscopy to monitor the evolution and definitely assign the nature of the excited states created after excitation in a series of rhenium bipyridine (bpy), tricarbonyl complexes. Initial studies were dedicated to the investigation of fac-[Re(bpy)(CO)$_3$L](BArF$_{24}$) where L is benzonitrile (ReBN), 4-dimethylaminobenzonitrile (Re4DMABN), and 3-dimethylaminobenzonitrile (Re3DMABN). These complexes exhibit strongly solvent-dependent luminescence. ReBN and Re4DMABN display strong emission with microsecond lifetimes in dichloromethane (DCM). Their luminescence quantum yields and lifetime values markedly decrease in (1:1 v:v) DCM:MeOH. Time-resolved nanosecond transient absorption lifetimes for these complexes mirror the luminescence lifetime values. Re3DMABN demonstrates markedly different luminescence behavior. The quantum yield is extremely low (< 0.005) for the complex in DCM and mixed DCM:MeOH. Nanosecond transient absorption measurement indicate a 23 μs for Re3DMABN in DCM, which diminishes to 30 ns in mixed DCM:MeOH. These steady-state luminescence and nanosecond transient absorption measurements clearly establish that Re3DMABN and Re4DMABN access very different thermally equilibrated excited states. Time-resolved transient infrared spectroscopy was used in order to fully understand the nature of these thermally equilibrated excited states. The thermally equilibrated excited state of Re4DMABN in DCM has metal-ligand-to-ligand charge transfer (MLLCT) character, which is identified by an increase in the frequency of the

symmetric and asymmetric stretching frequencies of the CO ligands and a decrease of the CN and phenyl frequencies. Formation of a 4DMABN (π^*) to bipyridine (π^*) ligand-to-ligand charge transfer (LLCT) state is found in MeOH/DCM solvent. This state is identified by characteristic shifts the carbonyl and phenyl ring stretching frequencies to drastically lower values. The lowest energy exited state of Re3DMABN in DCM is found to be a 3DMABN intra-ligand triplet state (^{3}IL). The ^{3}IL excited state is characterized by a decrease in frequency of the three CO stretching modes, CN stretching mode, and 3DMABN ring stretching mode. The CN stretching mode is the most diagnostic as it decreases by -127 cm^{-1}, which is attributed to the 3DMABN ligand triplet state. In mixed solvent, an equilibrium between the ^{3}IL and a MLLCT states is found. After obtaining these preliminary results, another complex, fac-[Re(dcebpy)(CO)$_3$(3DMABN)](BArF$_{24}$) (dcebpy= 4,4'-dicarboxyethyl-2,2'-bipyridine), was investigated in an attempt to observe a 3DMABN (π^*) to dcebpy (π^*) LLCT excited state. The inclusion of the dcebpy served to lower the ^{3}MLCT excited state energy of the complex below that of the ^{3}IL state and also adds an additional useful vibrational mode for TRIR studies. This complex does, in fact, thermally populate a LLCT excited state in both DCM and mixed DCM:MeOH. ReEBA shows a strong dependence on the solvent polarity and features solvent dependent frequency shifts for several vibrational reporters.

Chapter 4 illustrates the control of excited state energy transfer processes using variations in solution pH. These studies focus on Ru(II) complexes possessing two 4,4'-dicarboxy-2,2'-bipyridine ligands and a single, substituted bipyridine ligand, which is covalently linked directly to pyrene or linked to pyrene through a phenyl bridge. The energy of the Ru (dπ) to 4,4'-dicarboxy-2,2'-bipyridine (π^*) triplet metal-to-ligand

charge transfer (^{3}MLCT) state is pH dependent while the energy of the pyrene triplet state (^{3}pyrene) is not affected by changes in pH. At pH 0, the ^{3}MLCT state is the lowest energy state. At pH 8, the carboxylic acid substituents are deprotonated and the energy of the ^{3}MLCT state rises above that of ^{3}pyrene, resulting in a significant increase in the lifetime of the observed emission. Analysis of ultrafast and nanosecond time-resolved transient absorption spectra of the complexes result in a description of excited state that involves initial equilibration of the ^{3}MLCT and ^{3}pyrene states followed by relaxation to the ground state. The lifetime of the excited state is highly dependent on the position of this equilibrium. At pH 0, when the ^{3}MLCT is favored, the lifetime of the complex is 2 μs. As the pH of the solution is increased and population of the pyrene triplet state is favored, the lifetime increases to a value > 10 μs. The quenching of these excited states by dissolved oxygen is also pH dependent, paralleling the excited state lifetime.

SPECTROSCOPIC INVESTIGATION OF INTERSYSTEM CROSSING, ELECTRON TRANSFER, AND ENERGY TRANSFER IN Sn(IV), Re(I), AND Ru(II) COMPLEXES IN SOLUTION

A DISSERTATION

SUBMITTED ON THE SEVENTEENTH DAY OF DECEMBER 2014

TO THE DEPARTMENT OF CHEMISTRY

IN PARTIAL FULFILLMENT OF THE REQUIREMENT

OF THE SCHOOL OF SCIENCE AND ENGINEERING

OF TULANE UNIVERSITY

FOR THE DEGREE

OF

DOCTOR OF PHILOSOPHY

BY

_____

TOD ALAN GRUSENMEYER

APPROVED BY: _____

RUSSELL H. SCHMEHL, Ph.D.
CHAIR OF COMMITTEE

_____

IGOR V. RUBTSOV, Ph.D.

_____

JAMES P. DONAHUE, Ph.D.

_____
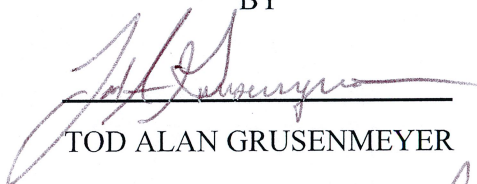
ROBERT A PASCAL JR., Ph.D.

_____

MARK J. FINK, Ph.D.

DEDICATED TO MY MOTHER AND FATHER

ACKNOWLEDGEMENTS

TABLE OF CONTENTS

LIST OF FIGURES

Chapter 3

Chapter 4

Chapter 4

Appendix A

Appendix B

xvii

CHAPTER 1: BASIC PHOTOCHEMICAL PROCESSES AND LIGHT INDUCED REACTIONS
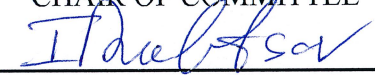
This initial Chapter will provide an overview of the underlying photochemical processes governing the general reactivity of the excited states discussed in Chapters 2, 3, and 4. The ensuing topics have been covered in a number of writings: essentially, every photochemistry text treats these subjects in detail.[1-16] A number of these sources present these topics from a quantum mechanical background. Here, I offer only a qualitative summary to provide a basic background to the subsequent material.

1.1 The Creation and Fate of an Electronic Excited State

Photochemistry is a broad discipline that, at its core, seeks to understand the reactivity of molecules after they have absorbed light. In this context, light encompasses all of the wavelengths of the electromagnetic spectrum that are capable of promoting electrons from outer (valence) occupied orbitals to higher energy unoccupied molecular orbitals. Empirically, it has been determined that wavelengths ranging from the far ultraviolet to near infrared (200 nm – 1000 nm) are capable of causing such electronic excitation of molecules. These transitions are not strictly limited to highest occupied molecular orbital (HOMO) to lowest unoccupied molecular orbital (LUMO) transitions and can involve the orbitals close to the HOMO and LUMO. Electronic transitions can also result in the vibrational excitation of the molecule within a given electronic state. Photoexcited molecules are energetically unstable and only exist for very short periods of time. Once a molecule has absorbed light and formed an excited state, it will seek to undergo some sort of chemical deactivation. Deactivation occurs via photochemical reactions to form products, radiative decay through the release of photons, non-radiative decay resulting in the loss of excitation energy as heat, or quenching of the excited state

by some species in solution. A great starting point for any photochemistry dialogue is a discussion of the chemical processes governing excited states and their effect on the deactivation of the excited state.

A generalized state diagram is shown in Figure 1.1. The diagram illustrates relative energy and detailed kinetic information for the given molecule. A diagram of this type is referred to as a Jabolonski diagram and is ubiquitous in the photochemistry literature.
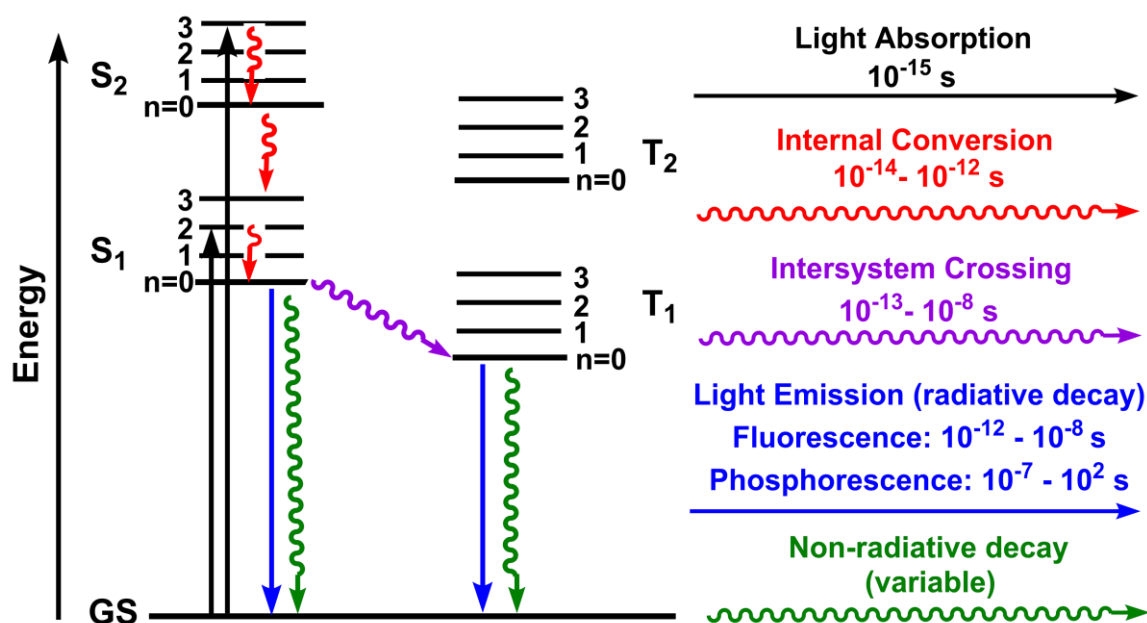
Figure 1.1 Generalized Jablonski diagram for a molecular chromophore. Pertinent deactivation pathways and rate information are color coded and labeled.

Light absorption is shown on the left-hand side of the diagram. It occurs from the ground state of the molecule (GS) to the S_1 or S_2 excited state. Here, S stands for singlet and reflects the fact that the spin of the electron in the excited state is still spin paired with the electron remaining in the ground state (s = +1/2 and -1/2). Excitation to the S_1 state represents the lowest energy singlet, electronic transition for a given molecule and results from excitation from the HOMO to the LUMO. Transitions to S_2 and all other higher

level S_n (n > 2) excited states result from excitation to and from other, higher energy frontier orbitals i.e. HOMO-1 to LUMO+1, HOMO-2 to LUMO+1, etc. Light absorption by a molecule is extremely fast, resulting in population of the excited state on the order of 10^{-15} s. Absorption transitions are vertical lines due to the fact that electronic excitation occurs faster than nuclear rearrangement can occur within the molecule; thus, the electronic transition occurs without changes in nuclear coordinates. This principle is known as the Franck-Condon approximation, and, therefore, the initially formed excited state is called a Franck-Condon excited state.

Generally, initial decay of the excited occurs via internal conversion. Internal conversion processes describe vibrational relaxation of the initially excited molecule within a particular electronic excited state or to a lower electronic excited state of the same spin multiplicity. In Figure 1.1, electronic excitation to the S_2 excited state results in the population of the n=3 vibrational level. The S_2 state rapidly decays to the n=0 vibrational level before further relaxing to populate the S_1 state. The S_1 state can then decay through intersystem crossing to a state of different spin multiplicity, radiative deactivation, or non-radiative deactivation. It is important to note that internal conversion processes are commonly fast relative to all other possible deactivation pathways. In this regard, reactivity in excited moieties not only commonly occurs from the n=0 vibrational level of a given excited state but from the n=0 vibrational level of the lowest energy, accessible, electronic excited state. That is to say, excitation of the S_2 excited state ordinarily results in reactivity from the n=0 vibrational level of the S_1 state or some lower energy excited state of different spin multiplicity (vide infra). This phenomenon is referred to as Kasha's rule. There are exceptions to this rule in the literature, but a vast

majority of chromophores follow Kasha's rule. With this in mind, the treatment of the remaining possible excited state reaction pathways will be discussed in terms of reactivity from the rapidly equilibrated S_1 excited state.

Deactivation of the S_1 state can directly replenish the ground state species. This occurs through one of two main pathways. The molecule can radiatively return to the ground state by emitting a photon of light or it can return to the ground state non-radiatively through molecular vibrations and concomitant loss of excitation energy as heat. Radiative deactivation from the S_1 state is referred to as fluorescence because it occurs to a ground state of identical spin multiplicity. Fluorescence lifetimes are on the picosecond to nanosecond time scale. Non-radiative deactivation of singlet excited states competes with fluorescence. Depending on the deactivation rate of the singlet excited state, the S_1 state can be quenched in discrete energy or electron transfer reactions. The theory and kinetics of excited state quenching will be presented in further detail later in Chapter 1. The S_1 state can also be deactivated via chemical reactions with the solvent or other moieties in solution to create unique photochemical products.

In some molecular systems, the S_1 state can undergo intersystem crossing to populate a lower energy triplet excited state, T_1, prior to radiative or non-radiative deactivation of the excited state. In this case, the triplet state designation refers to the fact that the spin of the electron in the excited state is no longer spin paired with the electron remaining in the ground state ($s = +1/2$ and $+1/2$ or $-1/2$ and $-1/2$); accordingly, the formation of the triplet excited state is facilitated by a change in spin angular momentum of the electron in the excited state. This change of spin state is generally observed when a heavy atom significantly contributes to the electron density distribution of the ground or

excited state. The inclusion of a heavy atom serves to enhance the rate of intersystem crossing relative to all other decay pathways. This effect is prominent in transition metal complexes of Re(I), Ru(II), Ir(III), Os(II), and Pt (II), where rates of intersystem crossing can approach 10^{13} s^{-1}! Intersystem crossing can also be observed in organic molecules containing heavy atoms, such as iodine. In these systems, intersystem crossing is much slower. Chapter 2 discusses the formation and reactivity of the long-lived triplet excited state of Sn(IV) Schiff Base Complexes. Intersystem crossing is found to occur with rate constants on the order of 10^{8} s^{-1}.

The T_1 excited state is subject to the same chemical decay pathways as the S_1 excited state. Radiative decay from the T_1 excited state to a singlet ground state is referred to as phosphorescence because it occurs between states of different spin multiplicities. It is important to note that radiative decay rate constants for phosphorescent transitions are generally much smaller than those for fluorescent transitions due to the spin change incurred during relaxation. Phosphorescent radiative decay rate constants range from the 10^{7} to 10^{-3} s^{-1}. Non radiative decay rate constants are also widely varied and are commonly competitive with radiative decay rate constants. The implications of the decrease in deactivation decay rate constant for phosphorescent transitions will also be discussed in greater detail later in Chapter 1.

1.2 The Kinetics of Excited State Decay

As mentioned above, excited state deactivation occurs from the lowest energy, thermally equilibrated excited state in a vast majority of molecules. And, the kinetics governing internal conversion are very fast relative to radiative or non-radiative deactivation of the excited state back to the ground state. The decay of an excited state

population ($[S^*]$) measured in a luminescence or transient absorption experiment can be expressed using a first-order kinetic decay in terms of the non-radiative (k_{nr}) and radiative (k_r) decay components. The combination of the non-radiative and radiative decay components of the excited state is generally expressed collectively as observed rate constant (k_o). The rate law for this first order expression is given in Equation 1.1 and the integrated rate law governing the first order decay dependent on k_r and k_{nr} is given in Equation 1.2.

$$-\frac{d[S*]}{dt} = (k_r + k_{nr})([S*]) = (k_o)([S*]) \tag{1.1}$$

$$[S*]_t = [S*]_0 exp^{-(k_o)t} \tag{1.2}$$

This allows for the fitting of lifetime decays obtained from luminescence and transient absorption measurements. It should also be noted that if two, unique excited state species are excited in a given experiment and they both decay according to the presented first-order kinetic model, the decay of the system will appear biexponential and reflect the effective k_o for each excited state.

The luminescence lifetime (τ) of a chromophore is defined as the inverse of k_o for the system (Equation 1.3). The lifetime of a chromophore can be easily estimated from a luminescence or transient absorption decay. When $t = \tau$, one e-fold worth (1/2.73) of the initial excited state population has decayed.

$$\tau_o = \frac{1}{k_o} = \frac{1}{k_r + k_{nr}} \tag{1.3}$$

Another important quantity, when discussing the decay of excited states, is the overall photonic efficiency of a process, or quantum yield (ϕ). The quantum yield relates the total number of photons that lead to a particular excited state event or outcome

relative to all of the photons absorbed by the excited state. In this dissertation, this quantity is generally expressed in terms of the quantum yield of luminescence. In particular, this value relates the number of emitting photons to the total absorbed photons (Equation 1.4).

$$\phi_{lum} = \frac{k_r}{k_r + k_{nr}} = \frac{\tau_o}{k_r} \qquad (1.4)$$

When k_r is small relative to k_{nr}, the luminescence quantum yield will approach zero. When the inverse is true, the luminescence quantum yield will approach unity. The quantum yield of luminescence for a given chromophore is relatively easy to determine as long as the quantum yield of luminescence of a reference chromophore (ϕ_S) is known. The quantum yield of an unknown chromophore can be determined from the integrated luminescence intensity of the standard (I_S) and unknown (I_{unk}) as well as the ground state absorption values of the standard (A_s) and the unknown (A_{unk}) (Equation 1.5).

$$\phi_{unk} = \phi_S * \frac{I_{unk}}{I_s} * \frac{A_s}{A_{unk}} \qquad (1.5)$$

Solutions of the standard and unknown with identical absorbance values at a particular wavelength are prepared. Any deviation in the absolute absorbance value is corrected for in Equation 1.5. The absorbance value of a sample is generally quite low when obtaining luminescence quantum yield values as this helps to avoid complications from the inner filtering effect that diminishes the intensity of the excitation source through the sample cell. Further, the luminescence standard should luminesce over the same wavelength range as the unknown sample so as to avoid inaccuracies resulting from the variability in detector sensitivity at different wavelengths, although this can be dealt with by correcting

emission spectra for the wavelength dependence of detector response. There are two recent publications that cover luminescence quantum yield standards[18] and measurements.[19] These articles provide a detailed overview on accurately determining luminescence quantum yields using the prescribed comparative method.

The preceding, detailed discussion is only valid for the limiting (but often encountered) case where the decay of the excited state is governed by radiative and non-radiative decay from the lowest energy, thermally equilibrated excited state. In the remainder of this section, I will discuss specialized kinetic conditions that are important in the interpretation and discussion of the data in subsequent Chapters. I will provide brief discussions of the kinetic case where intersystem crossing is competitive with radiative and non-radiative decay, the treatment of the decay data when triplet-triplet annihilation dominates excited state decay, and equal concentration, second order kinetics, which is important in fitting and understanding the recombination of charge separated species following photoinduced electron transfer reactions.

It is important to discuss a system where intersystem crossing is competitive with radiative and non-radiative decay from the singlet excited state as this is the exact kinetic scenario demonstrated in the series of Sn(IV) chromophores presented in Chapter 2. The lifetime, quantum yield of luminescence, and quantum yield of intersystem crossing for a chromophore under these conditions are given in Equations 1.6, 1.7, and 1.8, respectively.

$$\tau_o = \frac{1}{k_r + k_{nr} + k_{ISC}} \tag{1.6}$$

$$\phi_{lum} = \frac{k_r}{k_r + k_{nr} + k_{ISC}} \tag{1.7}$$

$$\phi_{ISC} = \frac{k_{ISC}}{k_r + k_{nr} + k_{ISC}} \tag{1.8}$$

In order to calculate the rate constant values for the individual processes, all three of these values must be known for the particular chromophores. In the case of the Sn(IV) chromophores discussed in Chapter 2, we were able to determine the lifetime of the singlet state using time correlated single photon counting, the luminescence quantum yield from steady state luminescence spectra, and the quantum yield of intersystem crossing from transient absorption measurements.

For complexes that access long-lived triplet excited states, it is also important to consider the contribution of triplet-triplet annihilation to the deactivation of the excited state. Triplet-triplet annihilation occurs when two excited triplet states interact to create one molecule in the singlet ground state and one molecule in the singlet excited state. This decay pathway is unique because it combines an equal concentration, second-order triplet-triplet annihilation kinetic decay term (k_{TT}) and a first-order decay term. The rate law for this combined kinetic decay is given in Equation 1.9 and the integrated rate law governing the first is given in Equation 1.10.[20,21]

$$-\frac{d[^3S*]}{dt} = (k_{TT})\left([^3S*]^2\right) + k_o[^3S*] \tag{1.9}$$

$$[^3S*]_t = \frac{[^3S*]_o exp^{-k_o t}}{1 + [^3S*]_o(\frac{k_{TT}}{k_o})(1 - exp^{-k_o t})} \tag{1.10}$$

Kinetic decay traces obtained from all of the Sn(IV) complexes in solution were non-exponential, regardless of chromophore concentration or laser power. For fits of transient absorption decays in acetonitrile with Equation 1.10, k_{TT} is on the order of 10^{10} s^{-1} and the value of k_o is on the order of 10^2 - 10^3 s^{-1}. The value of k_o obtained from these data fits is

substantiated by the single exponential lifetime values obtained for each of the complexes in solid PMMA matrices. In these experiments, k_o ranges from 80 s^{-1} for [PhSnLdeaCl$_2$] to 1,800 s^{-1} for [PhSnLBrCl$_2$].

Finally, a succinct presentation of equal concentration second order kinetics is also necessary. This kinetic treatment is important for describing the kinetic recombination of the charge separated species formed following photo-induced electron transfer reactions. The rate law for this process is given in Equation 1.11 and the integrated rate expression is given in Equation 1.12.

$$-\frac{d[S*]}{dt} = k_{SO}[S*]^2 \tag{1.11}$$

$$\frac{1}{[S*]_t} = k_{SO}t + \frac{1}{[S*]_o} \tag{1.12}$$

Equation 1.16 can be used to explicitly fit plots of 1/ΔAbs. vs. t obtained in a laser flash photolysis experiment; thus, allowing for the determination of the rate constant for electron-hole recombination following a photoredox reaction.

1.3 Bimolecular Quenching of Excited States: The Stern-Volmer Relationship

A molecular excited state can be deactivated by a number of bimolecular reactions, including the formation of ground state dimers, static quenching involving the incorporation of the ground state molecule and a quencher species prior to excitation, and dynamic quenching resulting from an excited chromphore diffusing in solution and interacting with a quencher molecule in solution. Although possible, the formation of ground state dimers and static quenching are rare; therefore, this section will provide a derivation and discussion of the expression governing the dynamic quenching of excited molecules in solution. This expression is obtained by comparing the quantum yield of luminescence of a particular species in the presence and absence of a quencher. The

derivation relating the lifetime and intensity of the quenched luminescence to the unquenched luminescence is given in Equation 1.13.

$$\frac{\phi_r^0}{\phi_r} = \frac{I_o}{I} = \frac{\tau_o}{\tau} \frac{\frac{k_r}{k_r + k_{nr}}}{\frac{k_r}{k_r + k_{nr} + k_Q[Q]}} = 1 + k_Q\tau_o[Q] = 1 + K_{SV}[Q] \qquad (1.13)$$

For dynamic quenching processes, the ratio of the unquenched luminescence intensity and lifetime to quenched luminescence intensity and lifetime depends on k_q, the bimolecular quenching rate constant of the excited state, the quencher concentration, and the unquenched lifetime of the excited state. In a typical experiment, the ratio of the unquenched to quenched luminescence intensity or the ratio of the unquenched to quenched luminescence lifetime, quencher concenration, and the unquenched lifetime are known. This allows for the determination of k_q for a particular quencher. It should also be noted that chromophores with longer unquenched luminescence lifetimes can be more efficiently quenched in bimolecular processes. In this regard, phosphorescent excited states are generally more efficient due to decreased rates of deactivation relative to fluorescent excited states.

1.4 The Use of Transient Absorption to Monitor Excited State Reactions

This section will briefly introduce Beer-Lambert's law, and then apply it to transient absorption measurements that are relevant to the research discussed in Chapters 2, 3, and 4. Beer-Lambert's law is given in Equation 1.14.

$$A = -\log T = -\log \frac{I_{sample}}{I_{reference}} = \epsilon l c \qquad (1.14)$$

For this series of equations, A is the absorbance of the sample, T is the transmittance of the sample, ϵ the extinction coefficient or molar absorptivity in units of $M^{-1}cm^{-1}$, l is the

path length of the cell in cm, and c in the concentration of the sample given in molarity, M. The absorbance of a sample varies logarithmically with the transmittance of the sample. $I_{reference}$ is the initial intensity of the light source and is generally collected after passing through a cuvette with a given volume of pure solvent. Some amount of the sample molecule is added to the solvent in the cuvette or a serial dilution of a stock solution of the sample molecule is added to the cuvette, and the intensity of the light passing through the cuvette is collected again (I_{sample}). The ratio of these two values represents the transmittance of the sample and can be used to determine the absorbance value of the solution. The absorbance of the solution also varies linearly with the solution concentration when using a fixed cell path length. The proportionality constant for this relationship is referred to as the molar absorptivity or extinction coefficient, ε, and is usually expressed in terms of $M^{-1}cm^{-1}$. The larger the value of ε at a given wavelength, the greater the number of photons absorbed per unit concentration at that wavelength.

In a given laser flash photolysis experiment, we excite some fraction of the ground state molecules in the path of the laser pulse. This results in a time-dependent absorption value at a given wavelength that is related to the linear combination of the initial ground state absorption spectrum and the absorption spectrum of the excited state. This expression is given in Equation 1.15

$$\Delta ABS_t = \varepsilon_{ES} * l * [ES]_t - \varepsilon_{GS} * l * \Delta[GS]_t \qquad (1.15)$$

where ΔABS_t is the change in absorbance of the sample at a given wavelength some time after the laser pulse, ε_{ES} and ε_{GS} are the molar absorptivity of the excited state and ground state at a given wavelength, the path length of the cell is typically 1 cm, and $[ES]_t$ and $\Delta[GS]_t$ are the concentration of the excited state and the change in ground state

concentration of the chromophore at some time after the laser pulse. The initial values of $[ES]_t$ and $\Delta[GS]_t$ are equivalent because the loss of ground state molecules is equal to the number of excited states created. They are both represented as positive values, by convention, so that in the transient absorption spectrum wavelengths where the ground state of the molecule absorb will result in a negative ΔABS value, whereas, absorption that is unique to the excited state of the molecule will appear with a positive ΔABS value. The transient absorption spectrum of a given chromophore can be complicated in cases when the excited state observed by transient absorption is also luminescent on the time scale of the measurement. This is manifest in the fact that the photons emitted by the molecule appear as negative ΔABS values because there is an enhancement in the intensity of light incident on the detector at these wavelengths relative to the reference intensity.

Application of Beer-Lambert's law can also allow for the determination of the molar absorptivity of the excited state at a given wavelength, if the ground and excited state absorption do not overlap then the total number of excited states created can be determined directly. The total number of excited states created can also be determined with the use of a chemical actinometer. To this end, the excited state of a given chromophore is completely quenched by a known energy transfer quencher (Q), and the molar absorptivity of the excited quencher (ε_Q) is known at given wavelength. Dividing the observed ΔABS by the known excited state molar absorptivity value of the quencher gives a rough estimate of the total excited created in a given laser pulse. This concentration value can then be applied to the transient absorption spectrum of a chromophore at wavelengths that are unique to the excited state. This yields a reasonable

approximation of the excited state molar absorptivity. The change in absorbance for a system following energy transfer is demonstrated in Equation 1.16.

$$\Delta ABS_t = \varepsilon_{ES} * l * [ES]_t + \varepsilon_Q * l * [Q]_t - \varepsilon_{GS} * l * \Delta[GS]_t \qquad (1.16)$$

For the case where the excited state of the complex is completely quenched by the acceptor, the observed absorbance only includes the absorbance of quencher because we have completely quenched all of the excited states and replenished the ground state of the complex. Again, if we know the excited state molar absorptivity of the quencher, we can determine the total concentration of excited states created in a given laser pulse. There is an expansive Journal of Physical Chemistry Reference Data[17] article that catalogs the known triplet-triplet absorption spectra of organic acceptors in solution. This article also includes a detailed discussion of the determination of excited state molar absorptivity values.

The one electron reduction and oxidation chemistry of a number of electron transfer quenchers is reversible. This allows for the determination of the molar absorptivity of the one electron reduced and oxidized species using spectroelectrochemistry. If the absorption spectra of the one electron oxidized (O) and reduced (R) species formed in a photo-redox reaction do not overlap with each other or the loss of ground state absorption after electron transfer, the concentration of the reduced and oxidized products can be easily determined using the excited state molar absorptivity value for a particular component of the system at a given wavelength. Even if the photo-redox products do have overlapping absorption at some wavelength, the concentration can be determined using $\Delta\varepsilon$ at that wavelength. The change in absorbance for the system following electron transfer is presented in in Equation 1.17.

$$\Delta ABS_t = \varepsilon_{ES} * l * [ES]_t + \varepsilon_O * l * [O]_t + \varepsilon_R * l * [R]_t - \varepsilon_{GS} * l * \Delta[GS]_t \quad (1.17)$$

In this case, if the initial excited state is completely quenchied, the transient absorption spectrum will represent absorption from the oxidized and reduced species and the loss of ground state absorption; thus, if we know molar absorptivity values for the reduced or oxidized species and they occur at unique wavelengths, we can determine the concentration of the electron transfer products. This can be extremely important when determining the rate constants of back electron transfer.

1.5 Closing Remarks

This Chapter provides a general overview of the behavior of, and the terminology used to describe molecules after light absorption and their subsequent deactivation. The excited state behavior of many systems is nuanced and variable. The work in the following Chapters utilizes ultrafast spectroscopic methods to observe the creation and evolution of molecular excited states. These measurements are used in combination with steady-state absorption and luminescence intensity, luminescence lifetime and nanosecond time-resolved absorption measurements to provide a complete kinetic understanding of the deactivation of the observed molecular excited states. This encompassing approach allowed for the thorough investigation of the excited state behavior of three distinct groups of inorganic molecules: Chapter 2 explores intersystem crossing and the reactivity of the singlet and triplet excited states in a series of Sn(IV) Schiff Base complexes, Chapter 3 utilizes ultrafast time-resolved transient infrared measurements to make definite excited state assignments in Re(I) complexes when luminescence and nanosecond transient absorption measurements are inconclusive, and

Chapter 4 explores the control of excited state energy transfer processes using variations in solution pH.

CHAPTER 1 REFERENCES

(1) Adamson, A. W.; Fleischauer, P. D. *Concepts of Inorganic Photochemistry;* John Wiley and Sons: New York, 1975.

(2) Balzani, V.; Campagna, S.; Accorsi, G. *Photochemistry and Photophysics of Coordination Compounds I;* Springer: Berlin; New York, 2007; Vol. 280.

(3) Balzani, V.; Campagna, S.; Accorsi, G. *Photochemistry and Photophysics of Coordination Compounds II;* Springer: Berlin ; New York, 2007; Vol. 281.

(4) Balzani, V.; Carassiti, V. *Photochemistry of Coordination Compounds;* Academic Press: New York, 1970.

(5) Balzani, V.; Ceroni, P.; Juris, A. *Photochemistry and Photophysics: Concepts, Research, Applications;* Wiley: Weinheim, 2014.

(6) Barltrop, J. A.; Coyle, J. D. *Principles of Photochemistry;* Wiley: New York, 1978.

(7) Coyle, J. D. *Introduction to Organic Photochemistry;* Wiley: New York, 1986.

(8) Figgis, B. M. *Introduction to Ligand Fields;* John Wiley and Sons: New York, 1966.

(9) Gilbert, A.; Baggott, J. E. *Essentials of Molecular Photochemistry;* Blackwell Scientific Publications: Oxford ; Boston, 1991.

(10) Hoffman, M. Z.; Bolletta, F.; Moggi, L.; Hug, G. L. *J. Phys. Chem. Ref. Data* **1989***, 18*, 219.

(11) Juris, A.; Balzani, V.; Barigelletti, F.; Campagna, S.; Belser, P.; Von Zelewsky, A. *Coord. Chem. Rev.* **1988***, 84*, 85-277.

(12) Kalyanasundaram, K. *Photochemistry of Polypyridine and Porphyrin Complexes;* Academic Press: London, 2002.

(13) Kalyanasundaram, K. *Coord. Chem. Rev.* **1982***, 46*, 159-244.

(14) Seery, M. The Photochemistry Portal: Principles, Applications, and Experimentation in Modern Photochemistry. *www.photochemistry.wordpress.com*.

(15) Turro, N. J.; Ramamurthy, V.; Scaiano, J. C. *Modern Molecular Photochemistry of Organic Molecules;* University Science Books: Sausalito, 2010.

(16) Valeur, B. *Molecular Fluorescence: Principles and Applications;* Wiley: Weinheim, 2002.

(17) Carmichael, I.; Hug, G. L. *J. Phys. Chem. Ref. Data* **1986***, 15*, 1.

(18) Brouwer, A. M. *Pure Appl. Chem.* **2011***, 83*, 2213.

(19) Resch-Genger, U.; Rurack, K. *Pure Appl. Chem.* **2013***, 85*, 2005.

(20) Bachilo, S. M.; Weisman, R. B. *J. Phys. Chem. A* **2000***, 104*, 7711.

(21) Singh-Rachford, T. N.; Castellano, F. N. *Coord. Chem. Rev.* **2010***, 254*, 2560.

CHAPTER 2: Sn(IV) Schiff Base Complexes: Triplet Photosensitizers for Photoredox Reactions

2.1 Traditional Transition Metal Photosensitizers

There has been a great deal of work on exploiting transition metal complex chromophores as sensitizers in artificial photosynthetic systems for conversion and storage of solar energy. The majority of such systems rely on the sensitizer to serve as a single electron donor or acceptor following visible light excitation. These chromophores are typically second and third row transition metal complexes because they have excited state lifetimes in the microsecond time regime, often exhibit stability in multiple oxidation states, and are luminescent, allowing both the excited state energy and lifetime to be determined conveniently. The desirable, relatively long excited state lifetimes result from the fact that the photoactive excited states are all of triplet spin multiplicity while the ground states are of singlet multiplicity. The formation of triplet excited states is facilitated by the presence of the metal due to large spin-orbit coupling matrix elements that enhance intersystem crossing. The majority of published work focuses on complexes of Ru(II), Os(II), Ir(III), Re(I) and Pt(II). A common criticism of artificial photosynthetic systems involving these complexes has been the relative scarcity of these elements; all are among the nine rarest elements in the earth's crust.

2.2 The Use of Sn Complexes as Photosensitizers

A clear challenge for the photochemistry community is the development of complexes that have redox and photophysical properties similar to those used in existing

artificial photosynthetic systems, but employ earth-abundant metals. Our intent is to utilize complexes that are easily prepared and have visible electronic transitions. The objective for the metal is to use an element with a large spin-orbit coupling matrix element (similar to the noble metals) that forms complexes that are stable in multiple oxidation states. Also, as a pedagogical point of interest, we wanted to investigate molecules that may contain non-phosphorescent long-lived excited states. In this regard, it appeared that complexes of either Sn(II) or Sn(IV) might be appropriate since Sn is relatively abundant in the earth's crust and has a spin-orbit coupling matrix element significantly greater than that of Ru, which is widely used in metal complex sensitizers[1].

There are a number of articles addressing the photoreactivity of Sn complexes in the literature. These reports mainly focus on the photochemistry of Sn(II) and Sn(IV) aquo, halide, hydroxo, and cluster complexes[2-8], Sn porphryins[9-28], phthalocyanines[29-33], and corroles[34-37], and transition metal complexes utilizing organotin compounds as a ligand[38-47]. The simple Sn(IV) complexes (halides, hydroxo, etc.) typically absorb in the ultraviolet, do not luminesce and exhibit irreversible photochemistry from LMCT excited states. Sn(II) complexes mainly access metal based s $\rightarrow$ p type excited states, some of which are luminescent at room temperature. Octahedral Sn(II) clusters also access s $\rightarrow$ p metal based excited states. These clusters show a red shift in their luminescence due to metal-metal bonding interactions. Sn(II)/Sn(IV) halide bridged dimers have also been investigated and are known to exhibit MMCT transitions. Metal-to-Ligand Charge Transfer (MLCT) transitions are observed in Sn(II) bpy complexes and porphyrins. The literature on Sn porphyrins, phthalocyanines and corroles is extensive and includes reports of catalytic hydrogen reduction, sensitization in organic solar cells, and donor-

acceptor arrays. Sn macrocycles are also known to efficiently sensitize singlet oxygen and have been used in schemes for pollutant remediation and photodynamic therapy; here the excited states are largely localized on the macrocycle. Given these Sn complexes as a basis and recognizing both the rich redox chemistry and the extraordinarily large spin-orbit coupling coefficient of Sn, recent reports of a series of fluorescent Sn(IV) Schiff base derivatives with visible absorption[48,49] appeared to be an excellent entrée for investigation of triplet state formation and reactivity in Sn(IV) complexes.

2.3 Experimental

2.3.1 Spectroscopy

^{1}H and 2D-COSY NMR spectra were recorded on a Varian 400 MHz NMR. UV-vis absorption spectra were obtained on a Hewlett-Packard 8452A diode array spectrophotometer. Photoluminescence spectra were obtained using a PTI Quantamaster spectrophotometer fit with a Hammamatsu R928 PMT detector.

2.3.2 Nanosecond Time-Resolved Transient Absorption.

Nanosecond transient absorption measurements were performed using a Qunatel Brilliant B Q-switched Nd:YAG laser-pumped OPO (Opotek) at a right angle to the analyzing light source. Excitation pulses were < 5 ns. An Applied Photophysics LKS.60 laser flash photolysis spectrometer was used for detection; the instrument is equipped with a 150 W pulsed Xe arc lamp as the analyzing light source, a single grating monochromator (Applied Photophysics 0.25 m) after the sample, and PMT detection (Hamamatsu R928). The output was recorded on an Agilent Infinium transient digitizer. Data was acquired and analyzed with Applied Photophysics LKS.60 software. The quantum yield of triplet state formation and excited state molar absorptivity was

determined for the series of complexes using a $[Ru(bpy)_3]^{2+}$ standard and photosensitization of anthracene. The change in optical density of a sample of $[Ru(bpy)_3]^{2+}$ at 370 nm resulting from a 10 mJ pulse of 450 nm laser light was determined. Using the excited state molar absorptivity of $[Ru(bpy)_3]^{2+}$ at 370 nm[50], the concentration of triplet excited states can be calculated. Samples of each Sn complex were absorbance matched with the $[Ru(bpy)_3]^{2+}$ standard and quenched with a 0.01 M solution of anthracene in acetonitrile. The resulting change in absorbance at 420 nm[51] allows for the determination of the concentration of anthracene triplet formed. The concentration of excited anthracene is equal to the concentration of Sn complex triplet excited states created in the laser pulse. The ratio of Sn triplet excited states created to the number of $[Ru(bpy)_3]^{2+}$ triplet excited states created gives the quantum yield of triplet state formation. The excited state molar absorptivity at any wavelength can also be determined by dividing the change in optical density immediately following excitation by the concentration of Sn complex triplet excited states created in the pulsed laser experiment.

2.3.3 Femtosecond Time-Resolved Transient Absorption

Ultrafast time-resolved transient absorption measurements were collected in collaboration with the group of Professor Jeffrey Rack at Ohio University. I greatly appreciative the effort of Albert King (OU graduate student) in collecting this data as well as providing detailed analysis of the kinetic decays obtained in the experiment.

Femtosecond transient absorption measurements were collected on an Ultrafast Systems HELIOS transient absorption spectrometer. A Spectra Physics Solstice laser, a one-box regenerative amplifier containing a Mai Tai femtosecond oscillator and

Empower pump laser, was employed to produce 800 nm pulses at a repetition rate of 1 kHz at 3.5 W average power and a pulse width of <100 fs. From this unit, the beam is split (50:50) with one beam directed to an optical parametric amplifier (TOPAS, Light Conversion) and the other to the HELIOS spectrometer (He-vis-3200) to create the pump (TOPAS) and probe (HELIOS) sources, respectively. The 800 nm probe beam passed through a CaF_2 plate to generate a white light continuum (~330-700 nm). The spectrum was integrated for 2 s each scan. The pump and probe beams were directed to a 2 mm path length cuvette containing the sample where they were spatially overlapped. The solution was vigorously stirred in the 2 mm path length cuvette during data collection. Transient absorption data were corrected by subtracting spectral background features that persisted from the previous pulse and as well as applying chirp correction and T0 corrections using Surface Xplorer Pro 1.1.5 software (Ultrafast Systems).

2.3.4 Time Correlated Single Photon Counting (TCSPC).

Luminescence lifetimes were obtained using the time correlated single photon counting technique. Each sample was excited using an IBH NanoLED pulsed diode laser source (441 nm excitation, 200 ps pulse width). The emitted light was collected at right angle to the excitation pulse and collected by an IBH Model TBX-04 cooled photomultiplier (PMT) detector. The output of the PMT served as the input for the stop channel of the time to amplitude converter (TAC, Tennelec TC-863). Start pulses for the TAC were obtained from the synchronous TTL output of the NanoLED laser source. The ouput from the TAC was directed to the multichannel analyzer (Ortec, Easy MCA) where the signal was accumulated. Laser light scattered from the nonluminescent solution was used to accumulate instrument response profiles. The data were analyzed using the

deconvolution routine in Origin 9.

2.3.5 Cyclic Voltammetry.

Cyclic voltammetry was performed on a CH Instruments CH1730A Electrochemical Analyzer. The working electrode was a glassy-carbon electrode, the counter electrode was a Pt wire, and the reference electrode was an aqueous $Ag^+/AgCl$ electrode. All cyclic voltammetry data was collected in acetonitrile solutions containing 0.1 M $TBAPF_6$. The presented sweep segments were collected at a scan rate of 100 mV/s.

2.3.6 Computational Details.

DFT calculations were performed using the Gaussian 09 software package.[52] All calculations were performed with the B3LYP functional. LANL2DZ with the electron core potentials of Hay and Wadt for Sn[53] and the 6-31G(d,p) basis set for all other atoms. No negative vibrational frequencies were observed, supporting the validity of the geometry optimized structures.

2.4 Sn(IV) Complexes of the form [PhSnNNOCl$_2$]

2.4.1 Synthesis

Ph_2SnCl_2, 8-aminoquinoline, 2-hydroxy-1-napthaldehyde, salicylaldehyde, 5-bromosalicylaldehyde, and 4-diethylaminosalicylaldehyde were all purchased from Sigma-Aldrich and used as received. Acetonitrile, absolute ethanol, diethylether, hexanes and toluene were obtained from Pharmco-AAPER and used as received.

2-hydroxy-1-naphthaldehydene-8-aminoquinoline (HLnap). The ligand 2-hydroxy-1-naphthaldehydene-8-aminoquinoline was synthesized as previously reported.[54] 1 g (6.9 mmol) 8-aminoquinoline and 1.19 g (6.9 mmol) 2-hydroxy-1-napthaldehyde were added to 40 mL absolute ethanol and allowed to stir for 12 hours. 2-hydroxy-1-

naphthaldehydene-8-aminoquinoline precipitates as the reaction progresses. The solid was isolated on fritted glass and washed with 25 mL cold absolute ethanol. 1.92 g (93% yield) of orange solid obtained. ^{1}H NMR (CDCl$_3$) δ: 9.29 (1 H, d, J = 11.1 Hz), 9.08 (1 H, d, J = 2.8 Hz), 8.20 (d, 1 H, J = 7.28 Hz), 8.00 (1 H, d, J = 8.28 Hz), 7.77 (1 H, d, J = 7.32 Hz), 7.68 (2 H, m), 7.60 (2 H, m), 7.51 (2 H, m), 7.28 (1 H, d, J = 7.48 Hz), 6.91 (1 H, d, J = 9.44 Hz).

[PhSnLnapCl$_2$]. 66.3 mg (4.6 x 10^{-4} mol) 8-aminoquinoline and 99.4 mg (4.6 x 10^{-4} mol) 2-hydroxy-1-napthaldehyde were added to 15 mL toluene and refluxed for 15 h. The reaction was removed from heat and allowed to cool to room temperature. 160 mg (4.6 x 10^{-4} mol) Ph$_2$SnCl$_2$ was added to the reaction vessel. The toluene was removed via rotary evaporation and the resulting orange precipitate was collected on fritted glass, washed with hexanes (30 mL) and diethylether (15 mL), and dried in vacuo. 229.5 mg (89% yield) of orange solid was obtained. The synthesis of the salicylaldhyde containing derivatives were carried out in identical fashion. ^{1}H NMR (CD$_3$CN) δ: 9.90 (1 H, J$_{Sn-H}$ = 97.7 Hz, 94.5 Hz), 8.85 (1 H, d, J$_{H-H}$ = 7.88 Hz), 8.55 (1 H, d, J$_{H-H}$ = 4.16 Hz), 8.49 (2 H, m), 8.33 (2 H, J$_{H-H}$ = 6.16 Hz), 8.17 (1 H, d, J$_{H-H}$ = 8.24 Hz), 8.08 (2 H, m), 7.87 (2 H, m), 7.69 (1 H, t, J$_{H-H}$ = 7.84 Hz), 7.62 (3 H, m), 7.48 (1 H, t, J$_{H-H}$ = 7.44 Hz), 7.01 (1 H, d, J$_{H-H}$ = 9.16).

[PhSnLdeaCl$_2$]. 74.3 mg (5.2 x 10^{-4} mol) 8-aminoquinoline, 99.4 mg (5.2 x 10^{-4} mol) 4-diethylaminosalicylaldehyde, and 189.5 mg (5.5 x 10^{-4} mol) Ph$_2$SnCl$_2$ were used in the synthesis. 246.8 mg (81% yield) of red solid was obtained. ^{1}H NMR (CD$_3$CN) δ: 8.74 (1 H, d, J$_{H-H}$ = 7.84 Hz), 8.70 (1 H, J$_{Sn-H}$ = 103.2 Hz, 99.5 Hz), 8.42 (1 H, d, J$_{H-H}$ = 4.08 Hz), 8.32 (2 H, J$_{H-H}$ = 7.48 Hz, J$_{Sn-H}$ = 134.8 Hz, 119.8 Hz), 8.14 (1 H, d, J$_{H-H}$ = 7.60

Hz), 7.97 (2 H, m), 7.74 (2 H, dd, J_{H-H} = 3.4 Hz, 7.08 Hz), 7.57 (3 H, m), 7.37 (1 H, d, J_{H-H} = 9.24 Hz), 6.48 (1 H, d, J_{H-H} = 9.20 Hz), 5.96 (1 H, s), 3.47 (4 H, q, J_{H-H} = 7.12 Hz), 1.19 (6H, t, J_{H-H} = 7.08 Hz).

[PhSnLsalCl$_2$]. 90 μl salicylaldehyde (8.2 x 10^{-4} mol), 121.2 mg (8.4 x 10^{-4} mol) 8-aminoquinoline, and 288.2 mg (8.4 x 10^{-4} mol) Ph$_2$SnCl$_2$ were used in the synthesis. 301.5 mg (71%) of yellow solid was obtained. ^{1}H NMR (CD$_3$CN) δ: 9.19 (1 H, J_{Sn-H} = 90.5 Hz, 87.0 Hz), 8.82 (1 H, d, J_{H-H} = 8.04 Hz), 8.50 (1 H, d, J_{H-H} = 4.24 Hz), 8.41 (1 H, d, J_{H-H} = 7.80 Hz), 8.29 (2H, J_{H-H} = 7.52 Hz, J_{Sn-H} = 135.8 Hz, 121.6 Hz), 8.20 (1 H, d, J_{H-H} = 8.28 Hz), 8.02 (1 H, t, J_{H-H} = 8.12 Hz), 7.81 (1 H, dd, J_{H-H} = 4.96 Hz, 8.28 Hz), 7.67 (1 H, d, J_{H-H} = 7.12 Hz), 7.60 (4 H, m), 6.98 (1 H, t, J_{H-H} = 7.44 Hz), 6.84 (1 H, d, J_{H-H} = 8.48 Hz).

[PhSnLBrCl$_2$]. 106.7 mg 5-bromosalicylaldehyde (5.3 x 10^{-4} mol), 74.2 mg (5.1 x 10^{-4} mol) 8-aminoquinoline, and 177.3 mg (5.2 x 10^{-4} mol) Ph$_2$SnCl$_2$ were used in the synthesis. 235.6 mg (78%) of yellow solid was obtained. ^{1}H NMR (CD$_3$CN) δ: 9.12 (1 H, J_{Sn-H} = 87.5 Hz, 84.8 Hz), 8.83 (1 H, d, J_{H-H} = 7.88 Hz), 8.50 (1 H, d, J_{H-H} = 4.36 Hz), 8.39 (1 H, d, J_{H-H} = 7.88 Hz), 8.27 (2 H, J_{H-H} = 6.12 Hz, J_{Sn-H} = 135.5 Hz, 121.5 Hz), 8.23 (1 H, d, J_{H-H} = 9.60 Hz), 8.03 (1 H, t, J_{H-H} = 7.84 Hz), 7.81 (2 H, m), 7.60 (4 H, m), 6.79 (1 H, d, J_{H-H} = 8.76 Hz).

2.4.2 Results and Discussion

Four tin complexes containing tridentate Schiff-Base ligands, [PhSnLnapCl$_2$], [PhSnLsalCl$_2$], [PhSnLBrCl$_2$], and [PhSnLdeaCl$_2$]; HLnap is 2-hydroxy-1-naphthaldehydene-8-aminoquinoline, HLsal is salicylaldehydene-8-aminoquinoline, HLBr is 5-bromosalicylaldehydene-8-aminoquinoline, and HLdea is 4-

diethylaminosalicylaldehydene-8-aminoquinoline) were synthesized and investigated. The ligands are prepared via an imine forming condensation reaction of 8-aminoquinoline with various salicylaldehyde derivatives and 2-hydroxy-1-napthaldehyde. The complexes were prepared in a one pot process via the addition of Ph_2SnCl_2 to a solution of the freshly prepared ligand in toluene. As the reaction progresses, the tin complex precipitates from solution. An illustration of these reaction schemes is shown in Figure 2.1. HLnap was independently prepared by reaction of the 2-hydroxy-1-napthaldehyde with 8-aminoquinoline in absolute ethanol as previously reported.[54]
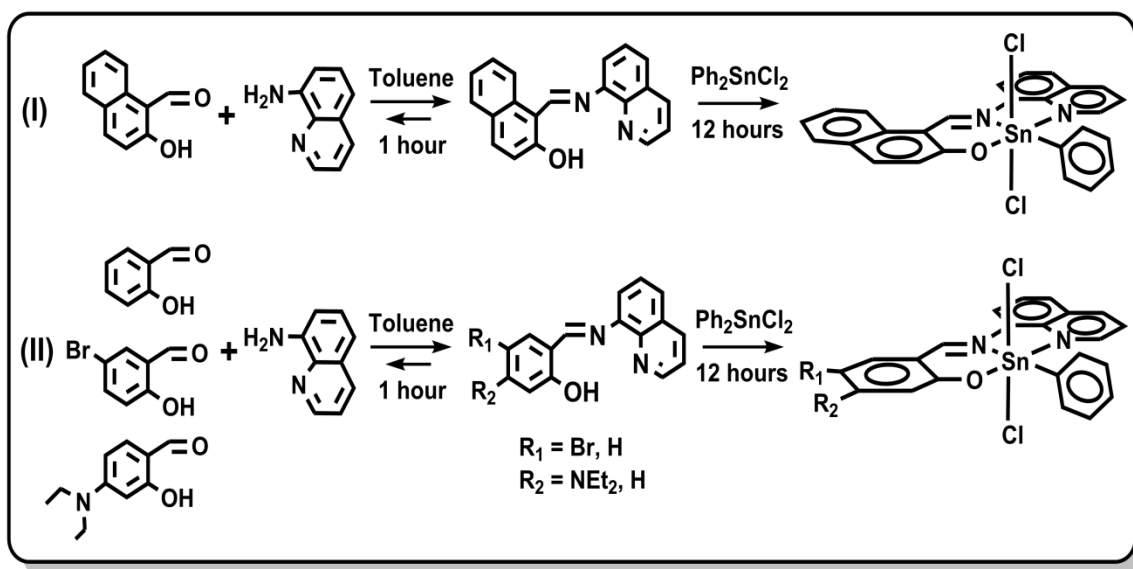
Figure 2.1 Reaction scheme utilized to synthesize the series of $PhSnLCl_2$ complexes. (I) Synthesis of $PhSnLnapCl_2$ from the in-situ generation of the NNO ligand from 8-aminoquinoline and 2-hydroxy-napthaldehyde. (II) Synthesis of the salicylaldhyde, NNO ligand derivatives: $PhSnLsalCl_2$, $PhSnLBrCl_2$, and $PhSnL4deaCl_2$.

Crystal structures have been obtained for all of the complexes and are presented along with pertinent refinement data in section 2.4.2.2 X-Ray Crystallography. Each structure confirms the presence of the phenyl ring and trans geometry of the chloride ligands. The complexes were further characterized by ^{1}H NMR spectroscopy; the spectra clearly indicate [119]Sn (8.59%) and [117]Sn (7.68%) coupling to the ortho protons of the tin bound

phenyl ring and the imine proton of the various NNO ligands. Other coupling assignments were made using ^{1}H-^{1}H COSY. A discussion of the ^{1}H NMR spectra of the complexes (Figures 2.2-2.6) is included in the following section, 2.4.2.1. ^{1}H NMR.

2.4.2.1 ^{1}H NMR
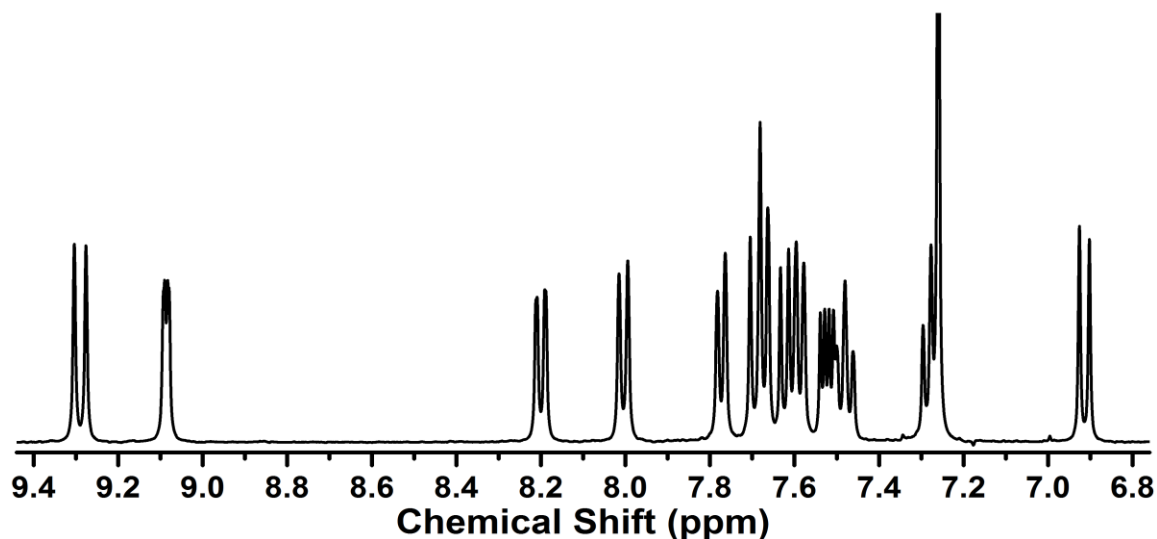
Figure 2.2 ^{1}H NMR spectrum of HLnap in d-chloroform. The spectrum has been edited to show only the resonances resulting from the ligand. The ^{1}H NMR spectrum of this complex also contains H_2O, a slight amount of EtOH.

The ^{1}H-^{1}H COSY spectrum (Figure 2.3) of [PhSnLnapCl$_2$] will be discussed in detail as assignment of the ^{1}H resonances for [PhSnLnapCl$_2$] also allows for the assignment of the ^{1}H resonances for all of the other complexes. The proton at 9.90 ppm does not couple to any other protons. The resonance at 8.33 ppm is coupled only to the multiplet at 7.62 ppm. The quinoline ring has two sets of three protons that should couple in a dtd fashion. One set contains the resonances at 8.49 (d), 8.05 (t), and 8.17 (d) ppm. The other contains the resonances at 8.55 (d), 7.84 (dd), and 8.85 (d) ppm. The resonance at 7.84 ppm appears as a doublet of doublets in NMR spectra of all the complexes. The 2-hydroxynapthaldehyde ring contains the coupling of the doublets at 8.08 and 7.01 ppm and the set of resonances at 7.87 (d), 7.48(t), 7.69 (t), and 8.46 (d) ppm.
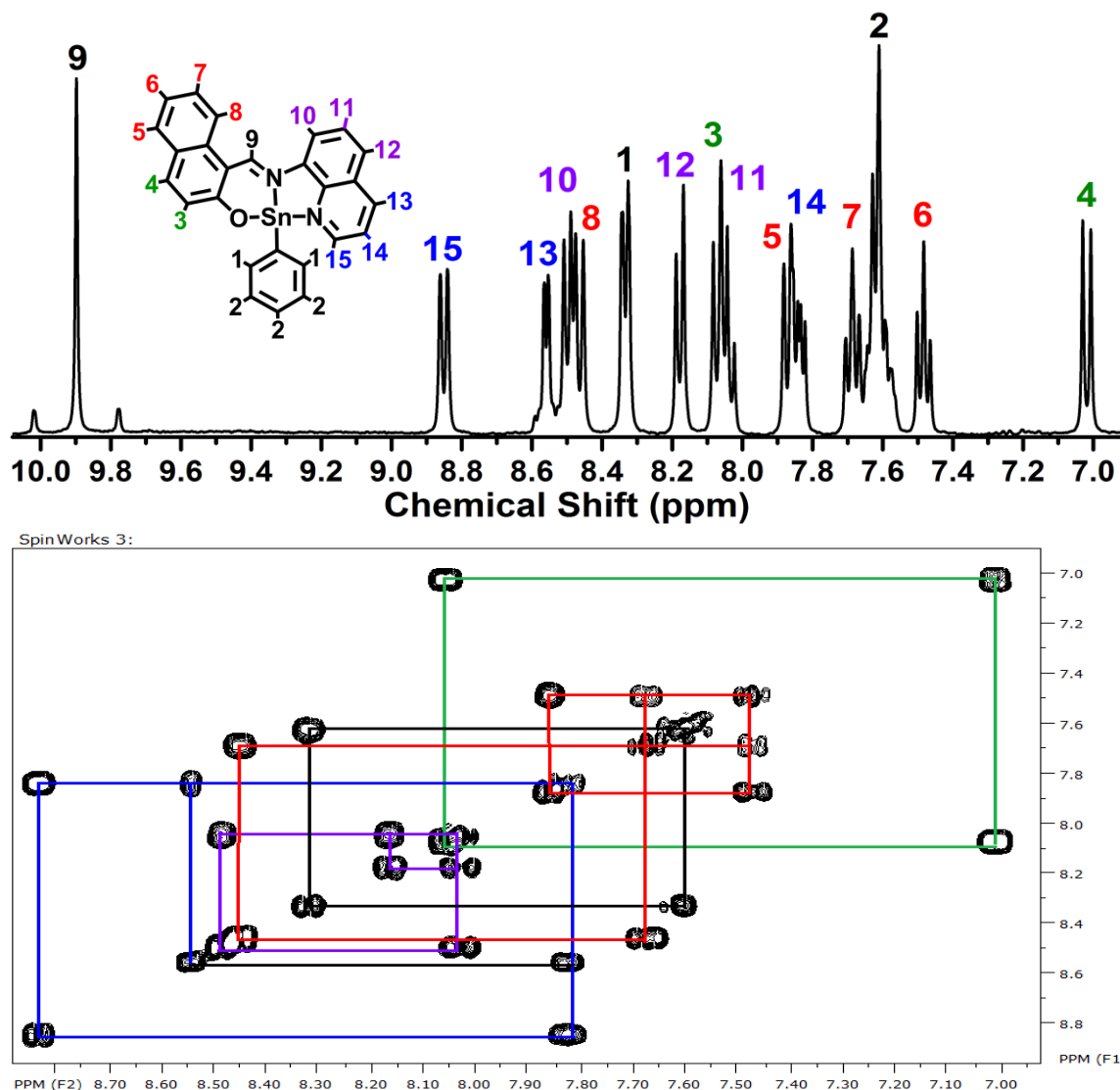
Figure 2.3 (Top) ^{1}H NMR spectrum of [PhSnLnapCl$_2$] in d$_3$-acetonitrile. The spectra have been edited to show only ^{1}H resonances resulting from the tin complex. The ^{1}H NMR spectrum of this complex also contains residual CH$_3$CN, H$_2$O, and n-hexane. (Bottom) ^{1}H COSY of [PhSnLnapCl$_2$] highlighting the region from 7 - 9 ppm.

Sn has three spin ½ isotopes: ^{119}Sn with a relative abundance of 8.7%, ^{117}Sn with a relative abundance of 7.1%, and ^{115}Sn with a relative abundance of 0.53% (coupling often not observed). The ortho-protons of the tin bound phenyl ring and the imine proton of the various NNO ligands couple with ^{119}Sn and ^{117}Sn. For all the complexes, the imine singlet occurs downfield of 8.7 ppm. The position of the imine resonance is significantly

influenced by the substitution of the aldehyde component of the ligand, ranging from 9.9

ppm in [PhSnLnapCl₂] to 8.74 ppm in [PhSnLdeaCl₂]. In contrast, the tin bound phenyl

ring is found as a doublet at ~8.30 ppm and a three proton multiplet at ~7.60 ppm in each

NMR spectrum. The splitting of the doublet resonance is most clear in the NMR

spectrum of [PhSnLBrCl₂] with coupling peaks at 8.11 ppm and on the downfield edge of

the 8.39 ppm resonance.
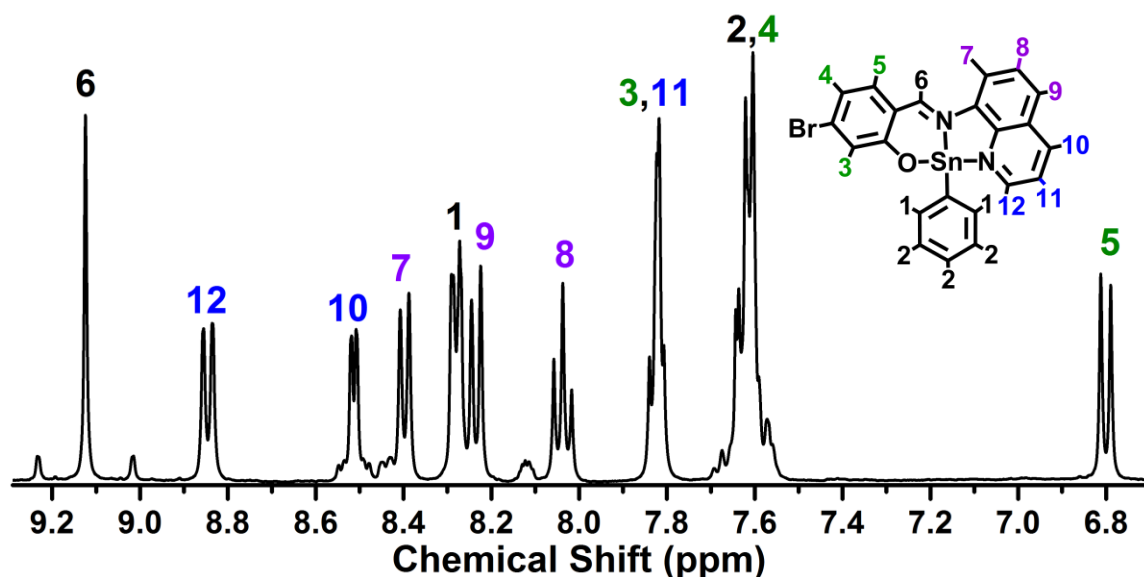
Figure 2.4 ¹H NMR spectrum of [PhSnLBrCl₂] in d₃-acetonitrile. The spectra have been edited to show only ¹H resonances resulting from the tin complex. The ¹H NMR spectrum of this complex also contains residual CH₃CN, H₂O, n-hexane.

The three resonances resulting from nitrogen containing ring of 8-aminoquinoline are

essentially identical in all of the spectra: the proton closest to the nitrogen atom appears

as the furthest downfield doublet (>8.8 ppm), the predicted triplet resonances occurs as a

doublet of doublets slightly downfield of 7.8 ppm, and the second doublet occurs

between 8.6 and 8.4 ppm with a characteristically small coupling constant (~4 Hz). The

three resonances belonging to the other ring of the quinoline moiety occur as a doublet at

~8.2 ppm, a triplet at ~8.0 ppm, and doublet which is found between 8.5-8.4 ppm in the

spectra of all complexes other than [PhSnLdeaCl$_2$] where it is found at 7.9 ppm.
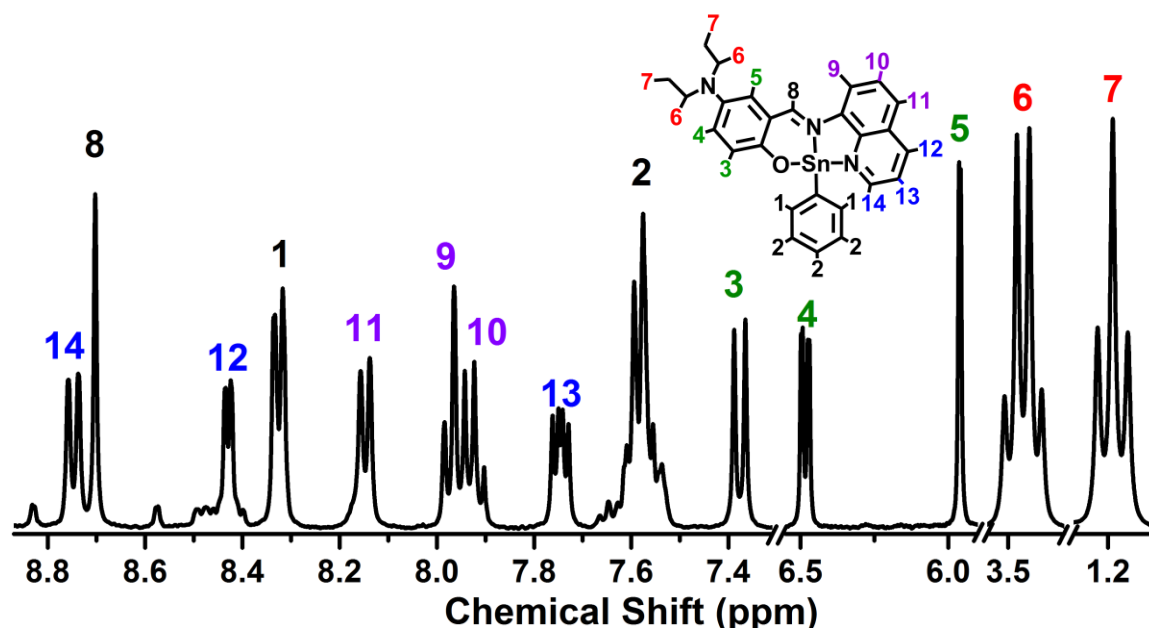
Figure 2.5 ^{1}H NMR spectrum [PhSnLdeaCl$_2$]in d$_3$-acetonitrile. The spectra have been edited to show only ^{1}H resonances resulting from the tin complex. The ^{1}H NMR spectrum of this complex also contains residual CH$_3$CN, H$_2$O, and n-hexane.

The assignment of the proton resonances from the aldehyde components of the ligands is straight-forward, as each salicylaldehyde derivative has unique substitution, and all of these resonances occur upfield of 7.9 ppm. In the ^{1}H NMR spectrum of [PhSnLBrCl$_2$], the singlet resonance and the one of the doublet resonances of 5-bromosalicylaldehyde overlap with the doublet of doublets of the quinoline ring and the meta and para proton multiplet of the Sn bound phenyl ring, respectively. One of the triplet, ^{1}H resonances of salicylaldehyde in [PhSnLsalCl$_2$] is also obscured by the Sn bound phenyl ring. All of the resonances from 4-diethylaminosalicylaldehyde are readily apparent in the spectrum of [PhSnLdeaCl$_2$]. The singlet resonance occurs at 5.96 ppm, making it the aromatic resonance with the furthest upfield chemical shift in all of the complexes. The aliphatic protons of the diethylamino substituent appear at 3.47 ppm and 1.19 ppm.
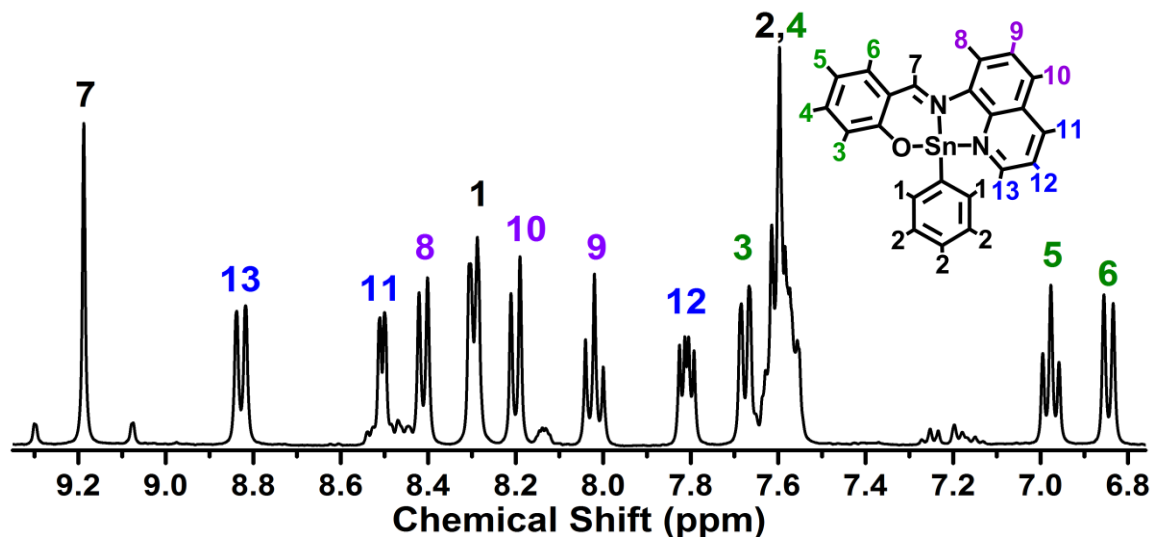
Figure 2.6 ^{1}H NMR spectrum of [PhSnLsalCl$_2$] in d$_3$-acetonitrile. The spectra have been edited to show only ^{1}H resonances resulting from the tin complex. The ^{1}H NMR spectrum of this complex also contains residual CH$_3$CN, H$_2$O, n-hexane, and toluene. The ^{1}H resonances of the residual toluene appear as the multiplet centered at 7.2 ppm.

2.4.2.2 X-Ray Crystallography

Selected bond lengths and angles are presented in Table 2.1. The two Sn coordinated nitrogen atoms are distinguished as the quinoline nitrogen, N$_Q$, and the imine nitrogen (linking the quinoline and the aldehyde), N$_I$. In addition, the Sn-N and Sn-Cl bond lengths for tetraphenylporphinatodichlorotin(IV) ([SnTPPCl$_2$]) as well as the bond lengths and angles obtained from the DFT geometry optimized singlet ground state are presented in Table 2.1. Thermal ellipsoid plots (50% probability) of the three [PhSnLBrCl$_2$] conformers are shown in Figure 2.7 and thermal ellipsoid plots (50% probability) of the remaining three complexes are show in Figure 2.8. A summary of crystal and structural refinement data is presented in Table 2.2. In crystals of [PhSnLBrCl$_2$], there are three independent conformers in the asymmetric unit and they primarily differ in the dihedral angle between the mean planes of the phenyl group and

the SnN_lCl_2 unit (2.9°, 28.7° and 32.1°). The bond lengths and angles for these conformers are given in Table 2.1 as [PhSnLBrCl$_2$] (1), [PhSnLBrCl$_2$] (2), and [PhSnLBrCl$_2$] (3), respectively.
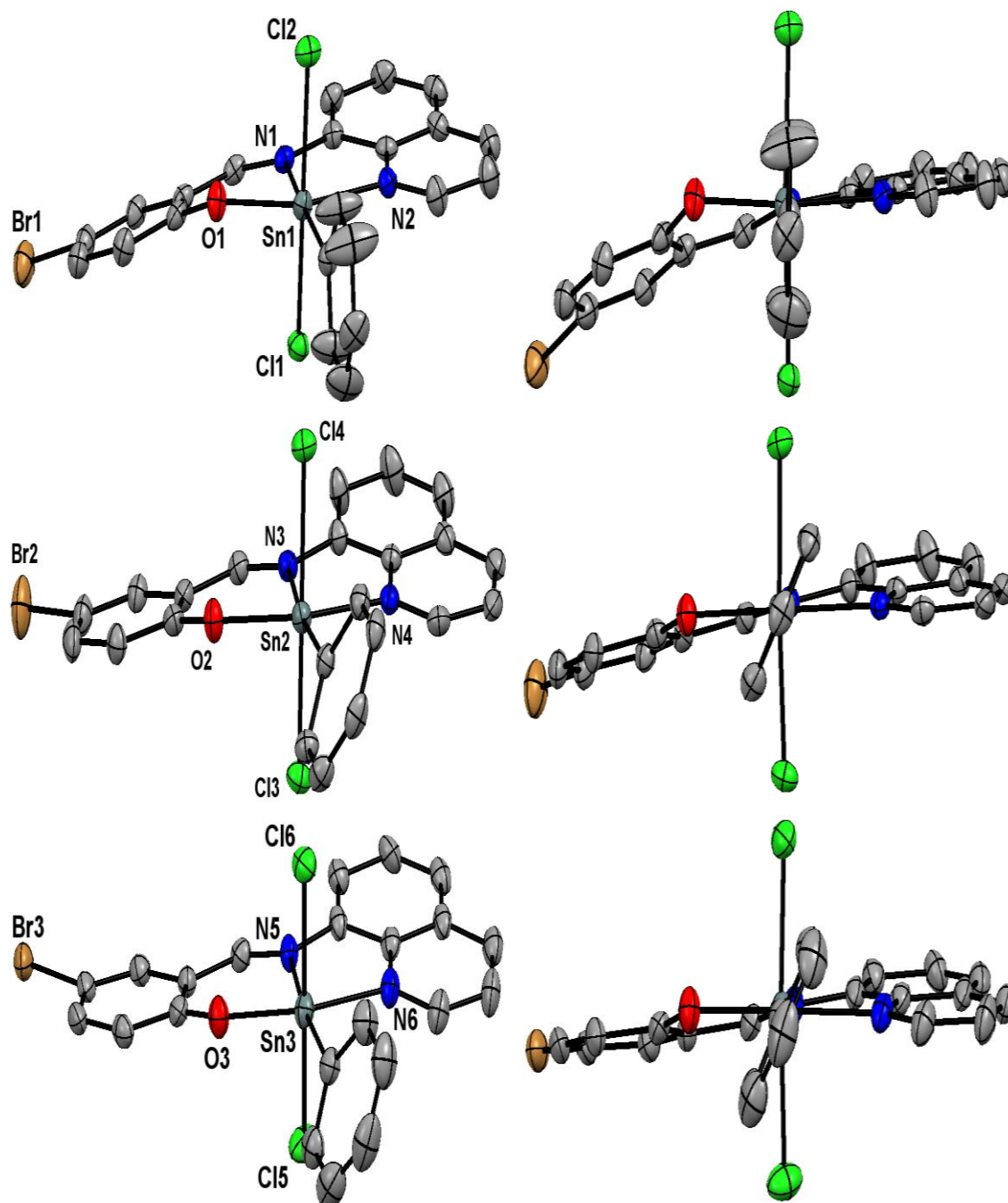
Figure 2.7 Thermal ellipsoid plots (50% probability) of the three [PhSnLBrCl$_2$] confirmers in the asymmetric unit. Top: PhSnLBrCl$_2$ (1) Middle: PhSnLBrCl$_2$ (2) Bottom: PhSnLBrCl$_2$ (3). Hydrogen atoms omitted for clarity.

Table 2.1 Selected Bond Lengths. The initial entries are the bond lengths obtained from x-ray structures with the estimated standard deviation presented in parenthesis. The values presented in square brackets are the bond lengths obtained from the DFT geometry optimized singlet ground state. The phenyl ring in the DFT geometry optimized singlet ground state of [PhSnLBrCl$_2$] is 6.5 degrees from the Cl-Sn-Cl axis.

Complex	PhSn Lnap Cl$_2$	PhSn Lsal Cl$_2$	PhSn LBr Cl$_2$ (1)	PhSn LBr Cl$_2$ (2)	PhSn LBr Cl$_2$ (3)	PhSn Ldea Cl$_2$	Sn TPP Cl$_2$[55]
Sn-N$_I$	2.196(2) [2.199]	2.220(2) [2.227]	2.230(2) [2.234]	2.214(2) [2.234]	2.205(2) [2.234]	2.167(1) [2.204]	2.098(2)
Sn-N$_Q$	2.233(2) [2.244]	2.230(2) [2.248]	2.230(2) [2.244]	2.236(2) [2.244]	2.235(3) [2.244]	2.242(2) [2.251]	
Sn-C	2.146(2) [2.147]	2.151(2) [2.146]	2.145(3) [2.144]	2.137(3) [2.144]	2.140(3) [2.144]	2.146(2) [2.150]	
Sn-O	2.045(2) [2.028]	2.036(2) [2.014]	2.033(2) [2.018]	2.050(2) [2.018]	2.036(2) [2.018]	2.036(1) [2.012]	
Sn-Cl	2.4761(6) [2.5330] 2.4676(6) [2.5298]	2.4755(7) [2.5320] 2.4430(7) [2.5264]	2.4723(8) [2.5275] 2.4625(8) [2.5232]	2.4716(8) [2.5275] 2.4632(7) [2.5232]	2.4670(8) [2.5275] 2.4424(8) [2.5232]	2.4996(4) [2.5403] 2.4691(4) [2.5342]	2.420(1)
Cl-Sn-Cl Bond Angle	169.74(2) [165.71]	166.85(2) [164.11]	166.78(3) [163.97]	167.66(3) [163.97]	168.36(3) [163.97]	169.24(2) [165.14]	
O-Sn-N$_Q$ Bond Angle	159.15(7) [159.75]	161.49(7) [161.45]	159.56(8) [161.37]	160.95(8) [161.37]	161.43(9) [161.37]	163.55(5) [162.37]	
C-Sn-N$_I$ Bond Angle	170.60(8) [173.15]	170.05(8) [171.73]	173.0(1) [171.8]	172.99(9) [171.84]	172.9(1) [171.8]	172.14(6) [171.52]	

The Sn-N$_I$ and the Sn-N$_Q$ bond lengths are similar for all of the molecules in the series. The shortest Sn-N$_I$ bond length of 2.167(1) Å and longest Sn-N$_Q$ bond length of 2.242(2) Å both occur in [PhSnLdeaCl$_2$]. All of the other Sn-N bond lengths fall within this 0.06 Å window and are approximately 0.1 Å longer than the Sn-N bonds in [SnTPPCl$_2$]. All of the Sn-C bonds are slightly shorter than the Sn-N bonds. The Sn-C bonds in [PhSnLnapCl$_2$], [PhSnLsalCl$_2$], and [PhSnLdeaCl$_2$] are all similar with lengths of 2.146(2) Å, 2.151(2) Å, and 2.146(2) Å, respectively.
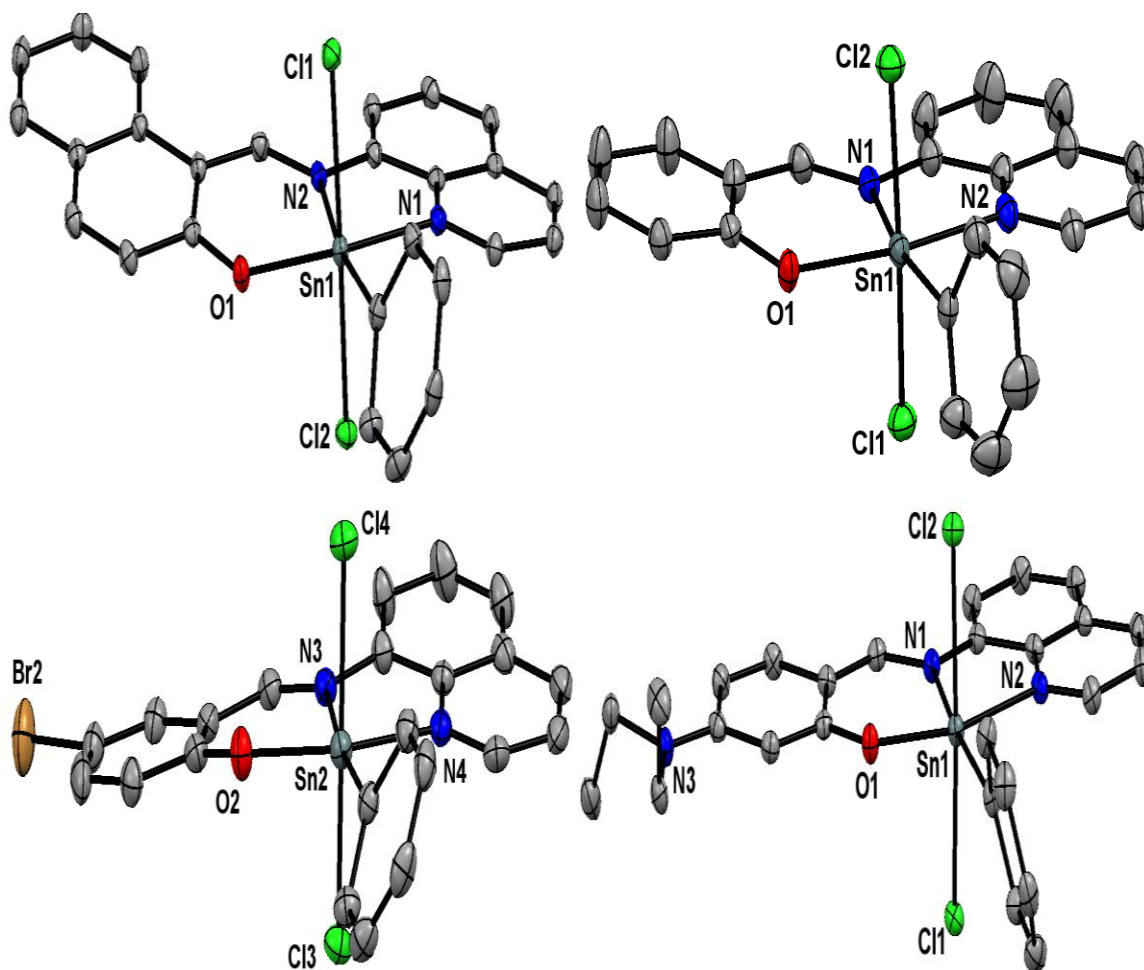
Figure 2.8 Thermal ellipsoid plots (50% probability) of (Top Left) [PhSnLnapCl₂], (Top Right) [PhSnLsalCl₂], (Bottom Left) [PhSnLBrCl₂], (Bottom Right) [PhSnLdeaCl₂]. Hydrogen atoms omitted for clarity.

For the set of [PhSnLBrCl₂] conformers, the Sn-C bond lengths are equivalent within experimental error, ranging from 2.137(3) Å to 2.145(3) Å. The Sn-O bond lengths are the shortest of all of the bonds in the coordination environment and are in the very narrow range 2.036(2) Å - 2.050(2) Å. The Sn-Cl bond lengths are significantly longer with values ranging from 2.4430(7) Å to 2.4996(4) Å. These are slightly longer than the Sn-Cl bond lengths observed in [SnTPPCl₂]. All of the crystallographically determined bond lengths are in good agreement with those obtained from DFT calculations. The most notable difference is in the determination of the Sn-Cl bond lengths where gas phase DFT

calculations yield bond lengths that are roughly 2.5% longer than in the crystallized molecules.

Table 2.2 Crystal and structural refinement data for the series of [PhSnNNOCl$_2$] complexes.

Compound	PhSnLnapCl$_2$	PhSnLsalCl$_2$	PhSnLBrCl$_2$	PhSnLdeaCl$_2$
Solvent	none	none	none	CH$_2$Cl$_2$
Formula	C$_{26}$H$_{18}$Cl$_2$N$_2$OSn	C$_{22}$H$_{16}$Cl$_2$N$_2$OSn	C$_{22}$H$_{15}$BrCl$_2$N$_2$OSn	C$_{26}$H$_{25}$Cl$_2$N$_2$OSn
FW (g/mol)	564.01	513.96	592.86	571.11
Xtl System	monoclinic	monoclinic	monoclinic	triclinic
Space Grp.	P2$_1$/c	C2/c	P2$_1$/n	P$\bar{1}$
Color, Habit	orange block	yellow plate	orange block	orange slab
a, Å	12.29999(15)	23.5629(5)	23.2013(8)	9.4970(6)
b, Å	10.4788(13)	11.2171(2)	10.8280(4)	11.2897(7)
c, Å	17.361(2)	16.9265(3)	28.3103(9)	12.8081(8)
a, deg.	90	90	90	79.475(2)
b, deg.	90.753(2)	90.4150(10)	98.767(2)	85.523(2)
g, deg.	90	90	90	89.2860(10)
V, Å^3	2237.4(5)	4473.68(15)	7029.1(4)	1346.04(15)
T, K	100(2)	150(2)	150(2)	100(2)
Z	4	8	12	2
[a]R1, [b]wR2	0.0393, 0.0696	0.0286, 0.0643	0.0609, 0.0832	0.0197, 0.0473
GoF	1.047	1.047	1.054	1.067

[a]R1 = $\Sigma||F_o|-|F_c||/ \Sigma||F_o|$. [b]wR2 = $\{[\Sigma w(F_o^2-F_c^2)^2/ \Sigma w(F_o^2)^2]\}^{1/2}$; w=1/[$\sigma^2(F_o^2)+(xP)^2$], where P=(F$_o^2$+2F$_c^2$)/3

The Cl-Sn-Cl bond angle is significantly less than 180° with the Cl atoms displaced away from the phenyl ring towards the imine nitrogen of the ligand such that the SnN$_I$Cl$_2$ unit is nearly planar. The departure of the Cl-Sn-Cl angle from 180° is dependent on the dihedral angle between the phenyl ring and the mean SnN$_I$Cl$_2$ plane. In [PhSnLsalCl$_2$], this angle is 13.3^o, resulting in a Cl-Sn-Cl bond angle of 166.85(2)°. In contrast, when this angle increases to 21.3^o in [PhSnLdeaCl$_2$] and 28.0° in [PhSnLnapCl$_2$] the Cl-Sn-Cl bond angle increases to 169.24(2)° and 169.74(2)°, respectively. For the series of [PhSnLBrCl$_2$] conformers observed in the asymmetric unit, as the dihedral angle increases from 2.9^o to 32.1^o the Cl-Sn-Cl bond angle increases from 166.78(3)° to 168.36(3)°. The distortions from this geometry seen in the solid state

structures can be seen to be due in part to contacts between the *o*-hydrogens on the phenyl group and the axial chlorine atoms. With the smallest dihedral angles these contacts are in the range $2.60 - 2.76$ Å which is about that of a normal van der Waals contact (2.74 Å).[56] The larger Cl-Sn-Cl and dihedral angles involve H⋯Cl contacts in the range $2.8 - 3.0$ Å. Although an exhaustive analysis of the packing has not been performed, it appears that the observed Cl-Sn-Cl and dihedral angles represent the best balance between minimizing the intramolecular H⋯Cl contacts and intermolecular contacts involving the phenyl ring which affect the dihedral angle. The O-Sn-N_Q bond angles vary from $159.15(7)°$ in [PhSnLnapCl$_2$] to $163.55(5)°$ in [PhSnLdeaCl$_2$]. As the dihedral angle between the plane of the phenyl ring and the SnN$_I$Cl$_2$ plane increases in [PhSnLBrCl$_2$], the O-Sn-N_Q bond angle increases from $159.56(8)°$ to $161.43(9)°$. There also is a slight disparity in the C-Sn-N_I bond angles across the series of molecules. [PhSnLnapCl$_2$] and [PhSnLsalCl$_2$] have similar C-Sn-N_I bond angles of $170.60(8)°$ and $170.05(8)°$. [PhSnLBrCl$_2$] and [PhSnLdeaCl$_2$] have slightly larger C-Sn-N_I bond angles of $172.9(1)°$ and $172.14(6)°$. Variations in the phenyl plane/SnN$_I$Cl$_2$ dihedral angle do not affect the C-Sn-N_I bond angle in the series of [PhSnLBrCl$_2$] conformers. The DFT calculated values for O-Sn-N_Q bond angles are all in very good agreement with the values obtained from the crystal structures. The calculated values for C-Sn-N_I are also in good agreement with the crystal structure values other than for [PhSnLnapCl$_2$] where the calculated bond angle is $3°$ larger than the observed value. The calculated values for the Cl-Sn-Cl bond angles are not in good agreement with observed values. All of the calculated values are at least $3°$ less than the actual bond angles.

2.4.2.3 Absorption and Luminescence Behavior

The electronic absorption spectra of the complexes in acetonitrile are shown in Figure 2.9 with extinction coefficients given in Table 2.3. The complexes are all yellow or orange in acetonitrile solution. The lowest energy absorption band varies from 420 nm − 462 nm across the series: [PhSnLsalCl$_2$] has an absorbance maximum at 420 nm, [PhSnLBrCl$_2$] has an absorbance maximum at 434 nm, [PhSnLnapCl$_2$] has an absorbance maximum at 452 nm, and [PhSnLdeaCl$_2$] has an absorbance maximum at 462 nm. All of the complexes also have higher energy absorption transitions.
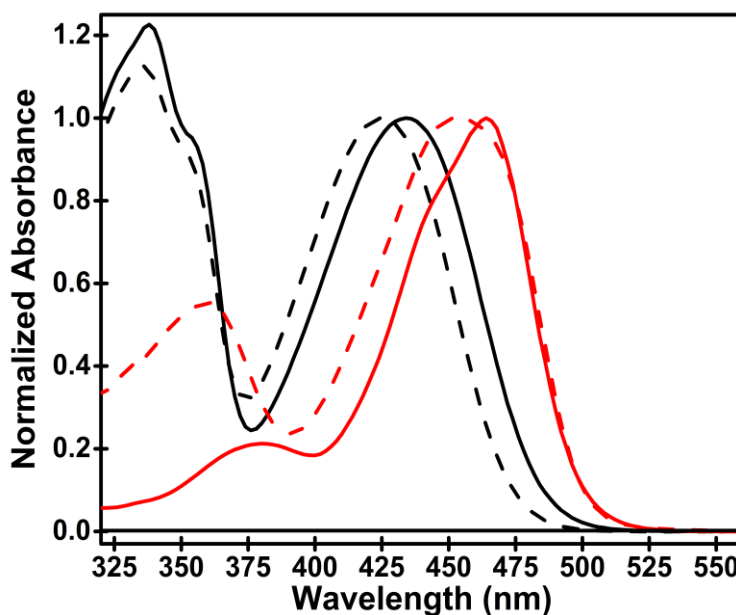
Figure 2.9 Absorption spectra of [PhSnLsalCl$_2$] (dashed black), [PhSnLBrCl$_2$] (solid black), [PhSnLnapCl$_2$] (dashed red), and [PhSnLdeaCl$_2$] (solid red) in acetonitrile.

[PhSnLsalCl$_2$] and [PhSnLBrCl$_2$] have nearly identical absorption bands at 330 nm with a shoulder at 360 nm.   [PhSnLnapCl$_2$] has an absorption transition at 365nm and [PhSnLdeaCl$_2$] has a broad absorption band at 380 nm. The HLnap ligand has two overlapping absorption bands at 450 nm and 473 nm and exhibits luminescence in acetonitrile. The fluorescence quantum yield of [PhSnLnapCl$_2$] is ~100 times greater than

the HLnap ligand. A comparison of the absorption and luminescence properties of HLnap

and [PhSnLnapCl$_2$] are shown in Figure 2.10.
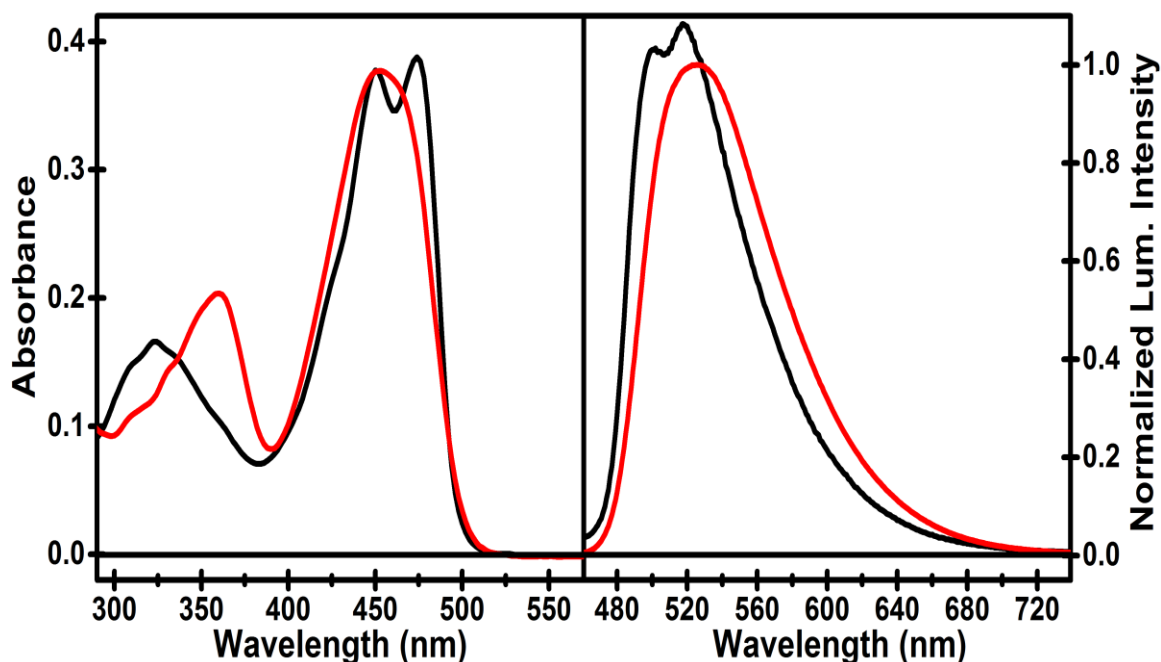
Figure 2.10 Left: Absorbance of HLnap (black) and [PhSnLnapCl$_2$] (red) in acetonitrile. Right: Normalized luminescence spectra of HLnap (black) and [PhSnLnapCl$_2$] (red).

All of the Sn(IV) complexes also display luminescence in acetonitrile solution. A

comparison of the luminescence spectra of each of the complexes in acetonitrile and

chloroform is shown in Figure 2.11. It is important to note that [PhSnLdeaCl$_2$] is the

only complex in the series that shows fluorescence solvatochromism , exhibiting a red

shift with increasing solvent polarity and suggesting that the singlet excited state of this

complex has significant charge transfer character. Fluorescence quantum yields of the

complexes in acetonitrile range from 0.14 for [PhSnLnapCl$_2$] to 0.01 for [PhSnLdeaCl$_2$]

suggesting the possibility of significant intersystem crossing to the triplet manifold. There

is no evidence of phosphorescence in fluid solution or 77 K glass. The fluorescence

lifetimes for the complexes were also determined by TCSPC. The collected lifetimes are

given in Table 2.3 for all of the complexes except [PhSnLdeaCl$_2$] which has a decay that

is faster than the resolution of our system (~ 300 ps). The fluorescence lifetimes and

quantum yields for our series of chromophores are similar to values previously reported

for the related [SnLCl$_3$] complexes.[48,49]

Table 2.3 Photophysical data collected for all chromophores. All data collected in acetonitrile.

Complex	[PhSnLnap Cl$_2$]	[PhSnLsal Cl$_2$]	[PhSnLBr Cl$_2$]	[PhSnLdea Cl$_2$]
Absorption λmax (nm)	452	424	434	462
Extinction Coefficient (M^{-1}cm^{-1})	20400	10800	11300	40700
Fluorescence λ$_{max}$ (nm)	524	532	541	602
Fluorescence λ$_{max}$ (cm^{-1})	19100	18800	18500	16600
Singlet Lifetime (ps), from TCSPC	1100 ± 100	660 ± 50	690 ± 40	----
[A]Durbin-Watson Value (d)	2.47	2.41	2.11	----
Fluorescence Quantum Yield ± 10%	0.14[B]	0.04[B]	0.06[B]	0.01[C]
E^0 (+/0) (V)	1.25	1.34	1.38	0.83
E^0 (0/-) (V)	-1.37	-1.23	-1.27	-1.22
Triplet Lifetime in PMMA (ms)	0.98 ± 0.09	1.1 ± 0.3	0.57 ± 0.02	11.9 ± 1.3
Triplet energy, (cm^{-1}) ± 300 cm^{-1}	15,300	16,300	16,200	15,500
Intersystem Crossing Efficiency ± 10%	0.36	0.59	0.72	0.05
[D]k_{isc} (s^{-1})	2.6 x 10^8	7.4 x 10^8	9.0 x 10^8	3.1 x 10^8
[D]k_r (s^{-1})	7.5 x 10^7	5.0 x 10^7	7.5 x 10^7	6.3 x 10^7
[D]k_{nr} (s^{-1})	3.6 x 10^8	4.6 x 10^8	2.8 x 10^8	5.9 x 10^9
Oxygen Quenching Rate Constant	2.1 x 10^9	2.1 x 10^9	2.2 x 10^9	2.3 x 10^9
[E]Quantum Yield of ^{1}O$_2$ Generation ± 20%	0.43	0.52	0.66	----

(A) Durbin-Watson values were determined using 200 data points. Fluorescence quantum yield values were determined using (B) tetracene[1] as a reference (C) [Ru(bpy)$_3$](PF6)$_2$[57] as a reference. (D) Kinetic values determined using the long decay component obtained from the ultrafast transient absorption spectrum of each chromophore. (E) The quantum yield of ^{1}O$_2$ was determined with [Ru(bpy)$_3$](PF6)$_2$[58] as a standard for all complexes.
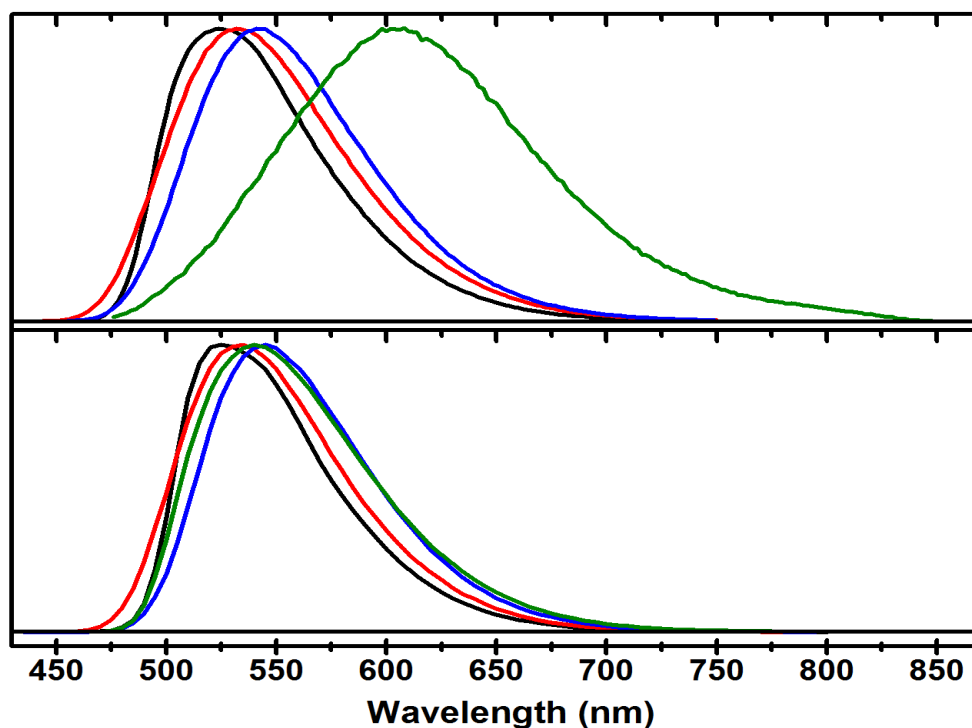
Figure 2.11 Normalized luminescence spectra of [PhSnLnapCl$_2$] (black), [PhSnLsalCl$_2$] (red), [PhSnLBrCl$_2$] (blue), and [PhSnLdeaCl$_2$] (green). Top: Spectra collected in acetonitrile. Bottom: Spectra collected in chloroform.

2.4.2.4 Nanosecond Time-Resolved Transient Absorption

Each chromophore has a unique, long-lived excited state absorption in de-aerated acetonitrile, which was assumed to be associated with the triplet state of the chromophore. The transient absorption spectra of all the chromophores at room temperature along with the ground state absorption over the same spectral window are shown in Figures 2.12-2.15. The key features of these spectra are bleaching of the ground state absorption and excited state absorption at all wavelengths to the red of 500 nm. The spectrum has three isobestic points and individual decays indicate a small (<5%) degree of permanent product formation. The dashed spectra indicates the changes observed in the ground state absorption following collection of the transient spectrum further indicating photodegradation in acetonitrile. Transient decays in acetonitrile solution were non-exponential, regardless of complex concentration or other experimental factors.
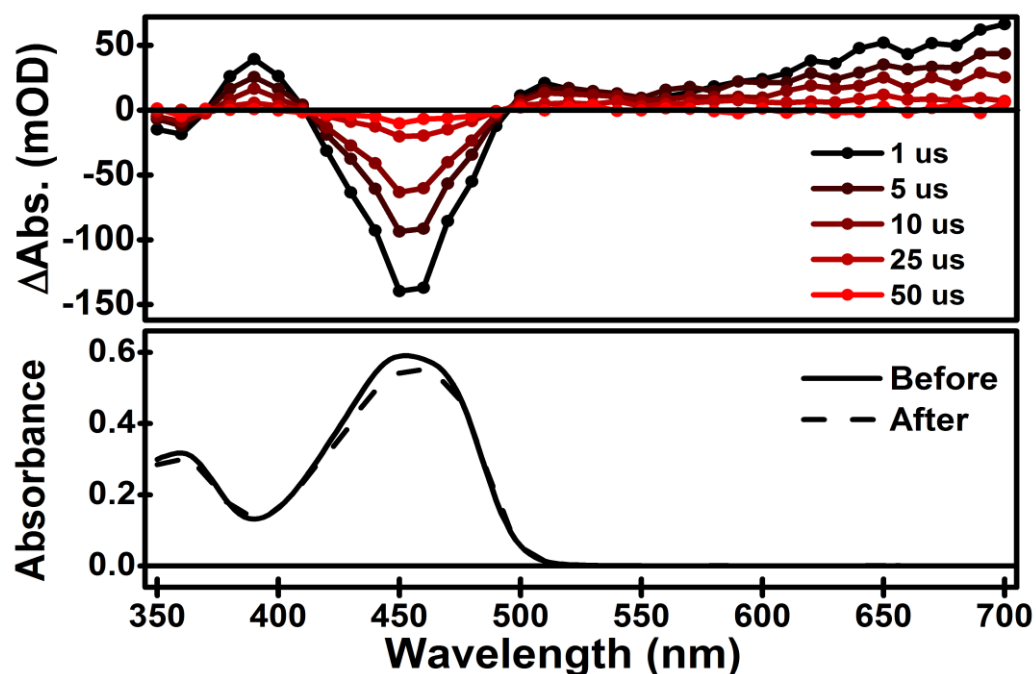
Figure 2.12 (Top) Nanosecond Transient Absorption Spectrum of [PhSnLnapCl$_2$] in acetonitrile. (Bottom) Ground state absorption spectrum of [PhSnLnapCl$_2$] (solid) before and (dashed) after collection of the TA spectrum.
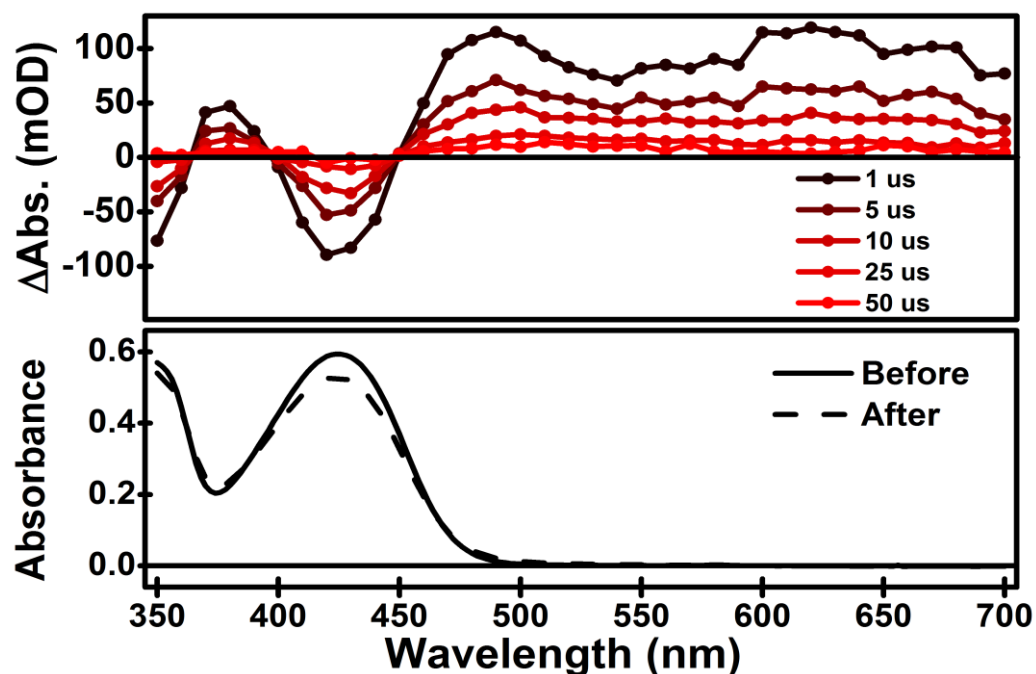
Figure 2.13 (Top) Nanosecond Transient Absorption Spectrum of [PhSnLsalCl$_2$] in acetonitrile. (Bottom) Ground state absorption spectrum of [PhSnLsalCl$_2$] (solid) before and (dashed) after collection of the TA spectrum.
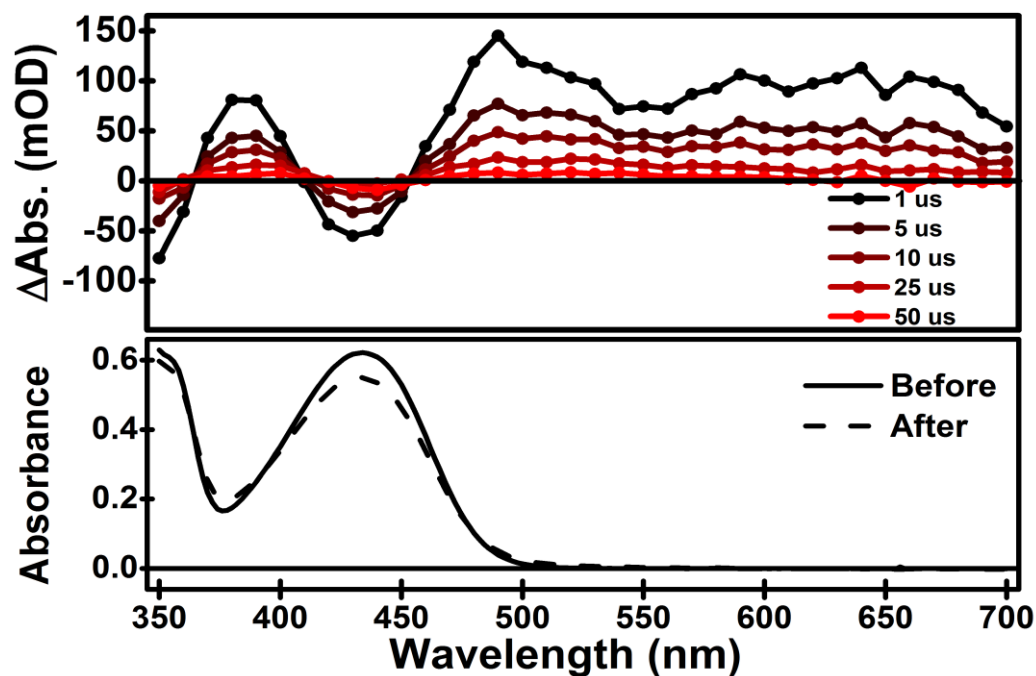
Figure 2.14 (Top) Nanosecond Transient Absorption Spectrum of [PhSnLBrCl$_2$] in acetonitrile. (Bottom) Ground state absorption spectrum of [PhSnLBrCl$_2$] (solid) before and (dashed) after collection of the TA spectrum.
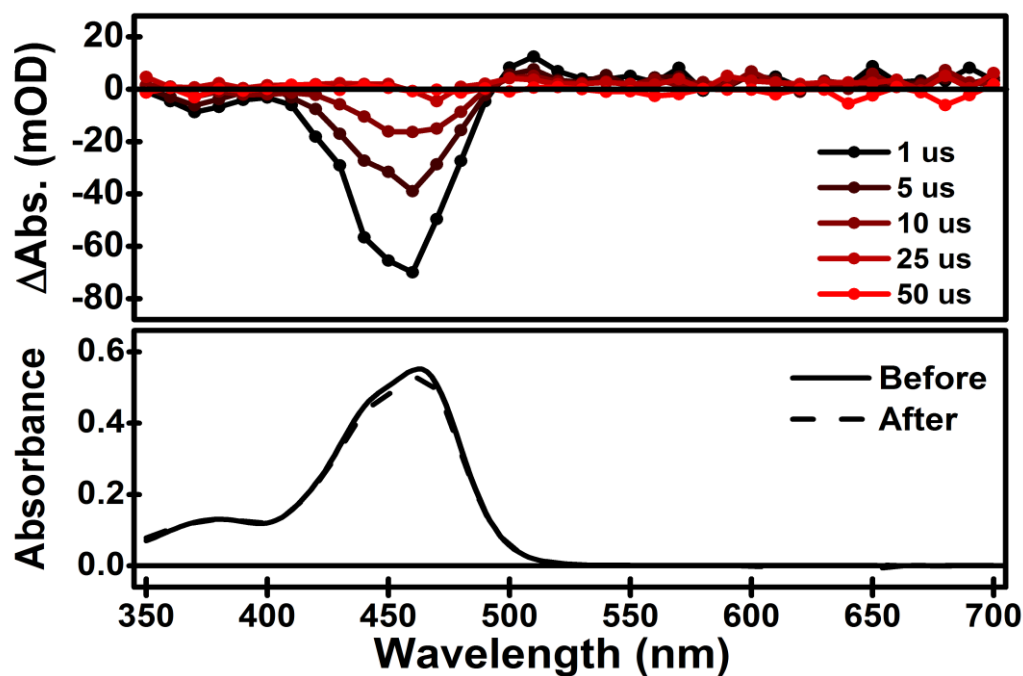
Figure 2.15 (Top) Nanosecond Transient Absorption Spectrum of [PhSnLdeaCl$_2$] in acetonitrile. (Bottom) Ground state absorption spectrum of [PhSnLdeaCl$_2$] (solid) before and (dashed) after collection of the TA spectrum.

Decays were best fit using a coupled first order and second order kinetic model (Equation 1.10) consistent with a triplet-triplet annihilation process competitive with radiative and non-radiative decay of the triplet excited state. Detailed analysis of the solution kinetics required knowledge of excited state molar concentrations. The excited state absorptivities were obtained from experiments involving triplet energy transfer to an acceptor with a known excited state absorptivity (anthracene) using solutions that were absorbance matched with $[Ru(bpy)_3]^{2+}$ at the excitation wavelength (see experimental 2.3.2 Nanosecond Time-Resolved Transient Absorption). The decay data was converted from absorbance units using the triplet-triplet extinction coefficients for each chromophore. The values of k_{TT} and k_o were obtained from fits of each data set. A transient absorption decay trace for $[PhSnLnapCl_2]$ is shown in Figure 2.16.
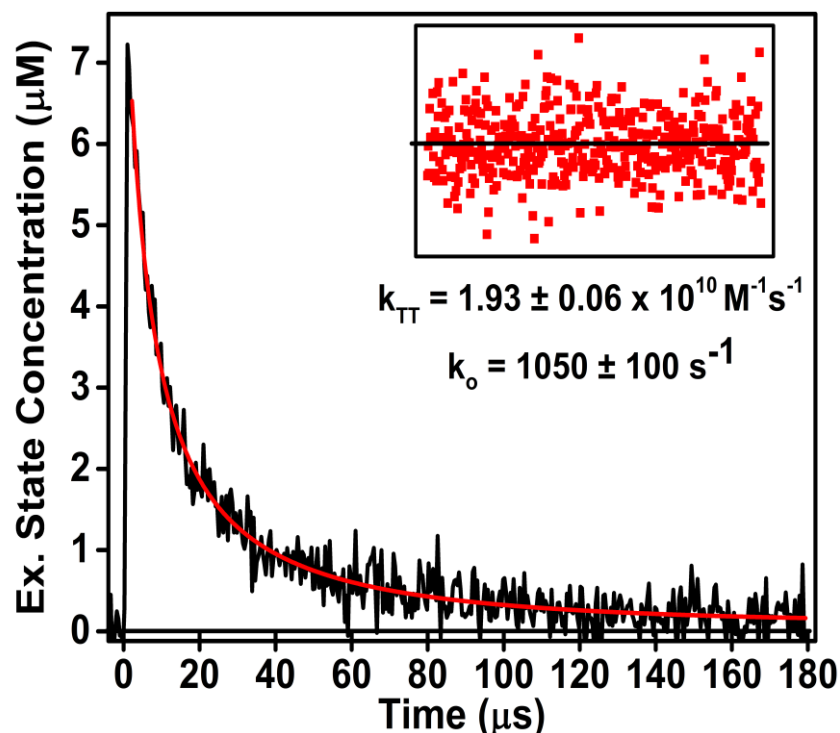
Figure 2.16 Transient absorption decay for $[PhSnLnapCl_2]$ in deaerated acetonitrile. The curve is fit with a coupled first order and second order kinetic model. The residual for the fit is shown in the inset with values of k_{TT} and k_o displayed in the image.

The intrinsic decay rate constants (k_o) of the triplet Sn complex are orders of magnitude smaller than the second order kinetic rate constants. The values of k_o range from 100 s^{-1} for [PhSnLdeaCl$_2$] to 2,200 s^{-1} for [PhSnLBrCl$_2$]. The second order kinetic rate constants are similar for all chromophores and range from 1.60 x 10^{10} s^{-1} for [PhSnLdeaCl$_2$] to 2.01 x 10^{10} s^{-1} for [PhSnLsalCl$_2$].

Given the observed solution behavior involving collisional reaction processes, the excited state decay dynamics were examined in solid poly(methyl methacrylate) matrices (PMMA). In PMMA, the transient absorption decays are single exponential and have lifetime values of 570 ms for [PhSnLBrCl$_2$], 1.1 ms for [PhSnLsalCl$_2$], 980 ms for [PhSnLnapCl$_2$], and 11.9 ms for [PhSnLdeaCl$_2$], resulting in a range of k_o values from 80 s^{-1} for [PhSnLdeaCl$_2$] to 1800 s^{-1} for [PhSnLBrCl$_2$]. This observation supports the validity of k_o values obtained from fits of the data with Equation 1.10. A transient absorption decay trace for [PhSnLBrCl$_2$] in PMMA is shown in Figure 2.17.
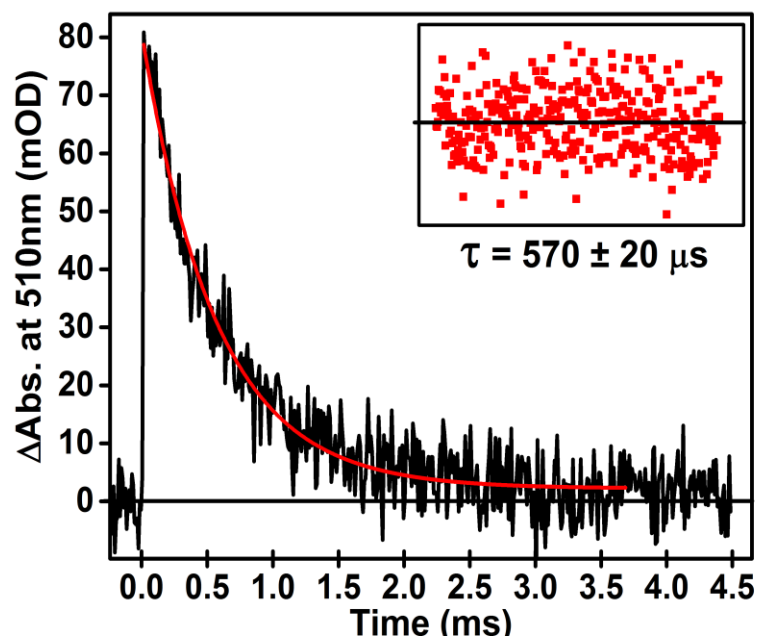
Figure 2.17 Transient absorption decay for [PhSnLBrCl$_2$] in a solid PMMA matrix. The curve is fit with a single exponential decay. The residual for the single exponential fit is shown in the inset with the lifetime value displayed in the image.

2.4.2.5 Femtosecond Time-Resolved Transient Absorption.

The femtosecond transient absorption spectra of the complexes in N_2 de-aerated acetonitrile at room temperature are shown in Figures 2.18-2.21. A summary of the kinetic information for the spectra is compiled in Table 2.4. In aggregate, all four complexes feature tri-exponential kinetics over the 200 fs to 3 ns time regime, with the longest lived transient spectrum (~3200 ps) resembling the earliest transient spectra recorded in the nanosecond transient absorption studies, illustrating continuity between the time regimes examined. For all four complexes, there is a fast sub-picosecond kinetic component ranging from about 100 fs to 800 fs. This is ascribed to an internal conversion process of the initially formed excited state. The long time kinetic phase for the complexes ranges from 15 ps to 2500 ps. Transient spectra over this time regime have isosbestic points and exhibit the loss of narrow peaks or structure to yield broad features. This kinetic component corresponds to relaxation of the singlet excited state to yield either ground state or triplet. The lifetimes of this component (Table 2.4) match well with the singlet lifetimes obtained by TCSPC (Table 2.3). In addition, all four complexes have a kinetic component that is intermediate in time (between sub-picosecond and the long time kinetic components), ranging from 1 to 70 ps for the different complexes. This kinetic phase is difficult to assign.

Table 2.4 Kinetic information obtained from femtosecond transient absorption spectra

Complex	[PhSnLnapCl$_2$]	[PhSnLsalCl$_2$]	[PhSnLBrCl$_2$]	[PhSnLdeaCl$_2$]
τ_1 (ps)	0.56 ± 0.05	0.75 ± 0.20	0.57 ± 0.12	0.13 ± 0.02
τ_2 (ps)	70.0 ± 7.6	40.8 ± 8.5	40.4 ± 17	1.05 ± 0.20
τ_3 (ps)	1390 ± 96	758 ± 66	767 ± 42	170 ± 17
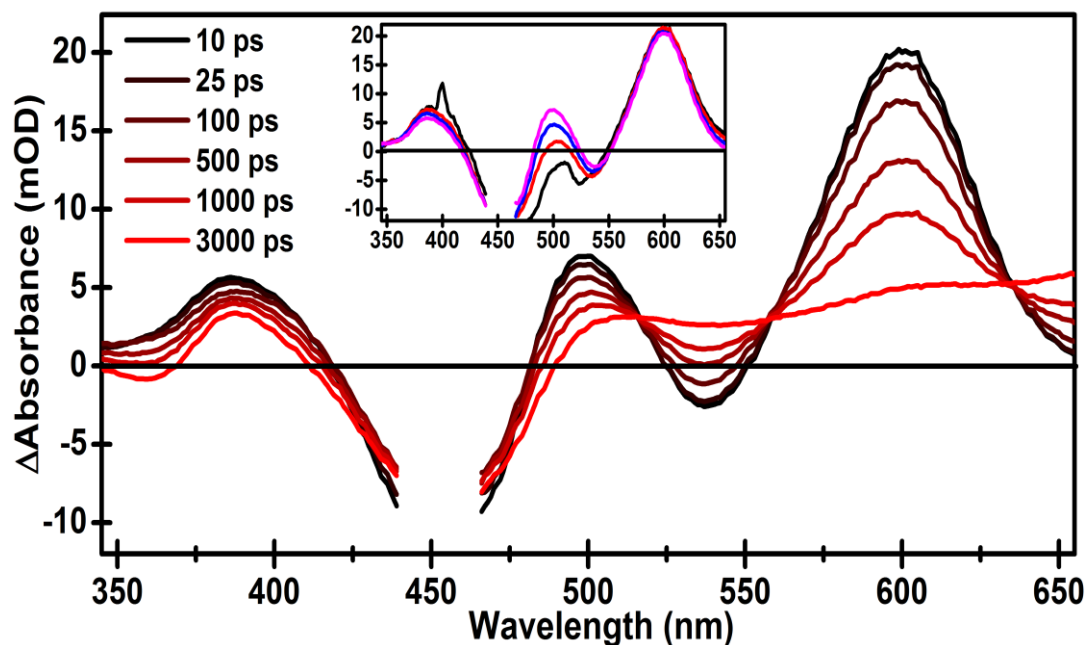
Figure 2.18 Ultrafast transient absorption spectrum of [PhSnLnapCl$_2$] in acetonitrile. Inset: Early time traces 0.300 ps (black), 0.500 ps (red), 1 ps (blue), and 5 ps (magenta). Evidence of the laser pulse has been omitted for clarity.
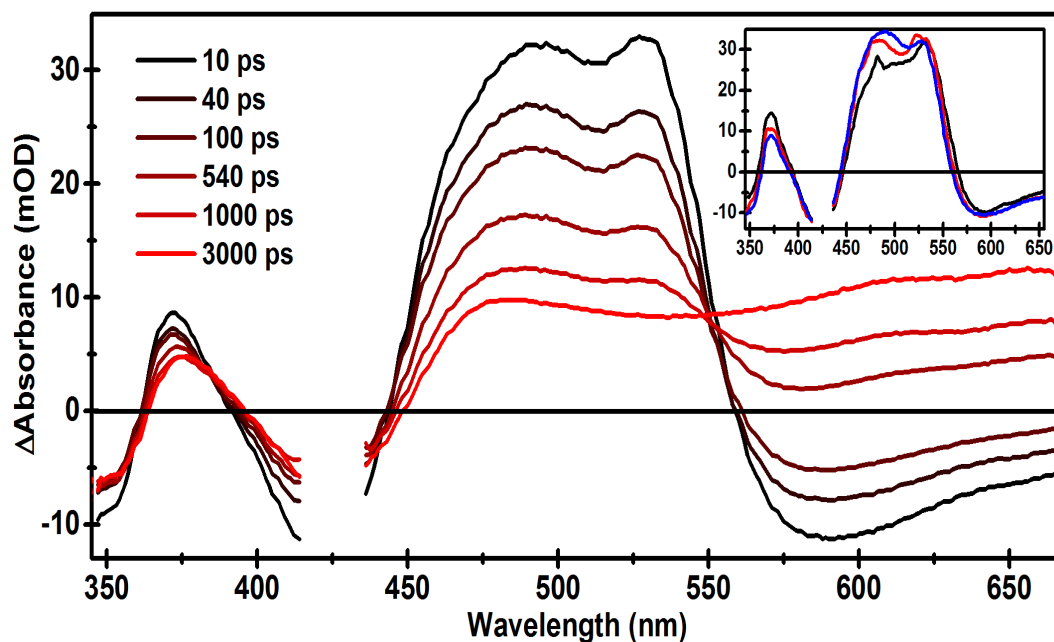
Figure 2.19 Ultrafast transient absorption spectrum of [PhSnLsalCl$_2$] in acetonitrile. Inset: Early time traces 0.300 ps (black), 0.500 ps (red), 1 ps (blue), and 5 ps (magenta). Evidence of the laser pulse has been omitted for clarity.
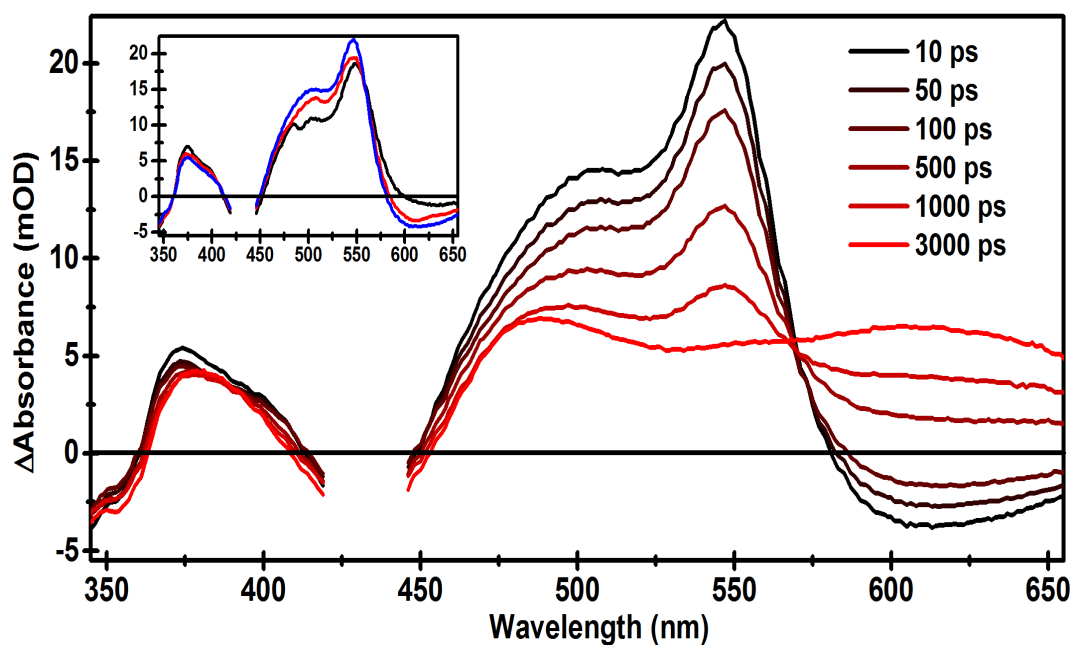
Figure 2.20 Ultrafast transient absorption spectrum of [PhSnLBrCl$_2$] in acetonitrile. Inset: Early time traces 0.300 ps (black), 0.500 ps (red), 1 ps (blue), and 5 ps (magenta). Evidence of the laser pulse has been omitted for clarity.
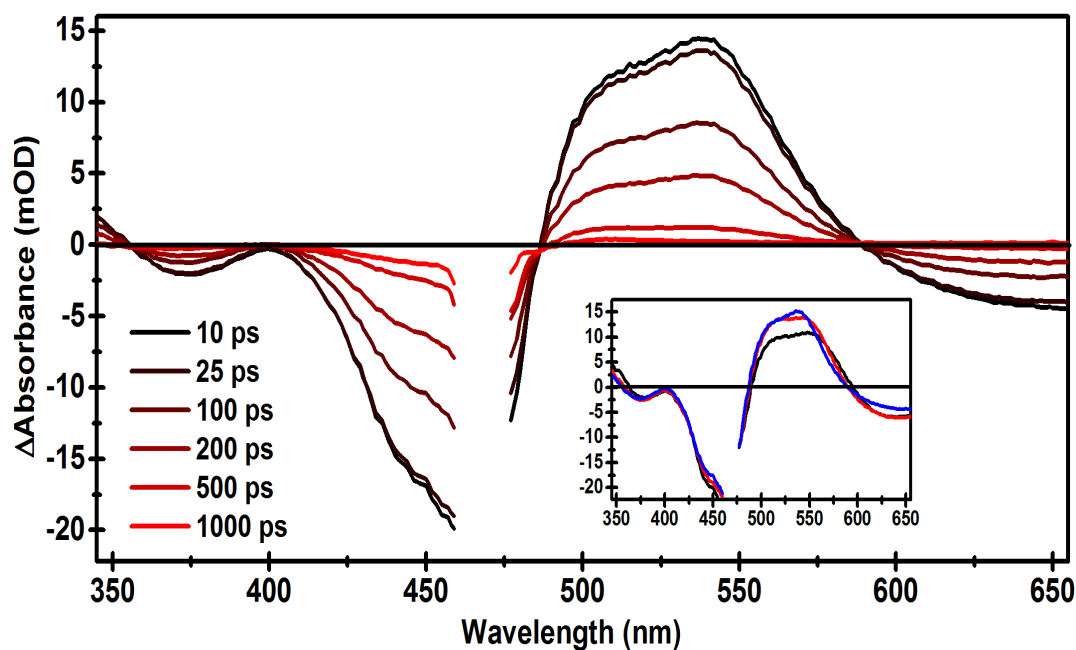
Figure 2.21 Ultrafast transient absorption spectrum of [PhSnLdeaCl$_2$] in acetonitrile. Inset: Early time traces 0.300 ps (black), 0.500 ps (red), 1 ps (blue), and 5 ps (magenta). Evidence of the laser pulse has been omitted for clarity.

2.4.2.6 Energy of the Triplet Excited State and the Quantum Yield of Triplet State Formation

Due to the non-phosphorescent nature of the triplet excited states in these systems, the triplet state energies of the complexes were obtained by evaluating the free energy dependence on the energy transfer rate constants for reacation of the Sn excited states with various triplet acceptors in acetonitrile.[59-61] The expression for the rate constant of an energy transfer process is given in Equation 2.1[59-61]

$$ k_q^{en} = \frac{k_d}{1 + \exp(-[E(*D,D) - E(*A,A)])/RT} \qquad (2.1) $$

where k_d is the diffusional rate constant, E(*D,D) is the energy of the donor excited state, and E(*A,A) is the energy of the acceptor state. The triplet state energies were calculated the using logarithmic plots of the free energy dependence on energy transfer shown in Figure 2.22. In fits of the experimental data, the values of E(*D,D) and k_d were calculated. The fit routine determined the value of k_d to be 1.2 x 10^{10} $M^{-1}s^{-1}$ for all chromophores. The energy values obtained from these plots are also presented in Table 2.3.

Energy transfer rate constant values are usually determined using the Stern-Volmer relationship. The treatment of the Stern-Volmer quenching data is complicated by the fact that excited state decay in solution is dominated by triplet-triplet annihilation. The existence of this decay path does not allow for the normal simplification of the expression; thus, quenching data cannot be fit using the deaerated lifetime of the complex in the absence of quencher. A detailed discussion of the decay of the excited state is necessary to justify our treatment of the data. The rate expression for the decay of an

excited molecule (S^*) that can be deactivated via a triplet-triplet annihilation process and that is in the presence of a quencher (Q) is given in Equation 2.2.

$$-\frac{d[S*]}{dt} = \left(k_r + k_{nr} + k_{TT}[S*] + k_q[Q]\right)[S*]$$ (2.2)

k_r and k_{nr} are the radiative and non-radiative decay rate constants for the excited state, k_{TT} is the bimolecular rate constant governing the triplet-triplet annihilation process, and k_q is the bimolecular rate constant for the quenching of the excited state by the quencher, Q. It is known from previous measurements that the value of $k_r + k_{nr} \leq 2$ x 10^3 s^{-1} (PMMA lifetime values) in these systems. Equal concentration second order kinetic fitting of excited state transient absorption decays in acetonitrile demonstrate that k_{TT} is on the order of 10^{10} M^{-1} s^{-1} (vide supra). In a laser pulse, 1-10 µM of Sn excited state is created. This value varies by an order of magnitude due the wide range of quantum efficiencies for triplet state formation in these systems (vide infra). Assuming an initial 5 µM Sn excited state concentration, the $k_{TT}[S^*]$ component of Equation 2.2 has a value of 5 x 10^4 s^{-1}, which is over an order of magnitude larger than that of $k_r + k_{nr}$. When the energy of a given triplet acceptor is much lower (>500 cm^{-1}) than the energy of the Sn excited state, k_q is diffusion limited. For typical experiments when k_q was assumed to be in this rate regime, 1mM quencher concentrations were utilized. This results in a value of $k_q[Q]$ of 10^7 s^{-1}, which is 200x larger than $k_{TT}[S^*]$ and well over 200x larger than $k_r + k_{nr}$. As the energy of the triplet acceptor increases relative to the energy of the Sn excited state, the value of k_q drops dramatically. For experiments utilizing acceptors with energies above 16000 cm^{-1}, quencher concentrations of 10 -100 µM were used to ensure that the value of $k_q[Q]$ remained at least an order of magnitude larger than $k_{TT}[S^*]$ and $k_r + k_{nr}$ (if these conditions were not met, interpretation of the quenching data was complicated because

transient absorbance decays clearly contained multiple components). So, even though the decay of these systems is complicated by the presence of a triplet-triplet annihilation pathway, it is still possible to create conditions where energy transfer quenching of the excited state is the dominant decay pathway with careful manipulation of the quencher concentration. Consequently, energy transfer rate constants for each chromophore with each quencher can be determined directly without the Stern-Volmer analysis since $k_q[Q]$ values are more than an order of magnitude greater than $k_r + k_{nr} + k_{TT}[S^*]$.
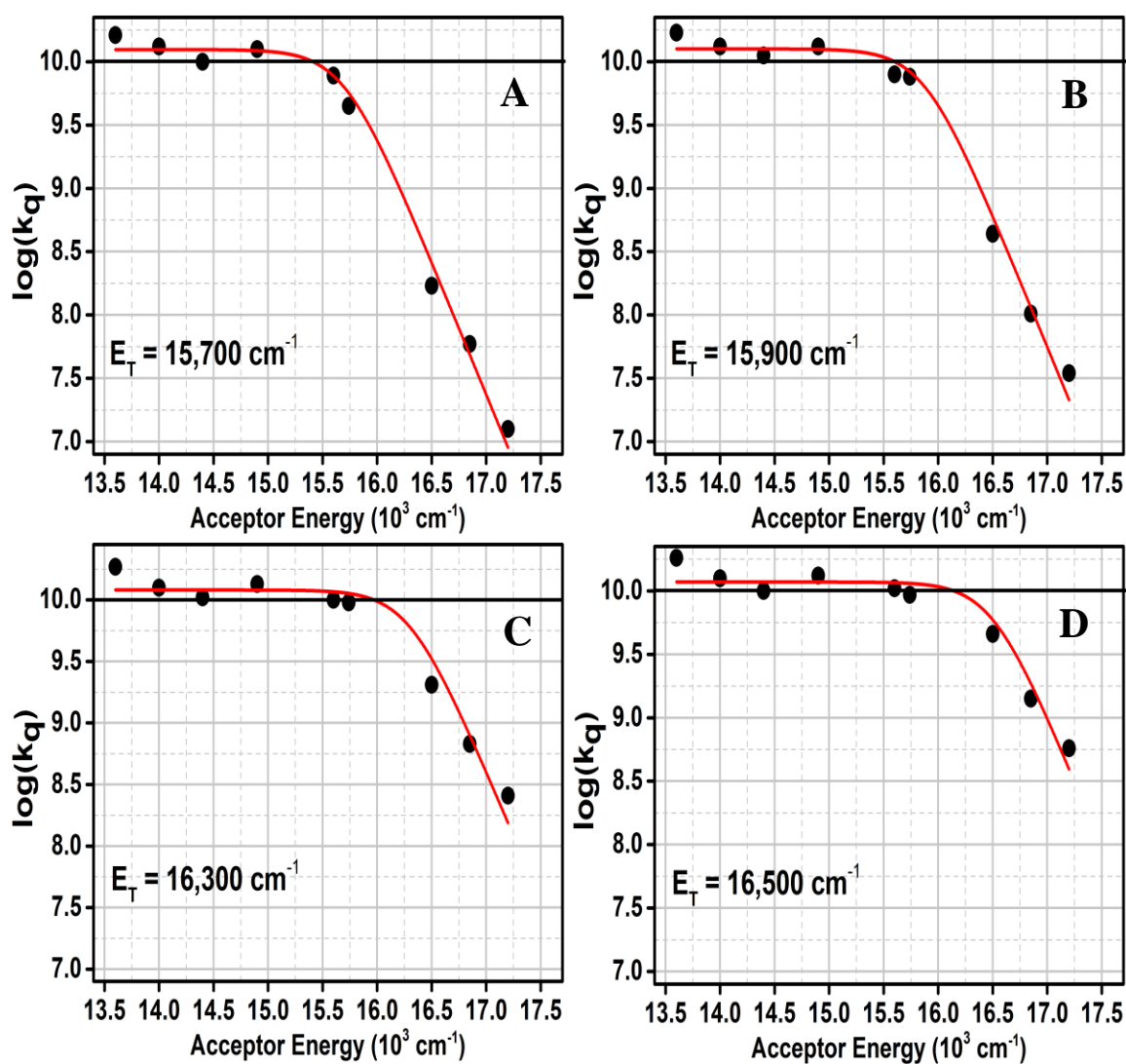
Figure 2.22 Fits of the individual quenching curves for (A) [PhSnLnapCl$_2$], (B) [PhSnLdeaCl$_2$], (C) [PhSnLBrCl$_2$], (D) [PhSnLsalCl$_2$]. The donor energy obtained from the data fit is presented in each image.

Data fits present a trend in the triplet state energies of the Sn complexes. The [PhSnLsalCl$_2$] and [PhSnLBrCl$_2$] have triplet energies of 16500 cm^{-1} and 16300 cm^{-1}, respectively. The triplet state energies of these complexes are approximately 500 cm^{-1} higher than [PhSnLdeaCl$_2$] and [PhSnLnapCl$_2$].

Intersystem crossing yields were obtained by sensitization of a triplet with a known excited state absorptivity (anthracene) and comparison with a known standard [Ru(bpy)$_3$]$^{2+}$ (see experimental 2.3.2 Nanosecond Time-Resolved Transient Absorption). The maximum change in optical density following excitation was used to calculate the excited state concentration of each species. The transient absorption decays used to determine the intersystem crossing efficiency are shown in Figure 2.23. This experiment results in a range of efficiencies: 0.72 for [PhSnLBrCl$_2$], 0.59 for [PhSnLsalCl$_2$], 0.36 for [PhSnLnapCl$_2$], and 0.05 for [PhSnLdeaCl$_2$].
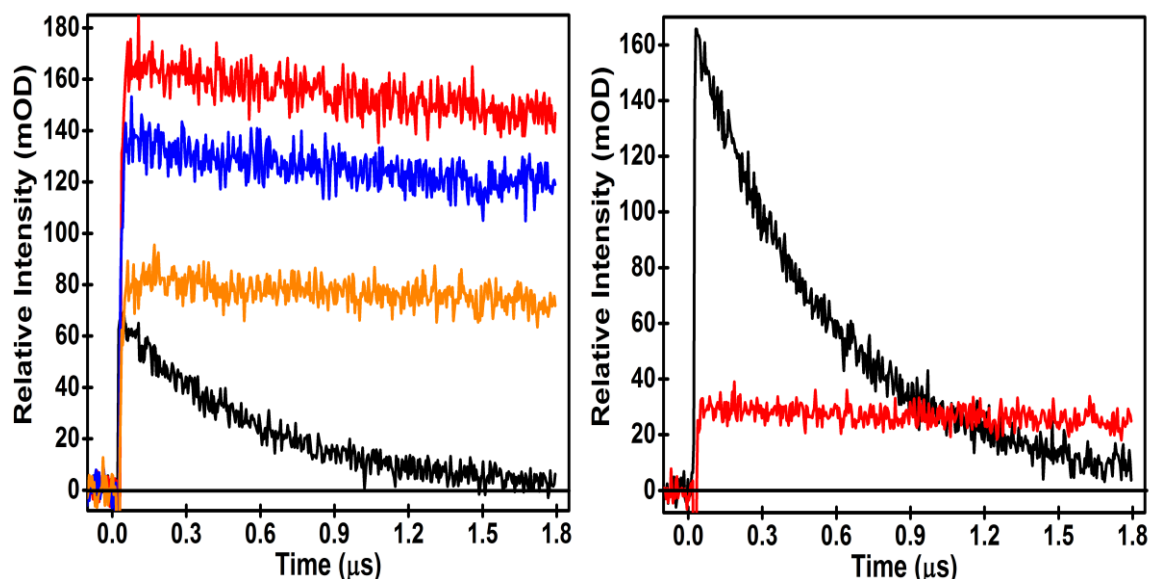
Figure 2.23 (Left) Transient absorption signals obtained from absorbance matched solutions of (black) [Ru(bpy)$_3$]$^{2+}$ and (red) [[PhSnLBrCl$_2$], (blue) [PhSnLsalCl$_2$], (orange) [PhSnLnapCl$_2$] containing 10 mM anthracene in acetonitrile.**.** (Right) Transient absorption signals obtained from absorbance matched solutions of (black) [Ru(bpy)$_3$]$^{2+}$ and (red) [PhSnLdeaCl$_2$] containing 10 mM anthracene in acetonitrile. [Ru(bpy)$_3$]$^{2+}$ decays were collected at 370 nm. [PhSnNNOCl$_2$] decays were collected at 420 nm, the maximum of the anthracene triplet absorbance (ε ^{3}AN/^{3}[Ru(bpy)$_3$]$^{2+}$ = 3).

2.4.2.7 Singlet Oxygen Sensitization

These complexes are also capable of sensitizing the formation of $^1O_2$. The collection of excited state lifetime measurements in the presence of oxygen allowed for the determination of a bimolecular quenching rate constants in CH_3CN, which were 2 x 10^9 $M^{-1}s^{-1}$ for all complexes. The quantum yield of singlet oxygen formation was determined from the comparison of the near infrared $^1O_2$ phosphorescence in air saturated solutions of each of the chromophores with an absorbance matched air saturated $[Ru(bpy)_3]^{2+}$ standard solution ($\Phi = 0.57^{58}$) . The quantum yields for singlet oxygen sensitization are 0.43 for $[PhSnLnapCl_2]$, 0.52 for $[PhSnLsalCl_2]$, and 0.66 for $[PhSnLBrCl_2]$. These values parallel the observed triplet yield efficiencies. No $^1O_2$ phosphorescence was observed from $[PhSnLdeaCl_2]$ sensitization; this is likely due to the extremely low triplet yield for the complex. The data used to determine the quantum yield for $[PhSnLBrCl_2]$ and $[PhSnLsalCl_2]$ are shown below in Figure 2.24.
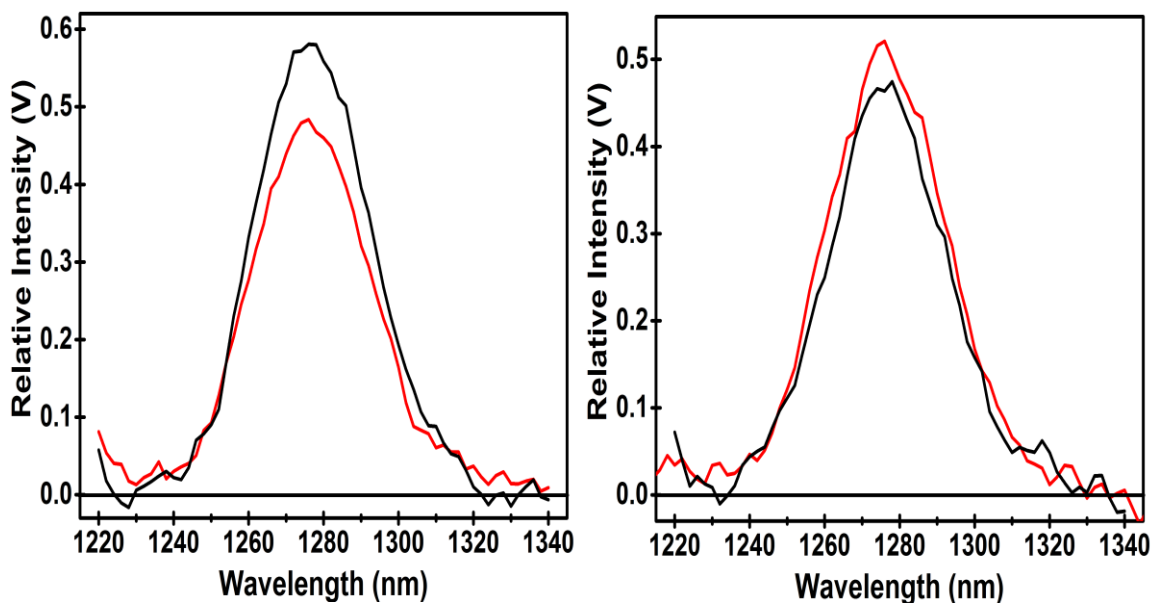
Figure 2.24 (Black) Sensitized $^1O_2$ phosphorescence observed in aerated acetonitrile solutions of $[Ru(bpy)_3]^{2+}$. (Red) Sensitized $^1O_2$ phosphorescence observed in aerated acetonitrile solutions of (Left) $[PhSnLBrCl_2]$, and (Right) $[PhSnLsalCl_2]$.

2.4.2.8 Photoinduced Electron Transfer Reactions

A key question relating to this class of complexes is the ability of the chromophores to serve as either excited state electron donors or acceptors. An estimate of the excited state oxidizing and reducing ability can be obtained from the energy of the triplet excited state and the electrochemical potentials obtained from cyclic voltammetry. The reductive and oxidative cyclic voltammograms of the each of the complexes in acetonitrile are shown in Figures 2.25-2.28. Cyclic voltammagrams of the complexes indicate that neither oxidation nor reduction is reversible at sweep rates up to the limit of our instrumentation (2 V/s). Approximate potentials based upon anodic and cathodic peak maxima were determined and are given in Table 2.3. The reduction potentials for all of the complexes are similar and have approximate values of -1.3 V vs. Ag/AgCl. The oxidation potentials for [PhSnLBrCl$_2$], [PhSnLsalCl$_2$], and [PhSnLnapCl$_2$] are all similar and occur around 1.3 V. As expected, [PhSnLdeaCl$_2$] is much easier to oxidize with a potential of 0.83 V.
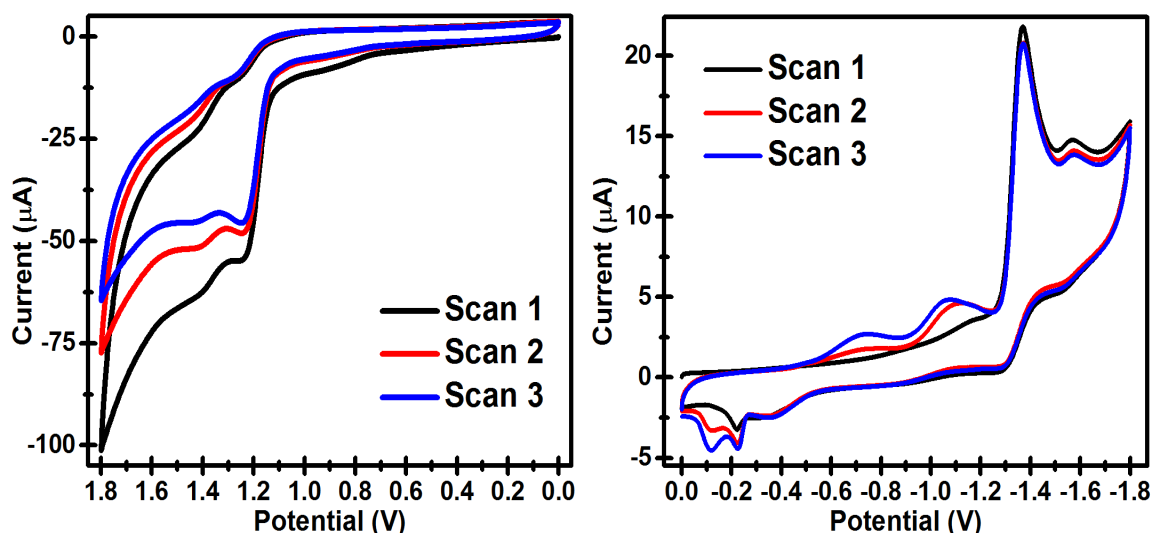
Figure 2.25 Cyclic voltammagrams of [PhSnLnapCl$_2$] in acetonitrile containing 0.1M [^{n}Bu$_4$N][PF$_6$]. Left: Anodic scan. Right: Cathodic scan. Three successive scans are shown in each figure. Solutions were deaerated argon prior to collection. The presented sweep segments were collected at a scan rate of 100 mV/s. Working electrode: glassy-carbon. Counter electrode: Pt wire. Reference electrode: Aqueous Ag$^+$/AgCl.
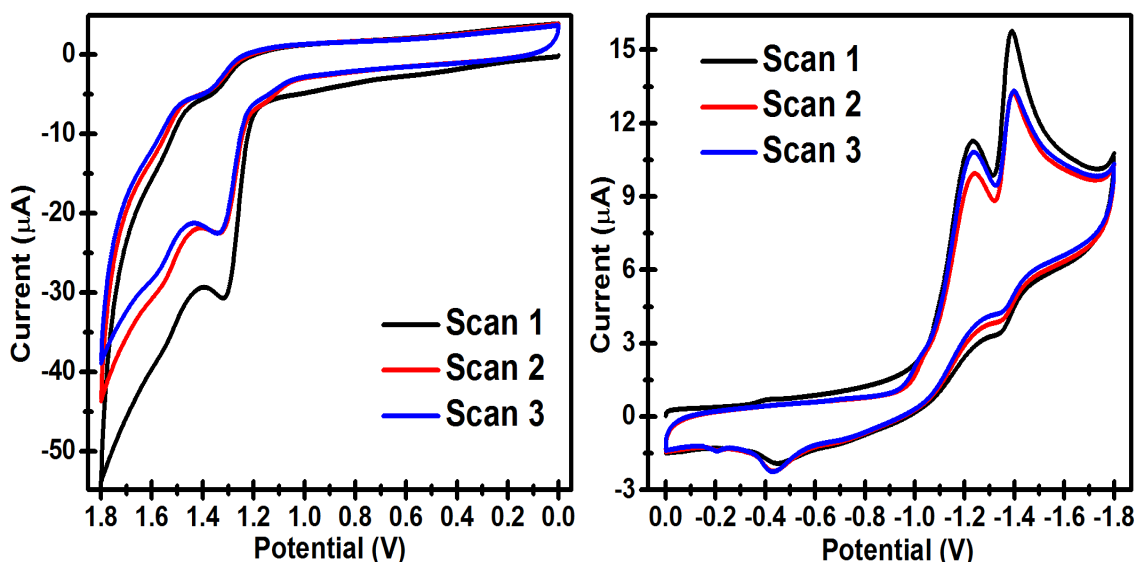
Figure 2.26 Cyclic voltammagrams of [PhSnLsalCl$_2$] in acetonitrile containing 0.1M [^{n}Bu$_4$N][PF$_6$]. Left: Anodic scan. Right: Cathodic scan. Three successive scans are shown in each figure. Solutions were deaerated argon prior to collection. The presented sweep segments were collected at a scan rate of 100 mV/s. Working electrode: glassy-carbon. Counter electrode: Pt wire. Reference electrode: Aqueous Ag$^+$/AgCl.
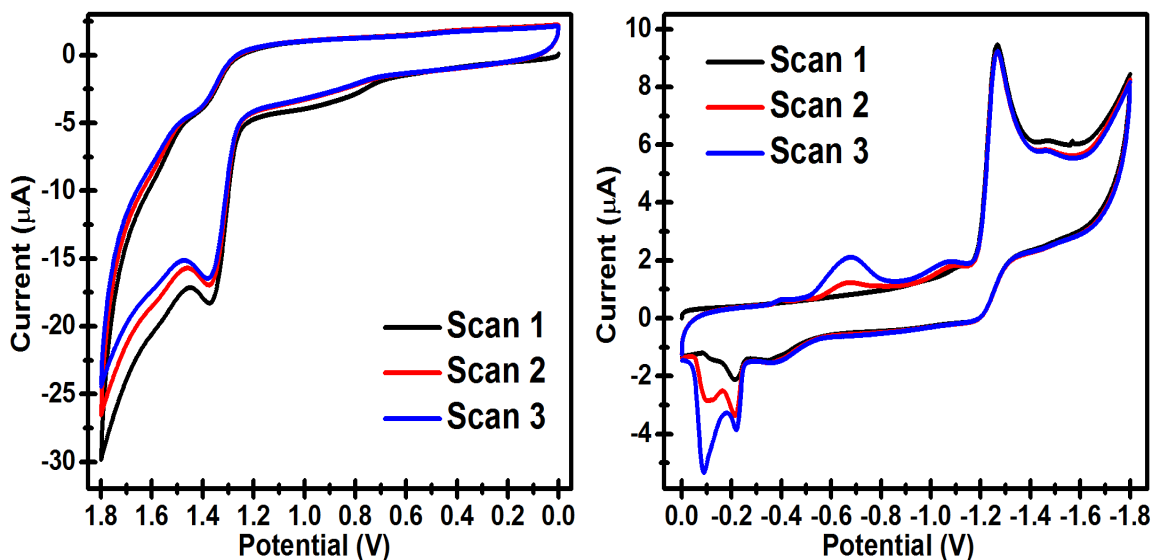
Figure 2.27 Cyclic voltammagrams of [PhSnLBrCl$_2$] in acetonitrile containing 0.1M [^{n}Bu$_4$N][PF$_6$]. Left: Anodic scan. Right: Cathodic scan. Three successive scans are shown in each figure. Solutions were deaerated argon prior to collection. The presented sweep segments were collected at a scan rate of 100 mV/s. Working electrode: glassy-carbon. Counter electrode: Pt wire. Reference electrode: Aqueous Ag$^+$/AgCl.
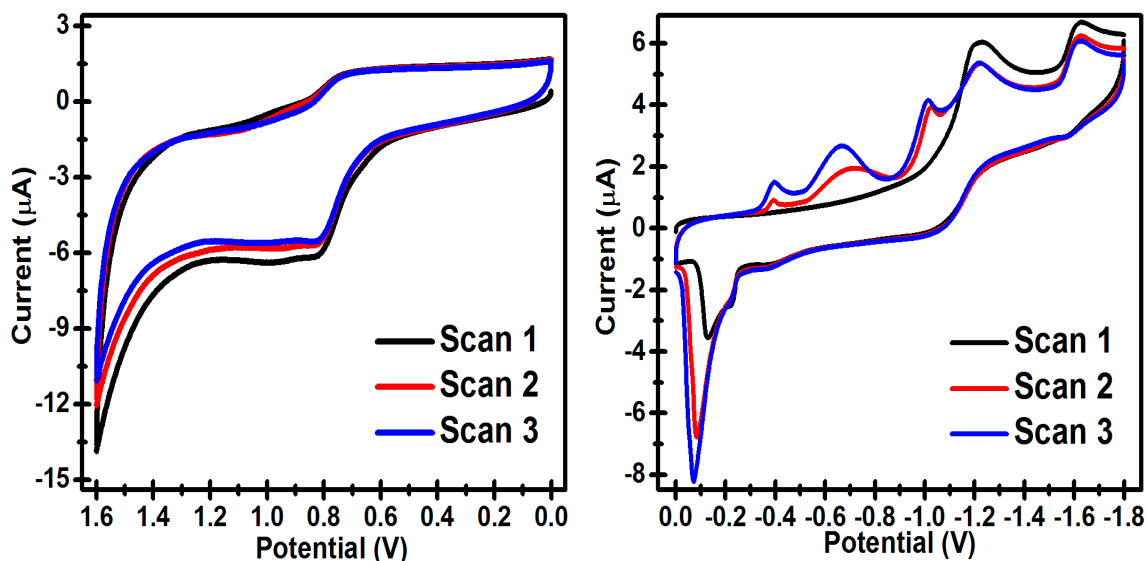
Figure 2.28 Cyclic voltammagrams of [PhSn(L4dea)Cl$_2$] in acetonitrile containing 0.1M [^{n}Bu$_4$N][PF$_6$]. Left: Anodic scan. Right: Cathodic scan. Three successive scans are shown in each figure. Solutions were deaerated argon prior to collection. The presented sweep segments were collected at a scan rate of 100 mV/s. Working electrode: glassy-carbon. Counter electrode: Pt wire. Reference electrode: Aqueous Ag$^+$/AgCl.

Given that the triplet excited state energies for all chromophores fall within ± 400 cm^{-1} of 2 eV (16,100 cm^{-1}), a crude estimate of the [PhSn(L)Cl$_2$]$^{*/-}$ potential is +0.70 for all chromphores. For excited state oxidation, the [PhSn(L)Cl$_2$]$^{+/*}$ potential is -0.70 V for [PhSnLBrCl$_2$], [PhSnLsalCl$_2$], and [PhSnLnapCl$_2$] and -1.2 V for [PhSnLdeaCl$_2$] vs Ag$^+$/AgCl, suggesting the complexes can serve as modest one-electron acceptors and donors, quite similar to [Ru(bpy)$_3$]$^{2+}$.. To provide a test of photoredox reactivity, reductive quenching with 10-methyl-phenothiazine (MPTH, E^0(+/0) = 0.7 V vs. Ag$^+$/AgCl) and oxidative quenching with methyl viologen (MV, E^0(2+/+) = -0.44 V vs. Ag$^+$/AgCl) was carried out in CH$_3$CN solutions. Transient spectra obtained in acetonitrile in the presence of 1 mM MPTH are shown in Figure 2.29 and 1 mM MV are shown in Figure 2.30 for all the complexes. For reductive quenching measurements with MPTH, the absorbance signal between 510 and 550 nm is clearly indicative of the MPTH cation

radical and is observed for all the complexes. Rate constants for quenching with MPTH obtained from transient absorption decays are 9 x 10^9 M^{-1}s^{-1} for [PhSnLBrCl$_2$], 7 x 10^9 M^{-1}s^{-1} for [PhSnLsalCl$_2$], 6 x 10^9 M^{-1}s^{-1} for [PhSnLnapCl$_2$], and 1 x 10^9 M^{-1}s^{-1} for [PhSnLdeaCl$_2$]. The rates of the back electron transfer reactions involving oxidized MPTH and the reduced Sn complexes are all diffusion limited (10^{10} M^{-1}s^{-1}).
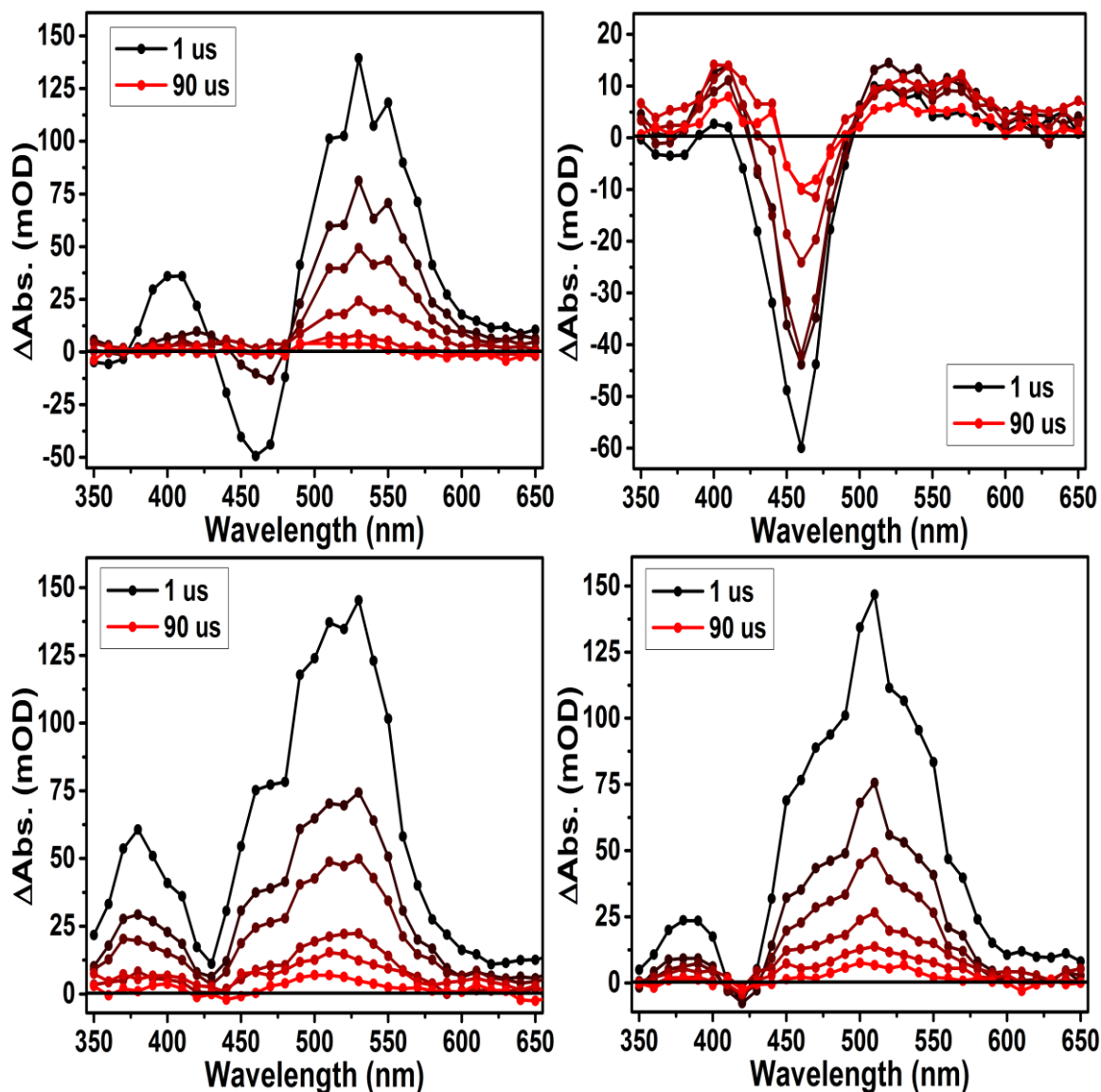
Figure 2.29 Transient absorption decays collected in deaerated acetonitrile in the presence of 1 mM MPTH: (Top Left) [PhSnLnapCl$_2$], (Top Right) [PhSnLdeaCl$_2$], (Bottom Left) [PhSnLBrCl$_2$], and (Bottom Right) [PhSnLsalCl$_2$]. Spectra are depicted at time delays of 1 μs, 5 μs, 10 μs, 25 μs, 50 μs, and 90 μs.

Oxidative quenching with MV also yielded transient spectra that strongly resemble the $MV^{+\bullet}$ ion with strong absorption at 395 nm and a broad absorption band with a maximum centered at 600 nm. Quenching rate constants with MV are 7 x 10^8 $M^{-1}s^{-1}$ for [PhSnLBrCl$_2$], 1 x 10^9 $M^{-1}s^{-1}$ for [PhSnLsalCl$_2$], 2 x 10^9 $M^{-1}s^{-1}$ for [PhSnLnapCl$_2$], and 1 x 10^{10} $M^{-1}s^{-1}$ for [PhSnLdeaCl$_2$]. Back electron transfer involving reduced MV and the oxidized Sn complexes is also diffusion limited.
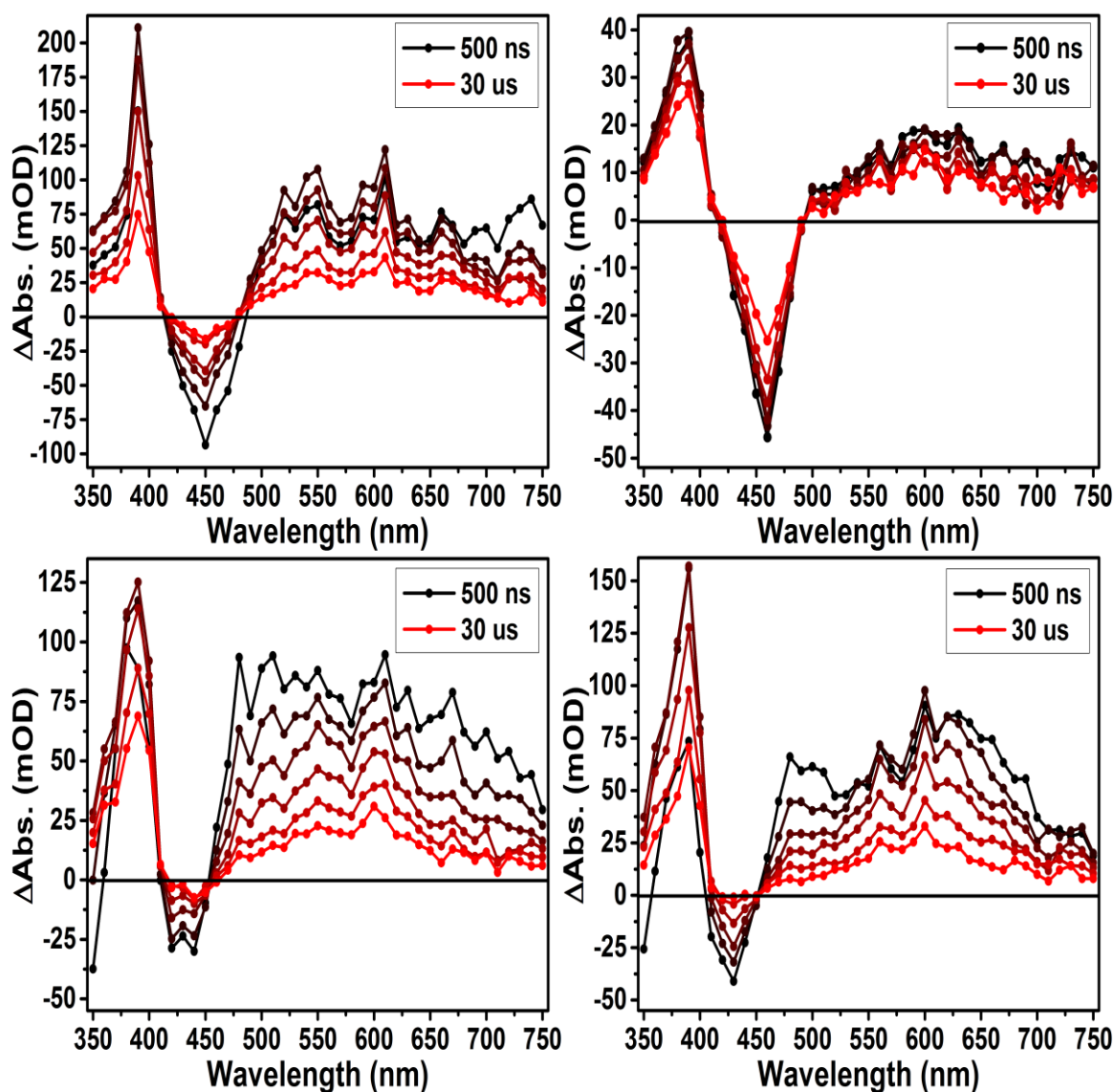
Figure 2.30 Transient absorption decays collected in deaerated acetonitrile in the presence of 1 mM MV: (Top Left) [PhSnLnapCl$_2$], (Top Right) [PhSnLdeaCl$_2$], (Bottom Left) [PhSnLBrCl$_2$], and (Bottom Right) [PhSnLsalCl$_2$]. Spectra are depicted at time delays of 500 ns, 2 μs, 5 μs, 10 μs, 20 μs, and 30 μs.

Control experiments of excitation in the absence of chromophore resulted in no transient absorbance in the visible.

Given the observation of long-lived triplet state formation and photoredox reactivity for the Sn(IV) complexes, possible energy and electron transfer photoreactivity for the free ligands alone was examined. The transient absorption spectrum of the HLnap ligand in deaerated acetonitrile as well as transient absorption spectra of the ligand in the presence of 9 mM 9-bromoanthracene and 1 mM MPTH are shown in Figure 2.31.
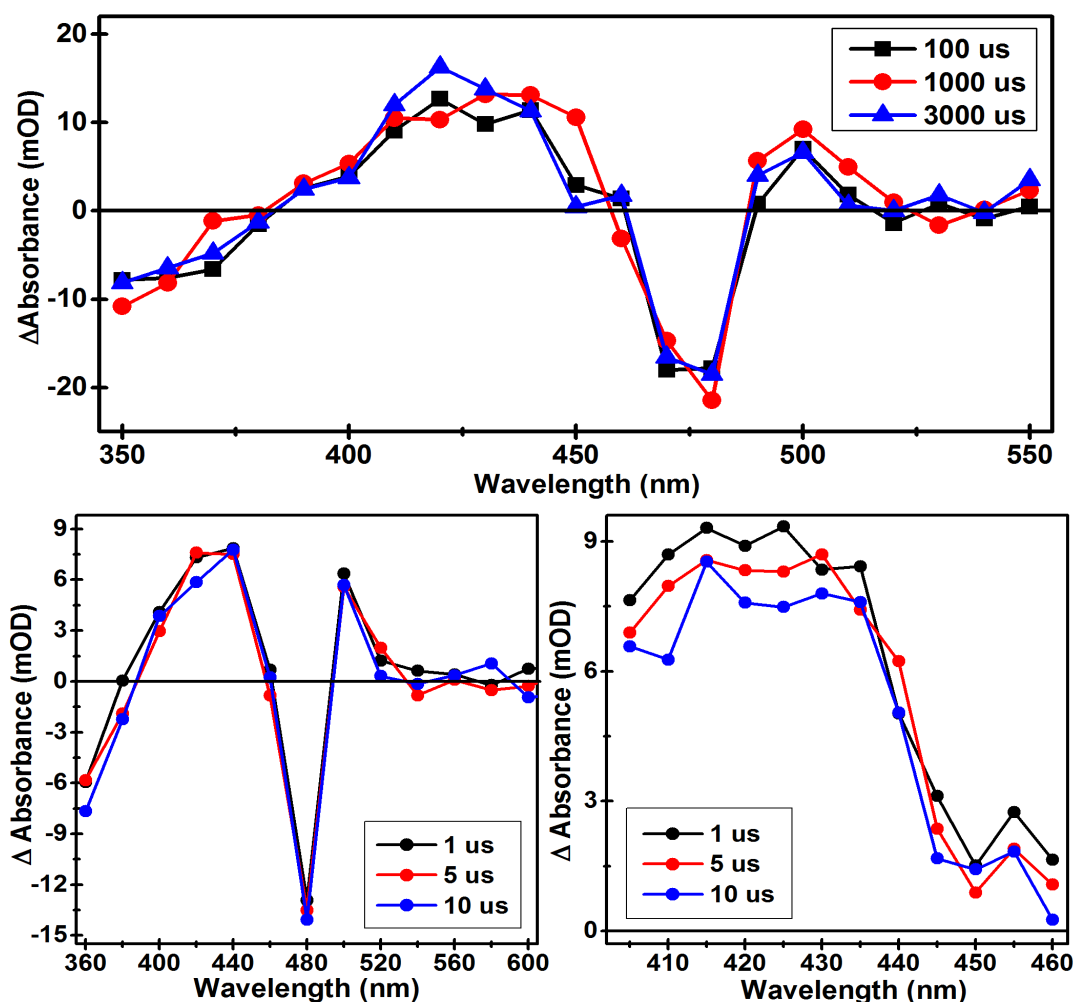
Figure 2.31 (Top) Nanosecond transient absorption spectrum of HLnap in deaerated acetonitrile. (Bottom Left) Nanosecond transient absorption spectrum of HLnap in deaerated acetonitrile in the presence of MPTH. Note: MPTZ cation radical is not observed in the TA spectrum. (Bottom Right) Nanosecond transient absorption spectrum of HLnap in deaerated acetonitrile in the presence of 8.9mM 9-bromoanthracene.

A transient species clearly remains in the ligand spectrum after 3 milliseconds; however, this species is not quenched by either MPTH or 9-bromoanthracene.

2.4.2.9 The Effect of Sn on the Observed Reactivity of the Complexes

Given the similarity of the absorption and fluorescence data of HLnap and [PhSnLnapCl$_2$], the possibility exists that the observed behavior of the complexes is essentially a simple extension of the behavior of the free ligand. A search of the literature does not yield any previous microsecond to millisecond transient absorption results for any of the ligands or complexes, although steady state and ultrafast experimental work has been done on HLnap. As a starting point it is useful to discuss the structurally related molecule salicylideneaniline (SalAn, made from the condensation of salicylaldehyde and aniline). An interesting feature of this and HLnap that differs from the Sn(IV) complexes is contribution of a keto tautomeric form which can exist in E and Z stereoisomeric forms with respect to the C-N imine linkage as shown in Figure 2.32.
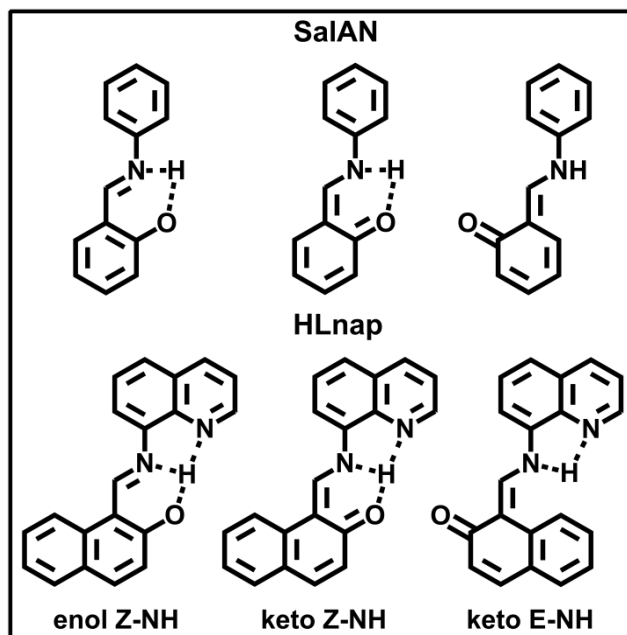
Figure 2.32 Structural representations of possible tautomers and stereoisomers of SalAn and HLnap.

The ground state absorption spectrum of SalAn does not possess a visible absorption transition above 400 nm and is invariant with changes in solvent polarity. The UV absorption bands in the SalAn spectrum are attributed to absorbance of the ground state enol tautomer. By contrast, there is a clear solvent dependence of the ground sate absorption spectrum of another Schiff base, napthylideneaniline (NapAn, made from the condensation of 2-hydroxynapthaldehyde and aniline); two absorption bands appear above 400 nm as the solvent polarity increases. This change in absorbance is ascribed to the formation of keto tautomer in solution.[62] It is clear that both the keto and enol form of NapAn are present in polar solvents.[62] The ground state absorption spectrum of the HLnap ligand features two strong absorption bands above 400 nm and the absorption spectrum is unchanged in solvents of varying polarity; this is attributed to a stabilization of the keto form through hydrogen bonding with the quinoline nitrogen (Figure 2.32).[63] The photochromic nature of the SalAn excited state was initially described in the 1960's in the crystalline state[64], low temperature matrices[65], and solution[65,66]. These initial reports assign this photochromic state as a ground state keto E-NH structure (Figure 2.32). Subsequent literature reports have examined the kinetic evolution of the excited state of salicylideneaniline[67-73] in fluid solution. Excitation of the enol form of SalAn results in sub-picosecond intramolecular proton transfer to form the fluorescent, keto, form followed by relaxation to a ground state species with either a cis-zwitterionic (iminium ion/ naphthoate) or the isomerized keto E-NH structure. This latter isomeric species has a lifetime of 400 μs in acetonitrile.

The absorption, luminescence and femtosecond time-resolved absorption spectrum of the HLnap ligand has also been reported.[74,75] The ultrafast spectroscopic

behavior consists of three spectral features of note: (1) two well defined bleaching bands corresponding to both of the local maxima in the ground state absorption spectrum at 450 nm and 475 nm that decay via a multi-exponential path that includes a very long lived component (> 5 ns), (2) an intense, broad absorption between 500-620 nm, containing two peaks at 525 nm and 580 nm that disappear over 30 ps, and (3) stimulated emission at wavelengths to the red of 620 nm that decays with a rate constant of 4 ps. The authors conclude that the behavior can be explained by processes that involve excitation of the Z-NH (Figure 2.29) ground state followed by decay of the initially formed vibronic state (relatively high in the manifold) to a mix of the S_1 and S_2 states of the Z-NH conformer over 700 fs. Stimulated emission of the S_1 state occurs over the first 4 ps, during which time a long lived state is formed; meanwhile the S_2 state decays to the ground state with a lifetime of 13 ps. The long lived state (> 5 ns) is attributed by the authors to formation of either a Z-NH triplet or possibly the keto E-NH isomer. The key postulate relating to the two components of the ultrafast behavior is the formation and relatively slow (13 ps) decay out of the S_2 state directly back to the ground state without relaxation to the S_1 state. Nanosecond transient absorption results for HLnap show a transient species that remains in solution after 3 milliseconds and does not participate in excited state electron transfer with MPTH or energy transfer with 9-bromoanthracene. These results are consistent with the formation of a ground state species as observed for SalAn, likely with either a cis-zwitterionic (iminium ion/ naphthoate) or the isomerized keto E-NH structure. It is clear that the presence of the Sn(IV) moiety yields complexes with very different excited state properties than the free ligands; the complexes exhibit enhanced luminescence, possess unique sub-picosecond and nanosecond time-resolved transient

absorption spectra which reveal lowest energy excited states different than those of the ligand, and have the ability to partake in excited state electron and energy transfer reactions from the triplet excited state.

2.4.2.10 Excited State Assignment of [PhSnNNOCl$_2$] Complexes

As mentioned above, the absorption and luminescence spectra of HLnap and the [PhSnLnapCl$_2$] are similar, suggesting a strong correspondence of the orbitals and states involved. The HOMO and LUMO obtained from DFT geometry optimized structures of the Sn(IV) complexes, shown in Figures 2.33-2.36, clearly illustrate that neither the Sn(IV) nor the coordinated phenyl contribute in any significant way to the HOMO or LUMO of any of the complexes. Small contributions to the HOMO from the coordinated Cl are seen for all the complexes other than [PhSnLdeaCl$_2$].
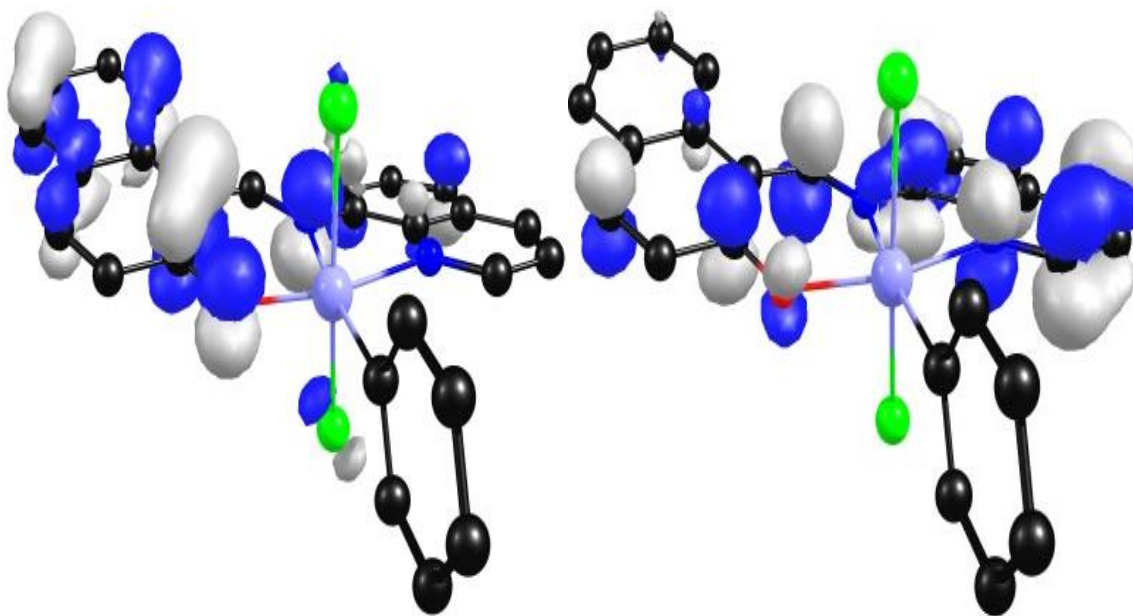
Figure 2.33 Illustrations of the HOMO (Left) and LUMO (Right) for B3LYP/LANL2DZ (Sn with ECP) 6-31G(d,p)(all other atoms) calculated structures of [PhSnLnapCl$_2$]. The depicted pair of orbitals are involved in the lowest energy allowed electronic transitions for [PhSnLnapCl$_2$].
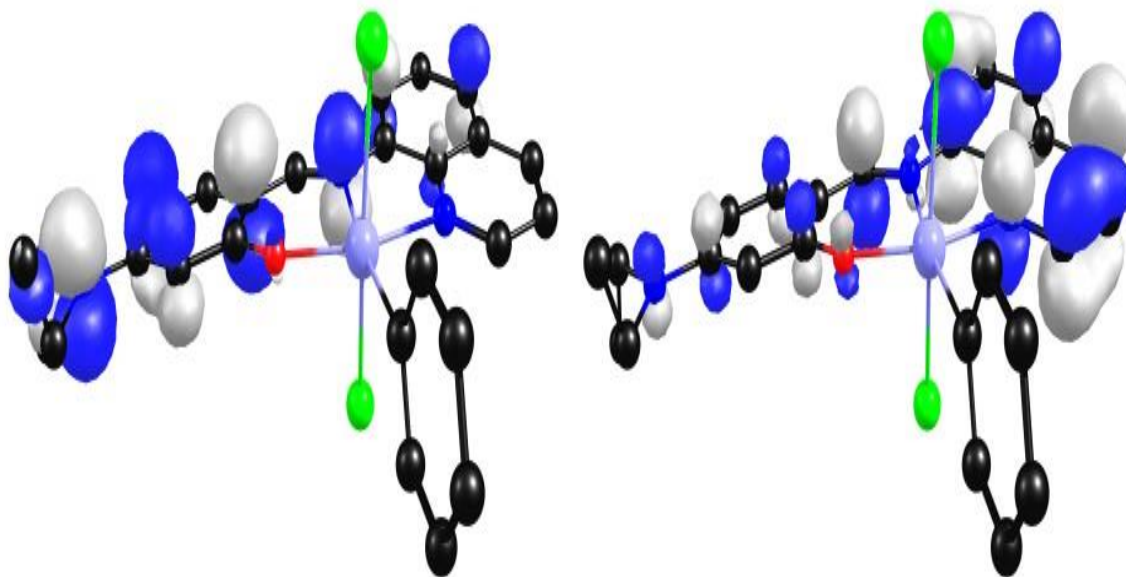
Figure 2.34 Illustrations of the HOMO (Left) and LUMO (Right) for B3LYP/LANL2DZ (Sn with ECP) 6-31G(d,p)(all other atoms) calculated structures of [PhSnLdeaCl$_2$]. The depicted pair of orbitals are involved in the lowest energy allowed electronic transitions for [PhSnLdeaCl$_2$].
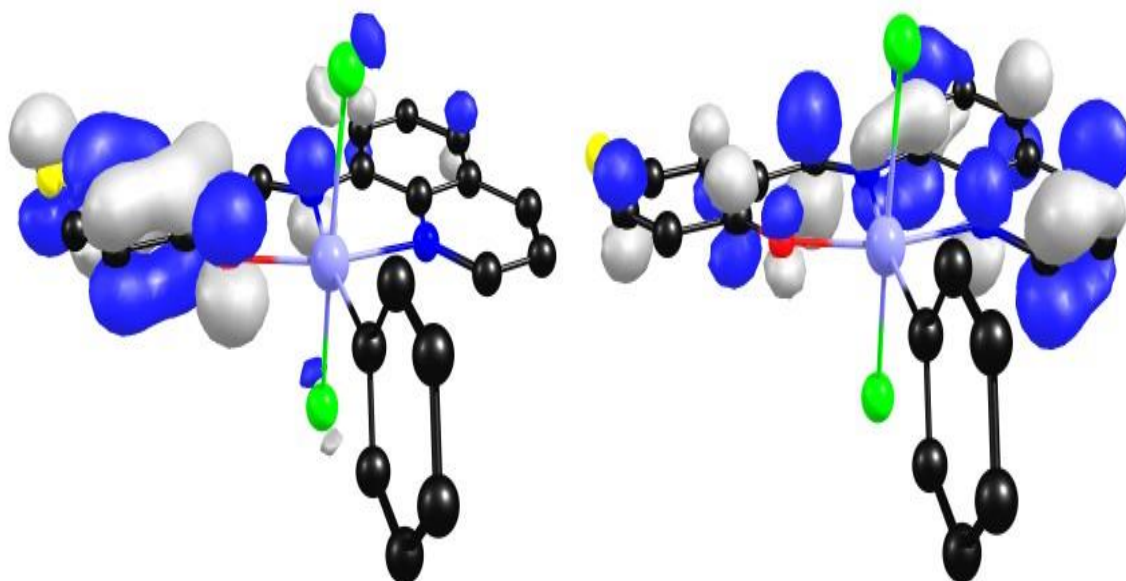
Figure 2.35 Illustrations of the HOMO (Left) and LUMO (Right) for B3LYP/LANL2DZ (Sn with ECP) 6-31G(d,p)(all other atoms) calculated structures of [PhSnLBrCl$_2$]. The depicted pair of orbitals are involved in the lowest energy allowed electronic transitions for [PhSnLBrCl$_2$].
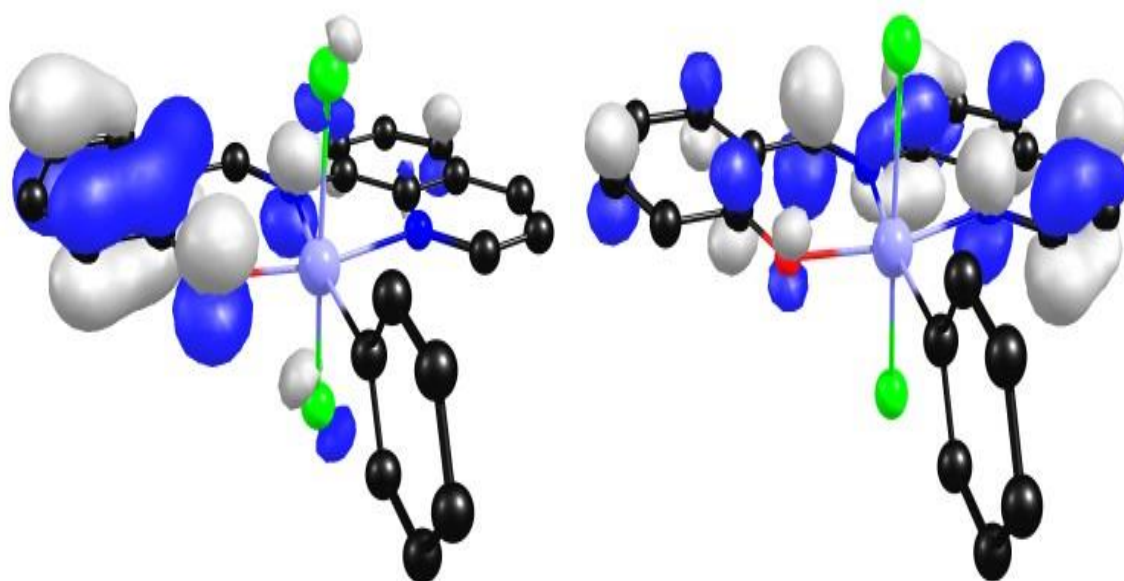
Figure 2.36 Illustrations of the HOMO (Left) and LUMO (Right) for B3LYP/LANL2DZ (Sn with ECP) 6-31G(d,p)(all other atoms) calculated structures of [PhSnLsalCl$_2$]. The depicted pair of orbitals are involved in the lowest energy allowed electronic transitions for [PhSnLsalCl$_2$].

The ultrafast transient spectral data for the complexes other than [PhSnLdeaCl$_2$] have common spectral features that differ from those of the nanosecond transients but evolve over a few nanoseconds to a final spectrum that closely corresponds to the longer time transients (> 10 ns). Thus, the sub-nanosecond kinetics results in the formation of the long lived triplet. Two of the three dynamic components of the decays of the ultrafast transients can be assigned: the subpicosecond decay is likely due to vibrational relaxation of the singlet manifold and the longest decay corresponds to relaxation of the singlet excited state (to triplet and ground state). The intermediate component varies from 70 ps for [PhSnLnapCl$_2$] to 1 ps for [PhSnLdeaCl$_2$], with the other two complexes closer to [PhSnLnapCl$_2$]. The time for all but the Ldea complex is much too long for solvation of the excited state and the explanation for such a long process is not clear. It is possible that

the initial excitation may lead to population of two different singlet states that decay with vastly different rate constants. In support of this is the observation that the ultrafast spectrum does not really change during the 40 - 100 ps time period over which the intermediate component decays. A potentially definitive experiment would be to excite the complexes at lower energy in an attempt to excited only the lowest energy of the two singlet states.

The luminescence lifetime values for the complexes obtained from TCSPC measurements are in good agreement with the long component of the decay of the ultrafast transient absorption spectrum for all chromophores. These values reflect the decay of the initially formed singlet excited state by radiative, non-radiative, and intersystem crossing processes. Using the experimentally obtained lifetime value, quantum yield of intersystem crossing, and the quantum yield of fluorescence, the rate constants of all three relaxation processes can be determined.

The rates of intersystem crossing vary from 2.6×10^8 s^{-1} for [PhSnLnapCl$_2$] to 9.0×10^8 s^{-1} for [PhSnLBrCl$_2$]. The intersystem crossing rate of [PhSnLBrCl$_2$] is 3 times greater than that of [PhSnLnapCl$_2$] and [PhSnLdeaCl$_2$], and only slightly greater than that of [PhSnLsalCl$_2$]. This implies that presence of a second heavy atom (Br) does not have a large effect on the observed rate of intersystem crossing. It is also important to note that the intersystem crossing rates for chromophores of this type are four orders of magnitude slower than those of well-known ruthenium polypyridyl chromophores. The radiative decay rates of the singlet state only differ by a factor of two across the series of four chromophores from 1.0×10^8 s^{-1} for [PhSnLnapCl$_2$] to 5.0×10^7 s^{-1} for[PhSnLsalCl$_2$] and

are in the range of radiative decay rate constants of organic chromophores with allowed π-π* transitions.

The largest difference in rate constants of the singlet excited states is observed for the non-radiative decay rate of [PhSnLdeaCl$_2$], which is an order of magnitude faster than the non-radiative decay rates for all of the other molecules in the series. It is perhaps not surprising that the ultrafast absorption spectrum is fundamentally different from the other three complexes, completely lacking the absorption feature that appears immediately upon excitation between 350 and 400 nm and remains. The solvent dependence of the absorption and luminescence behavior indicates that the excited singlet state has significant charge transfer character and relaxation of this excited state is the fastest of the four complexes ($k_{nr} = 6 \times 10^9$ s^{-1}). The effect of this is reflected in a relatively low quantum yield for fluorescence *and* a very low intersystem crossing efficiency.

Since none of the complexes exhibit phosphorescence from the long-lived transient absorbing species, a systematic effort was made to assign the transients. Examination of quenching of the long lived transients with a series of triplet quenchers indicated a systematic dependence of the quenching rate constant on the triplet energy of the quencher. The data were fit assuming a reversible energy transfer model[59-61] and the triplet energies (Table 2.3) obtained indicate a relatively small range for the complexes. Interestingly, the energy gaps between the singlet states (taken from the fluorescence maxima) and the triplet states are 3800 cm^{-1}, 2500 cm^{-1}, 2300 cm^{-1} and 1100 cm^{-1} for the Lnap, Lsal, LBr and the Ldea complexes, respectively. For the first three the relative efficiencies for populating the triplet state increase with decreasing S_1-T_1 gap, but the 4deaesal complex has a very low η_{isc} despite an apparently small S_1-T_1 gap. However,

the observed fluorescence originates from a state with a large degree of charge transfer character and the triplet may well represent a state that is more similar to the other complexes in electron distribution. At this point, we have no data that relates to the degree of charge transfer character in the triplet state of the Ldea complex, but the low intersystem crossing efficiency observed, despite the small apparent S_1-T_1 gap, clearly indicates a fundamental difference between this complex and the others.

The triplet energies of all the complexes are well above that of singlet oxygen and near-infrared emission spectra of aerated solutions of all the complexes other than the Ldea complex clearly showed the signature 1270 nm emission of singlet oxygen. Yields for oxygen formation were between 40 and 60% in acetonitrile. The lack of sensitized singlet oxygen emission in the Ldea complex is attributed to the very low yield of triplet states in this complex.

Electron transfer quenching experiments with an electron donor and electron acceptor with clearly identifiable radical ion absorbance in the visible ($MPTH^{+\bullet}$ and $MV^{+\bullet}$) served to illustrate the potential of the complexes to serve as both excited state oxidants and reductants. For reductive quenching with MPTH, the transient absorption spectrum following electron transfer quenching should reflect the sum of the radical ion species absorption less the absorption of the ground state complex and quencher (MPTH). Since MPTH has no visible absorbance and the absorption spectra of the starting complex and the MPTH cation radical are known, the only remaining unknown is the spectrum of the one-electron reduced form of the Sn complex. The voltammetric data clearly indicate that reduction of the complex is irreversible (probably E_rC_i process), thus we were unable to obtain the spectrum of the reduced complex by

spectroelectrochemistry. However, it should be noted that the transient spectra obtained following quenching with MPTH (Figure 2.29) *strongly* resemble spectra generated from the difference of the MPTH cation radical and the Sn complex ground state absorption. The implication is the that the absorbance of the reduced Sn complex in the visible is minimal, possibly suggesting reduction of the metal (to Sn(III)) rather than ligand localized reduction to make the ligand anion radical, which would very likely have strong visible absorption. However, the DFT results (Figures 2.33-2.36) clearly suggest that the LUMO is ligand localized. The back reaction of the reduced complex with the MPTH$^{+\bullet}$ is observed, but over the course of the acquisition of a transient absorption spectrum the MPTH$^{+\bullet}$ begins to accumulate in solution, indicating decomposition of the reduced Sn complex occurs on the hundreds of microseconds time scale. A similar behavioral trend was observed upon quenching with an oxidative quencher, MV (Figure 2.30): the transient spectrum of the long lived species resembled the difference between the MV cation radical absorbance and the ground state absorption of the complex. All the complexes served as effective one-electron donors, with the Ldea complex being the most effective. While we have no direct evidence, it is likely the oxidized complex reflects the ligand cation radical (see the HOMO of DFT in Figures 2.33-2.36). As above, back electron transfer occurs, but some decomposition of the oxidized Sn complex occurs on the time scale of the back reaction and reduced viologen gradually accumulates in solution.

2.4.2.11 Conclusions

The synthesis and characterization of a series of four fluorescent Sn(IV) Schiff base complexes with reasonably high yields of triplet state formation is described. The complexes absorb in the visible (λ_{max} = 420 to 462 nm) and their optical properties are easily tunable without laborious synthetic elaboration. The complexes are fluorescent, with low emission yields, and also form nonluminescent triplet excited states with formation yields ranging from 5 % to 70%. Ultrafast transient spectral studies provide lifetimes for the singlet excited states, with decays that correlate well with luminescence followed by TCSPC. The triplets were observed and kinetically evaluated using nanosecond transient absorption spectroscopy. The lifetimes of the triplet excited states are on the order of 500 μs − 10 ms in PMMA matrices. Triplet-triplet annihilation processes occur at near diffusion limited rates in solutions of the chromophores. The triplet state energies were estimated from the free energy dependence of energy transfer rate constants for reaction with a series of organic triplet acceptors. All the complexes other than the Ldea complex were good sensitizers for singlet oxygen emission. The photoexcited complexes react with both electron donors and acceptors in solution, although decomposition of both the complex radical anion and radical cation competes to some degree with back electron transfer. These results demonstrate the potential for the development of photosensitizers based on main group elements with high spin orbit coupling constants.

CHAPTER 2 REFERENCES

(1) Murov, S. L.; Carmichael, I.; Hug, G. L. In *Handbook of Photochemistry;* Dekker, M., Ed.; New York (NY), 1993; pp 420.

(2) Oldenburg, K.; Vogler, A.; Horváth, O. *Inorg. Chim. Acta* 1997*, 257*, 149.

(3) Oldenburg, K.; Vogler, A.; Miko, I.; Horvath, O. *Inorg. Chim. Acta* 1996*, 248*, 107-110.

(4) Oldenburg, K.; Vogler, A. *Z. Naturforsch , B: Chem. Sci.* 1993*, 48*, 1519-23.

(5) Nikol, H.; Becht, A.; Vogler, A. *Inorg. Chem.* 1992*, 31*, 3277-9.

(6) Volger, A.; Nikol, H. *Pure Appl. Chem.* 1992*, 64*, 1311.

(7) Kunkely, H.; Vogler, A. *Chem. Phys. Lett.* 1991*, 187*, 609-612.

(8) Vogler, A.; Paukner, A.; Kunkely, H. *Coord. Chem. Rev.* 1990*, 97*, 285-97.

(9) Kim, H.; Kim, W.; Mackeyev, Y.; Lee, G.; Kim, H.; Tachikawa, T.; Hong, S.; Lee, S.; Kim, J.; Wilson, L. J.; Majima, T.; Alvarez, P. J. J.; Choi, W.; Lee, J.. *Environ. Sci. Technol.* 2012*, 46*, 9606-9613.

(10) Kim, W.; Tachikawa, T.; Majima, T.; Li, C.; Kim, H.; Choi, W. *Energy Environ. Sci.* 2010*, 3*, 1789.

(11) Martinez-Diaz, M.; de, l. T.; Torres, T. *Chem. Commun.* 2010*, 46*, 7090-7108.

(12) Indelli, M. T.; Chiorboli, C.; Ghirotti, M.; Orlandi, M.; Scandola, F.; Kim, H. J.; Kim, H. *J. Phys. Chem. B* 2010*, 114*, 14273-14282.

(13) Seotsanyana-Mokhosi, I.; Kresfelder, T.; Abrahamse, H.; Nyokong, T. *J. Photochem. Photobiol. B: Biology* 2006*, 83*, 55-62.

(14) Rand, B. P.; Xue, J.; Yang, F.; Forrest, S. R. *Appl. Phys. Lett.* 2005*, 87*, 233508.

(15) Wang, S.; Tabata, I.; Hisada, K.; Hori, T. *J. Porphyrins Phthalocyanines* 2003*, 7*, 199.

(16) Wang, S.; Enomoto, K.; Tanizaki, S.; Tabata, I.; Hisada, K.; Hori, T.; Okubayashi, S. *Sen'i Gakkaishi* 2003*, 59*, 48-52.

(17) Okubayashi, S.; Ariga, S.; Shosenji, H.; Hori, T. *Sen'i Gakkaishi* 1997*, 53*, 431-437.

(18) Grewer, C.; Schermann, G.; Schmidt, R.; Voelcker, A.; Brauer, H. D.; Meier, A.; Montforts, F. P. *J. Photochem. Photobiol. B: Biology* 1991*, 11*, 285-93.

(19) Morgan, A. R.; Cheng, L. S.; Skalkos, D.; Garbo, G. M. *Photochem. Photobiol.* 1990*, 52*, 987-991.

(20) Szulbinski, W.; Strojek, J. W. *Inorg. Chim. Acta* 1986*, 118*, 91.

(21) Fuhrhop, J.; Krüger, W.; David, H. E. *Liebigs Ann. Chem.* 1983*, 1983*, 204-210.

(22) Sayer, P.; Gouterman, M.; Connell, C. R. *Acc. Chem. Res.* 1982*, 15*, 73-79.

(23) Harel, Y.; Manassen, J. *J. Am. Chem. Soc.* 1977*, 99*, 5817-5818.

(24) Gouterman, M.; Schwarz, F. P.; Smith, P. D.; Dolphin, D. *J. Chem. Phys.* 1973*, 59*, 676.

(25) Whitten, D. G.; Yau, J. C. N.; Carroll, F. *J. Am. Chem. Soc.* 1971*, 93*, 2291-2296.

(26) Becker, R. S.; Allison, J. B. *J. Phys. Chem.* 1963*, 67*, 2669-2675.

(27) Ohtani, M.; Kamat, P. V.; Fukuzumi, S. *J. Mater. Chem.* 2010*, 20*, 582-587.

(28) Fortage, J.; Goeransson, E.; Blart, E.; Becker, H.; Hammarstroem, L.; Odobel, F. *Chem. Commun. ,*2007, 4629-4631.

(29) Du, C.; Yu, J.; Huang, J.; Jiang, Y. *Energy Procedia* 2011*, 12*, 519.

(30) Idowu, M.; Nyokong, T. *J. Photochem. Photobiol. A: Chemistry* 2008*, 199*, 282-290.

(31) Nyokong, T. *J. Porphyrins Phthalocyanines* 2008*, 12*, 1005.

(32) Agboola, B.; Ozoemena, K. I.; Nyokong, T. *J. of Mol.Catal. A: Chemical* 2006*, 248*, 84-92.

(33) Nensala, N.; Nzimande, A.; Nyokong, T. *J. Photochem. Photobiol. A: Chemistry* 1996*, 98*, 129-135.

(34) Aviv-Harel, I.; Gross, Z. *Coord. Chem. Rev.* 2011*, 255*, 717-736.

(35) Aviv, I.; Gross, Z. *Chem. Commun.* 2007, 1987-1999.

(36) Walker, D.; Chappel, S.; Mahammed, A.; Brunschwig, B. S.; Winkler, J. R.; Gray, H. B.; Zaban , A.; Gross, Z. *J. Porphyrins Phthalocyanines* 2006*, 10*, 1259.

(37) Ventura, B.; Esposti, A. D.; Koszarna, B.; Gryko, D. T.; Flamigni, L. *New J. Chem.* 2005*, 29*, 1559.

(38) Pawlowski, V.; Kunkely, H.; Vogler, A. *Inorg. Chim. Acta* 1995*, 234*, 55-60.

(39) Pawlowski, V.; Kunkely, H.; Vogler, A. *Coord. Chem. Rev.* 1994*, 132*, 23.

(40) Makita, K.; Nomura, K.; Saito, Y. *J. of Mol. Catal.* 1994*, 89*, 143-149.

(41) Matsubara, T.; Saito, Y.; Yamakawa, T.; Shinoda, S. *J. of Mol. Catal.* 1993*, 79*, 29-37.

(42) Pawlowski, V.; Kunkely, H.; Vogler, A. *J. Am. Chem. Soc.* 1993*, 115*, 7029-30.

(43) Matsubara, T.; Saito, Y.; Yamakawa, T.; Shinoda, S. *J. of Mol. Catal.* 1991*, 67*, 175-184.

(44) Nomura, K.; Saito, Y.; Shinda, S. *J. of Mol. Catal.* 1989*, 50*, 303-313.

(45) Andrea, R. R.; De, L., Wim G. J.; Stufkens, D. J.; Oskam, A. *Inorg. Chem.* 1989*, 28*, 318-23.

(46) Holt, M. S.; Wilson, W. L.; Nelson, J. H. *Chem. Rev.* 1989*, 89*, 11.

(47) Donaldson, J. D. *Prog. Inorg. Chem.* 1968*, 8*, 287.

(48) Takano, K.; Takahashi, M.; Fukushima, T.; Takezaki, M.; Tominaga, T.; Akashi, H.; Takagi, H.; Shibahra, T. *Bull. Chem. Soc. Jpn.* 2012*, 85*, 1210.

(49) Takano, K.; Shibahara, T. *Chem. Lett.* 2008*, 37*, 70-71.

(50) Lachish, U.; Infelta, P. P.; Gratzel, M. *Chem. Phys. Lett.* 1979*, 62*, 317.

(51) Carmichael, I.; Hug, G. L. *J. Phys. Chem. Ref. Data* 1986*, 15*, 1.

(52) Gaussian 09, Revision D.01, M. J. Frisch, G. W. Trucks, H. B. Schlegel, G. E. Scuseria, M. A. Robb, J. R. Cheeseman, G. Scalmani, V. Barone, B. Mennucci, G. A. Petersson, H. Nakatsuji, M. Caricato, X. Li, H. P. Hratchian, A. F. Izmaylov, J. Bloino, G. Zheng, J. L. Sonnenberg, M. Hada, M. Ehara, K. Toyota, R. Fukuda, J. Hasegawa, M. Ishida, T. Nakajima, Y. Honda, O. Kitao, H. Nakai, T. Vreven, J. A. Montgomery Jr., J. E. Peralta, F. Ogliaro, M. J. Bearpark, J. Heyd, E. N. Brothers, K. N. Kudin, V. N. Staroverov, R. Kobayashi, J. Normand, K. Raghavachari, A. P. Rendell, J. C. Burant, S. S. Iyengar, J. Tomasi, M. Cossi, N. Rega, N. J. Millam, M. Klene, J. E. Knox, J. B. Cross, V. Bakken, C. Adamo, J. Jaramillo, R. Gomperts, R. E. Stratmann, O. Yazyev, A. J. Austin, R. Cammi, C. Pomelli, J. W. Ochterski, R. L. Martin, K. Morokuma, V. G. Zakrzewski, G. A. Voth, P. Salvador, J. J. Dannenberg,

S. Dapprich, A. D. Daniels, Ö. Farkas, J. B. Foresman, J. V. Ortiz, J. Cioslowski and D. J. Fox, Gaussian, Inc., Wallingford CT, 2009.

(53) Wadt, W. R.; Hay, P. J. *J. Chem. Phys.* 1985*, 82*, 284-298.

(54) Jiang, C.; Wang, J.; He, F. *Anal. Chim. Acta.* 2001*, 439*, 307.

(55) Collins, D. M.; Scheidt, W. R.; Hoard, J. L. *J. Am. Chem. Soc.* 1972*, 94*, 6689.

(56) Bondi, A. *J. Phys. Chem.* 1964*, 68*, 441.

(57) Caspar, J. V.; Meyer, T. J. *J. Am. Chem. Soc.* 1983*, 105*, 5583.

(58) Abdel-Shafi, A. A.; Worrall, D. R.; Ershov, A. Y. *Dalton Trans.* 2004*, 2004*, 30.

(59) Balzani, V.; Bolletta, F.; Scandola, F. *J. Am. Chem. Soc.* 1980*, 102*, 2152-2163.

(60) Herkstroeter, W. G.; Hammond, G. S. *J. Am. Chem. Soc.* 1966*, 88*, 4769-4777.

(61) Sandros, K. *Acta Chem. Scand.* 1964*, 18*, 2355.

(62) Salman, S. R.; Kanber, S. K.; Arslian, L. K. *Spectrosc. Lett.* 1990*, 23*, 870.

(63) Abbas, K. A.; Salman, S. R.; Kana'n, S. M.; Fataftah, Z. A. *Can. J. Appl. Spectrosc.* 1996*, 41*, 119.

(64) Cohen, M. D.; Schmidt, G. M. J. *J. Phys. Chem.* 1962*, 66*, 2442.

(65) Cohen, M. D.; Hirshberg, Y.; Schmidt G.M.J. *J. Chem. Soc.* 1964, 2051.

(66) Ottolenghi, M.; McClure, D. S. *J. Chem. Phys.* 1967*, 46*, 4620.

(67) Nakagaki, R.; Kobayashi, T.; Nakamura, J.; Nagakura, S. *Bull. Chem. Soc. Jpn.* 1977*, 50*, 1909.

(68) Barbara, P. F.; Rentzepis, P. M.; Brus, L. E. *J. Am. Chem. Soc.* 1980*, 102*, 2786.

(69) Becker, R. S.; Lenoble, C.; Zein, A. *J. Phys. Chem.* 1987*, 91*, 3509.

(70) Tuberville, W.; Dutta, P. K. *J. Phys. Chem.* 1990*, 94*, 4060.

(71) Yuzawa, T.; Takahashi, H.; Hamaguchi, H. *Chem. Phys. Lett.* 1993*, 202*, 221.

(72) Kownacki, K.; Mordzinski, A.; Wilbrandt, R.; Grabowska, A. *Chem. Phys. Lett.* 1994*, 227*, 270.

(73) Mitra, S.; Tamai, N. *Chem. Phys. Lett.* 1998*, 282*, 391.

(74) Fita, P.; Luzina, E.; Dziembowska, T.; Kopeć, D.; Piątkowski, P.; Radzewicz, C.; Grabowska, A. *Chem. Phys. Lett.* 2005*, 416*, 305.

(75) Fita, P.; Luzina, E.; Dziembowska, T.; Radzewicz, C.; Grabowska, A. *J. Chem. Phys.* 2006*, 125*, 184508.

Chapter 3: Evaluating the Extent of Intramolecular Charge Transfer in the Excited States of Rhenium(I) Donor-Acceptor Complexes

This chapter uses material from two American Chemical Society journal articles.

3.1 Intramolecular Electron Transfer in Transition Metal Complexes.

The mechanisms of photoinduced intramolecular electron transfer (ET) have been the subject of intensive study for more than 30 years.[1-7] Many of these systems contain an electron donor or acceptor that can be oxidized or reduced by an initial excited state, resulting in a charge separated (CS) state. The thermodynamic feasibility of creating a CS state can be estimated using the first oxidation and reduction potentials of the particular molecule. If the sum of the energy ($\Delta E_{1/2}$) necessary to oxidize the donor ($E(D^+/D)$) and reduce the acceptor ($E(A/A^-)$) is close to or below the energy of the initially formed excited state (E_{0-0}), creation of a CS state may be observed. Formation of this CS state may occur in discrete steps (i.e., formation of an excited state may be followed by an intramolecular electron-transfer step) or absorption may directly create an excited electronic state with significant charge separation. The electron-density distribution and degree of charge transfer associated with the initially formed and relaxed excited states are critical, but are often poorly characterized. For transition metal complexes with metal-to-ligand charge transfer (MLCT) excited states, the structural and charge polarization changes that follow from the initial excitation to the generation of the intramolecular

photoredox products can be subtle.[4,8,9] This is especially true when the *charge-separated state formed upon electron transfer is structurally similar to that* of the initial excited state. In this regard, fully understanding the subtleties of intramolecular electron transfer reactions often requires a spectroscopic approach that provides direct temporal information on the electron-density distribution within the molecule.

3.2. Rhenium Tricarbonyl-Diimine Complexes: Ideal Systems For Monitoring Intramolecular Electron Transfer Reactions.

Rhenium tricarbonyl-diimine complexes, fac-$[Re^I(N,N)((CO)_3L)]^{+/0}$ (+ when L is a neutral ligand with a substituent capable of electron donation to the excited complex and 0 when L is a halide), are appealing candidates for monitoring intramolecular charge-transfer processes because infrared stretching modes of the carbonyl (CO) and imine ligands provide information on charge localization in the system. In particular, the CO stretching modes of these complexes serve as powerful probes for monitoring the redistribution of electron density in the excited state because they are highly sensitive to changes in the electronic character of the metal center due to back-bonding interactions.[10-12] A wealth of previous research on fac-$[Re^I(N,N)((CO)_3L)]^{+/0}$ complexes[10,11,13-24] provides insight into the initial formation and subsequent evolution of the lowest energy MLCT states in these systems. Picosecond time-resolved changes in the CO stretching mode frequencies of the complexes indicate that formation of the vibrationally relaxed ^{3}MLCT state occurs within 1-10 ps after excitation. In all cases, the ^{3}MLCT state is luminescent. For systems where L is a halide ligand, the ^{3}MLCT states are weakly luminescent (emission yield < 0.05) and proceed to relax back to the ground state with time constants on the order of hundreds of nanoseconds. When the halide

ligand is substituted for a non-redox active ligand, the emission yields and luminescence lifetimes increase. Time-resolved infrared (TRIR) measurements results show rapid formation of the ^{3}MLCT state which is characterized by an increase in the carbonyl stretching frequencies due to a decrease in electron density at the metal center in the excited state. When L is a sufficient electron donor or acceptor, a decrease in both the luminescence lifetime and the quantum yield of luminescence of the ^{3}MLCT state is observed. This behavior is generally attributed to an increase in k_{nr} due to rapid charge recombination. The steady state luminescence data clearly indicate a reaction has occurred but do provide any information on the actual electronic structure of the molecule or any intermediate species formed after excitation. Examination of donor-acceptor systems using TRIR reveals picosecond time scale evolution from the initially formed ^{3}MLCT state to form CS species, and time-resolved changes in the infrared absorption spectrum yield key details in understanding the dynamics of the intramolecular electron transfer process.

Previous work by Schanze and co-workers used time-resolved UV-VIS methods to explore changes in the photophysical properties of fac-[Re^I(bpy)(CO)$_3$4DMABN]$^+$ (4DMABN = 4-dimethylaminobenzonitrile) in various mixtures of dichloromethane (DCM) and acetonitrile (ACN).[22] The complex exhibits strong emission at 540 nm (2.3 eV) with a lifetime of 650 ns in DCM. The lifetime, quantum yield, and maximum of this emission were in agreement with the compound fac-[Re^I(bpy)(CO)$_3$ACN]$^+$ (ACN = acetonitrile); thus, the authors attributed the luminescence of fac-[Re^I(bpy)(CO)$_3$4DMABN]$^+$ in DCM as a Re (dπ) to bpy (π*) MLCT state. Increasing the mole fraction of ACN results in a dramatic decrease in the luminescence quantum yield

(0.10 to < 0.001) and lifetime (650 ns to < 3 ns) with a subtle change in the emission maximum (500 cm^{-1}). Further, $\Delta E_{1/2}$ for the complex is lowered from 2.61 V in pure DCM to 2.46 V in ACN. This change in excited state behavior was attributed to formation of a 4DMABN (π^*) to bpy (π^*) interligand charge transfer (LLCT) state (fac-[Re^I(bpy$^-$)(CO)$_3$(4DMABN$^+$)]$^+$), which rapidly relaxes to the ground state. The electrochemical measurements suggest that in more polar solvent mixtures the charge separated state is stabilized relative to the MLCT state, allowing for the thermal population of the charge separated state from the initially excited MLCT state. This system seems primed for a beautiful set of time-resolved transient infrared measurements. In DCM, electronic excitation will result in the formation of the Re (dπ) to bpy (π^*) MLCT excited state. As a consequence, the amount of electron density at the rhenium center will be lowered causing an increase in the carbonyl stretching frequency. When the polarity of the solution is increased, electronic excitation will result in the formation of the initial Re (dπ) to bpy (π^*) MLCT excited state followed by the formation of a charge separated species, ([Re^I(bpy$^-$)(CO)$_3$(4DMABN$^+$)]$^+$). An initial increase in the CO stretching frequency (Re(dπ) to bpy (π^*) MLCT) should be followed by a relative decrease in the CO stretching frequencies as the DMABN donor is oxidized. The variation in CO stretching frequencies should also be accompanied by changes in the bpy imine stretches upon reduction as well as changes in 4DMABN ring vibrations as the donor becomes more electron deficient.

fac-[Re(bpy)(CO)$_3$4DMABN](BArF$_{24}$) and the parent molecule, fac-[Re(bpy)(CO)$_3$BN](BArF$_{24}$) (BN = benzonitrile), were synthesized and initially characterized using steady state photochemical methods. The initial data were in

agreement with those published by Schanze and co-workers[22]; however, time-resolved infrared results did not provide experimental support for charge separation in the excited state of fac-[Re(bpy)(CO)$_3$4DMABN](BArF$_{24}$). These results led to the synthesis of a second DMABN complex, fac-[Re(bpy)(CO)$_3$3DMABN](BArF$_{24}$), where 3DMABN is 3-dimethylaminobenzonitrile. All told, none of the initially synthesized rhenium complexes resulted in the expected excited state behavior. Nonetheless, these results demonstrate the limitations of traditional, steady state photochemical methods on the classification of excited state behavior, and that TRIR methods can play a pivotal role in elucidating differences in the excited state reactivity. We utilized our experience from the initial set of fac-[Re(bpy)(CO)$_3$L](BArF$_{24}$) measurements in the synthesis and characterization the structural analog, fac-[Re(dcebpy)(CO)$_3$3DMABN](BArF$_{24}$) (dcebpy = 4,4'-dicarboxylic acid diethyl ester-2,2'-bipyridine). This molecule does access a LLCT state upon excitation with visible light! This chapter presents a detailed discussion of the synthesis, redox, luminescence, nanosecond transient absorption and ultrafast transient infrared behavior of this group of complexes.

3.3 Experimental

3.3.1 Spectroscopy

NMR spectra were recorded on a Varian 400 MHz NMR spectrometer. MALDI spectra were obtained on a Bruker Autoflex III time of flight mass spectrometer. All UV-VIS absorption spectra were measured on a Hewlett-Packard 8452 diode array spectrophotometer. Luminescence spectra were obtained using a PTI scanning spectrofluorimeter.

3.3.2 MALDI-TOF Experimental Details

Mass spectrometric analysis was performed using a Bruker Autoflex III MALDI-TOF mass spectrometer. Data acquisition and analysis was performed using Bruker Daltonics FlexControl 3.0 software. The mass scale for the MALDI-TOF MS was calibrated using SpheriCal 600-1800 Da mass standards (Polymer Factory, Sweden). The mass of each selected monoisotopic peak was determined by using a centroid algorithm calculated by the 'FlexAnalysis' software, and compared to the theoretical value based on ^{1}H, ^{12}C, ^{14}N, ^{16}O, ^{23}Na, ^{32}S and ^{64}Zn. Mass spectra were simulated using ChemCalc (www.chemcalc.org).[25] Data were acquired using reflector-positive and linear-positive ion modes. The acquisition parameters in reflector-positive mode were as follows: an ion source 1 (IS1) voltage of 19.00 kV; an ion source 2 (IS2) voltage of 16.90 kV; a lens voltage of 8.50 kV; reflector of 21.00 kV; reflector 2 of 9.64 kV and a pulse ion extraction delay time of 20 ns. The acquisition parameters in linear-positive mode were as follows: an ion source 1 (IS1) voltage of 20.00 kV; an ion source 2 (IS2) voltage of 18.85 kV; a lens voltage of 8.50 kV and a pulse ion extraction delay time of 0 ns. The rhenium samples were prepared by dissolving 2 mg of the complex in 2 ml of chloroform. 5 μl of these solutions were spotted onto the plate.

3.3.3 Cyclic Voltammetry

Voltammograms were obtained using a CH Instruments CH1730A Electrochemical Analyzer. The working electrode was a glassy-carbon electrode, the counter electrode was a Pt wire, and the reference electrode was an aqueous Ag/AgCl electrode. Data were collected in acetonitrile and dichloromethane solutions containing

0.1M TBAPF$_6$. All samples were bubble deaerated with argon for 10 minutes prior to collection.

3.3.4 Nanosecond Time-Resolved Transient Absorption Spectroscopy

Transient absorption spectra in the UV and visible spectral regions were obtained by collecting transient decays at 10 nm intervals following pulsed laser excitation using a system involving an Applied Photophysics LKS 60 optical system/software and a Quantel Brilliant laser equipped with second and third harmonics and an OPOTEK OPO (420-670 nm) for tunable excitation. The excitation wavelength used for these complexes was 420 nm. Samples were deaerated with N$_2$ for 20 minutes prior to acquisition of transient decays.

3.3.5 Femtosecond Time-Resolved Transient Infrared (TRIR) Spectroscopy

Ultrafast time-resolved infrared spectroscopic measurements were collected in collaboration with the group of Professor Igor Rubtsov at Tulane Univeristy. I owe a debt of gratitude to Yuankai Yue of the Rubtsov Group, who collected all of the transient infrared data and greatly contributed to scientific discussions of the data and preparation of both manuscripts.

A three-pulse (UV/IR/Vis) experimental setup, capable of performing fs time-resolved infrared spectroscopy (TRIR), fs transient absorption spectroscopy (TA) and IR-perturbed transient absorption spectroscopy, has been built.[26] A laser beam at 804 nm produced by a Ti:Sapphire oscillator and regenerative amplifier featuring pulses of 44 fs duration and 1.1 mJ energy at 1 kHz repetition rate was split in three parts. One part of ca. 630 µJ/pulse was frequency doubled to generate 402 nm excitation pulses. After passing a 150 mm long delay stage (NRT150, Thorlabs), it was focused into the sample

with a 300 mm focal length lens. The second part of the fundamental beam of ca. 370 μJ/pulse was used to pump an in-house built optical parametric amplifier (OPA), which produces signal-idler pulse pairs. The signal-idler beam was focused into a 1.5 mm thick AgGaS$_2$ crystal to generate mid-IR pulses through a difference frequency generation process. The mid-IR beam was focused into the sample cell with a lens of 100 mm focal length. The third part of the 804 nm beam (ca. 7 μJ/pulse) was delayed by a delay stage of 600 mm length (Parker), intensity-tuned by a wave plate-polarizer pair, and focused into a 1 mm thick sapphire wafer with a 100 mm lens to generate white light continuum. The white light was then focused into the sample using a 40 mm achromatic lens.

The TRIR measurements described here were made using excitation pulses at 402 nm of 3-4 μJ pulse energy and mid-IR probe pulses. After passing through the sample, the mid-IR probe pulses were dispersed in a monochromator (TRIAX-190, HORIBA) and measured by an MCT detector (MCT-11-1.00, Infrared Associates). The mid-IR pulses are tunable from 1100 to 4000 cm^{-1} and have a spectral width of ca. 200 cm^{-1} (FWHM). A spectra resolution of 1 cm^{-1} was achieved.

3.3.6 TRIR Sample Preparation

Sample solutions for transient infrared experiments: solutions of 20 mM concentration were prepared in two solvents: pure dichloromethane (DCM) and methanol/DCM mixture (1:1 by volume), referred here as MeOH/DCM solvent. The spectroscopic grade solvents (Aldrich) were used as received. To avoid influence of sample degradation over laser excitation, the time-resolved measurements were performed in the flow cell (DLC2, Harrick) with an optical path length of 150 μm at 23.5 ± 0.5° C. A sample solution of ca. 2.5 mL was circulated by a micro annular gear pump

(mzr-2942, HNP Mikrosysteme). The IR spectra of the sample before and after the experiment differ by less than 10%.

3.4 [Re(bpy)(CO$_3$)L](BArF$_{24}$) Complexes

3.4.1 Synthesis

Toluene, dichloromethane (DCM), and n-hexane were purchased from PHARMCO-AAPER. Re(CO)$_5$Cl was purchased from Strem Chemical. 3-aminobenzonitrile, 2,2'-bipyridine, paraformaldehyde, and sodium cyanoborohydride were purchased from Sigma Aldrich. Benzonitrile and 4-dimethylaminobenzonitrile were purchased from Alfa Aesar. Sodium tetrakis (3,5-bis(trifluoromethyl)phenyl)borate (Na[BArF$_{24}$]) was previous synthesized in our laboratory.[27] All synthetic materials were used as received other than 3-aminobenzonitrile which was *N*-methylated using a literature method.[28] fac-[Re(bpy)(CO)$_3$Cl][29] and the fac-[Re(bpy)(CO)$_3$L](BArF$_{24}$)[30] complexes were all prepared as previously reported in the literature.

3-dimethylaminobenzonitrile (3DMABN): 1.01 g (8.46 mmol) 3-aminobenzonitrile, 2.52 g (83.3 mmol) paraformaldehyde, and 2.56 g (40.7 mmol) sodium cyanoborohydride were stirred in 50 ml glacial acetic acid for 22 hours under nitrogen. 0.92 g (74.2%) of a colorless liquid was obtained after work up.

fac-[Re(bpy)(CO)$_3$OTf]: 401.0 mg (0.87 mmol) fac-[Re(bpy)(CO)$_3$Cl] were added to 60 mL of DCM and the solution was allowed to stir for 5 minutes until all of the fac-[Re(bpy)(CO)$_3$Cl] was completely dissolved. 236.2 mg (0.90 mmol) AgOTf were added to the solution. The reaction was allowed to stir at room temperature for 2 hours. The solution was filtered through Celite. The filtrate was transferred to a round bottom flask and the DCM was completely removed via rotary evaporation. The resulting solid

was reconstituted in 3 mL DCM and n-hexane was added dropwise to the point of turbidity. The flask was placed in the freezer overnight. 472.1 mg (94.4%) of yellow solid was collect on a fritted glass filter.

fac-[Re(bpy)(CO)$_3$BN](BArF$_{24}$): 127.3 mg (0.22 mmol) fac-[Re(bpy)(CO)$_3$OTf] and 25 mL benzonitrile (0.24 mmol) were added to 30 mL of DCM. The solution was allowed to stir for 5 minutes until all of the fac-[Re(bpy)(CO)$_3$OTf] was completely dissolved. At this point, 195.2 mg (0.22 mmol) Na[BArF$_{24}$] was added to the solution. The reaction was stirred at room temperature for 4 hours. The solution was filtered through Celite. Rotary evaporation was used to lower the filtrate volume to ~5 mL. n-Hexane was added to the DCM to the point of turbidity, and the solution was placed in the freezer overnight. 248.3 mg (82.8%) of microcrystalline, yellow solid was collected on a fritted glass filter. ^{1}H NMR (CD$_2$Cl$_2$) δ: 9.09 (d, J= 5.29 Hz, 2 H, bpy), 8.30 (d, J= 11.8 Hz, 2 H, bpy), 8.20 (t, J= 7.92 Hz, 2 H, bpy) 7.71 (m, 11 H, BArF$_{24}$ + bpy + BN), 7.54 (s, 4 H, BArF$_{24}$), 7.4 (m, 4 H, BN).

fac-[Re(bpy)(CO)$_3$4DMABN](BArF$_{24}$): 109.6 mg (0.19 mmol) fac-[Re(bpy)(CO)$_3$OTf], 28.2 mg (0.19 mmol) 4DMABN, and 170.2 mg (0.19 mmol) Na[BArF$_{24}$] were added to 30 mL of DCM. The reaction was stirred at room temperature for 4 hours. 252.4 mg (84.1%) of microcrystalline, yellow solid was collected on a fritted glass filter. ^{1}H NMR (CD$_2$Cl$_2$) δ: 9.08 (d, J= 5.24 Hz, 2 H, bpy), 8.30 (d, J= 8.68 Hz, 2 H, bpy), 8.22 (t, J= 8.64 Hz, 2 H, bpy) 7.71 (m, 10 H, BArF$_{24}$ + bpy), 7.55 (s, 4 H, BArF$_{24}$), 7.19 (d, J= 9.76 Hz, 2 H, 4DMABN), 6.52 (d, J= 9.08 Hz, 2 H, 4DMABN), 2.98 (s, 6 H, 4DMABN).

fac-[Re(bpy)(CO)₃3DMABN](BArF₂₄): 108.9 mg (0.19 mmol) fac-[Re(bpy)(CO)₃OTf], 30.2 mg (0.21 mmol) 3DMABN, and 168.2 mg (0.19 mmol) Na[BArF₂₄] were added to 30 mL of DCM. The solution was allowed to stir overnight at room temperature for 12 hours. If a small amount of the 3DMABN ligand persists after precipitation of the complex from DCM with hexane, it can be removed on a silica column. The free ligand is luminescent and will elute in 1:1 DCM:n-hexane. Once the ligand has been flushed from the column, the complex can be obtained with pure DCM. 242.4 mg (80.7%) of microcrystalline, yellow solid was collected on a fritted glass filter. ^{1}H NMR (CD₂Cl₂) δ: 9.10 (d, J= 5.76 Hz, 2 H, bpy), 8.32 (d, J= 8.28 Hz, 2 H, bpy), 8.23 (t, J= 7.44 Hz, 2 H, bpy) 7.71 (m, 10 H, BArF₂₄ + bpy), 7.55 (s, 4 H, BArF₂₄), 7.20 (t, J= 8.24 Hz, 1 H, 3DMABN), 6.93 (d, J= 9.08 Hz, 1 H, 3DMABN), 6.61 (m, 2 H, 3DMABN), 2.89 (s, 6 H, 3DMABN).

Note: These complexes can be purified via column chromatography. The complexes have R_f values of 0.8 on silica when eluted with DCM.

3.4.2 Results and Discussion

The complexes were synthesized utilizing a simple, three step reaction scheme. Initially, fac-[Re(bpy)(CO)₃Cl] was obtained via the reaction of [Re(CO)₅Cl] and 2,2-bipyridine in toluene. The reaction is complete in less than two hours, when run under reflux, and can be accomplished on the gram scale. It is interesting to note that the addition of 2,2-bipyridine to a hot solution of [Re(CO)₅Cl] results in an immediate color change of the solution from colorless to yellow due to the lability of two of the carbon monoxide ligands. fac-[Re(bpy)(CO)₃Cl] was then reacted with AgOTf (OTf = trifluoromethanesulfonate) in dichloromethane at room temperature, resulting in the

formation of fac-[Re(bpy)(CO)$_3$OTf] and precipitation of AgCl. The complexes were prepared through the reaction fac-[Re(bpy)(CO)$_3$OTf] with the desired benzonitrile ligand in the presence of Na[BArF$_{24}$] in methylene chloride. The reactions proceed readily at room temperature due to the low solubility of NaOTf in methylene chloride (salt metathesis) and prompt coordination of the nitrile ligand to the Re center. A depiction of this reaction scheme is shown below in Figure 3.1.
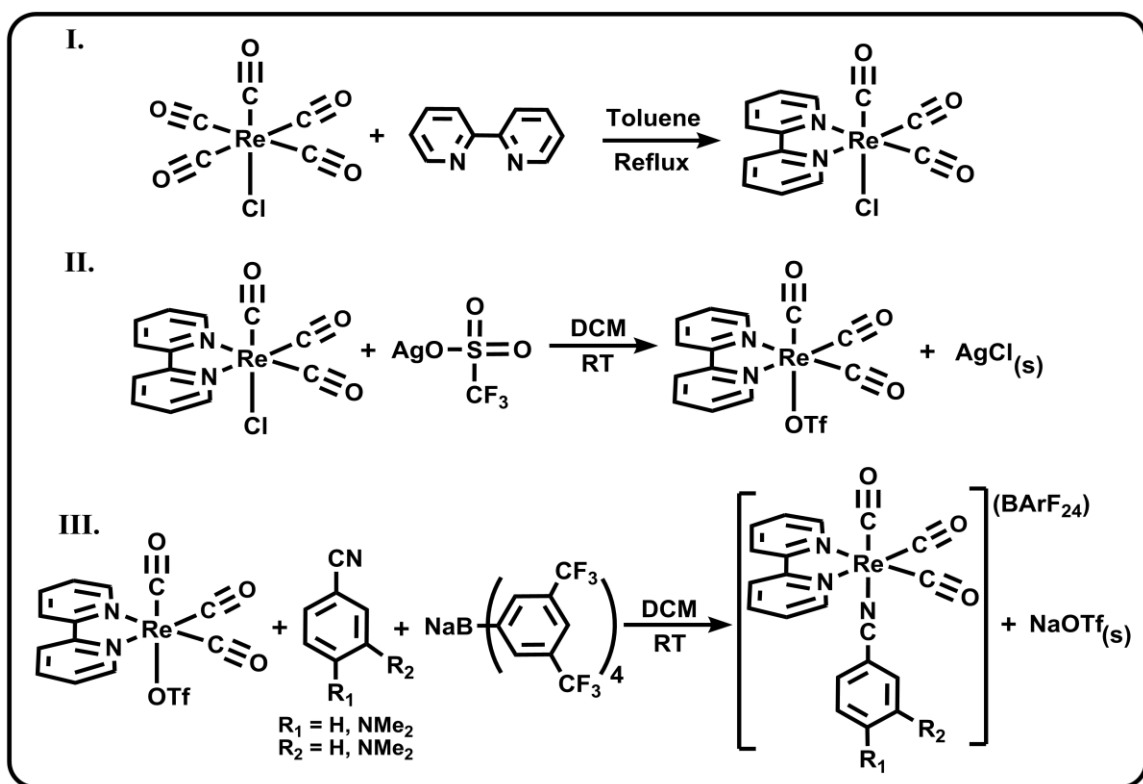
Figure 3.1 Full synthetic scheme utilized to obtain our series of fac-[Re(bpy)(CO)$_3$(L)](BArF$_{24}$) complexes.

The complexes were characterized using ^{1}H NMR, MALDI-TOF mass spectrometry and X-Ray Crystallography. Images of the ^{1}H NMR spectra of complexes are included in the following Section, 3.4.2.1, as Figures 3.2-3.4. MALDI-TOF results, including linear-positive and reflector-positive mass spectra and simulated molecular formulas for observed species, are collected in Section 3.4.2.2. These data encompass Figures 3.5-3.13

and Tables 3.1-3.3. ORTEP representations of all three complexes (Figure 3.14) as well as selected bond lengths (Table 3.4) and pertinent refinement data (Table 3.5) are presented in Section 3.4.2.3 X-Ray Crystallography.

3.4.2.1 ^{1}H NMR

The interpretation of the ^{1}H NMR spectra of all three complexes is straight-forward. The spectra have two sets of ^{1}H resonances in common. There are two, intense singlet peaks at 7.71 ppm and 7.55 ppm that integrate to eight and four, respectively. These signals correspond to the ortho and para protons of the $BArF_{24}$ counter-ion. The spectra also share a doublet at ~9.1 ppm, doublet at ~8.3 ppm, triplet at ~8.3 ppm, and a triplet that overlaps with the 7.71 ppm $BArF_{24}$ singlet resonance. All of these ^{1}H resonances integrate to two, and correspond to the bipyridine ligand. In ReBN, the ^{1}H resonances from benzonitrile occur as a multiplet at 7.41 ppm integrating to four and single proton resonance encompassed by the singlet $BArF_{24}$ at 7.71 ppm. This resonance has an integration value of 5. In the ^{1}H NMR spectrum of Re4DMABN, the doublets occurring at 7.19 ppm and 6.52 ppm as well as the singlet at 2.98 ppm belong to the 4DMABN ligand. The doublet signals each integrate to two and the singlet signal integrates to six. This is group of resonances is consistent with benzonitrile with a dimethylamino moiety in the para position. The ^{1}H resonances of the 3DMABN ligand in Re3DMABN occur as a triplet at 7.18 ppm, a doublet at 6.93 ppm, an overlapping singlet and doublet at 6.61 ppm and an intense singlet at 2.89 ppm. The four, aromatic ^{1}H resonances all integrate to one. The aliphatic singlet integrates to six. This collection of ^{1}H resonances clearly reflects benzonitrile with a dimethylamino moiety in the meta position. It is interesting to note that the methyl peaks of the dimethylamino group in

Re3DMABN are shifted slightly downfield relative to the methyl peaks of the dimethylamino group in Re4DMABN. This indicates that the dimethylamino group in Re4DMABN is more electron deficient than in Re3DMABN.
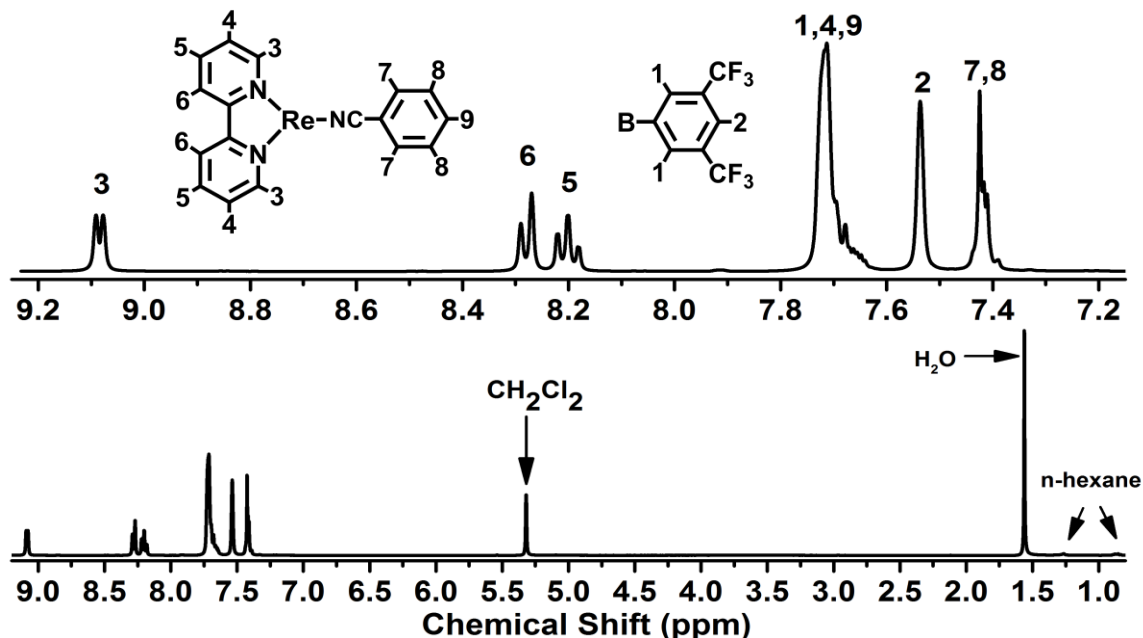
Figure 3.2 NMR spectrum of fac-[Re(bpy)(CO)$_3$BN](BArF$_{24}$) in CD$_2$Cl$_2$. Top: Enlarged view of the aromatic region of the NMR spectrum. Bottom: Entire NMR spectrum.
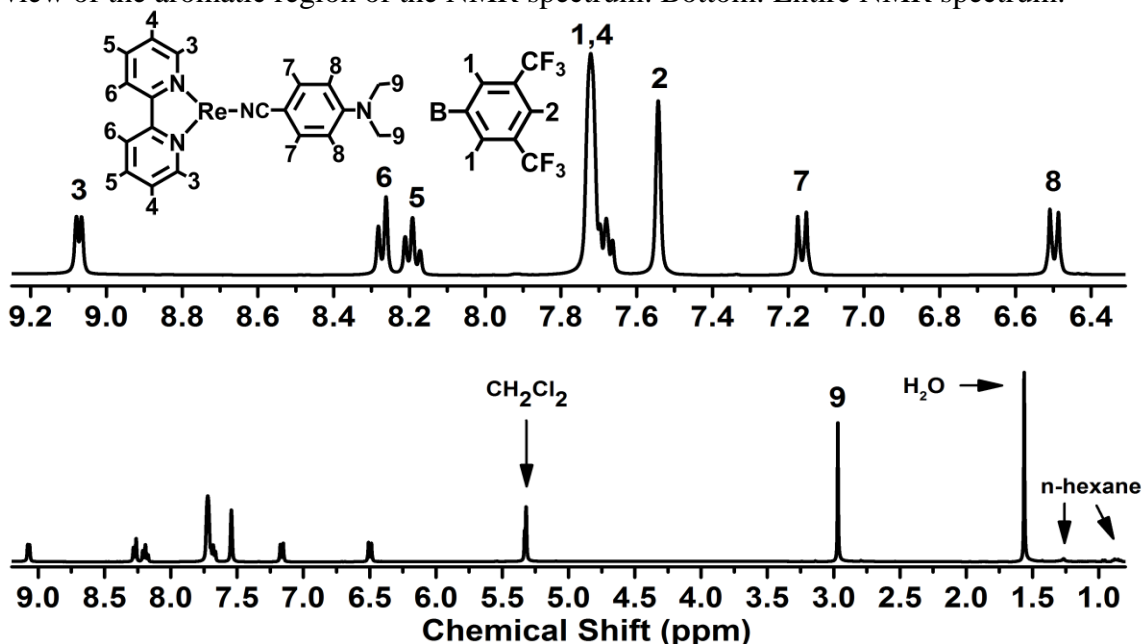
Figure 3.3 NMR spectrum of fac-[Re(bpy)(CO)$_3$4DMABN](BArF$_{24}$) in CD$_2$Cl$_2$. Top: Enlarged view of the aromatic region of the NMR spectrum. Bottom: Entire NMR spectrum.
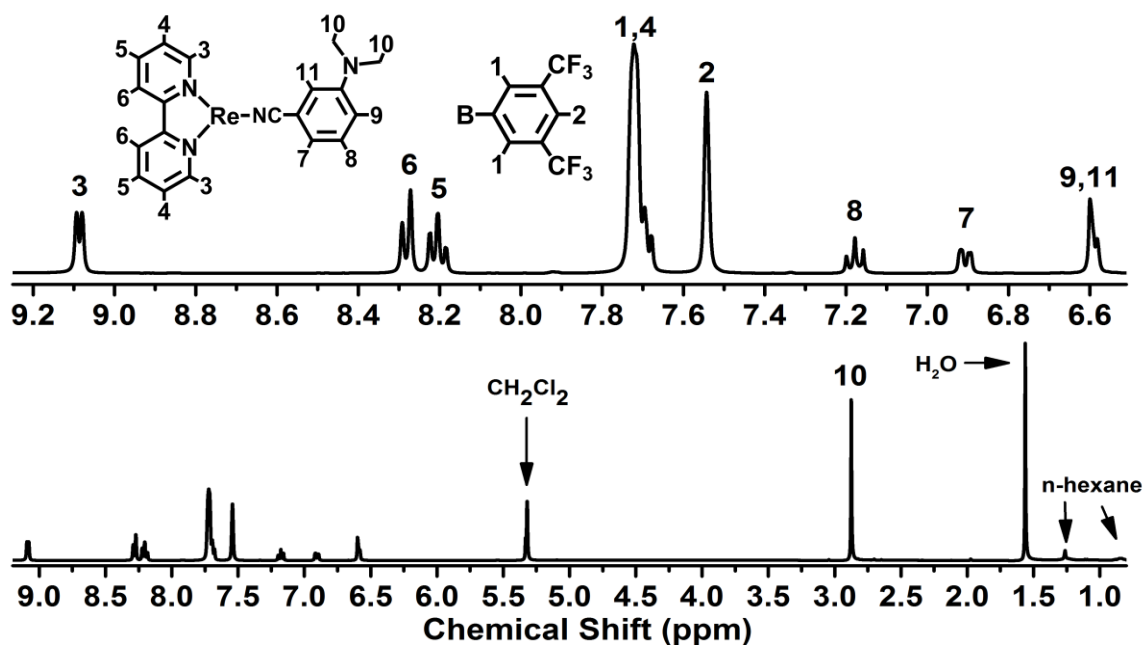
Figure 3.4 NMR spectrum of fac-[Re(bpy)(CO)$_3$3DMABN](BArF$_{24}$) in CD$_2$Cl$_2$. Top: Enlarged view of the aromatic region of the NMR spectrum. Bottom: Entire NMR spectrum.

3.4.2.2 MALDI-TOF

MALDI-TOF mass spectrometry was used to characterize each of the chromophores. It was possible to obtain mass spectra without the use of any matrix molecules or ionic dopants. This was very convenient, as dilute solutions of the molecules in chloroform could be directly applied to the sample plate for analysis, and did not require the typical procedure for optimizing dopant and matrix concentrations. All of the complexes experience a regular pattern of fragmentation upon ionization; the molecules routinely lose the nitrile containing ligand (L) as well as nCO lignads (n=1-3). They can also experience the loss of the nitrile containing ligand AND nCO ligands (n=1-3). The observed mass fragments occurs with the same 5 peak isotope distribution pattern indicative of a species containing common organic nuclei and rhenium. This pattern results from the existence of two principle isotopes of rhenium, ^{185}Re and ^{187}Re. They

occur with 37.4% and 62.6% natural abundance, respectively. It should also be noted that all of the mass fragments that were analyzed in these spectra occurred outside of the calibration window of the 600-1800 Da mass standard that was used to calibrate the instrument. Consequently, the experimental and calculated mass values agree with only unit mass resolution.

It is important to note that metastable ionic species can be observed in TOF mass spectrometry when data is collected in reflector mode. This occurs when a parent ion fragments between the ion source and the detector. This is problematic because any metastable ions that form during flight will experience a different acceleration at the reflector than the parent ion; thus, the mass values for the metastable ions will be observed between the mass of the parent ion and the fragments created at the source.[31-33] A clear indication that a mass peak results from a metastable species is that the peak will disappear from the spectrum when data is collected in linear mode.[34] If metastable ions fragment in the no field region of a linear detection experiment, the fragments maintain their velocity and will appear at the same mass as the parent ion. To discriminate between metastable ionic species and real mass fragments, comparisons of the linear and reflector mode mass spectra are shown for all of the complexes. Clearly, there are a number of metastable ion peaks in each of the reflector mode spectra. The most intense metastable ion peak in each spectrum is highlighted in red and occurs in the mass range between the $[M]^+$ and $[M-nCO]^+$ (n=1-3) and the $[M-L]^+$ mass for all of the complexes. This metastable ion mass peak likely results from the loss of L from the parent ion species in the no field zone. The remaining metastable species correspond to the loss of CO ligands in the no field region from the $[M]^+$ and $[M-L]^+$ mass fragments.
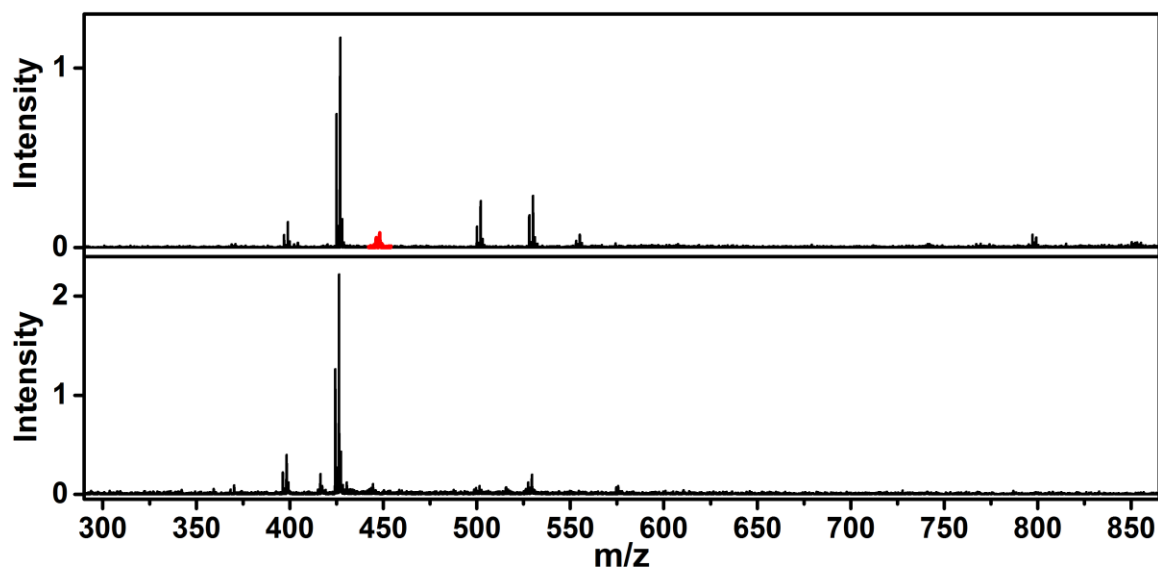
Figure 3.5 Top: Mass spectrum of fac-[Re(bpy)(CO)$_3$BN]$^+$ in reflector mode. Bottom: Mass spectrum of fac-[Re(bpy)(CO)$_3$BN]$^+$ in linear mode. The metastable species is highlight in red. Intensity values are shown in 10^4 counts.
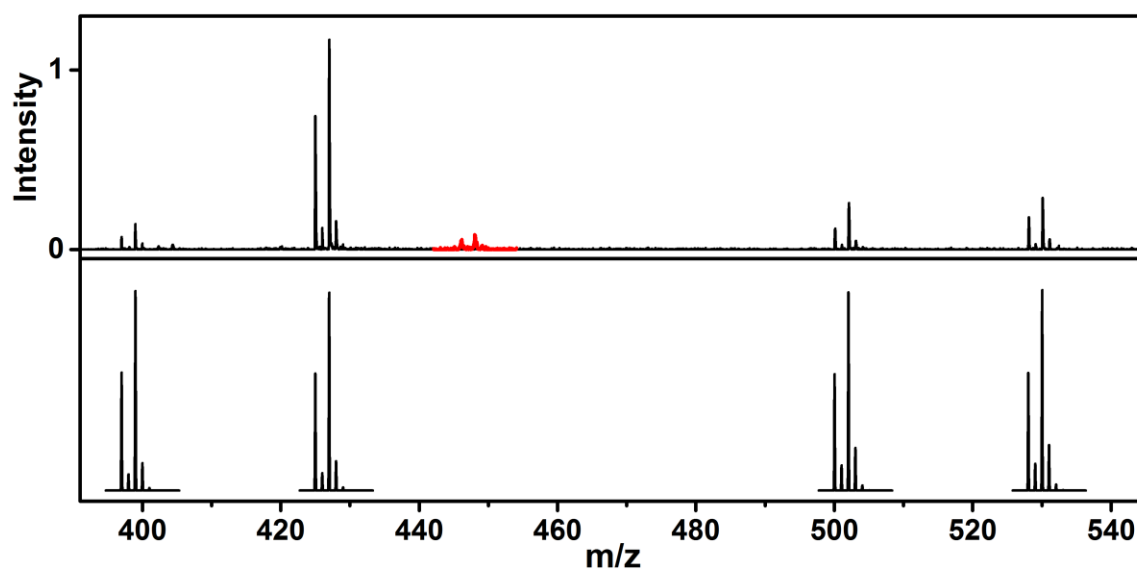
Figure 3.6 Top: Reflector mode mass spectrum of fac-[Re(bpy)(CO)$_3$BN]$^+$. Bottom: Simulated mass fragments for the molecular formulas presented in Table 3.1. The observed metastable species is highlight in red. Intensity values are shown in 10^4 counts.

Table 3.1 Simulated molecular formulas, corresponding fragments, and masses for fac-$[Re(bpy)(CO)_3BN]^+$.

Formula	Fragment	Calculated m/z	Actual m/z
$C_{22}H_{18}N_4O_3Re$	Parent $[M]^+$	530.05	530.12
$C_{21}H_{18}N_4O_2Re$	$[M-CO]^+$	502.06	502.12
$C_{13}H_8N_2O_3Re$	$[M-L]^+$	427.01	427.01
$C_{12}H_8N_2O_2Re$	$[M-CO-L]^+$	399.01	399.00
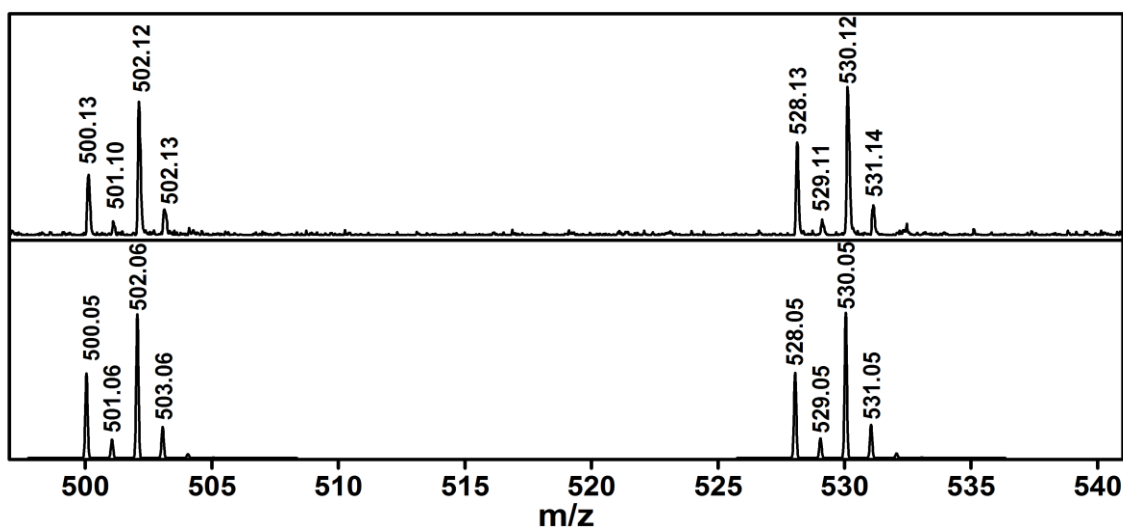
Figure 3.7 Top: Reflector mode mass spectrum of fac-$[Re(bpy)(CO)_3BN]^+$ which highlights the parent ion ($[M]^+$) and the parent ion with the loss of a CO ligand ($[M-CO]^+$). Bottom: Simulated mass spectra for $[M]^+$ and $[M-CO]^+$.
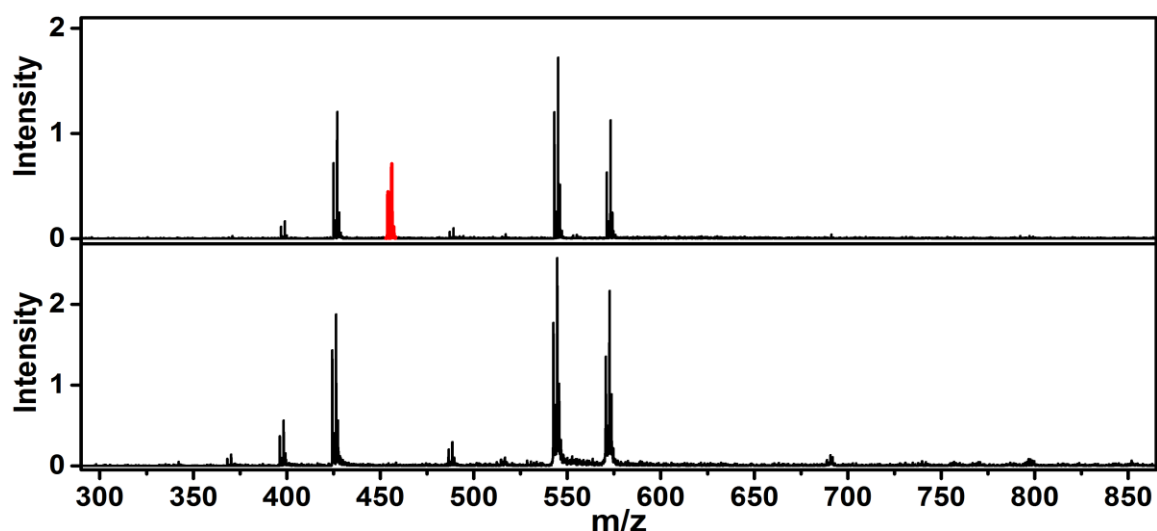
Figure 3.8 Top: Mass spectrum of fac-$[Re(bpy)(CO)_34DMABN]^+$ in reflector mode. Bottom: Mass spectrum of fac-$[Re(bpy)(CO)_34DMABN]^+$ in linear mode. The metastable species is highlight in red. Intensity values are shown in 10^4 counts.
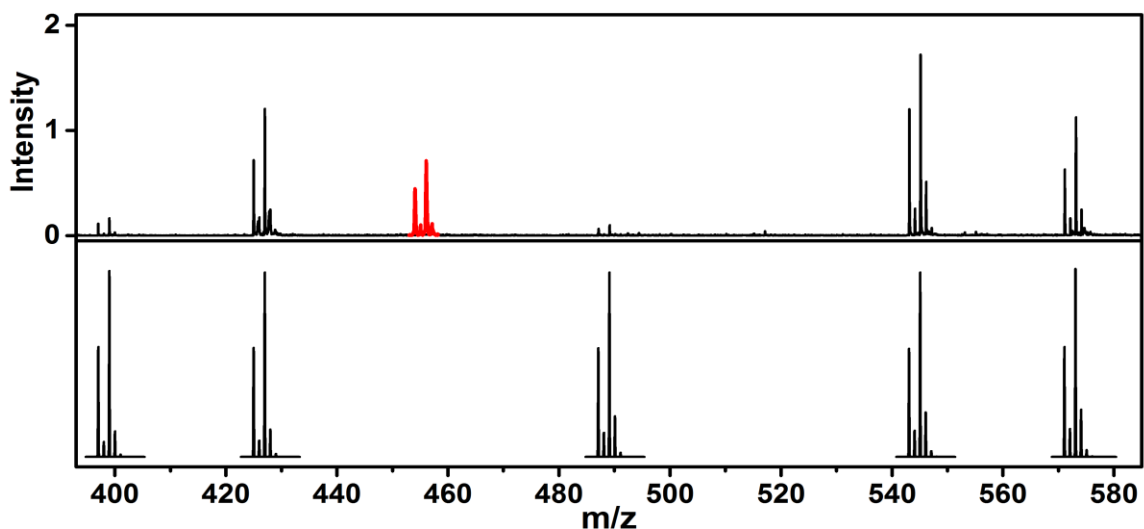
Figure 3.9 Top: Reflector mode mass spectrum of fac-[Re(bpy)(CO)$_3$4DMABN]$^+$. Bottom: Simulated mass fragments for the formulas presented in Table 3.2. The highest intensity metastable species is depicted in red. Intensity values are shown in 10^4 counts.

Table 3.2 Simulated molecular formulas, corresponding fragments, and masses for fac-[Re(bpy)(CO)$_3$4DMABN]$^+$.

Formula	Fragment	Calculated m/z	Actual m/z
C$_{22}$H$_{18}$N$_4$O$_3$Re	Parent [M]$^+$	573.09	573.16
C$_{21}$H$_{18}$N$_4$O$_2$Re	[M-CO]$^+$	545.10	545.17
C$_{19}$H$_{18}$N$_4$Re	[M-3CO]$^+$	489.11	489.15
C$_{13}$H$_8$N$_2$O$_3$Re	[M-L]$^+$	427.01	427.01
C$_{12}$H$_8$N$_2$O$_2$Re	[M-CO-L]$^+$	399.01	399.00
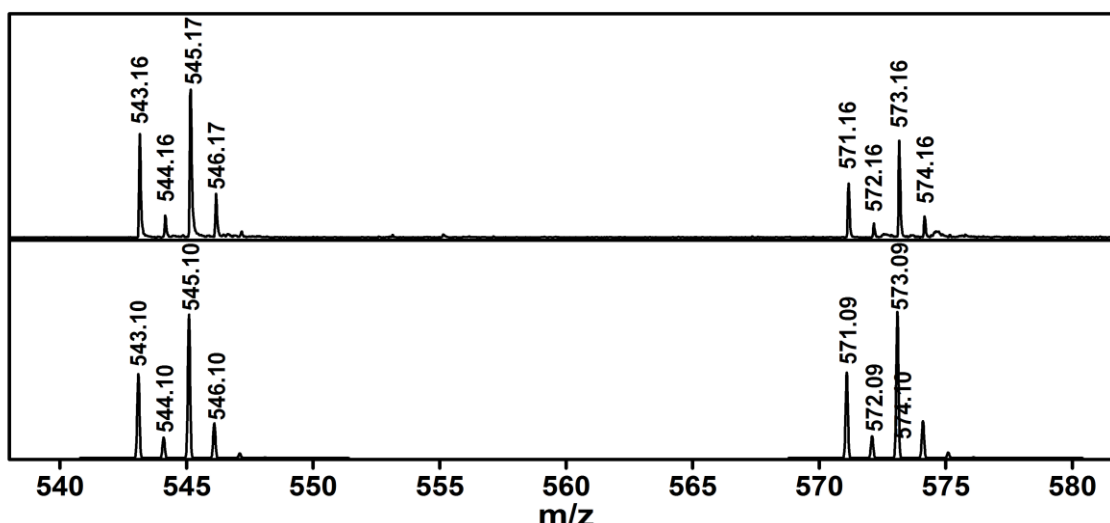
Figure 3.10 Top: Reflector mode mass spectrum of fac-[Re(bpy)(CO)$_3$4DMABN]$^+$ which highlights the parent ion ([M]$^+$) and the parent ion with the loss of a CO ligand ([M-CO]$^+$). Bottom: Simulated mass spectra for [M]$^+$ and [M-CO]$^+$.
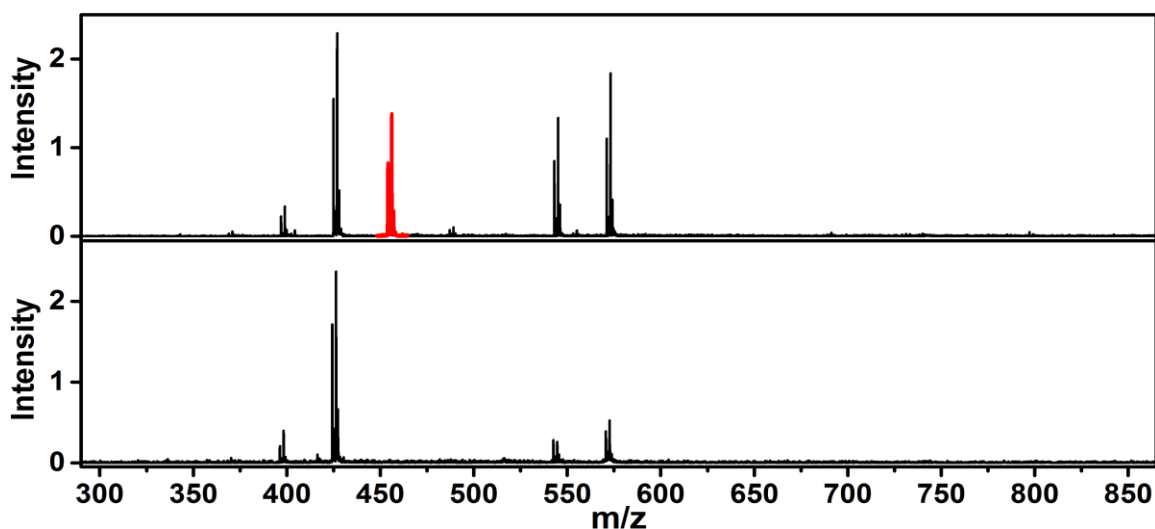
Figure 3.11 Top: Mass spectrum of fac-[Re(bpy)(CO)$_3$3DMABN]$^+$ in reflector mode. Bottom: Mass spectrum of fac-[Re(bpy)(CO)$_3$3DMABN]$^+$ in linear mode. The metastable species is highlight in red. Intensity values are shown in 10^4 counts.
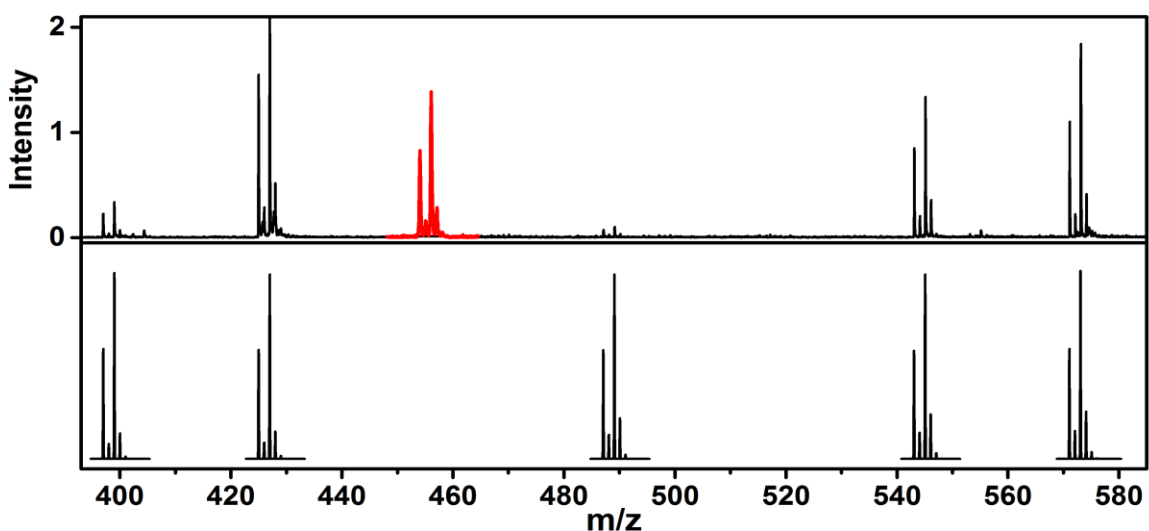
Figure 3.12 Top: Reflector mode mass spectrum of fac-[Re(bpy)(CO)$_3$3DMABN]$^+$. Bottom: Simulated mass fragments for the molecular formulas presented in Table 3.3. The species is highlight in red. Intensity values are shown in 10^4 counts.

Table 3.3 Simulated molecular formulas, corresponding fragments, and masses for fac-[Re(bpy)(CO)$_3$3DMABN]$^+$.

Formula	Fragment	Calculated m/z	Actual m/z
$C_{22}H_{18}N_4O_3Re$	Parent [M]$^+$	573.09	573.16
$C_{21}H_{18}N_4O_2Re$	[M-CO]$^+$	545.10	545.15
$C_{19}H_{18}N_4Re$	[M-3CO]$^+$	489.11	489.15
$C_{13}H_8N_2O_3Re$	[M-L]$^+$	427.01	427.01
$C_{12}H_8N_2O_2Re$	[M-CO-L]$^+$	399.01	399.00
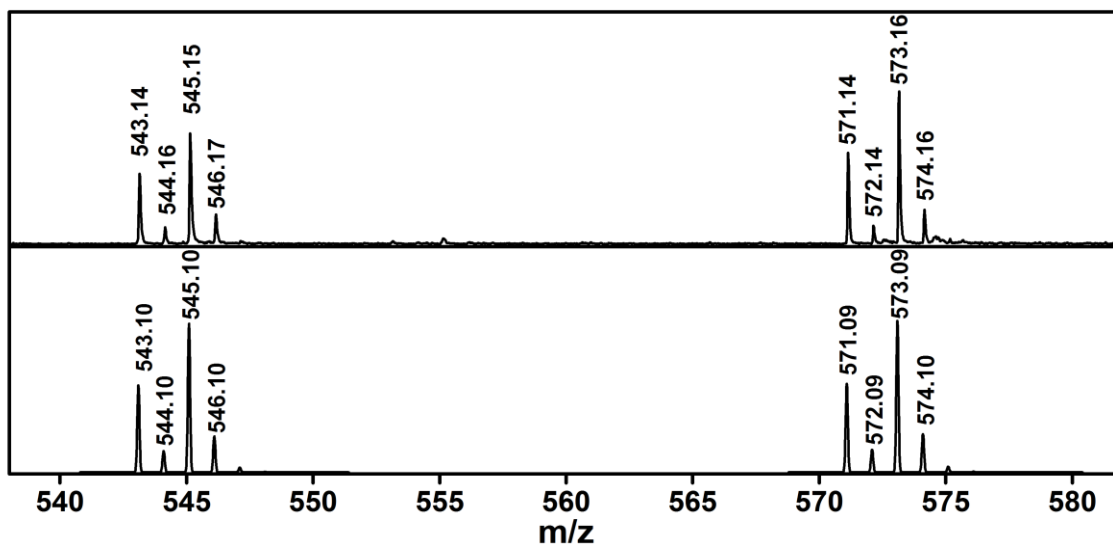
Figure 3.13 Top: Reflector mode mass spectrum of fac-[Re(bpy)(CO)$_3$3DMABN]$^+$ which highlights the parent ion ([M]$^+$) and the parent ion with the loss of a CO ligand ([M-CO]$^+$). Bottom: Simulated mass spectra for [M]$^+$ and [M-CO]$^+$.

3.4.2.3 X-Ray Crystallography

ORTEP representations of all three molecules are shown below in Figure 3.14.
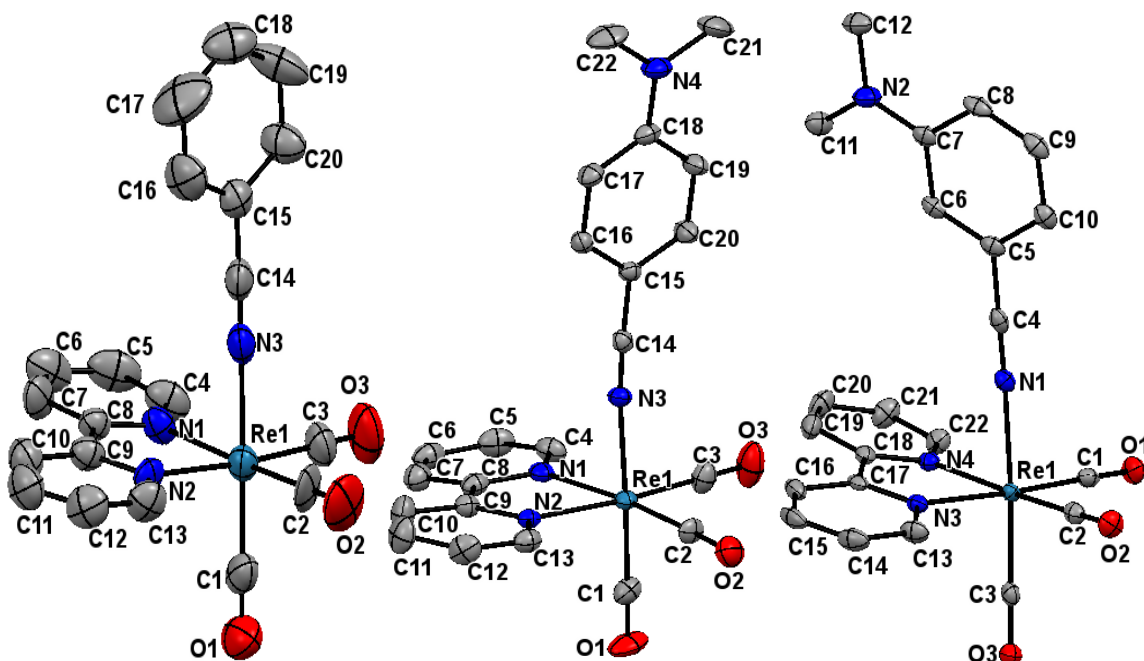
Figure 3.14 Thermal ellipsoid plots (50% probability) of fac-[Re(bpy)(CO)$_3$BN]$^+$ (left), fac-[Re(bpy)(CO)$_3$4DMABN]$^+$ (center), and fac-[Re(bpy)(CO)$_3$3DMABN]$^+$ (right). Hydrogen atoms and BArF$_{24}$ anions are omitted for clarity.

Selected rhenium, nitrile ligand, bipyridine, and carbonyl bond length and bond angle information is given below in Table 3.4. Bond length information is also given for the previously resolved free 4DMABN ligand.[35] No structural information is available for either BN or 3DMABN in the Cambridge Crystallographic Database. Due to variations in the atomic labels in the resolved crystal structure files, a standardized labeling scheme is used when discussing the bond lengths of the coordinated nitrile ligands and the free 4DMABN ligand. The scheme is depicted below along with Table 3.4.

Table 3.4 Selected bond lengths and bond angles obtained from single crystal structures of the fac-[Re(bpy)(CO)$_3$L](BArF$_{24}$) complexes and the previously resolved 4DMABN. Labeling scheme used for nitrile ligand bond lengths. All bond lengths given in Å.
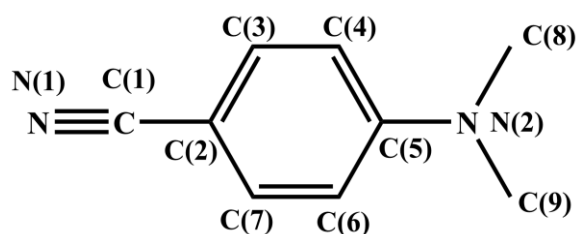
Compound	ReBN	Re4DMABN	Re3DMABN	4DMABN[35]
C(1)-N(1) length	1.14(1)	1.144(6)	1.150(3)	1.145(2)
C(1)-C(2) length	1.43(1)	1.424(6)	1.435(3)	1.436(2)
C(2)-C(3) length	1.35(2)	1.403(6)	1.396(4)	1.399(2)
C(3)-C(4) length	1.39(2)	1.371(6)	1.406(3)	1.379(2)
C(4)-C(5) length	1.41(2)	1.409(6)	1.415(4)	1.411(2)
C(5)-C(6) length	1.36(2)	1.411(6)	1.382(4)	1.414(2)
C(6)-C(7) length	1.38(2)	1.376(6)	1.352(3)	1.375(2)
C(7)-C(2) length	1.39(1)	1.392(6)	1.400(4)	1.389(2)
C(5)-N(2) length		1.363(6)	1.372(4)	1.366(2)
N(2)-C(8) length		1.450(7)	1.444(4)	1.447(2)
N(2)-C(9) length		1.456(7)	1.453(3)	1.450(2)
Re-N (nitrile) length	2.108(8)	2.134(4)	2.124(2)	
Re-N-C (nitrile) angle	178.27	174.29	177.68	
Avg. Re-N(bpy) length	2.172(7)	2.167(3)	2.171(2)	
CO (trans to nitrile) length	1.12(1)	1.142(5)	1.151(3)	
Re-C (trans to nitrile) length	1.95(1)	1.917(4)	1.930(2)	
Avg. CO (trans to bpy) length	1.15(1)	1.143(6)	1.149(4)	
Avg. Re-C (trans to bpy) length	1.93(1)	1.928(3)	1.929(3)	

A summary of crystal and structural refinement data is presented in Table 3.5. The resolved structures indicate that the average Re-N (bpy), average Re-C (carbonyls trans to bpy), and average CO (carbonyls trans to bpy) bond lengths agree within experimental error for all three complexes. The three benzonitrile ligands (BN, 3DMABN and 4DMABN) exhibit only minor differences in the Re-N and NC bond lengths; the bond angles and lengths in the phenyl rings also change very little among the three complexes.

Table 3.5 Crystal and structural refinement data for the series of fac-$[Re(bpy)(CO)_3L](BArF_{24})$ complexes.

Compound	ReBN	Re4DMABN	Re3DMABN
Solvent	none	none	none
Formula	$C_{52}H_{25}BF_{24}N_3O_3Re$	$C_{54}H_{30}BF_{24}N_4O_3Re$	$C_{54}H_{30}BF_{24}N_4O_3Re$
FW (g/mol)	1392.76	1435.83	1435.83
Xtl System	orthorhombic	monoclinic	triclinic
Space Grp.	$Pna2_1$	$P2_1/c$	$P\bar{1}$
Color, Habit	yellow block	yellow block	clear yellow block
a, Å	16.8751(18)	13.6239(12)	12.2427(3)
b, Å	16.1125(18)	15.1205(14)	14.2659(3)
c, Å	19.776(2)	28.362(3)	16.2785(4)
α, deg.	90	90	84.7050(10)
β, deg.	90	94.9290(10)	74.4170(10)
γ, deg.	90	90	76.9680(10)
V, Å^3	5377.2(10)	5821.0(9)	2666.53(11)
T, K	150(2)	100(2)	293(2)
Z	4	4	2
[a]R1, [b]wR2	0.0811, 0.1601	0.0552, 0.1071	0.0255, 0.0639
GoF	1.090	1.112	1.072

[a]$R1 = \Sigma||F_o|-|F_c||/ \Sigma||F_o|$. [b]$wR2 = \{[\Sigma w(F_o^2-F_c^2)^2/ \Sigma w(F_o^2)^2]\}^{1/2}$; w=$1/[\sigma^2(F_o^2)+(xP)^2]$, where P=$(F_o^2+2F_c^2)/3$

It is interesting to note that ALL of the bond lengths in the crystallographically resolved free 4DMABN compound agree within error with the resolved bond lengths of the Re coordinated 4DMABN in our complex. This observation implies that the interaction of the ligand with the metal has little to no electronic effect on the coordinated nitrile ligand in crystals of the complex. For both of the DMABN ligands, the Re-N (nitrile) bond length is slightly longer than that for the BN ligand. This observation, taken together with

the fact that both the Re-C (CO) bond length *trans* to the DMABN ligands is shorter and the *trans* CO bond length is longer for both the 3DMABN and 4DMABN complexes than for the BN complex, suggests that electron donation from the dimethylamine substituent diminishes the Re – nitrile back bonding interaction and increases the back-bonding to the *trans* CO in the electronic ground state.

3.4.2.4 Steady State Absorption, Luminescence, Nanosecond Transient Absorption

Figure 3.15 shows the UV-VIS absorption spectra of ReBN, Re4DMABN, and Re3DMABN in dichloromethane (DCM) and 1:1 (v:v) DCM:MeOH.
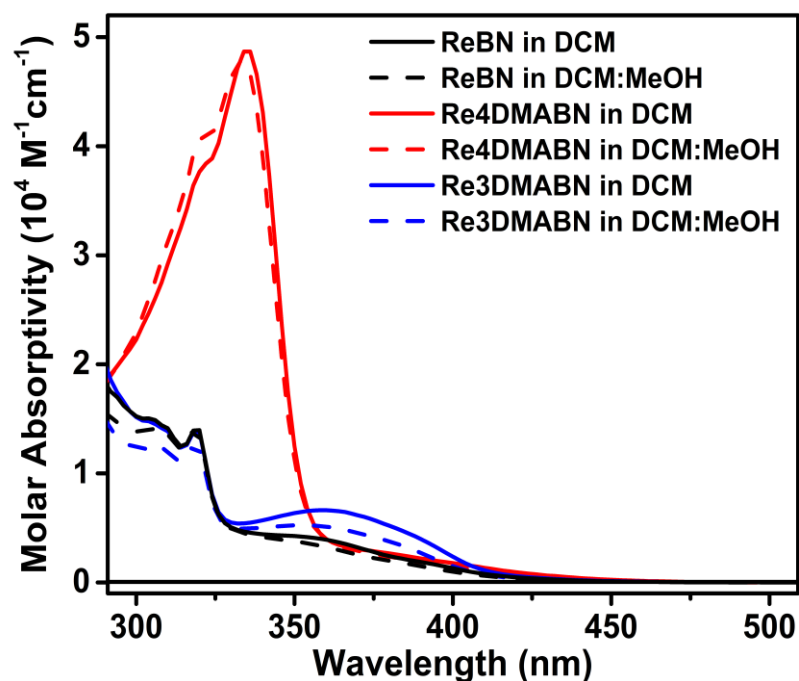
Figure 3.15 UV-Vis absorption spectra of fac-[Re(bpy)(CO)$_3$BN](BArF$_{24}$), fac-[Re(bpy)(CO)$_3$4DMBN](BArF$_{24}$), and fac-[Re(bpy)(CO)$_3$3DMABN](BArF$_{24}$) in DCM and 1:1 (v:v) DCM:MeOH.

ReBN and Re3DMABN have absorption maxima at ca. 305 nm and 315 nm. These transitions are assigned to bpy-localized π-π* transitions.[22] Re4DMABN has a unique, relatively high molar absorptivity absorption at 334 nm that, by comparison with the

4DMABN ligand, is assigned to an intraligand amine to nitrile charge transfer transition (ILCT).[22] The maximum of the 4DMABN intraligand absorption transition experiences a ~40 nm red shift upon coordination to rhenium, which is consistent with a stabilization of the highly polar ILCT excited state. This absorption transition overlaps with the bpy-localized π-π* transition, resulting in a shoulder at 320 nm. The broad, featureless absorption in Re3DMABN from 330 nm to 410 nm is also assigned to a 3DMABN intraligand absorption transition. The behavior of this absorption band is similar to that of 4DMABN in that the it has similar molar absorptivity to the free ligand and is also red shifted by ~30 nm relative to the free 3DMABN ligand. The weak ($\varepsilon < 6000$ M^{-1}cm^{-1}) absorption transitions that trail from 350 to 430 nm in all of the complexes are assigned to $d\pi$ (Re) $\rightarrow \pi$* (bpy) MLCT transitions based on previous literature reports.[24,36-38] The absorption spectra of the complexes in mixed DCM:MeOH are very similar to the spectra collected in DCM: ReBN and Re3DMABN experience a slight decrease in molar absorptivity across the entire absorption spectra and Re4DMABN shows a slight molar absorptivity enhancement for the shoulder in the 4DMABN ILCT transition at 320 nm.

All three complexes exhibit luminescence in both DCM and DCM:MeOH (1:1 v:v) at room temperature. The luminescence spectra in DCM and mixed DCM:MeOH solution are shown in Figure 3.16 Emission maxima, luminescence quantum yields, excited-state lifetimes, and radiative and non-radiative rate constants are given in Table 3.6. Luminescence and transient absorption decays for Re3DMABN are biexponential. The luminescence and absorption lifetime values for each of the decay components as well as their statistical contribution to the decay (lifetime measurements) signal are included in Table 3.6. Luminescence lifetime data for Re4DMABN in DCM:MeOH is

omitted because the lifetime decay is faster than the resolution of our instrument (<2 ns), and rate constant data is omitted in DCM:MeOH for Re4DMABN and Re3DMABN because the lifetime of the excited state cannot be determined for Re4DMABN and the luminescence quantum yield is very low for Re3DMABN. Based on previous literature reports the yellow luminescence from the ReBN complex is from the Re $(d\pi) \rightarrow$ bpy (π^*) MLCT state.[22]
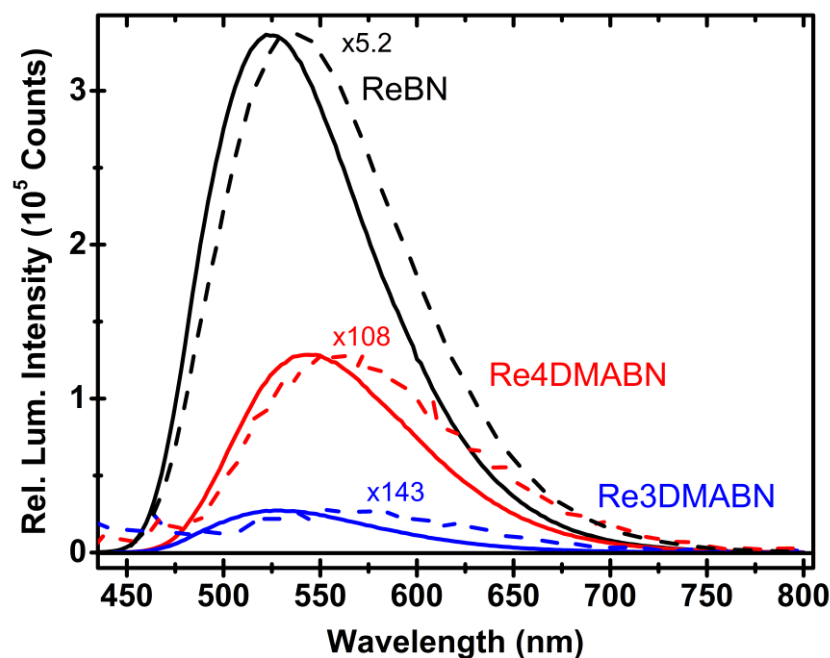
Figure 3.16 Luminescence spectra of fac-[Re(bpy)(CO)$_3$BN](BArF$_{24}$), fac-[Re(bpy)(CO)$_3$4DMBN](BArF$_{24}$), and fac-[Re(bpy)(CO)$_3$3DMABN](BArF$_{24}$) in (solid) DCM and (dashed) 1:1 (v:v) DCM:MeOH.

The proximity of the emission maxima and line shape of the luminescence from Re4DMABN and Re3DMABN in DCM suggests that the emission in these complexes also originates from a MLCT state. The Re3DMABN complex differs from the other two in that the emission is very weak in DCM: the luminescence quantum yield is two orders of magnitude lower than the other complexes. Further, the luminescence lifetime of Re3DMABN in DCM is more than a factor of 30 longer than the measured lifetime of the

other two complexes. Consequently, the radiative decay rate constant for Re3DMABN in

DCM is two orders of magnitude lower than the observed radiative decay rate constant

for both ReBN and Re4DMABN in DCM and mixed DCM:MeOH. The non-radiative

decay rate constant is also an order of magnitude slower than the non-radiative decay rate

constants for each of the chromophores in both DCM and mixed DCM:MeOH. This very

long lived and weak luminescence suggests that the emitting excited state in

Re3DMABN in DCM is *not* MLCT in origin.

Table 3.6 Emission maxima, luminescence quantum yields, excited-state lifetimes, and radiative and non-radiative rate constants for the series of fac-[Re(bpy)(CO)$_3$L](BArF$_{24}$) in deaerated DCM and MeOH/DCM (1/1) at room temperature.

Complex	ReBN		Re4DMABN		Re3DMABN	
Solvent	DCM	DCM MeOH	DCM	DCM MeOH	DCM	DCM MeOH
Luminescence λ_{max} (nm)	524	536	544	560	528	560
Luminescence Quantum Yield ($\pm$ 10%)	0.41[a]	0.10[a]	0.17[a]	0.002[a]	0.003[a]	<0.001[a]
Luminescence Lifetime (μs)	1.33 $\pm$ 0.05	0.78 $\pm$ 0.05	0.84 $\pm$ 0.02	____	35.0 $\pm$ 1.5(88%) 1.3 $\pm$ 0.1(12%)	0.57 $\pm$ 0.05(73%) 0.04 $\pm$ 0.01(27%)
TA Lifetimes (μs)	1.35 $\pm$ 0.1	0.78 $\pm$ 0.09	0.81 $\pm$ 0.07	____	23.3 $\pm$ 1.0 0.78 $\pm$ 0.02	0.03 $\pm$ 0.01
k_r (s^{-1})	3.1 x 10^5	1.3 x 10^5	2.0 x 10^5	____	130	____
k_{nr} (s^{-1})	4.4 x 10^5	1.1 x 10^6	1.0 x 10^6	____	5.0 x 10^4	____

[a] Quantum yield data determined using fac-[Re(bpy)(CO)$_3$ACN]$^+$ as the luminescent standard.[39]

Upon changing the solution to the more polar MeOH/DCM (1:1) mixture, all of the

complexes exhibit weaker luminescence and shorter excited-state lifetimes. The

magnitude of the change is much more pronounced in the two DMABN complexes. In

the two DMABM complexes, the luminescence lifetimes decrease by a factor of >100 in

the mixed solvent, as compared to a factor of 1.6-3 for ReBN. In Re3DMABN, the

excited state lifetime in DCM is more than 30 times larger than that of either of the other

complexes, but decreases precipitously in the mixed solvent, from 25μs in DCM to 30ns in MeOH/DCM. Such excited-state lifetime decreases in more polar solvents are often associated with the existence of strongly polarized excited states, which are higher in energy in nonpolar solvents but are stabilized in polar solvents and provide additional relaxation pathways to the ground state. Such polarized states could be either ligand-to-ligand charge separated states (LLCT), $[Re(CO)_3(bpy\dot{-})(DMABN+\cdot)]^+$ or highly polarized ligand-based states.

The nanosecond time-resolved transient absorption spectrum of each of the complexes in DCM is show in Figure 3.17. All of the complexes have excited state UV-VIS absorbance between 400 and 450 nm, which parallels the results of Schanze *et al*. for Re4DMABN in DCM and mixed DCM/CH$_3$CN solutions.[22] ReBN and Re4DMABN complexes exhibit bleaching at longer wavelengths that result from the luminescence of these complexes. Due to the very low luminescence quantum yield for Re3DMABN in DCM, luminescence in not observed in the transient absorption spectrum. Despite similarities among the transient spectra of the excited states in the three compounds (Figure 3.17), it is very likely that the equilibrated excited state of the Re3DMABN complex differs from the others since its radiative decay rate (Table 3.6) is nearly a factor of 1000 slower than the BN and 4DMABN complexes. The nanosecond transient absorption spectra of ReBN and Re3DMABN in DCM:MeOH have essentially identical features as those in DCM, but have shorter lifetimes (Table 3.6). As is the case for the luminescence lifetime of Re4DMABN, it is not possible to collect the nanosecond transient absorption spectrum of the complex in DCM:MeOH solution because the decay of the excited state is faster than the time resolution of our instrument.
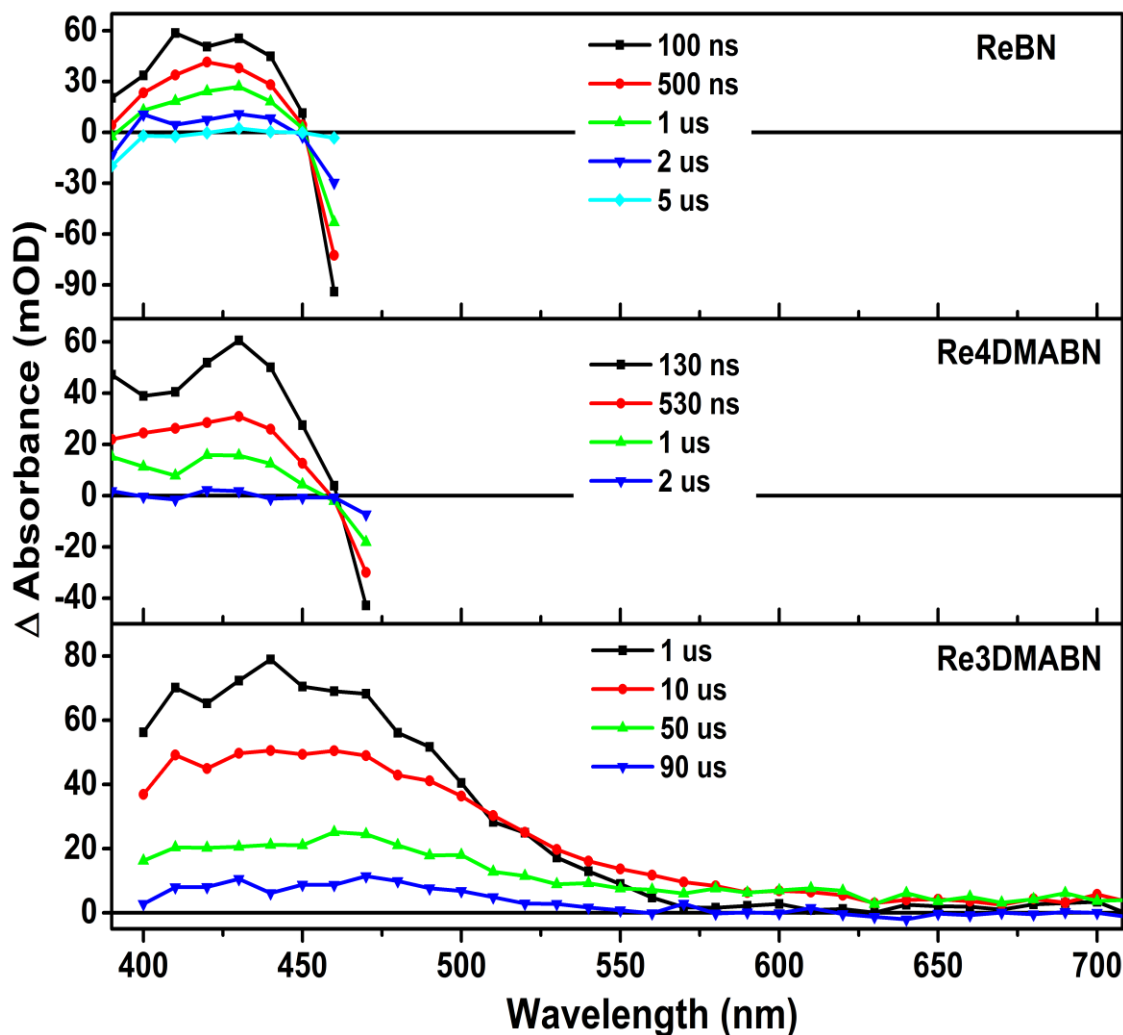
Figure 3.17 Time-resolved nanosecond transient absorption spectra of ReBN, Re4DMABN, and Re3DMABN collected in DCM. Luminescence is observed in the spectra of ReBN and Re4DMABN from 480-690 nm (appearing as negative absorbance); thus, these wavelengths have been omitted.

The lifetime values obtained from luminescence and transient absorption measurements agree within error for ReBN and Re4DMABM and are similar for Re3DMABN. This observation implies that the luminescence and excited state absorption occur from the same excited state. It is worth noting that we obtain statistically identical lifetime values for complexes when they have substantial excited state absorbance AND a high (> 0.10) luminescence quantum yield. In this regard, the interpretation of the

luminescence lifetime data for Re3DMABN is difficult due to the low luminescence quantum yield of the complex. Luminescence measurements involving low quantum yield species are notoriously susceptible to impurity emission. For instance, Re3DMABN has a quantum yield on the order of 0.001 and potential impurity species (fac-[Re(bpy)(CO)$_3$MeOH]$^+$ or fac-[Re(bpy)(CO)$_3$3ABN]$^+$ where 3ABN is the non-methylated version of 3DMABN) likely have luminescence yields on the order of 0.10; thus, a sample containing 1% by mass of either impurity would produce two, unique emitting populations with equivalent intensity. This treatment assumes that the species have identical ground state absorbance values at the excitation wavelength. Although the likelihood of impurity luminescence in Re3DMABN is mitigated by the observation of biexponential decay kinetics in transient absorption measurements and the fact that the complex was purified using column chromatography (See Section 3.4.1 Synthesis), the lifetime values from nanosecond transient absorption measurements are considered to be more reliable because they depend only on the concentration of the species in solution and will be exclusively used in further discussions of the excited state lifetime. The lifetime values obtained from TA measurements were also used in the preceding paragraphs discussing the lifetime of Re3DMABN.

3.4.2.5 Electrochemistry

Cyclic voltammograms of Re4DMABN and Re3DMABN in DCM and CH$_3$CN exhibit waves attributable to one-electron reduction and oxidation of the complex. Anodic and cathodic sweep segments in both solvents are shown for Re4DMABN and Re3DMABN in Figures 3.18 and 3.19. Redox potentials associated with these voltammograms are compiled in Table 3.7. Here CH$_3$CN was used in place of CH$_3$OH

since it was not possible to obtain voltammetric data in CH_3OH because of competing solvent redox processes. The waves observed at positive potentials in the voltammograms of both of the DMABN complexes likely occur more than 0.5 V more negative than the first oxidation of the ReBN complex (E^0(Re(II)/Re(I))), and are clearly associated with oxidation of the DMABN substituent.[40]
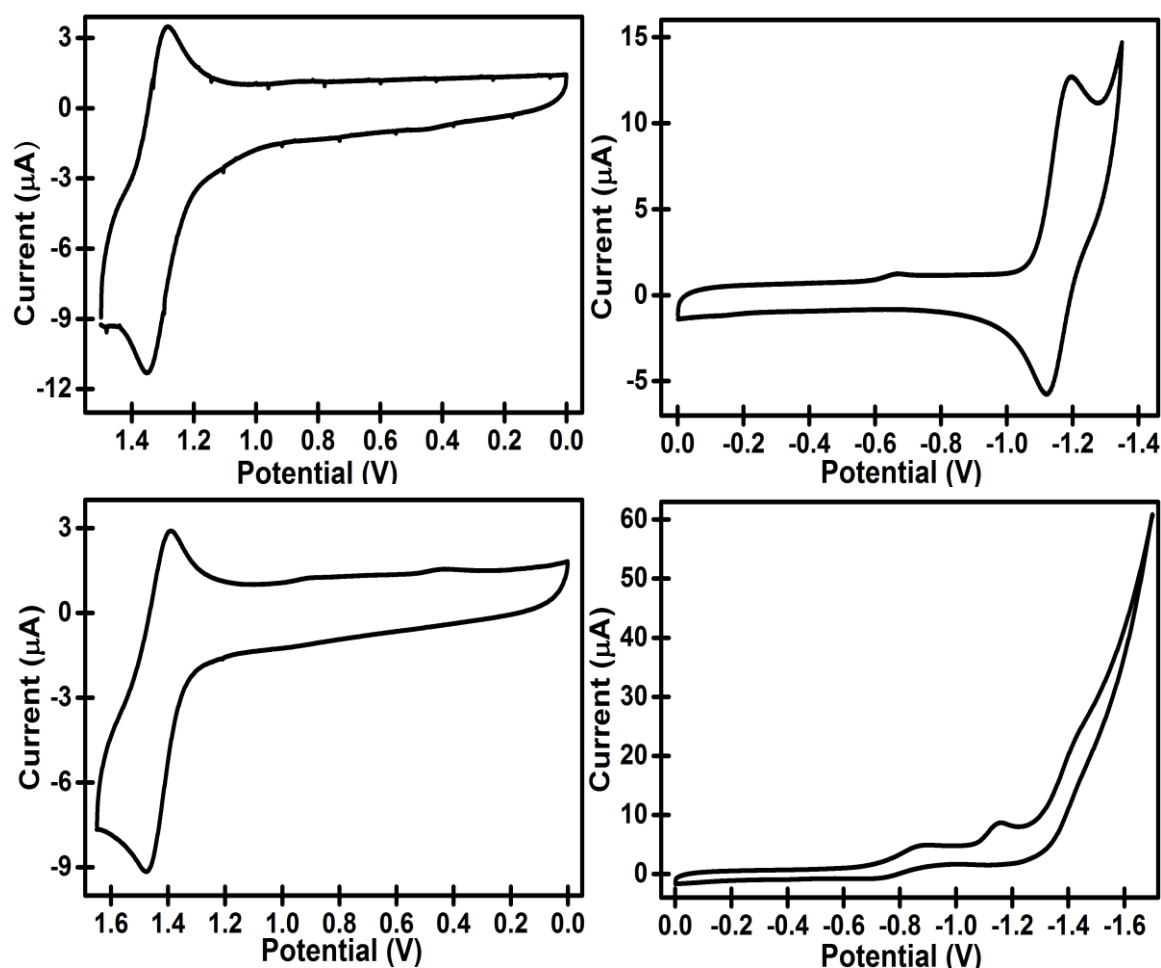
Figure 3.18 Cyclic voltammagrams of fac-[Re(bpy)(CO)$_3$(4DMABN)]$^+$ in (Top) CH_3CN and (Bottom) DCM. Anodic scans are shown on the left. Cathodic scans are shown on the right. The voltammagrams were collected in solutions containing 0.1M [^{n}Bu$_4$N][PF$_6$]. All samples were deaerated with argon for 10 minutes prior to collection. The presented sweep segments were collected at a scan rate of 100 mV/s. Working electrode: glassy-carbon electrode. Counter electrode: Pt wire. Reference electrode: Aqueous Ag$^+$/AgCl.
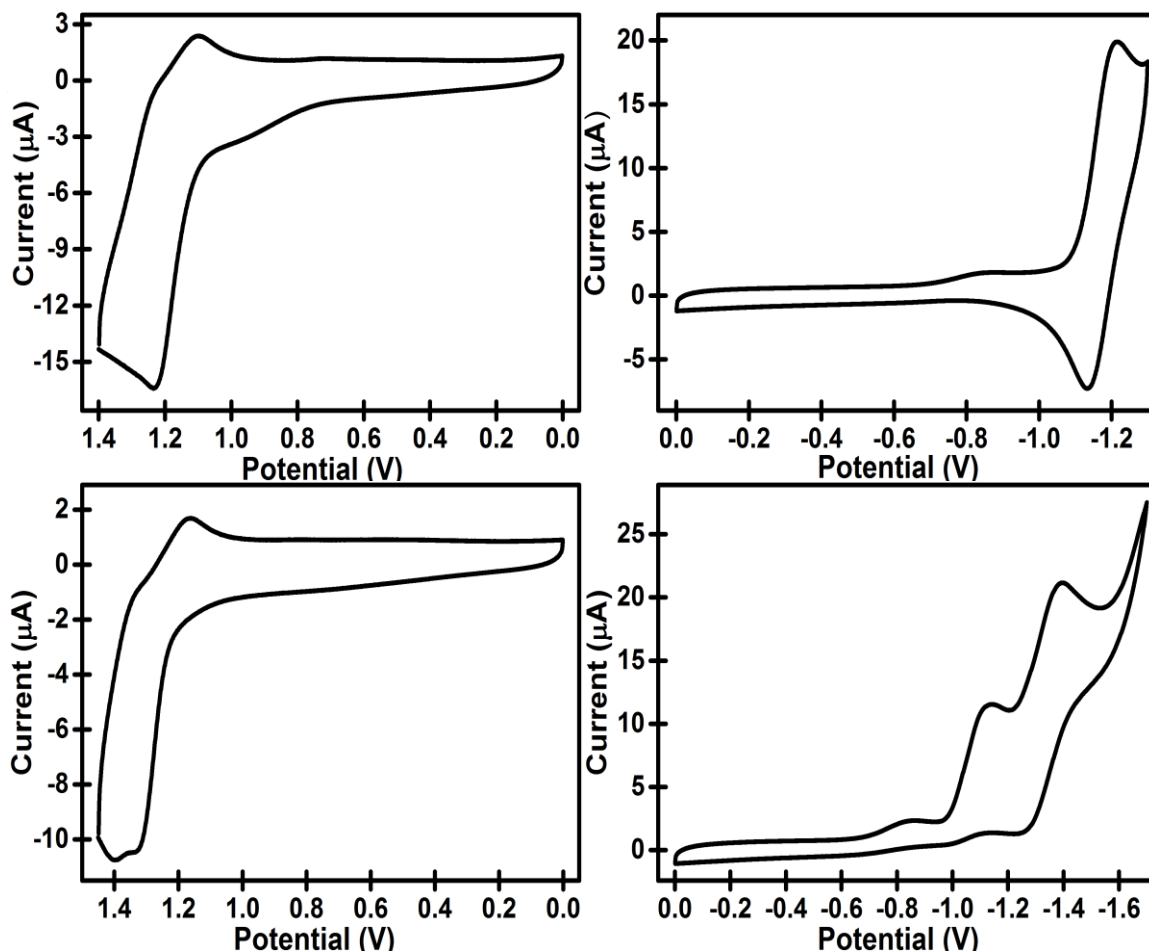
Figure 3.19 Cyclic voltammagrams of fac-[Re(bpy)(CO)$_3$3DMABN]$^+$ in (Top) CH$_3$CN and (Bottom) DCM. Anodic scans are shown on the left. Cathodic scans are shown on the right. The voltammagrams were collected in solutions containing 0.1M [^{n}Bu$_4$N][PF$_6$]. All samples were deaerated with argon for 10 minutes prior to collection. The presented sweep segments were collected at a scan rate of 100 mV/s. Working electrode: glassy-carbon electrode. Counter electrode: Pt wire. Reference electrode: Aqueous Ag$^+$/AgCl

The oxidation potentials of fac-[Re(bpy)(CO)$_3$L]$^+$ complexes, when L does not contain an electron donating substituent, can approach 2.0 V due to the highly electron deficient Re^I center (back-bonding with three CO ligands).[39] The oxidation is quasi-reversible in CH$_3$CN and DCM, suggesting that the cation radical reacts irreversibly within a few seconds of being formed (sweep rates were 0.1 Vs^{-1}). In addition, oxidation in DCM is observed at more positive potentials than in CH$_3$CN. Reductive

voltammograms in CH$_3$CN are reversible, and reductive waves occur at nearly the same potential for both complexes. The reductive behavior in DCM is irreversible, but cathodic peaks are clearly observed for both the DMABN complexes and were used to estimate E^0 (+/0) for the complex. The difference between E^0 (2+/+) and E^0 (+/0) provides an approximate value for the energy of the charge separated species, fac-[(Re[(bpy$\doteq$)(CO)$_3$(DMABN+·)]. The values of ΔE_{CS} are shown in Table 3.7. The emission maxima have energies at least 0.1 V lower than the estimated charge-separated states in each case and, while the true excited state energies will be somewhat higher, it is clear that the free energies for intramolecular electron transfer reaction will be close to zero. Also, the estimated ΔE_{CS} values are well in excess of 2 V, suggesting that back electron transfer from this state may reside in the Marcus inverted region.

Table 3.7 Redox potentials (in V) vs. Ag/AgCl for the complexes in DCM and CH$_3$CN. The energy difference between the peak anodic and peak catholic current (ΔE_p) and the difference between E^0(2+/+) and E^0(+/0) (ΔE_{CS}) for the complexes are also included.

Complex	E^0(2+/+) (ΔE_p, V) DCM	E^0(2+/+) (ΔE_p, V) CH$_3$CN	E(+/0) DCM	E^0(+/0) (ΔE_p, V) CH$_3$CN	ΔE_{CS}, V DCM (CH$_3$CN)
[Re3DMABN]	1.28 (0.24)	1.17 (0.14)	-1.13	-1.17 (0.08)	2.41 (2.34)
[Re4DMABN]	1.43 (0.09)	1.27 (0.07)	-1.16	-1.16 (0.08)	2.59 (2.43)

3.4.2.6 Infrared Absorption Spectra

Note: The following sections discussing the steady state and transient infrared absorption characteristics of the complexes utilize data, figures, and ideas that were mostly collected and developed by Professor Igor Rubtsov and his graduate student, Yuankai Yue. These data are crucial in understanding the excited state behavior of these complexes and necessary for a complete discussion of the chemical reactivity of these systems. I have

adapted discussions of the data from our manuscripts in an effort to summarize the general infrared absorption properties of these molecules, and applied this information to make definitive conclusions about the nature and evolution of each excited state. I also must acknowledge the work of Professor David Beratan, and his students, Zheng Ma and Peng Zhang. They provided advanced DFT computational support to both manuscripts. I have excluded these computational details and results from this dissertation.

The ground state infrared absorption spectra of the three compounds are shown in Figure 3.20. The infrared absorption spectrum of Re4DMABN is shown in both DCM and mixed DCM:MeOH to demonstrate the similarity of the spectra. The spectra contain several characteristic absorption peaks that can be assigned using DFT calculations (Gaussian '09.[41] B3LYP. LANL2DZ with ECP for Re, 6-31G** for all other atoms) as well as previous work on fac-[Re(bpy)(CO)$_3$L]$^+$ complexes.[22] A summary of the data and the assigned vibrational modes are given in Table 3.8.
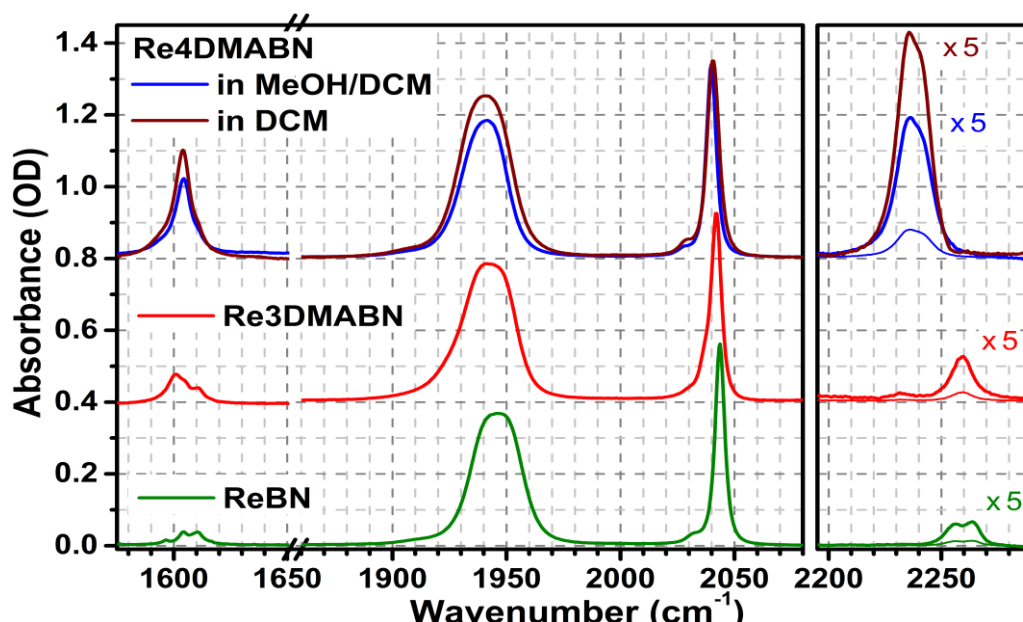
Figure 3.20 The ground state infrared absorption spectra of ReBN, Re4DMABN, and Re3DMABN. The spectrum of Re4DMABN is shown in DCM and DCM:MeOH. The spectra of ReBN and Re3DMABN are shown in DCM solution. The nitrile stretches highlighted in the right panel are scaled 5-fold, while thin lines show unscaled spectra.

The strongest peaks at 2040 and 1945 cm^{-1} belong to the symmetric (ν_{ss}) and asymmetric (ν_{as}) stretching modes of the three carbonyl ligands, respectively. The broad peak at ca. 1945 cm^{-1} consists of two, overlapping ν_{as}(CO) transitions. The relatively weak absorption peak around 2250 cm^{-1} belongs to the C≡N stretching mode. The infrared absorption peaks in the 1600-1615 cm^{-1} region of the spectra belong to phenyl ring stretches of the bipyridine and nitrile ligands. For all three complexes, DFT calculations predict symmetric rings stretching modes on the bpy ligand (ν_{ss}(bpy)) and benzonitrile ligands (ν_{ss}(Ph)) occurring around 1650 cm^{-1} within 5 cm^{-1} of one another. The absorption peak at 1612 cm^{-1} appears with a constant frequency and oscillator strength in all three complexes. This mode is assigned as ν_{ss}(bpy). The lower-frequency peak at 1604 cm^{-1} has different IR intensities in each of the compounds. This mode is assigned as ν_{ss}(Ph). Interestingly, not only is the ν_{ss}(Ph) peak in Re4DMABN much stronger than that of ν_{ss}(bpy), but its extinction coefficient is comparable to that of the ν(CO) transitions. It is important to note that the ν_{ss}(Ph) mode involves symmetric stretching motion of the phenyl ring along the long axis of the ligand and its IR intensity is strongly dependent of the ligand polarization.

The fac-[Re(bpy)(CO)$_3$L]$^+$ structural motif is attractive for investigating intramolecular electron transfer reactions because the CO stretching modes of these complexes are highly sensitive to changes in the electron density at the metal center.[10-12] The fact that the CO absorption peaks for these complexes show only small differences in both their central frequencies and their IR intensities suggests that the ground state charge of Re is similar in all three complexes.

The CN stretching modes of ReBN and Re3DMABN occur at similar frequency and with similar intensity. In Re4DMABN, the frequency of the CN stretch $\nu(CN)$ is shifted to lower frequency by 24 cm^{-1}. Accompanying this decrease in stretching frequency is a nearly 3-fold increase in the IR intensity of the CN stretch. These observations suggest that the nitrile group of the coordinated 4DMABN ligand has a lower bond order than the nitrile group in both ReBN and Re3DMABN. The combination of the enhancement of the $\nu_{ss}(Ph)$ intensity and the lowered bond order of the nitrile group implies that the 4DMABN ligand in Re4DMABN is polarized in the ground state. In this regard, the coordinated 4DMABN ligand likely has some contribution from the quinoidal resonance form shown in Figure 3.21.
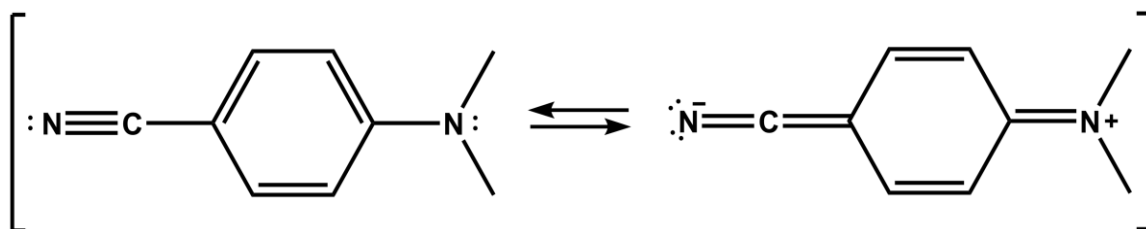
Figure 3.21 Resonance forms of 4DMABN. The quinoidal form, pictured on the right, is not possible for 3DMABN.

Table 3.8 Experimental and DFT computed ground-state vibrational frequencies (in cm^{-1}) of several characteristic modes for the three compounds in DCM. The difference between computed values and experimentally observed values for each stretching mode are presented in parenthesis with the DFT results.

ReBN		Re4DMABN		Re3DMABN		Assignment	
Exper.	DFT, GS (Δ)	Exper.	DFT, GS (Δ)	Exper.	DFT, GS (Δ)		
2260	2340 (80)	2236	2316 (80)	2260	2344 (84)	$\nu(C\equiv N)$	
2043	2105 (62)	2040	2100 (60)	2042	2100 (58)	$\nu_{ss}(CO)$	
1946	2010 (64) 2000 (54)	1941	1999 (58) 1994 (53)	1942	2003 (61) 1997 (55)	$\nu_{as}(CO)$ {	as$_2$ as$_1$
1612	1651 (39)	1611	1651 (40)	1612	1651 (39)	$\nu_{ss}(bpy)$	
1604	1648 (44)	1604	1653 (49)	1601	1647 (46)	$\nu_{ss}(Ph)$	

3.4.2.7 Transient Infrared Spectroscopy

In an effort to understand the differences in the characteristics of the excited states for the three complexes, TRIR spectra were measured in the spectral regions of the CO (1900 to 2150 cm^{-1}), CN (2150 to 2310 cm^{-1}), and ring (1540 to 1640 cm^{-1}) vibrations. TRIR spectra in the CO stretching region were previously reported for a variety of rhenium tricarbonyl[10,11,14,20,23,42] and other transition metal complexes, and a general understanding of the associated spectral changes has been reached. Removal of electron density from the metal in Re-to-bpy MLCT transitions leads to a decrease of the Re(dπ) backbonding to the π^* orbitals of CO ligands and to an increase of the CO stretching frequencies.[37] Conversely, decreases of the CO frequencies indicate an increase of electron density at the metal.

ReBN in DCM: Long-lived MLCT State. The TRIR of ReBN in DCM is shown in Figure 3.22.
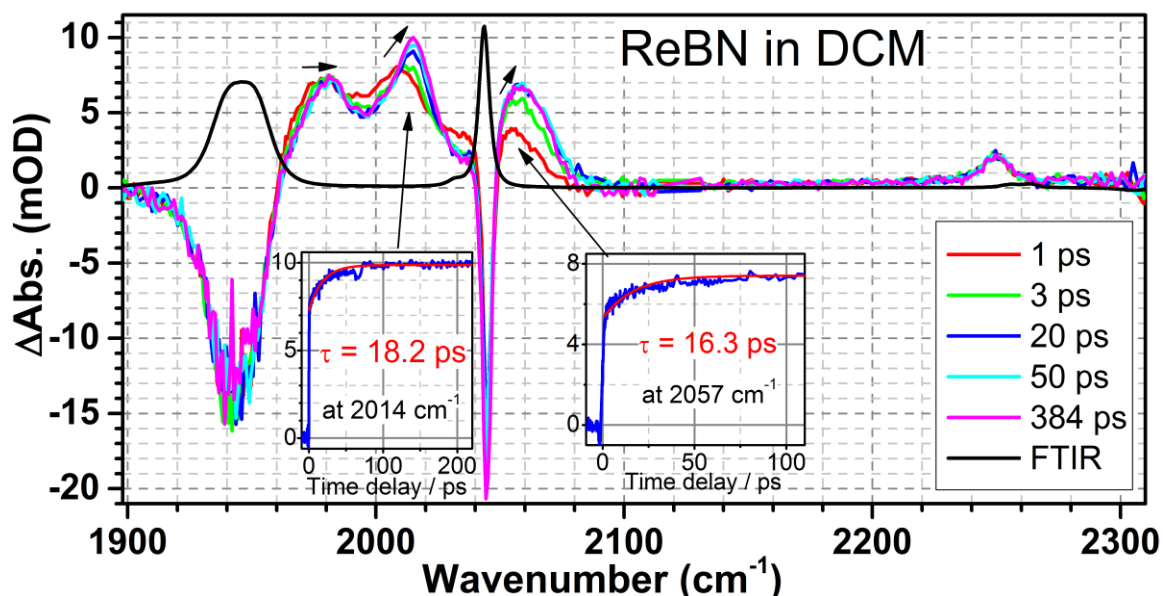
Figure 3.22 Transient infrared spectrum of ReBN in DCM following 402 nm excitation. Insets show kinetics measured at indicated frequencies and their fits to a single exponential function. The arrows indicate the directions of the spectral changes in the excited state.

The two ν_{as}(CO) peaks that overlap in the ground state are well resolved in the excited state, with the maxima at small delay times of 1976 and 2017 cm^{-1}. The large frequency increase of all three CO peaks observed instantaneously upon excitation, +64 (as$_1$), +30 (as$_2$), and +11 cm^{-1} (ss), is in accord with formation of a Re (dπ) $\rightarrow$ (π^*) bpy MLCT state. (The dynamics occurring faster than the instrument response time of ca. 200 fs is described as instantaneous.) The excited-state absorption peaks show dynamics with a characteristic time of ca. 17 ps (Figure 3.22), which results in a further shift to higher frequencies of all three CO peaks by +5 (as$_1$), +6 (as$_2$), and +2.5 cm^{-1} (ss), peak narrowing, as well as growth of the ν_{ss}(CO) and ν_{as1}(CO) peak amplitudes. Such dynamics can be assigned to a combination of solvation, vibrational cooling, and electronic relaxation among different excited states.[11,43,44] There is considerable evidence in the literature to indicate that the electronic relaxation to the lowest triplet MLCT state in complexes with heavy metals such as Re occurs within several hundred femtoseconds.[17,42] The solvation process in DCM is very fast with the slowest solvation component reported at 1.0 ps.[45] Thus, vibrational cooling remains the most likely cause of the observed dynamics.[11] Vibrational relaxation to the lowest MLCT state following 402 nm excitation deposits ca. 6000 cm^{-1} (using the luminescence peak at 524 nm) of excess energy into the complex within the first few hundred femtoseconds after excitation, resulting in excitation of a range of vibrational modes in the complex. Anharmonic coupling of these modes with the CO modes causes frequency shifts of the latter.[43,44,46-48] Thus, cooling of the complex causes the CO peaks to narrow and shift to higher frequencies. A thermalization time in a nonpolar solvent under similar concentration and excitation conditions was previously found to be ca. 20 ps using relaxation-assisted 2DIR

spectroscopy.[47] The CO modes are clearly the most sensitive to the excess energy, possibly because of a large dipole-dipole contribution to their interaction energy with the other modes in the complex.

There is a small instantaneous shift of the CN mode frequency of ca. -10 cm^{-1} upon electronic excitation; in addition, the CN transition dipole in the excited state increases ~4 fold. The ps excited-state dynamics affecting the CO modes does not perturb the CN mode, confirming that the BN ligand is not involved significantly in the MLCT transition. No further spectral changes beyond 50 ps are found for **ReBN** in the 430 ps time window; *the overall excited state lifetime of ~0.8 μs is attributed to the lifetime of MLCT state of* **ReBN**.

Re4DMABN in DCM: The Lowest Energy Excited State is Different than in ReBN. The TRIR spectra of Re4DMABN in DCM is shown in Figure 3.23.
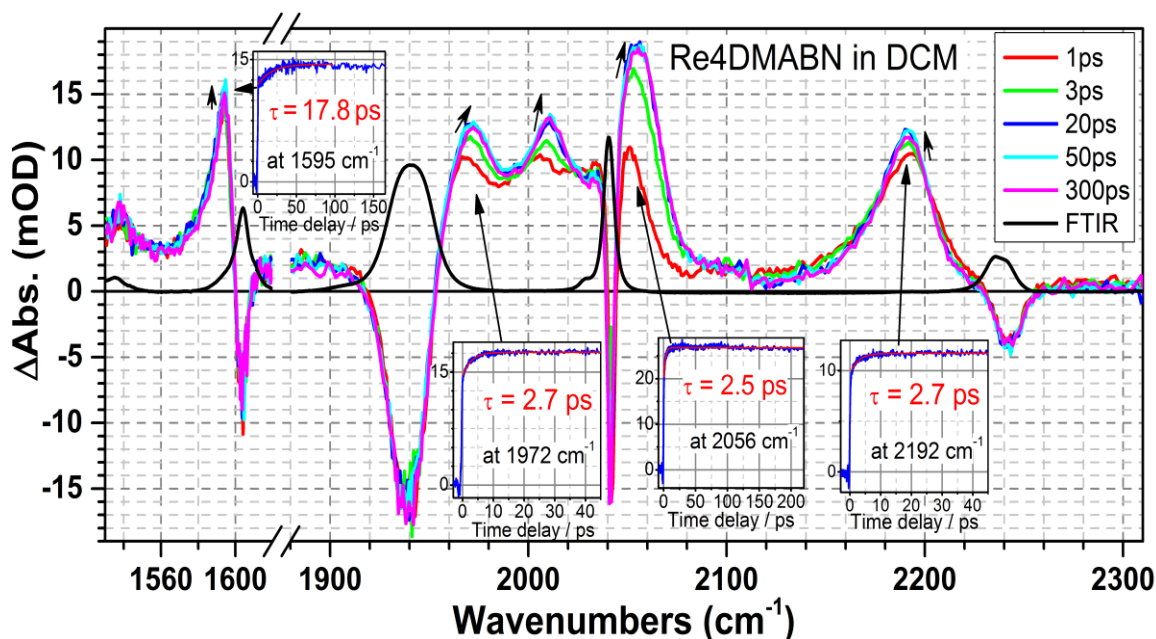
Figure 3.23 Transient infrared spectrum of Re4DMABN in DCM following 402 nm excitation. Insets show kinetics measured at indicated frequencies and their fits to a single exponential function. The arrows indicate the directions of the spectral changes in the excited state.

The TRIR spectra of Re4DMABN in the CO region are similar to those of ReBN, implying that a similar MLCT state is formed upon excitation; however, the CN stretching frequency in Re4DMABN decreases by 46 cm^{-1} in the excited state and exhibits a large increase in intensity. This indicates a further change of the CN bond order toward a double bond limit. In addition, the ν_{ss}(Ph) peak at 1604 cm^{-1}, shows a 10 cm^{-1} decrease in frequency, indicating electron density redistribution in the 4DMABN ligand core in the excited state. Only small spectral changes occur over the first 50 ps for all the modes examined, and no further changes are observed between 50 and 430 ps. Relaxation times of ca. 2.7 ps and ca. 18 ps are observed. Because both time components are much slower than the solvation time in DCM[45] and peaks shift to higher frequencies and narrow, the dynamics are assigned primarily to vibrational cooling of the complex, as with the ReBN complex. Despite the similarities in luminescence intensity, band shape, and lifetime, and transient absorption spectra of Re4DMABN and ReBN, the time-resolved transient infrared spectra clearly indicate significant electron density redistribution within the coordinated 4DMABN ligand. *The resulting state can be viewed as having "mixed" triplet metal-ligand (Re - DMABN) to ligand (bpy) charge transfer character (i.e., MLLCT).*

Re4DMABN in MeOH/DCM: Initial formation of a MLLCT State followed by equilibration with a LLCT state. The TRIR spectra of Re4DMABN in DCM:MeOH is shown in Figure 3.24. The instantaneously observed spectrum (1 ps) is nearly identical to the spectrum of the complex in DCM. All ν(CO) modes shift to higher frequency along with a splitting of the energy ν_{as}(CO) modes. This is accompanied by an instantaneous shifts of ν(CN) and ν_{ss}(Ph) to lower frequencies coupled with increased IR

absorption intensity. This collective behavior is consistent with the prompt formation of a MLLCT excited state.
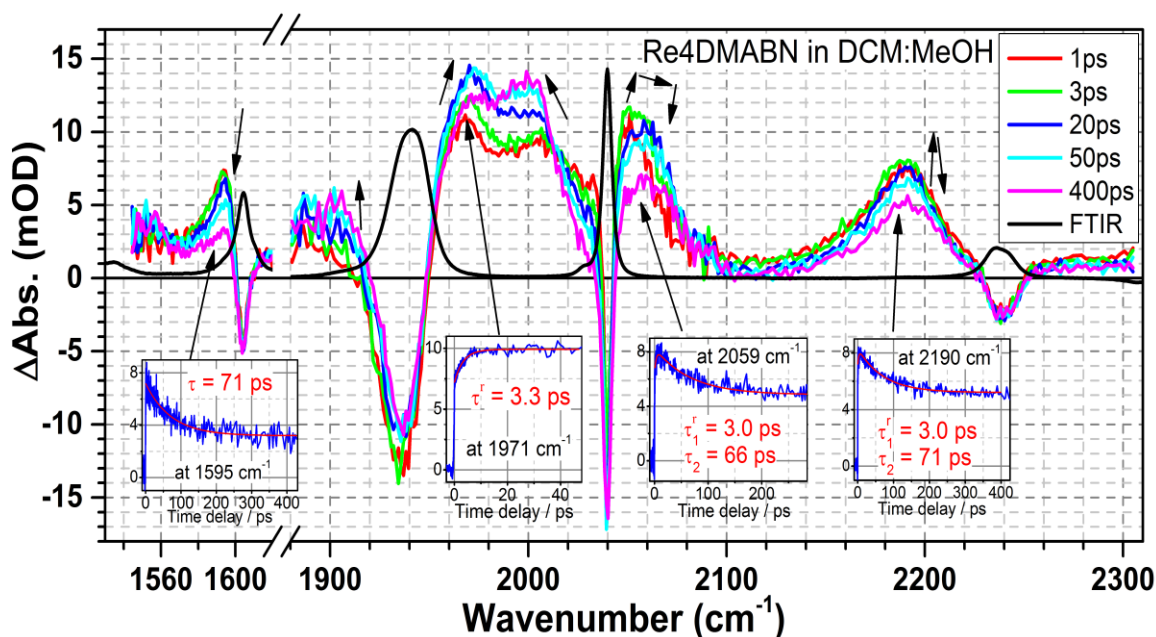
Figure 3.24 Transient infrared spectrum of Re4DMABN in DCM:MeOH following 402 nm excitation. Insets show kinetics measured at indicated frequencies and their fits to a single exponential function. The arrows indicate the directions of the spectral changes in the excited state.

The early time evolution of the CO and CN modes in the excited state of Re4DMABN in DCM:MeOH are similar to the early time dynamics in DCM: the CO stretches increase in frequency and become more narrow, and there is a small increase in the intensity of the observed CN stretch. These spectral changes occur with a characteristic time of approximately 3 ps. These dynamics clearly involve vibrational cooling of the system but may also be influenced by solvation of the excited state.[45] A unique excited state process with a characteristic decay time of 70 ps is observed in Re4DMABN in mixed DCM:MeOH. This is characterized by a decrease in the frequency of all three CO modes, which indicates a slight increase in electron density at the metal center.

Concomitantly, ν(CN) and ν_{ss}(Ph) peaks decrease by factors of 1.65 and 2.1, respectively. No new CN spectral region peaks are observed as a result of the peak decay at 2190 cm^{-1}, which likely indicates that any new peak formed is weak and broad. The 70 ps decay of 1595 cm^{-1} stretch results in the formation of a persistent peak at 1555 cm^{-1}.

The 70 ps process is too slow to be associated with solvation or cooling. This behavior is likely due to solvent facilitated structural rearrangements or electronic relaxation from the initially formed MLLCT to form a unique excited state species. Analysis of the individual decays show only a partial conversion (~52%) of the initially formed MLLCT excited state. Compared to the MLLCT state, the new state is characterized by increased electron density at Re, significant reduction of the ν_{ss}(Ph) frequency, and high electronic asymmetry in the three Re-N bonds (large splitting of the two ν_{as}(CO) modes). The observed changes in these features are consistent with the formation of a 4DMABN (π^*) to bpy (π^*) interligand charge transfer (LLCT) state. *These data in combination with the rapid excited state decay of Re4DMABN in DCM:MeOH (very low luminescence quantum yield and lack of nanosecond transient absorption spectrum) are consistent with the assignment of an equilibrium between an initially formed MLLCT excited state and a 4DMABN (π^*) to bpy (π^*) LLCT excited state with rapid relaxation to the ground state.*

Re3DMABN in DCM: Formation of a Long-lived ^{3}IL State. The TRIR spectra of Re3DMABN in DCM are shown in Figure 3.25. Immediately following excitation, all of the CO stretching modes shift to higher frequency, ν(CN) is shifts to slightly lower frequency (12 cm^{-1}), and the ground state absorption corresponding to ν_{ss}(Ph) only demonstrates a bleach signal. The CO frequency shifts, +70 (as$_1$), +30 (as$_2$), and +17 cm^{-1}

(ss), are the largest among all three compounds, suggesting preparation of a slightly more positive Re center in Re3DMABN when compared to ReBN and Re4DMABN. The shift of 12 cm^{-1} of the CN stretching mode is larger than the shift found in ReBN (-10 cm^{-1}) but much smaller than is found in Re4DMABN (-50 cm^{-1}). The combination of these features confirm the formation of an initial MLCT (Re→bpy) excited state.
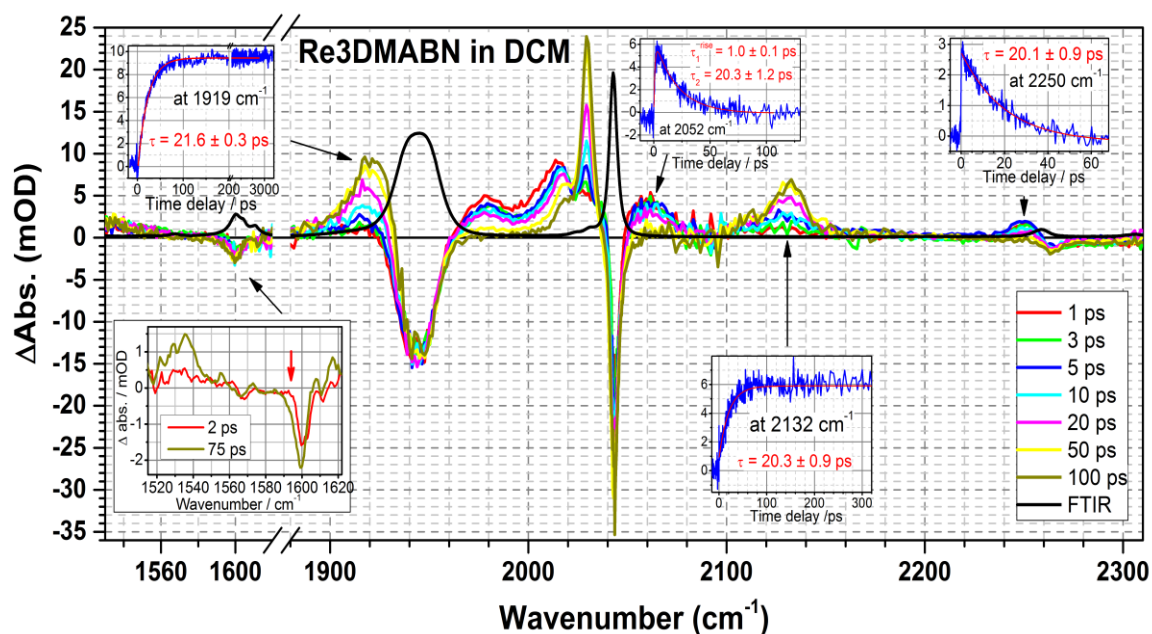
Figure 3.25 Transient infrared spectrum of Re3DMABN in DCM following 402 nm excitation. Insets show kinetics measured at indicated frequencies and their fits to a single exponential function. The arrows indicate the directions of the spectral changes in the excited state.

After the initial, rapid formation of an MLCT state, Re3DMABN evolves to an excited state species with distinct features over a characteristic time of 20 ps. There is a dramatic change in the three CO modes: the two ν_{as}(CO) modes overlap and shift to a frequency that is **26 cm^{-1} less than the ground state frequency** and ν_{ss}(CO) becomes very narrow, and shifts to a frequency that is **12 cm^{-1} lower than the ground state frequency**. Both ν(CN) and ν_{ss}(Ph) shift to dramatically lower frequencies -127 and -66 cm^{-1}, respectively. This indicates a large change in charge distribution on the 3DMABN

ligand. The decrease in the CO stretching frequencies correspond to an increase in the electron density at the Re metal center. In addition, the excited state formed after 20 ps features high symmetry with respect to the three facial CO ligands, which is apparent from the narrowness of $\nu_{ss}(CO)$ and the coalescence the two $\nu_{as}(CO)$ modes. This collective behavior is considerably different from that seen in ReBN and Re4DMABN. What is the nature of this excited state? The data suggest that this state is not LLCT in character because the formation of a LLCT state would likely result in a lowering of the symmetry with respect to the CO groups due to different charges on the bpy and 3DMABN ligand. Also, the overall excited state lifetime of this complex is extremely long (23 μs). With these facts in mind, the dramatic change in $\nu(CN)$ was explored. In the triplet state of 4DMABN in hexane, the CN stretching frequency is found to be 175 cm^{-1} below that in the ground state.[49] Although no similar data is available for 3DMABN, formation of a strongly polarized (amine $\rightarrow$ CN) triplet state seems plausible. To further elucidate the nature of the excited state, the ability of the complex to participate in energy transfer reactions was explored. Pyrene has a well-established triplet energy (16900 cm^{-1}) that is significantly lower than the excited state energy of Re3DMABN and possesses a unique triplet-triplet absorption spectrum that makes it easy to monitor in nanosecond transient absorption spectroscopy. The transient absorption spectrum of Re3DMABN in the presence of 1 mM pyrene in deaerated DCM is shown in Figure 3.26. The transient absorption spectrum clearly illustrates a lack of absorbance from excited Re3DMABN and the appearance of the characteristic pyrene triplet absorption transitions at 415 and 520 nm. Pyrene is an effective quencher of the observed excited state with a bimolecular quenching rate constant (determined from Stern-Volmer analysis) of 4.9 x 10^9 M^{-1}s^{-1}.

This combination of TRIR, lifetime, and excited state quenching data thoroughly supports the assignment of the thermally equilibrated excited state of Re3DMABN in DCM as a triplet state localized on the 3DMABN ligand.
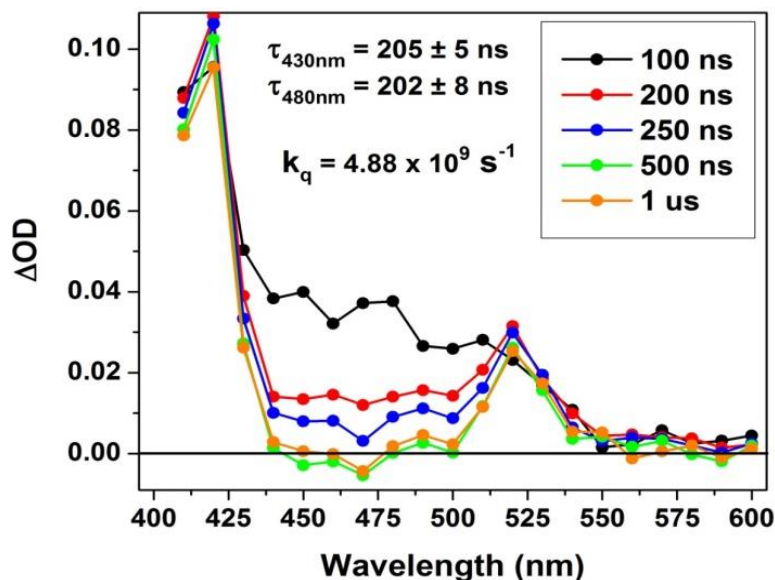
Figure 3.26 Nanosecond transient absorption spectrum of Re3DMABN in deaerated DCM in the presence of 1mM pyrene.

Re3DMABN in MeOH/DCM: Equilibrium of MLCT and ^{3}IL Excited States.

The TRIR spectra of Re3DMABN in DCM:MeOH are shown in Figure 3.27. Upon excitation, the initially detected excited state is very similar to that in DCM. The overlapping asymmetric CO modes separate and shift to higher frequency. A broadening of the symmetric CO stretch is accompanied by a shift to higher frequency. The nitrile stretching mode experiences a slight decrease in frequency. The symmetric phenyl stretch on the 3DMABN ligand also exhibits a bleach of its ground state absorption peak. As with DCM, these spectral features are assigned to the formation of the Re $\rightarrow$ bpy MLCT state.

The spectral changes observed in the picosecond dynamics of Re3DMABN in DCM:MeOH differ dramatically from those in DCM. None of the CO stretching modes

shift to lower frequency. Instead, the CO modes increase in frequency and become narrower with a time constant of 7 ps. This behavior is consistent with the solvation and vibrational cooling of a ^{3}MLCT excited state. The CN stretch in the excited state evolves similarly to that in DCM. The initial positive absorption at 2244 cm^{-1} decreases but persists. Simultaneously, an IR absorption band grows in at 2125 cm^{-1}. The frequency shift in the mixed solvent (-135 cm^{-1}) is even larger than that in DCM (-127 cm^{-1}). Methanol absorption prevented measurements below 1560 cm^{-1}, so the frequency of the ν_{ss}(Ph) mode in the relaxed state(s) could not be determined.
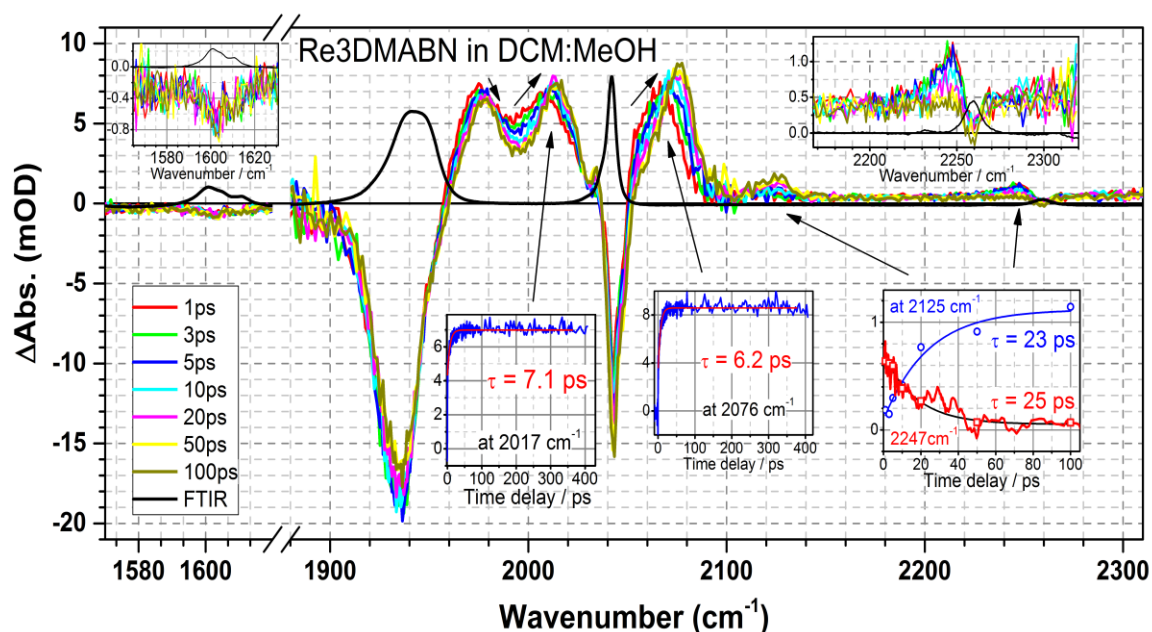
Figure 3.27 Transient infrared spectrum of Re3DMABN in DCM:MeOH following 402 nm excitation. Insets show kinetics measured at indicated frequencies and their fits to a single exponential function. The arrows indicate the directions of the spectral changes in the excited state.

The dominant relaxed excited state for Re3DMABN in DCM:MeOH has less electron density at the Re metal center than in the ground state (CO frequency upshift), asymmetric facial environment for the CO groups (splitting of the two ν_{as}(CO) modes), and displays a slight lowering of the ν(CN). The localized 3DMABN triplet state that is

observed in DCM is also clearly seen in MeOH/DCM: a sharp, $\nu_{ss}(CO)$ peak at 2035 cm^{-1} accompanies the characteristic ^{3}IL nitrile stretch at 2120 cm^{-1}. Using the amplitude of the peak at 2035 cm^{-1} in comparison to the bleach signal from the ground state $\nu_{ss}(CO)$ peak, the contribution of the local triplet state in MeOH/DCM mixture is estimated to be ~15%. *Increasing the polarity of the medium results in significant lowering of the ^{3}MLCT state energy such that it becomes the dominant state but remains in equilibrium with the 3DMABN localized ^{3}IL state.*

3.4.2.8 Conclusions

The excited state properties of a series of Re^I(bpy)(CO)$_3$L compounds were studied using steady-state and time-resolved transient infrared and UV-vis absorption, cyclic voltammetry and luminescence intensity and lifetime measurements. Re4DMABN and Re3DMABN exhibit voltammetric waves attributable to the one-electron reduction of bipyridine and the one-electron oxidation of the dimethyl amino moiety. ΔE_{cs} for the complexes differs by less than 200 mV in DCM and CH$_3$CN. Despite these observed similarities in the electrochemical behavior of Re4DMABN and Re3DMABN it is clear that the nature of the lowest energy excited states observed is very different. ReBN and Re4DMABN exhibit strongly solvent-dependent luminescence behavior. Both complexes display strong emission in dichloromethane (DCM) with microsecond lifetimes. In mixed DCM:MeOH, the luminescence quantum yield of ReBN decreases by a factor of four and the luminescence lifetime decreases by a factor of two, whereas the luminescence quantum yield of Re4DMABN decreases by two orders of magnitude and the luminescence lifetime decreases to the point that it is no longer resolvable with our instrumentation (< 20 ns). The luminescence collected from solutions of Re3DMABN is

very weak in both DCM and DCM:MeOH. The interpretation of this data is difficult due to potential complications from impurity emission (See Section 3.4.2.4). The nanosecond transient absorption spectra of the complexes are similar and characterized by a broad positive absorption feature from 400 - 470 nm; however, the lifetime (23 μs) of Re3DMABN is more than an order of magnitude longer than ReBN and Re4DMABN. Time-resolved transient infrared measurements allow for a detailed examination of the electron density distribution in the excited state of each chromophore. For the Re4DMABN in DCM, essentially instantaneous formation of a long-lived (0.8 μs) triplet MLLCT excited state is found, while formation of a LLCT (4DMABN $\rightarrow$ bpy) state in close proximity to the MLLCT state is observed in mixed DCM:MeOH. The presence of the LLCT state is believed to be responsible for drastic shortening of the excited-state lifetime in mixed solvent. A pure MLCT excited state is formed within 0.2 ps of excitation of Re3DMABN in both solvent systems, although its dynamics and evolution are solvent dependent. In DCM, a long-lived (23 μs) intraligand triplet (^{3}IL, $^3(\pi - \pi^*)$) state is formed while, in mixed DCM:MeOH, an equilibrium is observed between the ^{3}IL and MLCT state. To definitively understand the excited state behavior of these complexes detailed characterization utilizing a number of experimental methods was necessary. Notably, the employment of multiple infrared modes on different ligands in TRIR measurements is crucial in assessing the nature of the electronic states.

3.5 [Re(dcebpy)(CO₃)L](BArF₂₄) Complexes

In the preceding section describing the excited state reactivity of fac-[Re(bpy)(CO)₃BN](BArF₂₄), fac-[Re(bpy)(CO)₃4DMABN](BArF₂₄), and fac-[Re(bpy)(CO)₃3DMABN](BArF₂₄), it was demonstrated that none of the chromophores

exclusively accessed the desired ligand-to-ligand charge transfer excited state. The observed excited state reactivity in these molecules was influenced by unanticipated factors: the expected behavior of Re4DMABN was altered by the polarized nature of the 4DMABN ligand in the electronic ground state of the molecule, and the performance of Re3DMABN was affected by the presence of a ^{3}IL state capable of thermally equilibrating with the initially excited ^{3}MLCT state. With these results in mind, we endeavored to synthesize a chromophore capable of accessing a LLCT excited state. The use of the 3DMABN as the electron donating moiety was preferable to 4DMABN because the meta substitution of the amino group does not allow for electronic coupling of the ligand and metal in the ground state of the molecule. The use of the 3DMABN ligand necessitated a decrease of ΔE_{cs} for the system in order to mitigate equilibration with the ^{3}IL state of the ligand. It is well-established in the literature that the inclusion of an ester substituted bipyridine ligand in place of bipyridine will significantly lower the reduction potential of the complex[50], and, subsequently ΔE_{cs}. The structural analogs, fac-[Re(dcebpy)(CO)$_3$3DMABN](BArF$_{24}$) (dcebpy = 4,4'-dicarboxylic acid diethyl ester-2,2'-bipyridine) and fac-[Re(dcebpy)(CO)$_3$BN](BArF$_{24}$) were synthesized and characterized using identical experimental methodology as the set of fac-[Re(bpy)(CO)$_3$L](BArF$_{24}$) complex. The inclusion of dcebpy resulted in the anticipated decrease in the one-electron reduction potential of the complex by 0.39 mV in CH$_3$CN (ΔE_{CS} = 1.95 V) and 0.34 mV in DCM (ΔE_{CS} = 1.94 V). The energy of the initially populated ^{3}MLCT state of the dcebpy systems can be estimated from the luminescence spectra of fac-[Re(dcebpy)(CO)$_3$BN](BArF$_{24}$). In DCM, the luminescence maximum of the complex occurs at 566 nm (2.19 eV) and, in mixed DCM:NM (NM = nitromethane),

the luminescence maximum of the complex is observed at 586 nm (2.11 eV). Predictably, time-resolved transient infrared spectra of fac-[Re(dcebpy)(CO)$_3$3DMABN](BArF$_{24}$) provide clear evidence of the formation of a LLCT excited state in both DCM and NM!

3.5.1 Synthesis

Benzene and n-hexanes were purchased from Fisher Scientific. Toluene, absolute ethanol, dichloromethane (DCM), and pentane were purchased from PHARMCO-AAPER. [Re(CO)$_5$Cl] was purchased from Strem Chemical. 3-aminobenzonitrile, paraformaldehyde, and sodium cyanoborohydride were purchased from Sigma Aldrich. Benzonitrile was purchased from Alfa Aesar. Sodium tetrakis(3,5-bis(trifluoromethyl)phenyl)borate[27] (Na[BArF$_{24}$]) and 2,2'-bipyridine-4,4'-dicarboxylic acid[51] were previous synthesized in our laboratory. The esterification of 2,2'-bipyridine-4,4'-dicarboxylic acid was accomplished using a literature method.[52] All other synthetic materials were used as received other than 3-aminobenzonitrile which was *N*-methylated using a published method.[28] fac-[Re(dcebpy)(CO)$_3$Cl][29] and the fac-[Re(dcebpy)(CO)$_3$L](BArF$_{24}$)[30] complexes were all prepared with modification to previously reported methods in the literature.

2,2'-bipyridine-4,4'-dicarboxylic acid diethyl ester (dcebpy): 1.92 g (7.9 mmol) 2,2'-bipyridine-4,4'-dicarboxylic acid was added to a mixture of 20 mL concentration H$_2$SO$_4$ and 45 mL absolute ethanol and refluxed for 9 hours. 1.04 g (44% yield) of crystalline material was obtained after work up. ^{1}H NMR (CD$_2$Cl$_2$) δ: 8.93 (s, 1 H), 8.54 (d, J= 4.84 Hz, 2 H), 7.89 (d, J= 4.24 Hz, 2 H), 4.43 (q, J= 7.12 Hz, 4 H), 1.43 (t, J=7.12 Hz, 6 H).

fac-[Re(dcebpy)(CO)₃Cl]: 306.9 mg (0.85 mmol) of [Re(CO)₅Cl] and 254.8 mg (0.85 mmol) dcebpy were added to 40 mL toluene in a round bottom flask. The reaction was run at reflux for 3 hours. Upon completion of the reaction, the toluene was removed via rotary evaporation. The solid was collected and rinsed with 30 mL diethyl ether and 30 mL n-hexane. 483.9 mg (96.8% yield) of orange solid was collected on fritted glass. ^{1}H NMR (CD₂Cl₂) δ: 9.19 (d, J= 5.04 Hz, 2 H, dcebpy), 8.88 (s, 1 H, dcebpy), 8.10 (d, J= 5.88 Hz, 2 H, dcebpy), 4.52 (q, J= 7.2 Hz, 4 H, dcebpy), 1.46 (t, J=7.08 Hz, 6 H, dcebpy).

fac-[Re(dcebpy)(CO)₃BN](BArF₂₄) (ReEB): 74.4 mg (0.12 mmol) fac-[Re(dcebpy)(CO)₃Cl] and 31.4 mg AgOTf (0.12 mmol) were added to 15 mL of DCM. The solution was allowed to stir at room temperature for 2 hours. At this point, 13 mL (0.13 mmol) benzonitrile and 106.4 mg (0.12 mmol) Na[BArF₂₄] were added to the solution. The reaction was stirred at room temperature for another 4 hours. The solution was placed in the freezer overnight to ensure complete precipitation of AgCl and NaOTf. The solid was separated from the solution using a filter paper loaded with Celite. Rotary evaporation was used to lower the filtrate volume to ~5 mL. The remaining DCM was loaded onto a short silica column and eluted with DCM. The desired yellow band elutes with a R_f 0.60. Attempts to precipitate the product from DCM with n-hexanes resulted in an intractable paste. The paste was triturated with 10 mL of pentane. After decanting the pentane, the complex was reconstituted in benzene and precipitated with pentane. 118.8 mg (63.0% yield) yellow solid was collected on a fritted glass filter. ^{1}H NMR (CD₂Cl₂) δ: 9.26 (d, J= 5.96 Hz, 2 H, dcebpy), 9.00 (s, 1 H, dcebpy), 8.27 (d, J= 5.28 Hz, 2 H, dcebpy) 7.71 (s, 9H, BArF₂₄ + BN), 7.54 (s, 4 H, BArF₂₄), 7.45 (m, 4 H, benzonitrile), 4.54 (q, J= 7.16 Hz, 4 H, dcebpy), 1.46 (t, J=7.12 Hz, 6 H, dcebpy).

fac-[Re(dcebpy)(CO)$_3$3DMABN](BArF$_{24}$) **(ReEBA):** The complex was synthesized following the same procedure as fac-[Re(dcebpy)(CO)$_3$BN](BArF$_{24}$) with a slight modification. 49.9 mg (0.082 mmol) fac-[Re(dcebpy)(CO)$_3$Cl], 24.4 mg AgOTf (0.095 mmol) , 12.7 mg (0.087 mmol) 3DMABN, and 77.1 mg (0.087 mmol) Na[BArF$_{24}$] were reacted. After decanting the pentane, the complex was reconstituted in methanol and precipitated with water. 118.1 mg (90.9%) of yellow solid was collected on a fritted glass filter. ^{1}H NMR (CD$_2$Cl$_2$) δ: 9.26 (d, J=6.08 Hz, 2 H, dcebpy), 9.00 (s, 1 H, dcebpy), 8.26 (d, J= 6.08 Hz, 2 H, dcebpy) 7.71 (s, 8 H, BArF$_{24}$), 7.55 (s, 4 H, BArF$_{24}$), 7.19 (t, J= 6.04 Hz, 1 H, 3DMABN), 6.91 (d, J= 6.68 Hz, 1 H, 3DMABN), 6.62 (d, J= 6.08 Hz, 1 H, 3DMABN), 6.61 (s, 1 H, 3DMABN), 4.55 (q, J= 7.28 Hz, 4 H, dcebpy), 2.89 (s, 6 H, 3DMABN), 1.47 (t, J=7.28 Hz, 6 H, dcebpy).

3.5.2 Results and Discussion

The complexes fac-[Re(dcebpy)(CO)$_3$3DMABN](BArF$_{24}$) (ReEBA) and fac-[Re(dcebpy)(CO)$_3$BN](BArF$_{24}$) (ReEB) were synthesized using a similar three step procedure described in Section 3.4.2 for the synthesis of the series of fac-[Re(bpy)(CO)$_3$L](BArF$_{24}$) chromophores. The only deviation from this protocol was the use of 4,4'-dicarboxylic acid diethyl ester-2,2'-bipyridine in the initial reaction with Re(CO)$_5$Cl. It is worth noting that the work-up of the dcebpy containing complexes was more involved than the purification and isolation of the fac-[Re(bpy)(CO)$_3$L](BArF$_{24}$) complexes. For ReEB, attempts to precipitate the complex from DCM with n-hexane resulted in an intractable, orange oil. The complex was obtained as a pure, yellow solid by triturating the oil in pentane, reconstituting the resulting paste in benzene, and precipitating with pentane. Attempts to precipitate ReEBA from DCM with n-hexane also

resulted in an orange oil. This complex could also be obtained as a tractable solid using a trituration and subsequent precipitation procedure. ReEBA was triturated with pentane, followed by precipitation from methanol with water. The complexes were characterized using ^{1}H NMR and MALDI-TOF mass spectrometry. Images of the ^{1}H NMR spectra of complexes are included in Section, 3.5.2.1, as Figures 3.28 and 3.29. MALDI-TOF results, including linear-positive and reflector-positive mass spectra and simulated molecular formulas for the observed species, are collected in Section 3.5.2.2. These data are shown in Figures 3.30-3.35 and Tables 3.9 and 3.10.

3.5.2.1 ^{1}H NMR

The interpretation of the ^{1}H NMR spectra of ReEB (Figure 3.28) and ReEBA (Figure 3.29) is also simple. The ^{1}H resonances of the BArF$_{24}$ counter-ion are observed at 7.71 ppm and 7.55 ppm in both spectra.
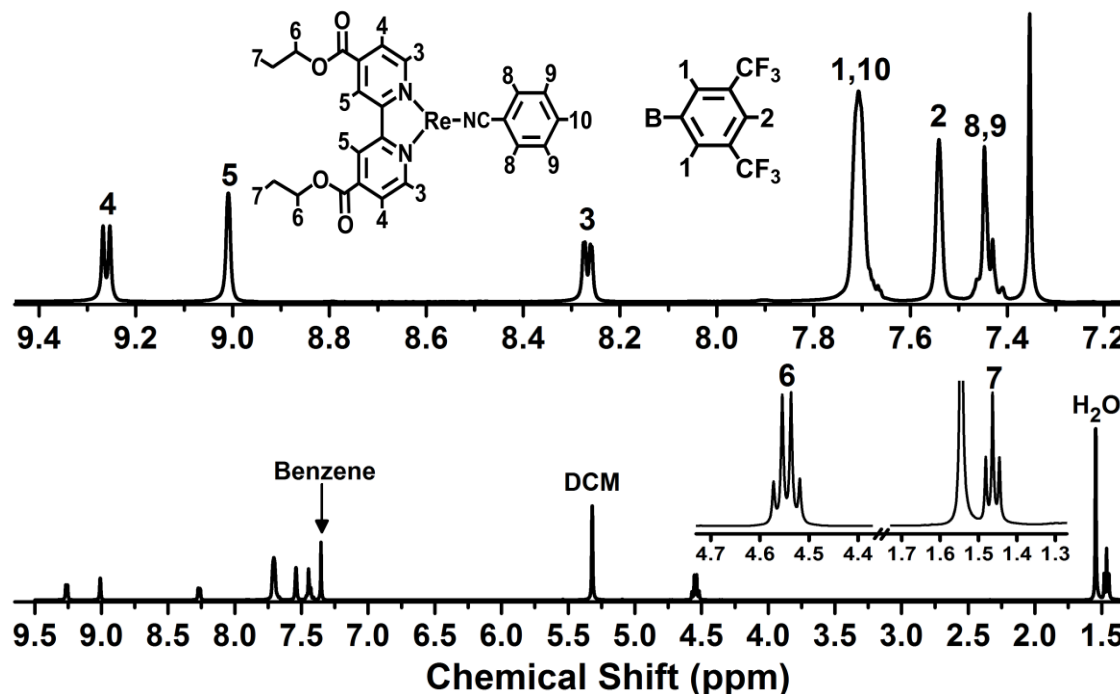
Figure 3.28 NMR spectrum of fac-[Re(dcebpy)(CO)$_3$BN](BArF$_{24}$) in CD$_2$Cl$_2$. Top: Enlarged view of the aromatic region of the NMR spectrum. Bottom: Entire NMR spectrum. Inset: Magnification of the aliphatic region of the spectrum.

The spectra of ReEB and ReEBA share three ^{1}H peaks representing the dcebpy ligand: a doublet integrating to two at 9.28 ppm, a singlet integrating to two at 9.01 ppm, and a doublet integrating to two at 8.26 ppm. For ReEB, the BN ^{1}H signal occurs as a multiplet at 7.41 ppm integrating to four and a single proton resonance incorporated into the BArF$_{24}$ resonance at 7.71 ppm. The singlet at 7.35 ppm in the ReBN spectrum is the result of residual benzene in the solid material. The aromatic peaks associated with 3DMABN ligand in ReEBA occur as a triplet at 7.19 ppm, a doublet at 6.91 ppm, and a coinciding singlet and doublet at 6.61 ppm. All integrate to one. The dimethylamino resonance occurs as a singlet at 2.89 ppm, integrating to six.
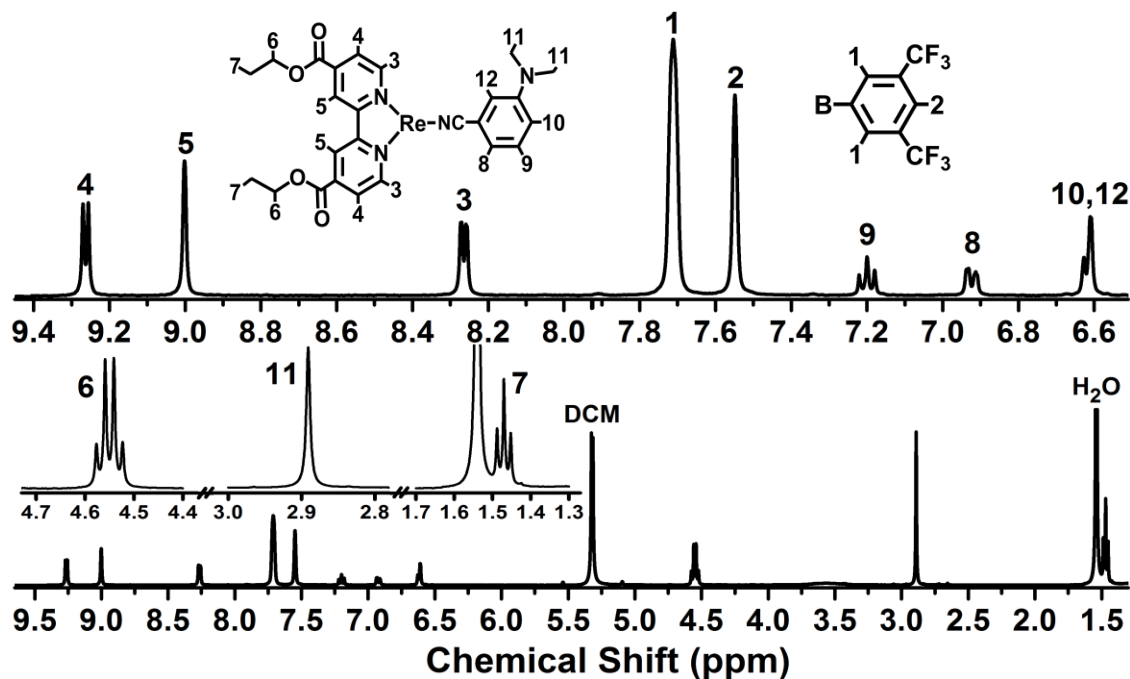
Figure 3.29 NMR spectrum of fac-[Re(dcebpy)(CO)$_3$3DMABN](BArF$_{24}$) in CD$_2$Cl$_2$. Top: Enlarged view of the aromatic region of the NMR spectrum. Bottom: Entire NMR spectrum. Inset: Magnification of the aliphatic region of the spectrum

3.5.2.2 MALDI-TOF

MALDI-TOF mass spectrometry was also used to characterize both of the fac-[Re(dcebpy)(CO)$_3$L](BArF$_{24}$) complexes. The MALDI-TOF behavior of the fac-

$[Re(dcebpy)(CO)_3L](BArF_{24})$ chromophores is similar to that of the fac-$[Re(bpy)(CO)_3L](BArF_{24})$ chromophores. Likewise, these spectra were collected by directly applying dilute solutions of the molecules to the sample plate for analysis. The dcebpy complexes also routinely lose the L ligand as well as nCO ligands (n=1-3) upon fragmentation. They regularly experience the loss of the nitrile containing ligand AND nCO ligands (n=1-3). Most of the observed mass fragments occur with the same 5 peak isotope distribution pattern indicative of a species containing common organic nuclei and rhenium. The spectrum of ReEB is unique in that we observe a substantial amount of a high mass species at 1161.16 m/z. The isotope distribution pattern and mass for this species can be replicated using a molecular formula of $[Re_2CO_3BN]^+$. This species has a slightly more complex isotope distribution pattern, reflecting the three possible statistical combinations of ^{185}Re and ^{187}Re in a dimeric species. $[Re_2(CO)_3BN]^+$ is likely created as a result of initial fragmentation of ReEB in the laser pulse. There is no evidence of this species in the preceding ^1H NMR of the complex or in the steady state IR spectrum of the complex. As with the fac-$[Re(bpy)(CO)_3L](BArF_{24})$ complexes, only unit mass resolution was achieved.

The observation of metastable ionic species in TOF mass spectrometry is discussed in detail in Section 3.4.2.2. The spectrum of ReEBA is comparable to the spectra of all three fac-$[Re(bpy)(CO)_3L](BArF_{24})$ complexes; multiple, metastable ion peaks are observed in the reflector mode spectrum of the complex and the most intense metastable ion peak occurs in the mass range between the $[M]^+$ and $[M-nCO]^+$ (n=1-3) and the $[M-L]^+$ mass, reflecting In the spectrum of ReEB, there are two equally intense metastable ionic species are observed. The first occurs between the $[M^+]$ and

$[Re_2(CO)_3BN]^+$ mass fragments. This is likely due to fragmentation of the $[Re_2(CO)_3BN]^+$ species. The second metastable species is observed between the $[M-L]^+$ and $[M-CO-L]^+$ mass fragments. This species likely reflects the loss of a CO ligand from the $[M-L]^+$ fragment.
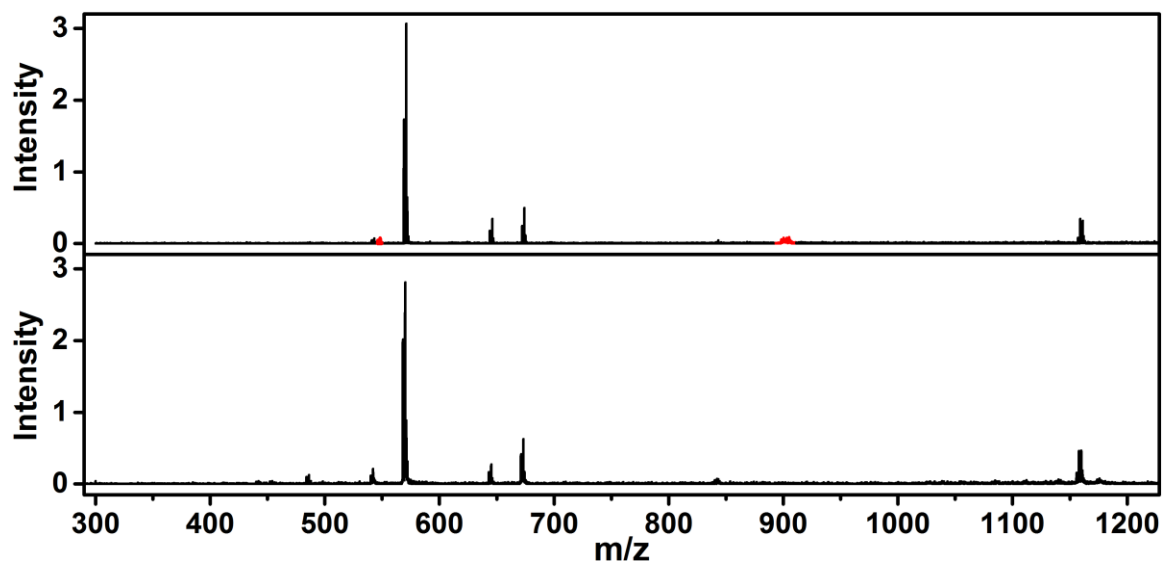
Figure 3.30 Top: Mass spectrum of fac-$[Re(dcebpy)CO_3BN]^+$ in reflector mode. Bottom: Mass spectrum of fac-$[Re(dcebpy)CO_3BN]^+$ in linear mode. The metastable species are highlight in red. Intensity values are shown in 10^4 counts.
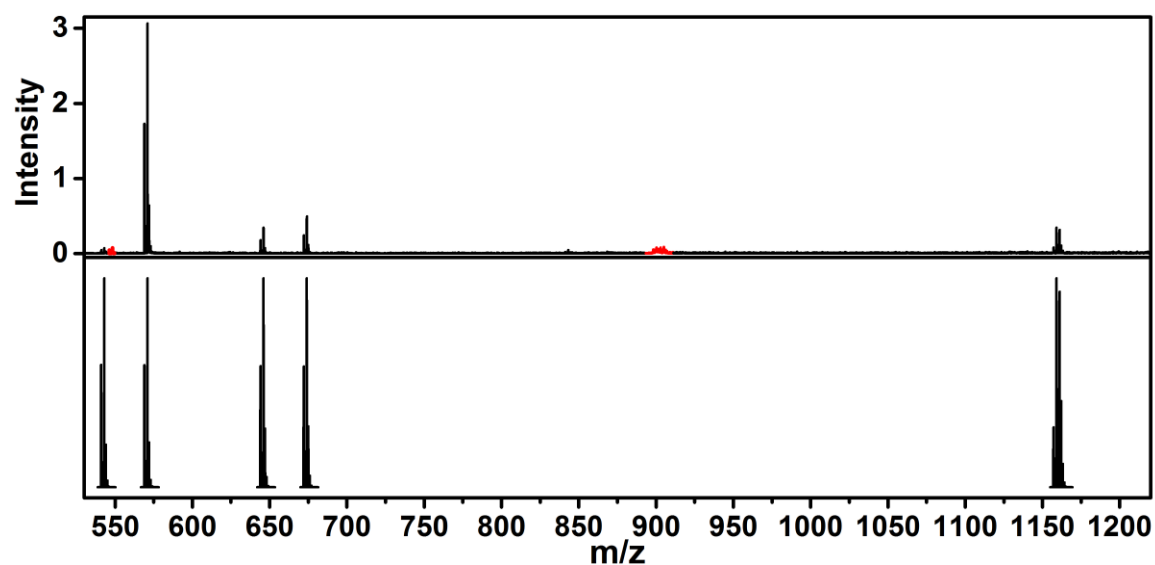
Figure 3.31 Top: Reflector mode mass spectrum of fac-$[Re(dcebpy)(CO)_3BN]^+$. Bottom: Simulated mass fragments for the molecular formulas presented in Table 3.9. The metastable species are highlight in red. Intensity values are shown in 10^4 counts.

Table 3.9 Simulated molecular formulas, corresponding fragments, and masses for fac-$[Re(dcebpy)(CO)_3BN]^+$.

Formula	Fragment	Calculated m/z	Actual m/z
$C_{12}H_8N_2O_2Re$	$[Re_2CO_3BN]^+$	1161.16	1161.16
$C_{26}H_{21}N_3O_7Re$	Parent $[M]^+$	674.09	674.12
$C_{25}H_{21}N_3O_6Re$	$[M-CO]^+$	646.10	646.11
$C_{19}H_{16}N_2O_7Re$	$[M-L]^+$	571.05	571.01
$C_{18}H_{16}N_2O_6Re$	$[M-CO-L]^+$	543.06	543.11
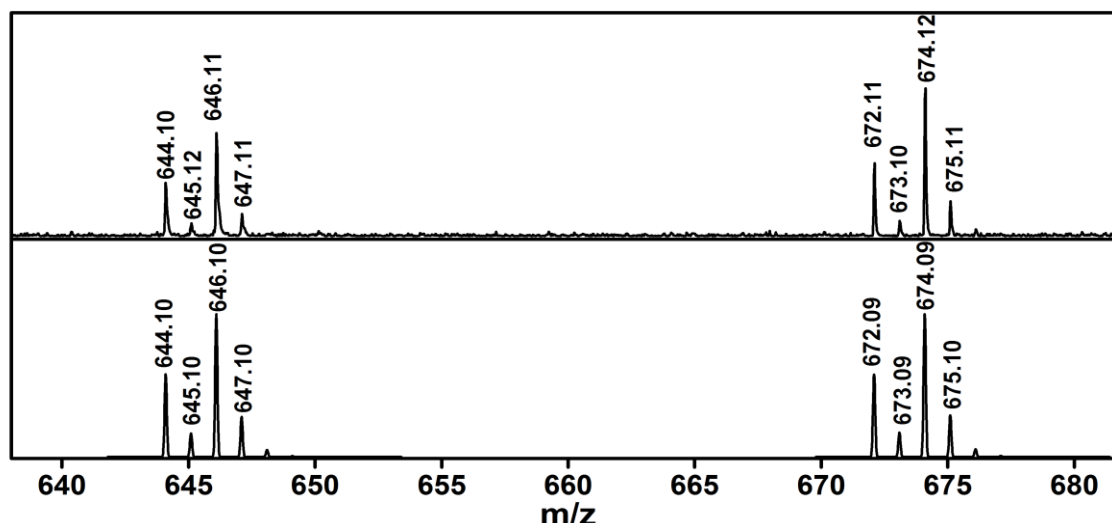
Figure 3.32 Top: Reflector mode mass spectrum of fac-$[Re(dcebpy)(CO)_3BN]^+$ which highlights the parent ion ($[M]^+$) and the parent ion with the loss of a CO ligand ($[M-CO]^+$). Bottom: Simulated mass spectra for $[M]^+$ and $[M-CO]^+$.
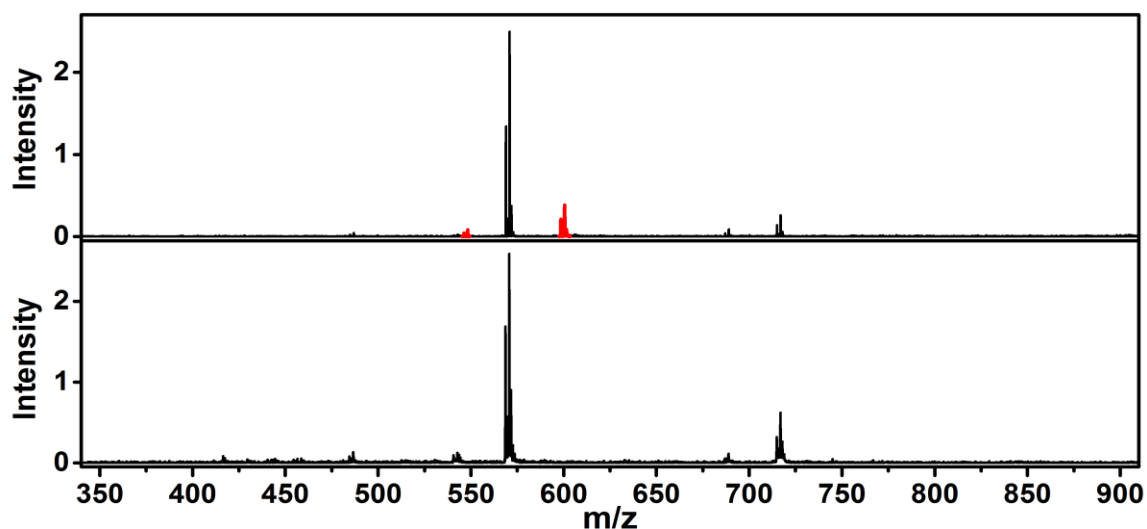
Figure 3.33 Top: Mass spectrum of fac-$[Re(dcebpy)CO_33DMABN]^+$ in reflector mode. Bottom: Mass spectrum of fac-$[Re(dcebpy)(CO)_33DMABN]^+$ in linear mode. The metastable species are highlight in red. Intensity values are shown in 10^4 counts.
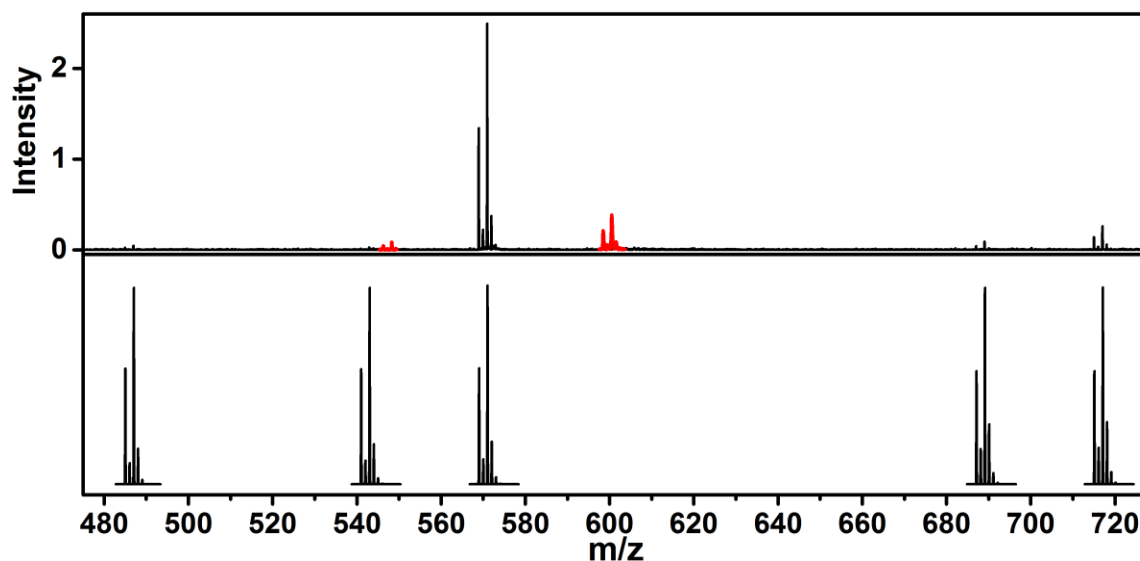
Figure 3.34 Top: Reflector mode mass spectrum of fac-[Re(dcebpy)(CO)₃3DMABN]⁺. Bottom: Simulated mass fragments for the molecular formulas presented in Table 3.10. The metastable species are highlight in red. Intensity values are shown in 10^4 counts.

Table 3.10 Simulated molecular formulas, corresponding fragments, and masses for fac-[Re(dcebpy)(CO)₃3DMABN]⁺.

Formula	Fragment	Calculated m/z	Actual m/z
$C_{28}H_{26}N_4O_7Re$	Parent [M]⁺	717.14	717.03
$C_{27}H_{26}N_4O_6Re$	[M-CO]⁺	689.14	689.05
$C_{19}H_{16}N_2O_7Re$	[M-L]⁺	571.05	570.94
$C_{18}H_{16}N_2O_6Re$	[M-CO-L]⁺	543.06	542.96
$C_{16}H_{16}N_2O_4Re$	[M-3CO-L]⁺	487.07	486.97
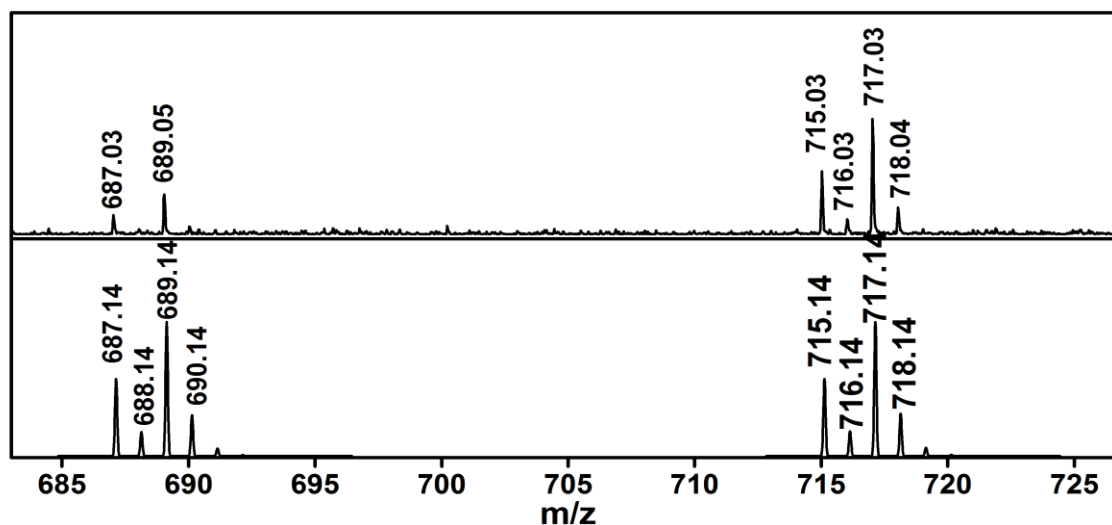
Figure 3.35 Top: Reflector mode mass spectrum of fac-[Re(dcebpy)(CO)₃3DMABN]⁺ which highlights the parent ion ([M]⁺) and the parent ion with the loss of a CO ligand ([M-CO]⁺). Bottom: Simulated mass spectra for [M]⁺ and [M-CO]⁺.

3.5.2.3 Electrochemistry

The anodic and cathodic sweep segments obtained in DCM and CH_3CN from cyclic voltammetric measurements on ReEBA are shown in Figures 3.36. The voltammograms exhibit waves attributable to one-electron reduction and oxidation of the complex. Redox potentials associated with voltammograms of Re3DMABN and ReEBA are compiled in Table 3.11.
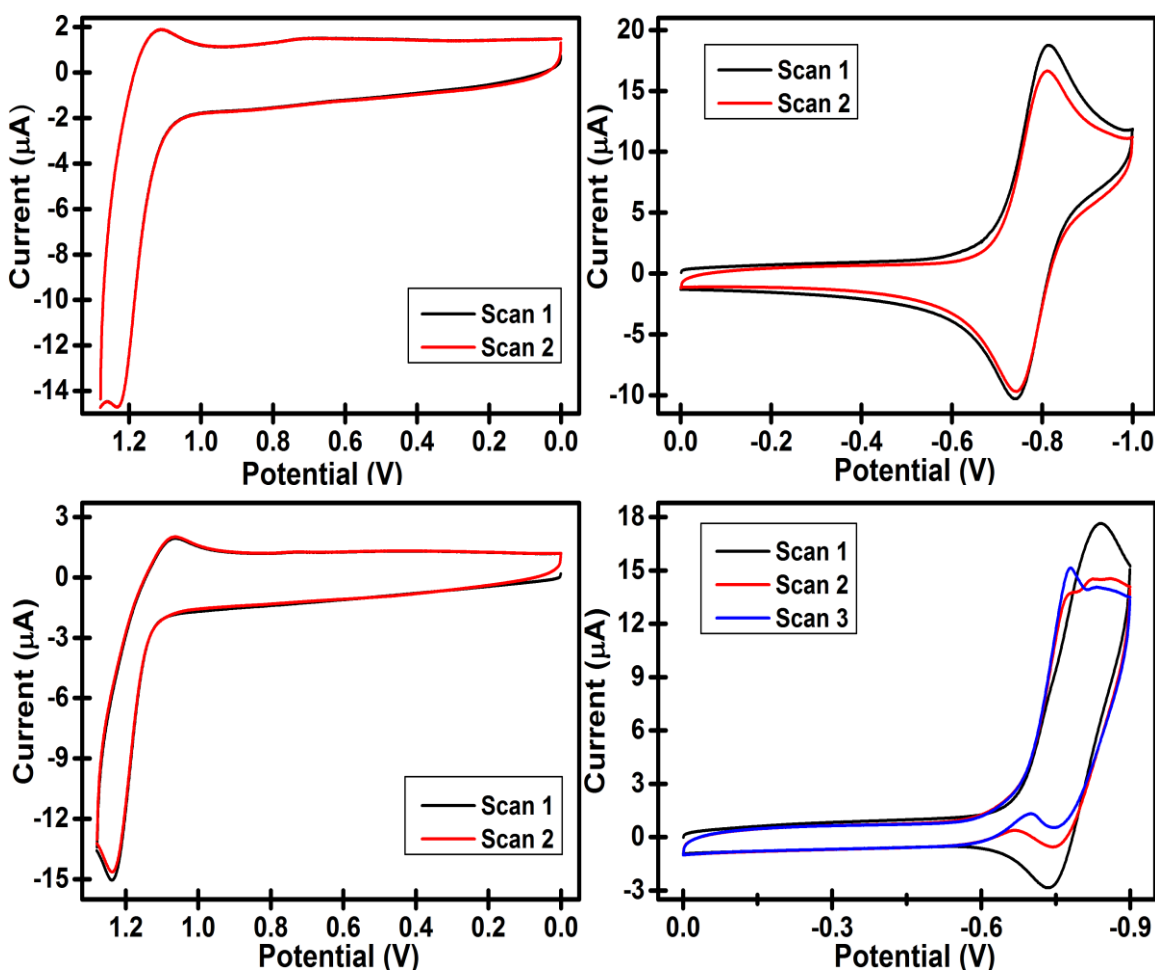
Figure 3.36 Cyclic voltammagrams of fac-[Re(dcebpy)(CO)$_3$3DMABN]$^+$ in (Top) CH_3CN and (Bottom) DCM. Anodic scans are shown on the left. Cathodic scans are shown on the right. The voltammagrams were collected in solutions containing 0.1 M [^{n}Bu$_4$N][PF$_6$]. All samples were deaerated with argon for 10 minutes prior to collection. The presented sweep segments were collected at a scan rate of 100 mV/s. Working electrode: glassy-carbon electrode. Counter electrode: Pt wire. Reference electrode: Aqueous Ag$^+$/AgCl

The oxidation potential of ReEBA, reflecting the oxidation of 3DMABN[40], is decreased by 130 mV in DCM upon changing the diimine ligand from bpy to dcebpy. The oxidation potential of the complex in CH_3CN is identical in ReEBA and Re3DMABN. The oxidation in both solvents is quasi-reversible, suggesting that the cation radical reacts irreversibly within a few seconds of being formed (sweep rates were 0.1 Vs^{-1}). The reductive voltammogram of ReEBA in CH_3CN is reversible, whereas the reductive voltammogram in DCM initially appears to be quasi-reversible but develops an irreversible reduction at -0.7 V with increasing scans. The reductive electrochemical behavior of ReEBA in DCM is likely due to precipitation of the complex onto the electrode surface upon reduction, affecting the observed chemistry of additional scans. The quasi-reversible nature of the initial voltammetric scan in DCM easily allows for the determination of E^0 (+/0) for the complex. As expected, the addition of the carboxyl ester substituents on the bpy ligand lower the first one electron reduction potential by 0.34 and 0.39 V in DCM and CH_3CN, respectively. The lowering of the first reduction potential of the complex also results in a decrease in the estimated energy of the charge separated state (ΔE_{CS}): ΔE_{CS} decreased from 2.34 V in Re3DMABN to 1.95 V in ReEBA in CH_3CN and decreased from 2.41 V in Re3DMABN to 1.94 V in ReEBA in DCM. This intended, dramatic reduction of ΔE_{CS} will likely make it impossible for the charge separated excited state to be influenced by the ^3IL state of the 3DMABN ligand.

Table 3.11 Redox potentials of ReEBA and Re3DMABN in DCM and CH_3CN vs. Ag/AgCl.

Complex	$E^0(2+/+)$ DCM	$E^0(2+/+)$ CH_3CN	$E^0(+/0)$ DCM	$E^0(+/0)$ CH_3CN	ΔE_{CS} DCM	ΔE_{CS} CH_3CN
Re3DMABN	1.28 V	1.17 V	-1.13 V	-1.17 V	2.41 V	2.34 V
ReEBA	1.15 V	1.17 V	-0.79 V	-0.78 V	1.94 V	1.95 V

3.5.2.4 Steady State Absorption, Luminescence, Nanosecond Transient Absorption

The UV-vis absorption spectra of ReEB and ReEBA in DCM and 1:1 (v:v) DCM:MeOH are shown in Figure 3.37. ReEB and ReEBA have two, localized absorption maxima at approximately 320 nm and 340 nm, which are assigned to dcebpy-localized π-π* transitions. These absorption bands have nearly identical structure and extinction coefficients as the bpy-localized π-π* transitions of the fac-[Re(bpy)(CO)$_3$L](BArF$_{24}$) complexes, while being red-shifted relative to those in the fac-[Re(bpy)(CO)$_3$L](BArF$_{24}$) complexes.
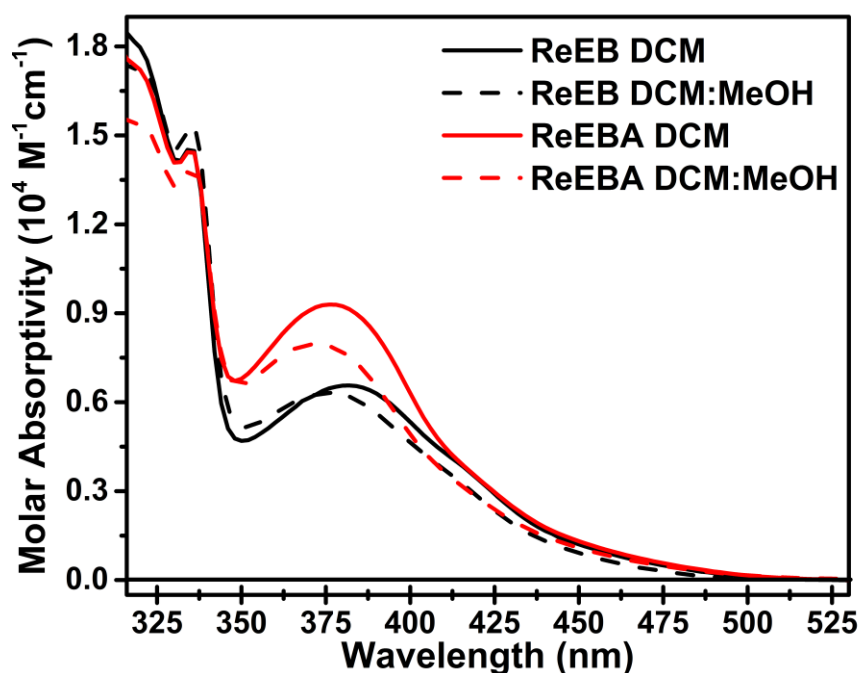
Figure 3.37 UV-Vis absorption spectra of fac-[Re(dcebpy)(CO)$_3$BN](BArF$_{24}$) and fac-[Re(dcebpy)(CO)$_3$3DMABN](BArF$_{24}$) in DCM and 1:1 (v:v) DCM:MeOH.

The decreased reduction potential of the dcebpy ligand leads to a stabilization of the LUMO (π*) and a subsequent decrease in the energy of the π-π* transition. The broad, low extinction efficient (< 9000 M^{-1}cm^{-1}) absorption bands centered at ~382 nm in ReEB and ~378 nm in ReEBA are assigned to $d\pi$ (Re) $\rightarrow$ π* (dcebpy) MLCT transitions.[36-38]

The stabilization of the LUMO in ReEB and ReEBA also has an effect on the energy of MLCT transition. The $d\pi$ (Re) $\rightarrow$ π^* (dcebpy) transitions are ~40 nm lower in energy (2300 cm^{-1}, 0.29 eV for a 400 nm – 440 nm shift) than $d\pi$ (Re) $\rightarrow$ π^* (bpy) MLCT transitions in fac-[Re(bpy)(CO)$_3$L](BArF$_{24}$) complexes. The MLCT transition in ReEBA appears to be broader and have an enhanced extinction coefficient relative to ReEB. These differences in the ReEBA absorption spectrum are the result of a broad, 3DMABN ligand localized absorption transition centered at 360 nm (this can be clearly seen in the absorption spectrum of Re3DMABN shown in Figure 3.15). An increase in solvent polarity only results in minor changes to the absorption spectra of the complexes: the molar absorptivity of the dcebpy-localized π-π^* and MLCT absorptions transitions are slightly decreased and the energy of the MLCT transitions is slightly increased in mixed DCM:MeOH.

An initial attempt to collect the luminescence spectrum of ReEBA in mixed DCM:MeOH yielded an interesting and unexpected result. A qualitative change in the UV-vis absorbance spectrum (Figure 3.38) was observed for the complex following the experiment. There is a slight decrease in absorbance at 375 nm (MLCT) and a slight increase in absorbance at 330 nm (dcebpy π-π^*). These changes are accompanied by the appearance of a isosbestic point at 400 nm. This net chemistry is likely the result of solvent (MeOH) substitution of the 3DMABN ligand. Solvent substitution reactions following visible light excitation of transition metal chromophores are well established in the literature.[53,54] Due to this undesirable chemistry in DCM:MeOH, all further photochemical experiments on ReEB and ReEBA will be carried out in 1:1 (v:v) mixtures of DCM and nitromethane (NM) or pure NM. NM has similar polarity to MeOH

but does not participate in solvent substitutions reactions with ReEBA. It should be noted that this reactivity is not observed in luminescence intensity measurements of Re3DMABN in mixed DCM:MeOH.
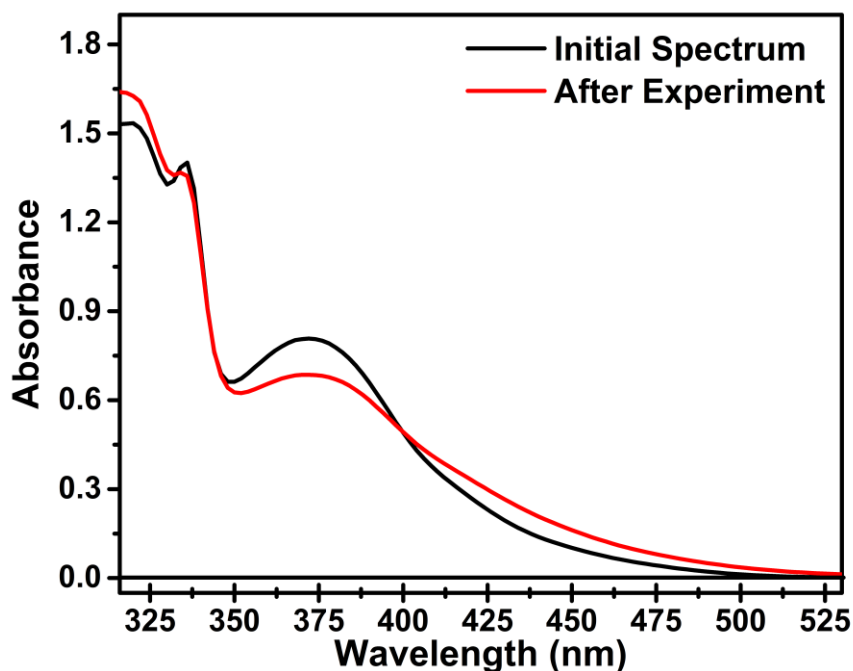
Figure 3.38 UV-Vis absorption spectrum of fac-[Re(dcebpy)(CO)$_3$BN](BArF$_{24}$) in 1:1 (v:v) DCM:MeOH before and after collecting luminescence data.

The luminescence spectra of ReEB and ReEBA in DCM and DCM:NM are shown in Figure 3.39. Luminescence quantum yield, lifetime and rate constant information is presented in Table 3.12 along with the luminescence data for Re3DMABN for comparison. Lifetime and rate constant data are not shown for ReEBA in DCM:NM because the decay of the excited state is faster than the resolution of our instrumentation (< 20 ns). Again, the strong, yellow luminescence from ReBN resulted from relaxation from the Re (dπ) $\rightarrow$ bpy (π*) ^{3}MLCT state back to the ground state.[22] The luminescence observed from ReEB in DCM is also quite strong with a luminescence quantum yield of 0.25, has a lifetime on the order of 1 μs, and a maximum at 568 nm, which is red-shifted

by 42 nm (1400 cm^{-1}, 0.170 mV) relative to ReBN. The band shape of this luminescence

is also similar to the band shape of the ReBN luminescence. The combination of the high

luminescence quantum yield, microsecond lifetime, similarity of band shape, and

decrease in luminescence energy relative to ReBN (dcebpy LUMO stabilized relative to

bpy LUMO) strongly suggests that the luminescence from ReEB is also from a ^{3}MLCT

(Re (dπ) $\rightarrow$ dcebpy (π*)) state.
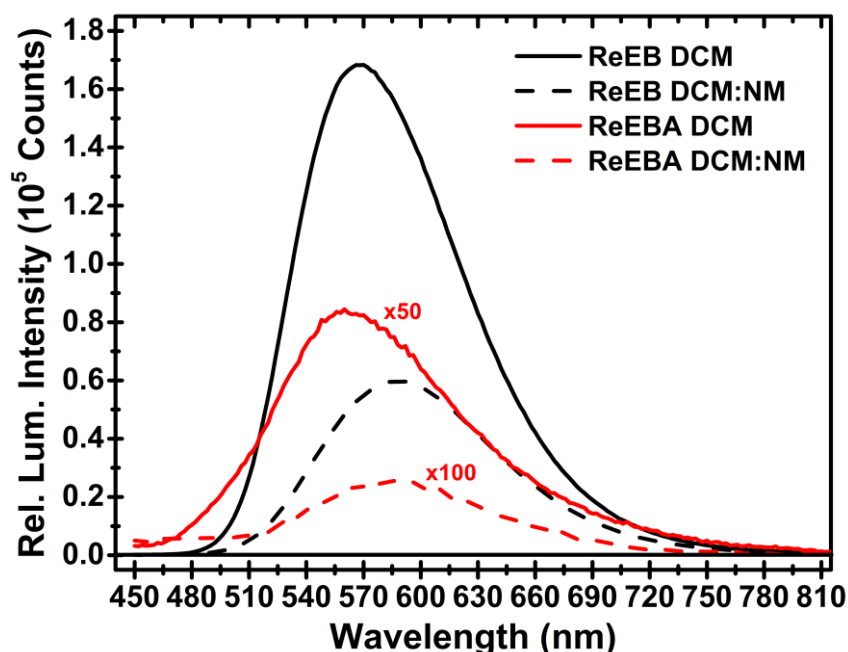
Figure 3.39 Luminescence spectra of fac-[Re(dcebpy)(CO)$_3$BN](BArF$_{24}$), fac-[Re(dcebpy)(CO)$_3$3DMBN](BArF$_{24}$), in (solid) DCM and (dashed) 1:1 (v:v) DCM:NM. The ReEBA luminescence spectra are magnified to demonstrate spectral feautres.

The luminescence of ReEBA in DCM is very interesting. The complex exhibits weak

luminescence (QY= 0.003) with a maximum at 562 nm. This luminescence maximum is

BLUE-shifted by 5 nm relative to the luminescence observed from ReEB. The

luminescence from ReEBA is also broader than the luminescence from ReEB. Lifetime

decays collected for ReEBA in DCM are biexponential. The decay of the excited state is

dominated by a relatively short (compared to ReEB), 40 ns component. As discussed in

Section 3.4.2.4, low quantum yield species are notoriously susceptible to impurity emission from a small amount of a contaminant with a high luminescence quantum yield; therefore, nanosecond transient absorption measurements are considered more reliable because the signal depends on the relative concentration (and absorptivity) of the species excited at a given wavelength. The nanosecond transient absorption spectrum of ReEBA in DCM (vida infra, Figure 3.41) is characterized by positive absorbance from 350 nm - 540 nm. The lifetime of this species is found to be 50 ± 10 ns at all wavelengths. It is clear that the signal is the result of the principally absorbing species due to the large change in absorbance (ΔOD) observed in the nanosecond transient absorption spectrum. This nanosecond transient absorption result implies that the 40 ns lifetime component of the ReEBA luminescence decay is a result of radiative decay from the ReEBA excited state. Consequently, this lifetime value can be used to determine the radiative and non-radiative decay rate constants for the excited state of the complex: the radiative decay constant is a factor of two smaller than the radiative decay rate constants for both ReBN and ReEB in DCM, and the non-radiative decay rate constant is more than an order of magnitude smaller than the non-radiative decay rate constants for ReBN and ReEB. The enhanced non-radiative decay rate constant could result from a highly polar or charge separated excited state, which imparts additional relaxation pathways to the ground state. This relatively short luminescence lifetime also indicates that the ^{3}IL state of the 3DMABN ligand does not influence the excited state of ReEBA

Both complexes exhibit weaker luminescence and have shorter excited-state lifetimes in mixed DCM:NM. The luminescence maximum of ReEB shifts to 586 nm and the quantum yield decreases by a factor of 3. The lifetime of ReEB decreases to 470 ns.

This modest decrease in luminescence quantum yield coupled with a corresponding decrease in the luminescence lifetime result in a radiative decay rate constant for the excited state on the order of 10^5 s^{-1} and a non-radiative decay rate constant for the excited state on the order of 10^6 s^{-1}. These data indicate that the luminescence from ReEB in DCM:NM is also originates from a ^{3}MLCT state. ReEBA experiences a similar red shift from 562 nm to 582 nm. The luminescence from ReEBA is incredibly weak and the lifetime (< 20 ns) of the complex is unresolvable using our instrumental setup. The lack of quantum yield and lifetime data for ReEBA in DCM:NM make a definitive discussion of the nature of the weakly luminescence excited state difficult; however, the absence of these data clearly imply the luminescence is not from a ^{3}MLCT state.

Table 3.12 Emission maxima, luminescence quantum yields, excited-state lifetimes, and radiative and non-radiative rate constants for fac-[Re(dcebpy)(CO)$_3$BN](BArF$_{24}$) and fac-[Re(dcebpy)(CO)$_3$3DMABN](BArF$_{24}$) in deaerated DCM and 1:1 (v:v) DCM:NM at room temperature. Luminescence data for fac-[Re(bpy)(CO)$_3$3DMABN](BArF$_{24}$) is included for comparison.

Complex	Re3DMABN		ReEB		ReEBA	
Solvent	DCM	DCM/MeOH	DCM	DCM/NM	DCM	DCM/NM
λ_{max}, nm	528	565	566	586	562	584
QY$_{lum.}$	0.003[d]	< 0.001[d]	0.26[d]	0.09[d]	0.003[c,d]	<<0.0001[d]
$\tau_{lum.}$, μs	31[a]	-	0.94 ± 0.02	0.47 ± 0.02	0.04 ± 0.005[c]	-
τ_{TA}, μs (λ, nm)[b]	23.3 ± 1.0 (450)	0.02 ± 0.005 (450)	0.91 ± 0.02 (350)	0.44 ± 0.02 (480)	0.05 ± 0.01 (480)	-
k_r, s^{-1}	130		2.8 x 10^5	2.0 x 10^5	6.0 x 10^4	-
k_{nr}, s^{-1}	5.0 x 10^4		8.1 x 10^5	2.0 x 10^6	2.0 x 10^7	-

[a] the mean value of two components is shown;
[b] the lifetime measured by nanosecond transient absorption at indicated wavelengths;
[c] A second emission component is observed with a lifetime of ~ 800 ns; this is believed to be due to an impurity Re complex;
[d] Quantum yield data determined using fac-[Re(bpy)(CO)$_3$ACN]$^+$ as the luminescent standard.[39]

The nanosecond time-resolved absorption spectra of ReEB in DCM and mixed DCM:NM and ReEBA in DCM are shown in Figures 3.40 and 3.41, respectively. As is the case for the luminescence lifetime of ReEBA, it is not possible to collect the nanosecond transient absorption spectrum of the complex in DCM:NM solution because the decay of the excited state is faster than the time resolution of our instrument. The lifetime data collected from these measurements are included in Table 3.12.
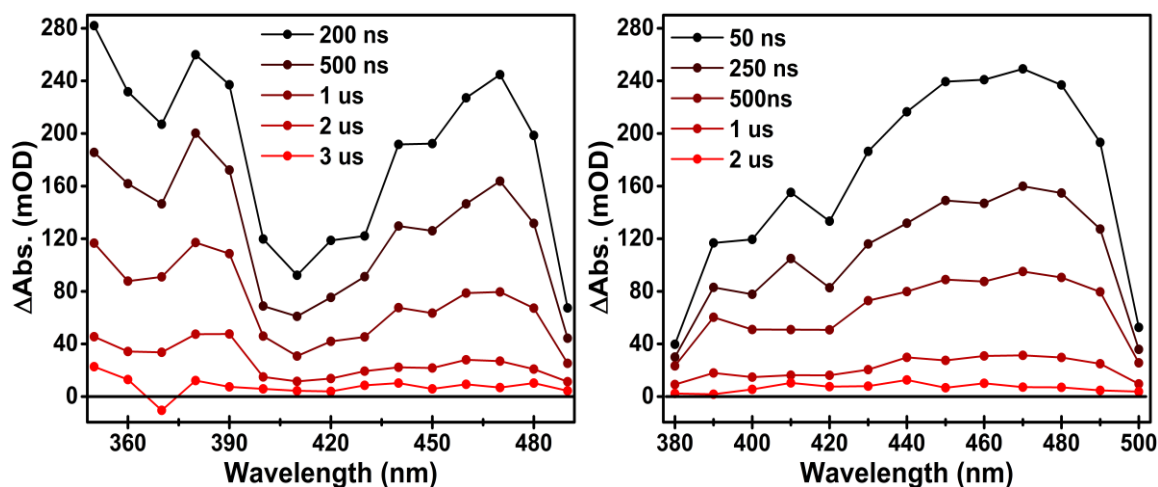
Figure 3.40 Nanosecond time-resolved transient absorption spectra of ReEB in (left) DCM and (right) DCM:NM.

Both complexes have excited state UV-Vis absorbance between 350 and 540 nm. The spectra of both complexes exhibit bleaching at longer wavelengths due to the luminescence of the complexes. The lifetime values obtained from luminescence and transient absorption measurements agree within error for both complexes, suggesting that the luminescence and excited state absorption occur from the same excited state. Once more (vide supra, the nanosecond transient absorption results for ReEBA are discussed on page 66), this result has particularly interesting consequences on the interpretation of the luminescence lifetime data acquired from ReEBA. It is clear that the observed nanosecond TA signal is the result of the principally absorbing species due to the large

change in absorbance (ΔOD). This strongly suggests that the dominant, 40 ns component of the luminescence lifetime decay is from the luminescent ReEBA excited state, allowing for the determination of the radiative and non-radiative decay rate constants for the excited state of the ReEBA. Interestingly, k_r is a factor of two smaller than the radiative decay rate constants for both ReBN and ReEB and k_{nr} is more than an order of magnitude smaller than the non-radiative decay rate constants for ReBN and ReEB. The differences in rate constant data indicate that the luminescence from ReEBA is NOT from a ^{3}MLCT state and that the ^{3}IL state of the 3DMABN ligand does not influence the excited state of ReEBA in DCM.
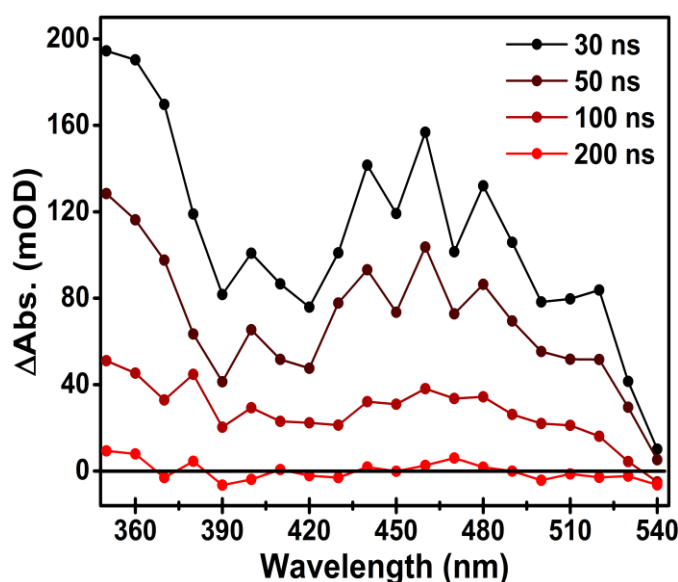
Figure 3.41 Nanosecond time-resolved transient absorption spectra of ReEBA in DCM

3.5.2.5 Infrared Absorption Spectra

Note: Again, the following sections discussing the steady state and transient infrared absorption characteristics of the ReEBA utilizes data, figures, and ideas that were mostly collected and developed by Professor Igor Rubtsov and his graduate student, Yuankai Yue. These data are crucial in understanding the excited state behavior of these

complexes and necessary for a complete discussion of the chemical reactivity of these systems. I have adapted discussions of the data from our manuscripts in an effort to summarize the general infrared absorption properties of these molecules, and applied this information to make definitive conclusions about the nature and evolution of each excited state. I must also acknowledge the work of Professor David Beratan, and his students, Zheng Ma and Peng Zhang. They provided advanced DFT computational support to both manuscripts. I have excluded these computational details and results from this dissertation.

The ground state infrared absorption spectra of the ReEBA in DCM and NM are shown in Figure 3.42.
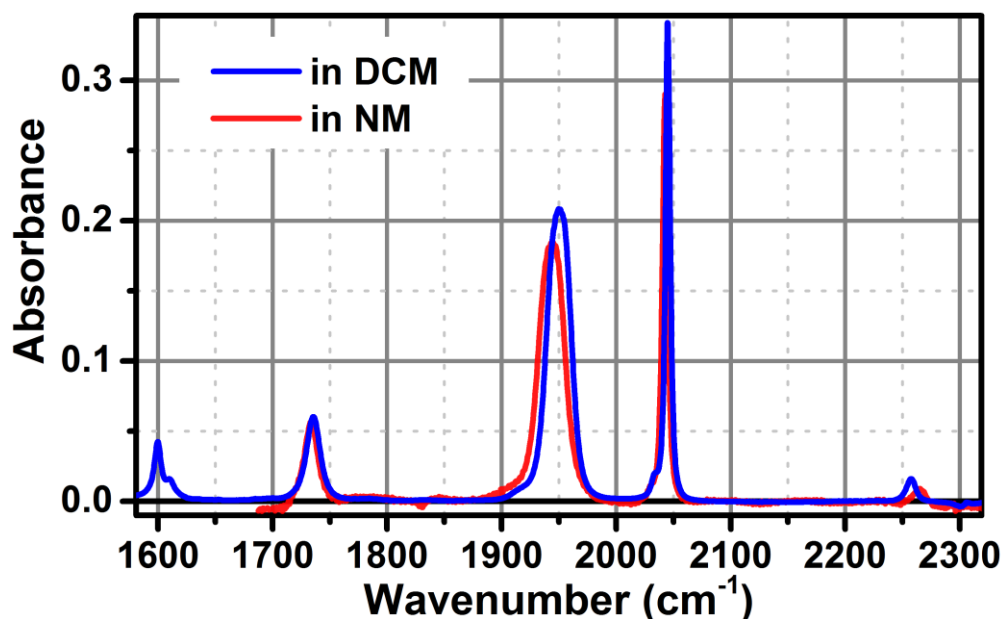
Figure 3.42 Ground state FTIR absorption spectra of ReEBA in DCM and NM .

The IR spectra of ReEBA are similar to the ground state IR spectra of all three fac-$[Re(bpy)(CO)_3L](BArF_{24})$ complexes, making the assignment of the characteristic absorption bands straight-forward. These assignments are complemented with results from DFT calculations (Gaussian '09.[41] LANL2DZ with ECP for Re, 6-31G** for all

other atoms). Table 3.13 contains DFT and experimental peak maxima data as well as the assigned vibrational modes. The strong absorption peaks at 2043 cm^{-1} and 1946 cm^{-1} belong to the symmetric and two overlapping asymmetric stretching modes of the three facial carbonyl ligands, respectively. The weak peak at 2260 cm^{-1} is the C≡N stretching mode of the 3DMABN ligand. The overlapping bands at 1610 cm^{-1} and 1600 cm^{-1} involve phenyl ring stretches on the dcebpy and 3DMABN ligands: the 1610 cm^{-1} band represents the ring stretching modes of the dcebpy, ν_{ss}(dcebpy), and the 1600 cm^{-1} band signifies the phenyl ring stretch of 3DMABN, ν_{ss}(ph). The IR absorption peak at 1735 cm^{-1} is unique to the spectra of ReEBA and belongs to the C=O stretching modes of the ester groups on the dcebpy ligand. The ground state IR spectra of ReEBA in DCM and absorption around 1600 cm^{-1}. NM are practically identical for all the modes of above 1700 cm^{-1}. ν_{ss}(dcebpy) and ν_{ss}(ph) are excluded from the NM spectrum because they overlap with a strong solvent.

Table 3.13 Experimental and DFT ground-state vibrational frequencies (in cm^{-1}) of several characteristic modes for ReEBA in both DCM and NM.

ReEBA in DCM		ReEBA in NM		Assignment
Exper..	DFT, GS	Exper.	DFT, GS	
2258	2341	2266	2343	ν(C≡N)
2046	2106	2043	2104	ν_{ss}(C≡O)
1949	2009 / 2003	1945	2007 / 2000	ν_{as}(CO) $\{$ as$_1$ / as$_2$
1735	1789	1734	1786	ν_{ss}(C=O)
1735	1788	1734	1786	ν_{as}(C=O)
1610	1612/1604	N/A	1613/1605	ν_{ss}(bpy)
1600	1646	N/A	1646	ν_{ss}(Ph)

3.5.2.6 Transient Infrared Spectroscopy

The transient time-resolved infrared absorption spectra (TRIR) were measured from 1600 cm^{-1} to 2300 cm^{-1} to cover the spectral region of the C≡N (2120 cm^{-1} to 2300

cm^{-1}), C≡O (1800 cm^{-1} to 2120 cm^{-1}), C=O (1640 cm^{-1} to 1800 cm^{-1}) and ring (1480 cm^{-1} to 1620 cm^{-1}) ring vibration modes. Each vibrational mode indicated above is localized on a specific ligand of the complex and therefore reports on changes in electron density at the respective moiety.

ReEBA in DCM: Instantaneous formation of a ^{3}MLCT excited state followed by formation of LLCT excited state

The TRIR spectrum of ReEBA in DCM is shown in Figure 3.43. All of the infrared absorption modes of ReEBA change upon 402 nm excitation. The initial spectral changes are essentially instantaneous, occurring within the 200 fs time resolution of the instrument. The ν(C≡N) peak decreases by 15 cm^{-1} and its intensity increases by ~ a factor of 5 in the excited state. The shift and intensity changes are similar to those observed for early time TRIR data for Re3DMABN and Re4DMABN.
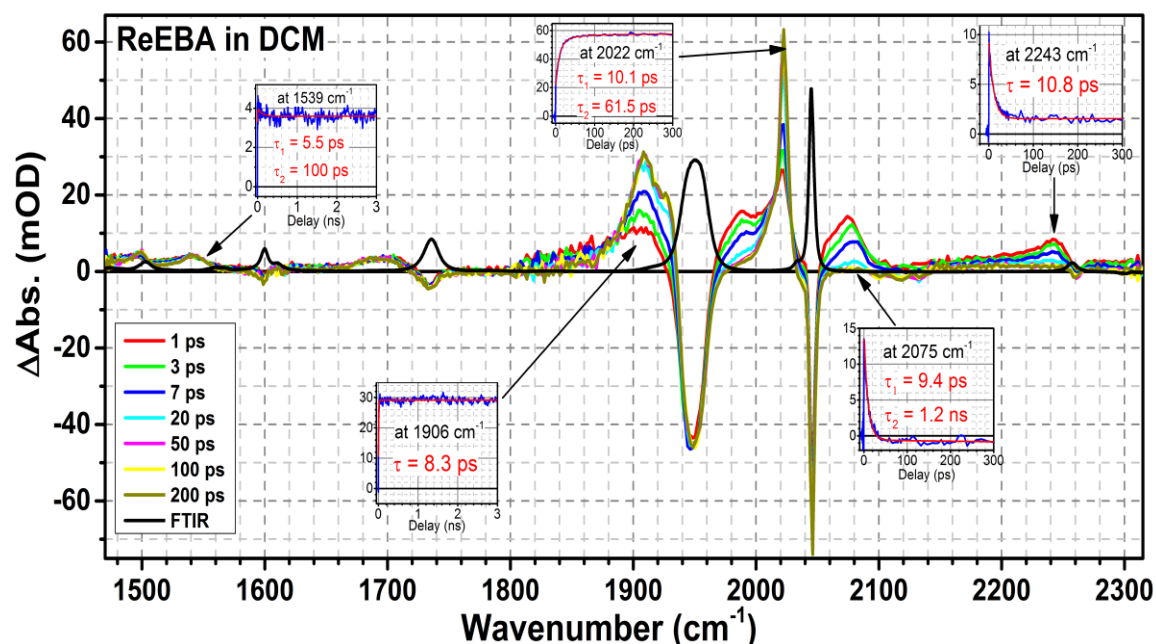
Figure 3.43 Transient infrared spectrum of ReEBA in DCM following 402 nm excitation. Insets show kinetics measured at indicated frequencies and their fits to a single or biexponential function.

The C≡O stretching modes experience a dramatic increase in frequency upon excitation. The frequency upshift values of 74 (as1), 42 (as2), and 28 cm^{-1} (ss), are slightly larger than those for Re3DMABN in DCM at short times following the laser pulse. This indicates that the initially formed state features more positive charge on Re in ReEBA. The two ν_{as}(C≡O) modes that overlap in the ground state are resolved in the excited state, indicating a decreased symmetry among the three carbonyl ligands. The C=O modes of the ester groups absorb at 1694 cm^{-1}, which is ca. 39 cm^{-1} lower than their ground state frequency. The ν(C=O) peak in the excited state is much broader and experiences a slight decrease in IR frequency relative to the ground state. The ν_{ss}(dcebpy) ring stretching mode also experiences a notable downshift if the excited state, appearing as a broad peak at 1540 cm^{-1}. This is also consistent with an increase in electron density on the dcebpy ligand in the excited state. All of these instantaneously observed changes in the excited state are consistent with the rapid formation of a MLCT excited state.

The transient IR spectra of ReEBA experience drastic changes with a characteristic time of 10 ps. None of these changes result in the recovery of the ground state features, indicating the formation of a new excited state. The state formed with a 10 ps time constant is assigned as an LLCT excited state. The ν(C≡N) mode is instrumental in assigning the LLCT state. ν(C≡N) shifts to lower frequencies by 120 cm^{-1} in the ^{3}IL state of 3DMABN that is accessed in Re3DMABN. In the TRIR spectra of ReEBA, the large frequency shift of ν(C≡N) is not observed and is relatively unaffected by the evolution from the MLCT excited state. The C≡O peaks at 1990 and 2070 cm^{-1} decay to the baseline signifying a complete depletion of the MLCT state. Concomitant with the decay of the 1990 and 2070 cm^{-1}, the C≡O peaks at ca. 1908, 1926 and 2022 cm^{-1}

increase in intensity. These C≡O frequencies are lower than those in the ground state by 39, 21 and 24 cm^{-1}, respectively. The cumulative shift of all three ν(C≡O) modes to lower frequency represent the accumulation of negative charge at the Re center. The C=O absorption peak at 1695 cm^{-1} and the broad, ν_{ss}(dcebpy) at 1540 cm^{-1} both experience peak narrowing and a slight amplitude increase of less than 10%. The formation of the initial MLCT excited state involves large charge redistribution to the dcebpy ligand but the subsequent evolution to the second state only involves an incremental increase in electron density on the ligand. There is a 5.5 ps component that is only reflected in the growth of the 1540 cm^{-1} (ν_{ss}(dcebpy)). This kinetic feature is likely associated with solvation and vibration cooling in DCM.[11,43-45] The 1540 cm^{-1} and 2022 cm^{-1} vibrational modes demonstrate a small 100 ps component. The assignment of this kinetic element is difficult because it is too long to involve solvation and vibrational cooling. A kinetic component on the order of 10's of ps is also observed in the TRIR of Re4DMABN and Re3DMABN in DCM:MeOH. One possibility is that this component reflects slight structural rearrangements in each excited state. The features observed after the early time evolution remain in the final, 3 ns TRIR spectrum collected for ReEBA. This signifies a continuity of the TRIR data and the nanosecond time-resolve transient absorption data. In this regard, the observed TA spectrum of ReEBA in DCM reflects absorption of the LLCT excited state and solidifies the assignment of the short luminescence decay component of the complex in DCM as LLCT state emission.

ReEBA in NM: Instantaneous formation of a ^{3}MLCT excited state followed by formation of LLCT excited state

The TRIR spectra of ReEBA measured in NM are shown in Figure 3.44. Due to solvent absorption, no spectra were recorded below 1650 cm^{-1} in NM. Although the spectral evolution and the features of ReEBA in NM are similar to those in DCM, there are several differences noteworthy differences between the spectra. First, the lifetime of the LLCT state in NM (2.4 ns) is much shorter than that in DCM (43 ns). The NM lifetime value is estimated from the decay of the TRIR spectra. This short decay is highlighted in the decay trace at 1907 cm^{-1} shown in Figure 3.44.
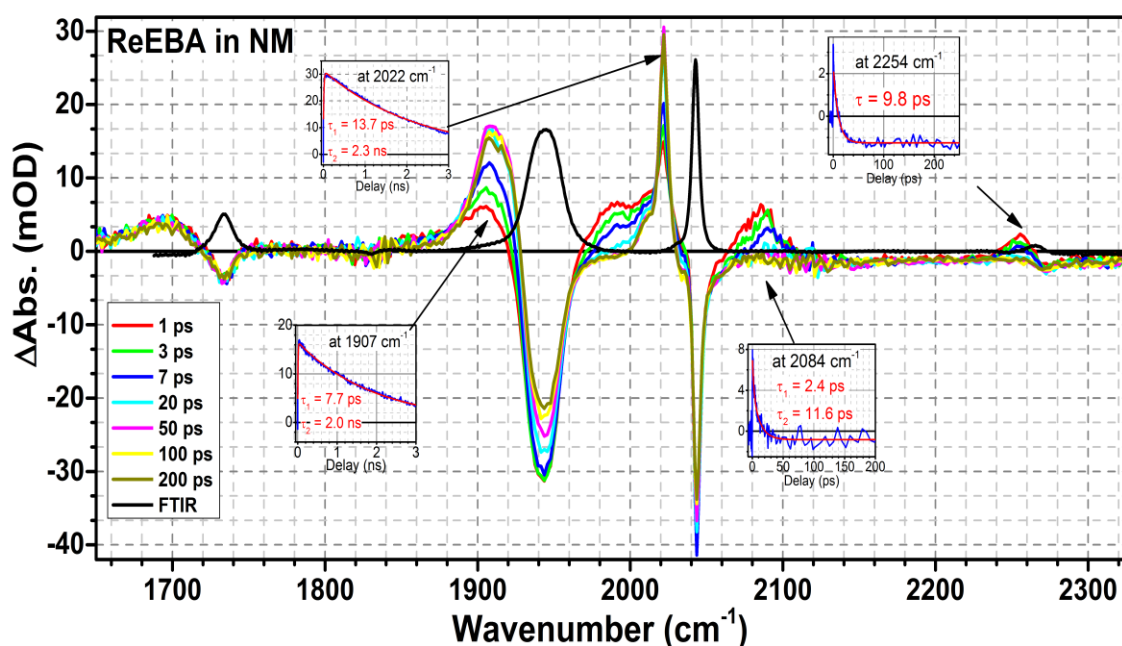
Figure 3.44 Transient infrared spectrum of ReEBA in NM following 402 nm excitation. Insets show kinetics measured at indicated frequencies and their fits to a single or biexponential function.

The three C≡O peaks in the MLCT state experience larger frequency increases in NM. The C≡O absorption modes in Re3DMABN and Re4DMABN also experience a more dramatic frequency shift in DCM:MeOH. Additionally, there is also an absence of the

additional rise of C=O absorption mode at 1690 cm^{-1} following initial MLCT state formation. These observations point to a larger positive charge on Re in the MLCT state and a larger negative charge on dcebpy in initial MLCT state formation in NM.

3.5.2.7 Conclusions

The excited-state dynamics of ReEBA and ReEB were studied in DCM and NM solvents using time-resolved infrared and electronic spectroscopy and DFT analysis. The lowest energy excited state of ReEBA was assigned to a full-electron (3DMABN $\rightarrow$ dcebpy) LLCT state using the following observations (1) The luminescence quantum yield of ReEBA is two orders of magnitude smaller than that in ReEB, indicating that the MLCT state luminescence is quenched by formation of the LLCT state. The lifetime of the lowest energy excited state of ReEBA decreases dramatically with an increase in solvent polarity, which is indicative of forming a strongly-polarized state. (2) Characteristic changes in the vibrational frequencies of the excited state, including a large frequency decrease of the C≡O modes (more electron density at Re), the absence of the ^{3}IL state C≡N peak at 2130 cm^{-1}, and frequency decreases in the ν(C=O) and ν(dcebpy) modes, agree well with the formation of the LLCT state. The observation of a LLCT state in this system was accomplished by tuning the redox properties of the electron accepting ligand (dcebpy) and decoupling the redox active group of the electron donating ligand 3DMABN from the metal. Both of these chemical modification were suggested by the results from our study of the fac-[Re(bpy)(CO)$_3$L](BArF$_{24}$) chromophores.

CHAPTER 3 REFERENCES

(1) Barbara, P. F.; Jarzeba, W. *Adv. Photochem.* **1990***, 15*, 1.

(2) Beratan, D. N.; Skourtis, S. S.; Balabin, I. A.; Balaeff, A.; Keinan, S.; Venkatramani, R.; Xiao, D. *Acc. Chem. Res.* **2009***, 42*, 1669.

(3) Gust, D.; Moore, T. A. In *Intramolecular Photoinduced Electron-Transfer Reactions of Porphyrins;* 2000.

(4) Meyer, T. J. *Pure Appl. Chem.* **1990***, 62*, 1003.

(5) Rettig, W. *Top. Curr. Chem.* **1994***, 169*, 253.

(6) Skourtis, S. S.; Waldeck, D. H.; Beratan, D. N. *Annu. Rev. Phys. Chem.* **2010***, 61*, 461.

(7) Verhoeven, J. W. *J. Photochem. Photobiol., C* **2006***, 7*, 40.

(8) Endicott, J. F.; Watzky, M. A.; Song, X.; Buranda, T. *Coord. Chem. Rev.* **1997***, 159*, 295.

(9) Macqueen, D. B.; Perkins, T. A.; Schmehl, R. H.; Schanze, K. S. *Mol. Cryst. Liq. Cryst.* **1991***, 194*, 113.

(10) Kleverlaan, C. J.; Stufkens, D. J.; Clark, I. P.; George, M. W.; Turner, J. J.; Martino, D. M.; van Willigen, H.; VlÄ•ek, A. *J. Am. Chem. Soc.* **1998***, 120*, 10871.

(11) Liard, D. J.; Busby, M.; Matousek, P.; Towrie, M.; Vlcek, A. *J. Phys. Chem. A* **2004***, 108*, 2363.

(12) Dattelbaum, D. M.; Omberg, K. M.; Hay, P. J.; Gebhart, N. L.; Martin, R. L.; Schoonover, J. R.; Meyer, T. J. *J. Phys. Chem. A* **2004***, 108*, 3527.

(13) Blanco-Rodriguez, A.; Towrie, M.; Sykora, J.; Zalis, S.; Vlcek, A. *Inorg. Chem.* **2011***, 50*, 6122.

(14) Bernhard, S.; Omberg, K. M.; Strouse, G. F.; Schoonover, J. R. *Inorg. Chem.* **2000***, 39*, 3107.

(15) Bredenbeck, J.; Helbing, J.; Hamm, P. *J. Am. Chem. Soc.* **2004***, 126*, 990.

(16) Busby, M.; Gabrielsson, A.; Matousek, P.; Towrie, M.; Di Bilio, A. J.; Gray, H. B.; Vlcek, A. *Inorg. Chem.* **2004***, 43*, 4994.

(17) Cannizzo, A.; Blanco-Rodriguez, A.; El Nahhas, A.; Sebera, J.; Zalis, S.; Vlcek, A.; Chergui, M. *J. Am. Chem. Soc.* **2008***, 130*, 8967.

(18) El Nahhas, A.; Consani, C.; Blanco-Rodriguez, A.; Lancaster, K. M.; Braem, O.; Cannizzo, A.; Towrie, M.; Clark, I. P.; Zalis, S.; Chergui, M.; Vlcek, A. *Inorg. Chem.* **2011***, 50*, 2932.

(19) Koutras, A.; Skea, J. E. F.; Stufkens, D. J.; Vlcek, A. *Coord. Chem. Rev.* **1998***, 177*, 127.

(20) Gabrielsson, A.; Busby, M.; Matousek, P.; Towrie, M.; Hevia, E.; Cuesta, L.; Perez, J.; Zalis, S.; Vlcek, A. *Inorg. Chem.* **2006***, 45*, 9789.

(21) Liard, D. J.; Vlcek, A. *Inorg. Chem.* **2000***, 39*, 485.

(22) Perkins, T. A.; Humer, W.; Netzel, T. L.; Schanze, K. S. *J. Phys. Chem.* **1990***, 94*, 2229.

(23) Vlcek, A.; Busby, M. *Coord. Chem. Rev.* **2006***, 250*, 1755.

(24) Vlcek, A. *Top. Organomet. Chem.* **2010***, 29*, 73.

(25) Patiny, L.; Borel, A. ChemCalc: A Building Block for Tomorrow's Chemical Infrastructure. *J. Chem. Inf. Model.* **2013***, 53*, 1223-1228.

(26) Lin, Z.; Lawrence, C. M.; Xiao, D.; Kireev, V. V.; Skourtis, S. S.; Sessler, J. L.; Beratan, D. N.; Rubtsov, I. V. *J. Am. Chem. Soc.* **2009***, 131*, 18060.

(27) Yakelis, N. A.; Bergman, R. G. *Organometallics* **2005***, 24*, 3579-3581.

(28) Gribble, G. W.; Nutaitis, C. F. *Synthesis* **1987***, 1987*, 709.

(29) Smieja, J. M.; Kubiak, C. P. *Inorg. Chem.* **2010***, 49*, 9283-9289.

(30) Hevia, E.; Perez, J.; Riera, V.; Miguel, D.; Kassel, S.; Rheingold, A. *Inorg. Chem.* **2002***, 41*, 4673-4679.

(31) Kaufmann, R.; Chaurand, P.; Kirsch, D.; Spengler, B. *Rapid Comm. Mass Spectrom.* **1996***, 10*, 1199-1208.

(32) Spengler, B. *J. Mass Spectrom.* **1997***, 32*, 1019-1036.

(33) Spengler, B.; Kirsch, D.; Kaufmann, R.; Cotter, R. J. *Rapid Comm. Mass Spectrom.* **1991***, 5*, 198-202.

(34) Li, Y.; Hoskins, J. N.; Sreerama, S. G.; Grayson, S. M. *Macromolecules* **2010**, *43*, 6225-6228.

(35) Jameson, G. B.; Sheikh-Ali, B. M.; Weiss, R. G. *Acta Crystallogr., Sect. B: Struct. Sci.* **1994**, *50*, 703.

(36) Striplin, D. R.; Crosby, G. A. *Coord. Chem. Rev.* **2001**, *211*, 163.

(37) Fraser, M. G.; Clark, C. A.; Horvath, R.; Lind, S. J.; Blackman, A. G.; Sun, X. -.; George, M. W.; Gordon, K. C. *Inorg. Chem.* **2011**, *50*, 6093.

(38) Worl, L. A.; Duesing, R.; Chen, P.; Della Ciana, L.; Meyer, T. J. *J. Chem. Soc., Dalton Trans.* **1991**, 849.

(39) Caspar, J. V.; Meyer, T. J. Application of the Energy Gap Law to Nonradiative, Excited-State Decay. *J. Phys. Chem.* **1983**, *87*, 952-7.

(40) Il'ichev, Y. V.; Kuhnle, W.; Zachariasse, K. A. *J. Phys. Chem. A* **1998**, *102*, 5670.

(41) Gaussian 09, Revision D.01, M. J. Frisch, G. W. Trucks, H. B. Schlegel, G. E. Scuseria, M. A. Robb, J. R. Cheeseman, G. Scalmani, V. Barone, B. Mennucci, G. A. Petersson, H. Nakatsuji, M. Caricato, X. Li, H. P. Hratchian, A. F. Izmaylov, J. Bloino, G. Zheng, J. L. Sonnenberg, M. Hada, M. Ehara, K. Toyota, R. Fukuda, J. Hasegawa, M. Ishida, T. Nakajima, Y. Honda, O. Kitao, H. Nakai, T. Vreven, J. A. Montgomery Jr., J. E. Peralta, F. Ogliaro, M. J. Bearpark, J. Heyd, E. N. Brothers, K. N. Kudin, V. N. Staroverov, R. Kobayashi, J. Normand, K. Raghavachari, A. P. Rendell, J. C. Burant, S. S. Iyengar, J. Tomasi, M. Cossi, N. Rega, N. J. Millam, M. Klene, J. E. Knox, J. B. Cross, V. Bakken, C. Adamo, J. Jaramillo, R. Gomperts, R. E. Stratmann, O. Yazyev, A. J. Austin, R. Cammi, C. Pomelli, J. W. Ochterski, R. L. Martin, K. Morokuma, V. G. Zakrzewski, G. A. Voth, P. Salvador, J. J. Dannenberg, S. Dapprich, A. D. Daniels, Ö. Farkas, J. B. Foresman, J. V. Ortiz, J. Cioslowski and D. J. Fox, Gaussian, Inc., Wallingford CT, 2009.

(42) Blanco-Rodriguez, A.; Gabrielsson, A.; Motevalli, M.; Matousek, P.; Towrie, M.; Sebera, J.; Zalis, S.; Vlcek, A. *J. Phys. Chem. A* **2005**, *109*, 5016.

(43) Hamm, P.; Ohline, S.; Zurek, M.; Roschinger, T. *Laser Chem.* **1999**, *19*, 45.

(44) Hamm, P.; Ohline, S. M.; Zinth, W. *J. Chem. Phys.* **1997**, *106*, 519.

(45) Horng, M. L.; Gardecki, J. A.; Papazyan, A.; Maroncelli, M. *J. Phys. Chem.* **1995**, *99*, 17311.

(46) Kasyanenko, V. M.; Lin, Z.; Rubtsov, G. I.; Donahue, J. P.; Rubtsov, I. V. *J. Chem. Phys.* **2009**, *131*, 154508/1.

(47) Lin, Z.; Keiffer, P.; Rubtsov, I. V. *J. Phys. Chem. B* **2011***, 115*, 5347.

(48) Rubtsov, I. V.; Fayer, M. In *Ultrafast Infrared Vibrational Spectroscopy;* 2013; pp 333.

(49) Ma, C.; Kwok, W. M.; Matousek, P.; Parker, A. W.; Phillips, D.; Toner, W. T.; Towrie, M. *J. Phys. Chem. A* **2001***, 105*, 4648.

(50) Juris, A.; Balzani, V.; Barigelletti, F.; Campagna, S.; Belser, P.; von Zelewsky, A. *Coord. Chem. Rev.* **1988***, 84*, 85.

(51) Hoertz, P. G.; Staniszewski, A.; Marton, A.; Higgins, G. T.; Incarvito, C. D.; Rheingold, A. L.; Meyer, G. J. Toward Exceeding the Shockley Queisser Limit: Photoinduced Interfacial Charge Transfer Processes that Store Energy in Excess of the Equilibrated Excited State. *J. Am. Chem. Soc.* **2006***, 128*, 8234-8245.

(52) Maerker, G.; Case, F. H. The Synthesis of some 4,4'-Disubstituted 2,2'-Bipyridines1. *J. Am. Chem. Soc.* **1958***, 80*, 2745-2748.

(53) Adamson, A. W.; Fleischauer, P. D., Eds.; In *Concepts of Inorganic Photochemistry;* John Wiley and Sons: New York, 1975.

(54) Balzani, V.; Carassiti, V. In *Photochemistry of Coordination Compounds;* Academic: New York, 1970.

CHAPTER 4: pH Control of Intramolecular Energy Transfer and Oxygen

Quenching in Ru(II) Complexes Having Coupled Electronic Excited States

Reproduced in part with permission from Grusenmeyer, T. A., Chen, J., Jin, Y., Nguyen, J., Rack, J.J., Schmehl, R.H. *J. Am. Chem. Soc.* **134** (17), 7497-7506. Copyright 2012 American Chemical Society. DOI: 10.1021/ja300866s.

4.1 Intramolecular Energy Transfer in Metal Complexes with Coupled Electronic

Excited States

The dissipation of excitation energy can be quite complex in electronically excited chemical systems that contain two or more independent (or weakly coupled) chromophores with excitation energies separated by relatively small energy gaps.[1-3] The excitation energy can be shuttled between the independent chromophores while the system as a whole relaxes to the ground state.[4] If one of the chromophoric units is photoreactive, additional relaxation paths are introduced. Recently there have been numerous reports of the photophysical behavior of metal diimine complexes, mostly complexes of Ru(II), covalently linked to aromatic hydrocarbons.[5-14]
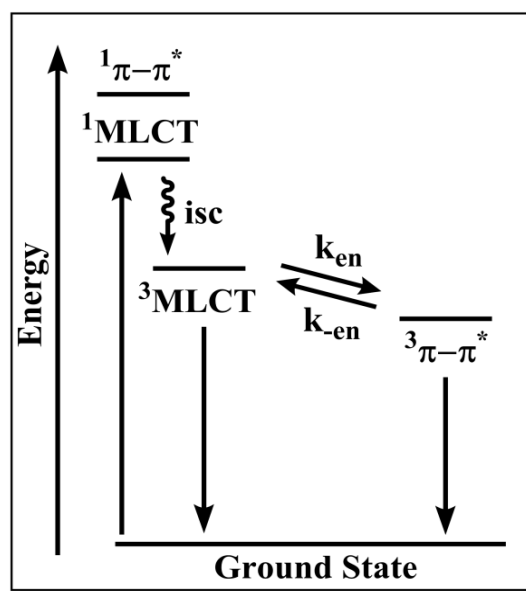
Figure 4.1. Generalized state diagram for complexes having nearly isoenergetic MLCT and IL excited states.

Metal-to-ligand charge transfer (MLCT) excitation results in population of the triplet excited state manifold within a few hundred femtoseconds[15] with full thermal equilibration to the zeroth vibrational level on the picosecond timescale.[16,17] The triplet MLCT state formed initially can, depending on the energy gap and nature of the covalent linkage, transfer energy reversibly to a pendant aromatic hydrocarbon chromophore (^{3}IL). A generalized state diagram for systems of this type is shown in Figure 4.1. There has been considerable attention given to this topic because of the reversible energy transfer between the ^{3}MLCT state and the ^{3}IL state of pyrene, which has been summarized in reviews.[12,18] For many of these systems, the ^{3}MLCT state is luminescent, and the luminescence lifetime of the complex is increased as a result of reversible energy transfer between the ^{3}MLCT state and the long lived ^{3}IL state of pyrene.[5,19,20] In addition, luminescence generally exhibits greater sensitivity to oxygen quenching which is directly related to the longer lived covalently linked aromatic hydrocarbon triplet state.[21] Recently, such covalently linked bichromophoric molecules have been used as sensitive phosphorescent indicators of dissolved oxygen in hypoxic environments.[21] The key to observing reversible energy transfer in these systems is maintaining a small ($< 1000 \text{ cm}^{-1}$; < 3 kcal) energy gap between the participating excited states, although details of the free energy dependence of the reversible energy transfer and the overall relaxation are lacking.

4.2 The Use of Solution pH to Control Intramolecular Energy Transfer in Metal Complexes with Coupled Electronic Excited States

In the late 1970s, Wrighton and coworkers reported the photophysical behavior of Ru(II) complexes having two 2,2'-bipyridine (bpy) ligands and a single 4,4'-dicarboxy-

2,2'-bipyridine (dcbH$_2$) ligand.[22] In aqueous solution the luminescence energy of the complex decreases upon lowering of the pH of the solution and protonation of the carboxyl groups of the substituted bipyridine. The authors also demonstrated that the average pKa of the carboxyl ligands is greater when the complex is in the ^{3}MLCT state, consistent with an increase in electron density on the carboxy-bipyridine ligand in the excited state. More recently, Nazeeruddin et al. thoroughly examined the ground and excited state acid dissociation processes of [(dcbH$_2$)$_2$Ru(bpy)]Cl$_2$ in solutions of sulfuric acid and sodium hyrdoxide.[23] While there are four dissociable protons in the complex, only two experimentally distinct pK values were determined, indicating that the first deprotonation from each bpy occurs at or near the same pH. Moreover, the authors demonstrated that, just as with [(dcbH$_2$)$_2$Ru(bpy)]Cl$_2$, the luminescence maximum was dependent on pH over the pH range 0 to 7. For both complexes, the excited state has an energy of ~16100 cm^{-1}(620 nm, 2.00 eV) at solution pH values above 7 and an energy of ~15200 cm^{-1} (655 nm, 1.88 eV) at solution pH values at or below 1. These data clearly show that the lowest energy ^{3}MLCT excited state in ruthenium compounds containing 4,4'-dicarboxy-2,2'-bipyridine can be varied with pH. Previous reports have also shown that the lowest energy ^{3}MLCT excited state for the complex [(bpy)$_2$Ru(pyr-bpy)]Cl$_2$, where pyr-bpy is 4-(1-pyrenyl)-2,2'-bipyridine, establishes an exited state equilibrium with the ^{3}IL state located on the pyrene, resulting in a lengthening of the excited state lifetime from for [Ru(bpy)$_3$]Cl$_2$ to 30 μs for [(bpy)$_2$Ru(pyr-bpy)]Cl$_2$.[5-14] The energy of the ^{3}IL state was estimated to be 630 nm (15900 cm^{-1}, 1.97 eV) from the luminescence spectrum of [(bpy)$_2$Ru(pyr-bpy)]Cl$_2$, which falls between the excited state energies of [(dcbH$_2$)$_2$Ru(bpy)]$^{2+}$ and [(dcb)$_2$Ru(bpy)]$^{2-}$. These results suggest that for the

chromophore $[(dcbH_2)_2Ru(pyr\text{-}bpy)]Cl_2$ excitation of the complex at pH 1 will result in the population of a ^3MLCT state located on the protonated $dcbH_2$ ligand, whereas excitation of the complex at pH values higher than 7 will result in initial population of a ^3MLCT located on the deprotonated dcb ligand that can thermally equilibrate with the ^3IL state of pyr-bpy.

This chapter will demonstrate the pH dependence of the luminescence lifetime of $[(dcbH_2)_2Ru(pyr\text{-}bpy)]^{2+}$ and $[(dcbH_2)_2Ru(pyr\text{-}phen\text{-}bpy)]^{2+}$ (pyr-phen-bpy is 4-(p-(1-pyreneyl)phenyl)-2,2'-bipyridine). At pH 0, when the ^3MLCT is favored, the lifetime of the pyr-bpy complex is 1.8 μs and the lifetime of the pyr-phen-bpy is found to be 1 μs. The lifetime of both chromophores is lengthened at pH 8 upon increasing the energy of the ^3MLCT state. The lifetime of the pyr-bpy complex increases to 15 μs and the lifetime of the pyr-phen-bpy complex increases to 5 μs. Analysis of ultrafast and nanosecond time-resolved transient absorption spectra of the complexes result in a description of the excited state that involves initial equilibration of the ^3MLCT and ^3IL states followed by relaxation to the ground state. Fitting of the nanosecond time-resolved decays allows for the calculation of the equilibrium constant and Gibbs free energy for the $^3MLCT - {}^3IL$ state equilibrium of each chromophore at pH 0 and pH 8. The determination of the value of ΔG for each equilibrium process allows for the estimation of the ^3IL state energy. The quenching of the equilibrated $^3MLCT - {}^3IL$ excited states by dissolved oxygen is also pH dependent, paralleling the excited state lifetime. Further, this work presents the computation of the excited state pKa values for the 4,4'-dicarboxy-2,2'-bipyridine ligands.

4.3 Experimental

4.3.1 Spectroscopy

NMR spectra were recorded on a Varian 400 MHz NMR. All UV-vis absorption spectra were obtained on a Hewlett-Packard 8452A diode array spectrophotometer. Photoluminescence spectra were obtained using a Spex Fluorolog Fluoroimeter equipped with a 450 W Xe arc lamp and a SPEX 0.34 m spectrograph/CCD detector (Andor IDUS). Photoluminescence lifetime measurements were collected using the visible output of an OPO (OPOTEK) which was pumped by the third harmonic of a Quantel Brilliant B Q-switched Nd:YAG laser. Excitation pulses were generally < 5 ns and were tuned to the absorption λ_{max} of each chromophore. Emitted light was detected through a single grating monochromator (Applied Photophysics 0.25 m) with PMT detection (Hamamatsu R928). The output was recorded on an Agilent Infinium transient digitizer. Each decay was recorded at the emission λ_{max} and was the average of 500 pulses.

4.3.2 Nanosecond Time-Resolved Transient Absorption

Nanosecond transient absorption measurements were performed using a Quantel Brilliant B Q-switched Nd:YAG laser-pumped OPO (Opotek) as the pump source at a right angle to the analyzing light source. Excitation pulses were < 5ns and were tuned to the λ_{max} of the compound being interrogated. An Applied Photophyics LKS.60 laser flash photolysis spectrometer was used for detection; the instrument is equipped with a 150 W pulsed Xe arc lamp as the analyzing light source, a single grating monochromator (Applied Photophysics 0.25m) after the sample, and PMT detection (Hamamatsu R928). The output was recorded on an Agilent Infinium transient digitizer and decays and spectra were acquired and analyzed with Applied Photophysics LKS.60 software.

4.3.3 Femtosecond Time-Resolved Transient Absorption

Ultrafast time-resolved transient absorption measurements were collected in collaboration with the group of Professor Jeffrey Rack at Ohio University. I am thankful for the contributions of Ohio University graduate student, Yuhuan Jin, to this work. He was responsible for the collection of all the ultrafast transient absorption data presented in this chapter.

Femtosecond transient absorption measurements were collected on an Ultrafast Systems Helios transient absorption spectrometer. A Spectra Physics Solstice laser, a one-box regenerative amplifier containing a Mai Tai femtosecond oscillator and Empower pump laser, was employed to produce 800 nm pulses at a repetition rate of 1 kHz at 4.5 W average power and a pulse width of < 100 fs (4.5 mJ per pulse). From this unit, the beam is split (50:50) with one beam directed to an optical parametric amplifier (TOPAS, Light Conversion) and the other to the Helios spectrometer (HE-vis-3200) to create the pump (472 nm; TOPAS) and probe (Helios) sources, respectively. The 800 nm probe beam passed through a CaF_2 plate to generate a white light continuum (~330 - 700 nm). The spectrum was integrated for 2 s for each scan. The pump and probe beams were directed to a 2 mm pathlength cuvette containing the sample where they were spatially overlapped. The solution was vigorously stirred in the 2 mm path length cuvette during data collection. Transient absorption data were corrected by subtracting spectral background features that persisted from the previous pulse and appeared pre-pulse as well as applying chirp correction using Surface Xplorer Pro 1.1.5 software (Ultrafast Systems). Solutions were deaerated with N_2 prior to collection of the data.

4.4 Synthesis

The ligands and complexes 4-(1-pyrenyl)-2,2'-bipyridine (pyr-bpy)[24], 2,2'-bipyridine-4,4'-dicarboyxlic acid (dcbH$_2$)[25], cis-[(dcbH$_2$)RuCl$_2$][26], and [(Bz)Ru(bpy)Cl]Cl (Bz = benzene)[27], were all prepared as previously reported in the literature. The ligand and complexes 4-(p-(1-pyreneyl)phenyl)-2,2'-bipyridine (pyr-phen-bpy), [(dcbH$_2$)$_2$Ru(pyr-bpy)]Cl$_2$, and [(dcbH$_2$)$_2$Ru(pyr-phen-bpy)]Cl$_2$ were prepared by Dr. Jin Chen when she was a member of the Schmehl Group. The synthetic procedures and characterization of the molecules appear in her dissertation[28] and our published work.[29]

[(dcbH$_2$)$_2$Ru(bpy)]Cl$_2$. 75 mg [(Bz)Ru(bpy)Cl]Cl and 95.1 mg dcbH$_2$ were added to 2 mL DMF. The mixture was refluxed under nitrogen for 4 hours during which the reaction color changed from yellow to purple to dark red. After the reaction, the mixture was added to 50 mL of acetone and cooled in the freezer to precipitate the product. 100.2 mg (72.6 %) of dark red solid was collected on fritted glass. 25 mg of this solid was purified via prep TLC. The compound was eluted with a 1:1 mixture of 0.25 M HCl:CH$_3$CN on 1 mm thick alumina. Three distinct bands are observed on the alumina plate. A yellow band with a R_f value of approximately 0.80 and a purple band with a Rf value of approximately 0.75 completely separate from a fluorescent orange band that streaks over the bottom third of the TLC plate. The fluorescent orange material was collected by rinsing the silica with water. 16.2 mg (64.8 %) of orange solid was obtained after the water was removed via rotary evaporation. ^{1}H NMR (CD$_3$OD with one drop of NaOH in D$_2$O) δ: 9.05 (s, 4 H), 8.69 (d, J = 8.1 Hz, 2 H), 8.12 (t, J = 7.8 Hz, 2 H), 7.88 (d, J = 5.7 Hz, 2 H), 7.82 (m, 8 H), 7.49 (t, J = 6.5 Hz, 2 H).
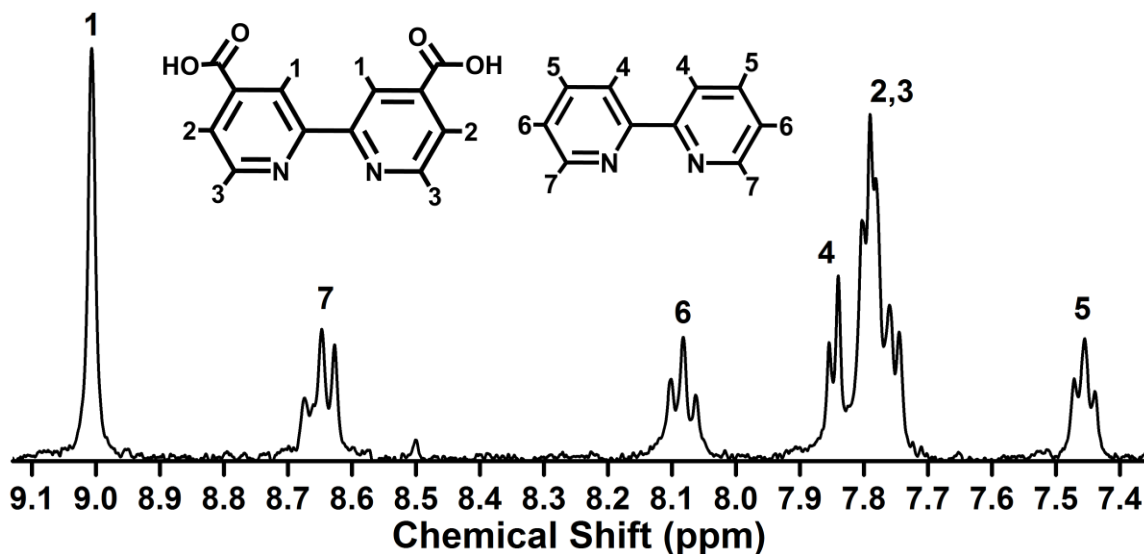
Figure 4.2. Aromatic region of the ^{1}H NMR spectrum of [(dcbH$_2$)$_2$Ru(bpy)]Cl$_2$. The spectrum was collected in methanol with a single drop of NaOH in D$_2$O added to the solution.

4.5 Results and Discussion

Three heteroleptic ruthenium diimine complexes, [(dcbH$_2$)$_2$Ru(bpy)]Cl$_2$, [(dcbH$_2$)$_2$Ru(pyr-phen-bpy)]Cl$_2$, and [(dcbH$_2$)$_2$Ru(pyr-bpy)]Cl$_2$ where dcbH$_2$ is (4,4'-dicarboxy-2,2'-bipyridine, pyr-bpy is 4-(1-pyreneyl)-2,2'-bipyridine and pyr-phen-bpy is 4-(p-(1-pyreneyl)phenyl)-2,2'-bipyridine, were prepared and investigated. Molecular mechanics minimized ball and stick representations (obtained using Spartan '09) of the pyrene containing complexes are shown in Figure 4.3.
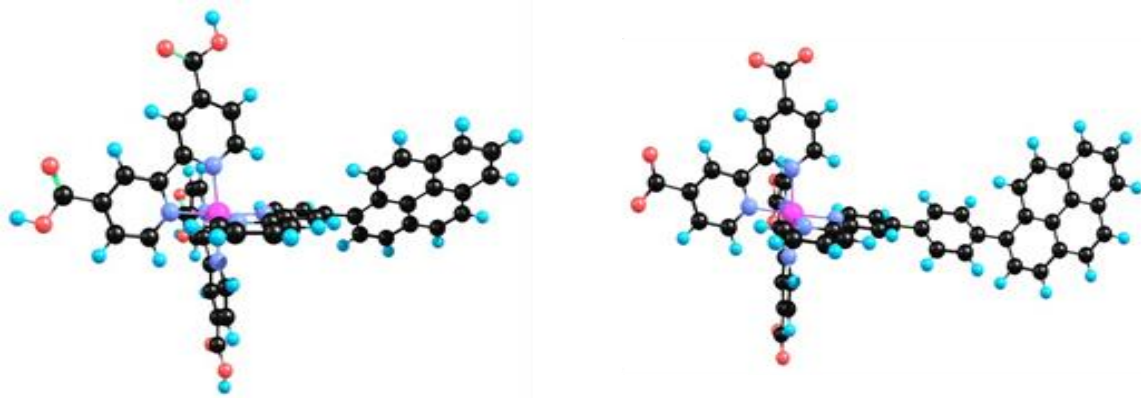
Figure 4.3. Graphical representations of the chromophores [(dcbH$_2$)$_2$Ru(pyr-bpy)]$^{2+}$ (left) and [(dcb)$_2$Ru(pyr-phen-bpy)]$^{2-}$ (right).

The synthesis of the pyr-bpy ligand was reported earlier[5] and the synthesis of the pyr-phen-bpy was achieved by Suzuki coupling of 4-(p-bromophenyl)-2,2'-bipyridine with pyrene-1- boronic acid; the boronic acid derivative was prepared from reaction of triisopropylborate with pyrene-1-bromide.[28] The complexes containing the pyrene modified bipyridine ligands were made by reaction of cis-$[(dcbH_2)_2RuCl_2]$ with the pyrene containing ligand. The complexes were characterized by ^{1}H NMR spectroscopy, ESI mass spectrometry in negative ion mode, uv-visible absorption spectroscopy, and cyclic voltammetry measurements. A few of the complexes contain trace amounts (not detectable by ESI mass spectrometry) of a luminescent component, likely $[(dcbH_2)_3Ru]^{2+}$ (*vide infra*).

4.5.1 Absorption Behavior

In basic water/methanol (1:1) solutions $[(dcbH_2)_2Ru(bpy)]Cl_2$ has two ligand localized absorption maxima, at 288 nm and at 300 nm, as well as a single metal-to-ligand-charge transfer (MLCT) absorption at 462 nm with a shoulder at 436 nm. In acidic aqueous methanol solution, the absorption observed at 288 nm is unchanged, but the ligand localized absorption at 300 nm shifts to 308 nm. Similarly, the metal-to-ligand charge transfer absorption is observed at 478 nm with a shoulder at 442 nm. No clear separation of the Ru to bpy MLCT and the Ru to $dcbH_2$ MLCT absorption bands is observed, regardless of the degree of protonation of the carboxylated bipyridine ligand. These results mirror those of Nazeruddin's earlier work.[23] The spectrophotometric characteristics of the pyrene-bipyridine containing chromophores have the same signatures as $[(dcbH_2)_2Ru(bpy)]Cl_2$ but also have a single broad band with a maximum between 300 and 400 nm that corresponds to a pyrene localized $\pi \rightarrow \pi^*$ transition. A

consistent change in the MLCT spectra of all the complexes is observed in lowering the pH from 8 to 0; in each case the absorbance of the shoulder increases to be equivalent with that of the 478 nm maximum. Addition of zinc persulfate to a solution of the pyr-bpy ligand in water/methanol (1:1) results in broadening of the pyrene localized $\pi \rightarrow \pi^*$ absorption. Upon coordination of zinc, the absorbance of the ligand reaches zero at 430nm; thus, we are confident that we are not directly pumping pyrene localized absorption transitions in any of our transient absorption or luminescence measurements for which excitation is a wavelengths > 450 nm.

4.5.2 Luminescence Behavior

For all the chromophores, the luminescence maximum gradually shifts to the red as the pH increases from 0 to 2.5. However, a much larger blue shift of the emission maximum occurs as the pH is further increased to 8. Figure 4.4 shows emission spectra as a function of pH for $[(dcbH_n)_2Ru(bpy)]^{(2n-2)}$, $[(dcbH_n)_2Ru(pyr-bpy)]^{(2n-2)}$, and $[(dcbH_n)_2Ru(pyr-phen-bpy)]^{(2n-2)}$ (n=0-2) in 1:1 oxygenated and deoxygenated H_2O:MeOH solutions. The spectra are broad, lack vibronic structure, and appear to have a bandwidth that does not change significantly with pH. The emission spectra of the pyrene containing complexes are quite similar to $[(dcbH_2)_2Ru(bpy)]^{2+}$, suggesting that the emission arises from the ^{3}MLCT state. The sensitivity of the luminescence to oxygen quenching is also pH dependent, especially for the pyrene containing complexes, and is most sensitive in alkaline solution. Of the three complexes, the pyr-bpy chromophore exhibits the highest degree of oxygen quenching in air saturated solutions and the largest pH dependence. The quenching ratio ($\frac{I_0}{I}$) in basic aqueous methanol is 12.2, whereas the

quenching ratio of the pyr-phen-bpy chromophore is 4.8, and the bpy complex luminescence is quenched by only a factor of 2.
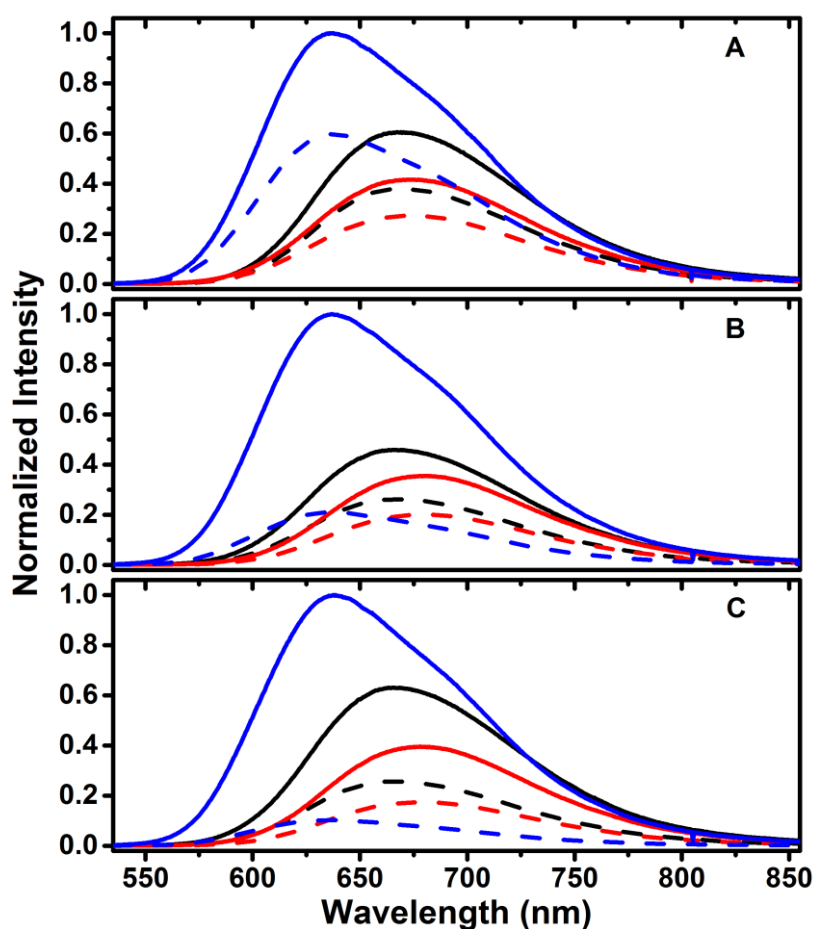
Figure 4.4. The oxygenated (dashed) and deoxygenated (solid) luminescence spectra of the chromophores at pH 0, pH 2.5, and pH 8. (A) $[(dcbH_2)_2Ru(bpy)]^{2+}$ (B) $[(dcbH_2)_2Ru(pyr-ph-bpy)]^{2+}$ (C) $[(dcbH_2)_2Ru(pyr-bpy)]^{2+}$.

Excited state lifetimes determined for $[(dcbH_2)_2Ru(bpy)]Cl_2$ over the pH range 0 to 9 are single exponential and the degree of oxygen quenching is the same for both luminescence intensity and lifetime measurements. Lifetimes obtained by luminescence and transient absorption decays are summarized in Table 4.1. The luminescence behavior of the pyrene containing complexes is complicated by the fact that the decays become double exponential in neutral and basic solutions. Transient absorption decays, on the other

hand, were cleanly single exponential at all pHs examined (vide infra). Since transient absorption is much less sensitive to impurity contributions than luminescence measurements, we believe that the additional luminescence decay component is due to traces of a complex impurity that lacks the pyrene modified bipyridine. The most likely impurity, based on the synthetic procedure employed is $[Ru(dcbH_2)_3]Cl_2$. The presence of luminescence from an impurity of this type would serve to explain the differences observed between intensity and lifetime oxygen quenching measurements for the pyrene containing complexes.

4.5.3 Nanosecond Time-Resolved Transient Absorption

Nanosecond time resolved transient difference spectra provide a wealth of information about the nature of the excited states of the complexes. Samples were excited with output of a Nd:YAG pumped OPO at 460 nm and point by point transient spectra (ΔAbs. vs. λ) were obtained every 10 nm between 330 and 700 nm. Spectra were generated from the collected decays at various times following excitation. Representative transient spectra of the three complexes are shown in Figure 4.5 for samples at pH 0 and pH 8. Figures 4.5A and B show nanosecond transient behavior for $[(dcbH_2)_2Ru(bpy)]^{2+}$, the parent complex, at the two pH values. The spectra both show a positive absorption in the 350-400 nm region and a bleach between 400 and 500 nm. The additional longer wavelength bleach signal in both spectra (> 600 nm) results from luminescence of the complexes that is not corrected for in the experiment. Figures 4.5C and D illustrate the TA of the pyr-phen-bpy complex in acid and base. There are strong similarities between the parent complex and the pyr-phen-bpy complex spectra at pH 0. In basic solutions, the spectrum of the pyr-phen-bpy exhibits a bleach of the ground state absorption in the 400 -

500 nm region, but it is greatly diminished. A new bleach is observed between 300 and 400 nm and a broad positive absorption is evident from 500 – 600 nm. Thus there are obvious differences between the parent complex and the observed transient of the pyr-phen-bpy complex.
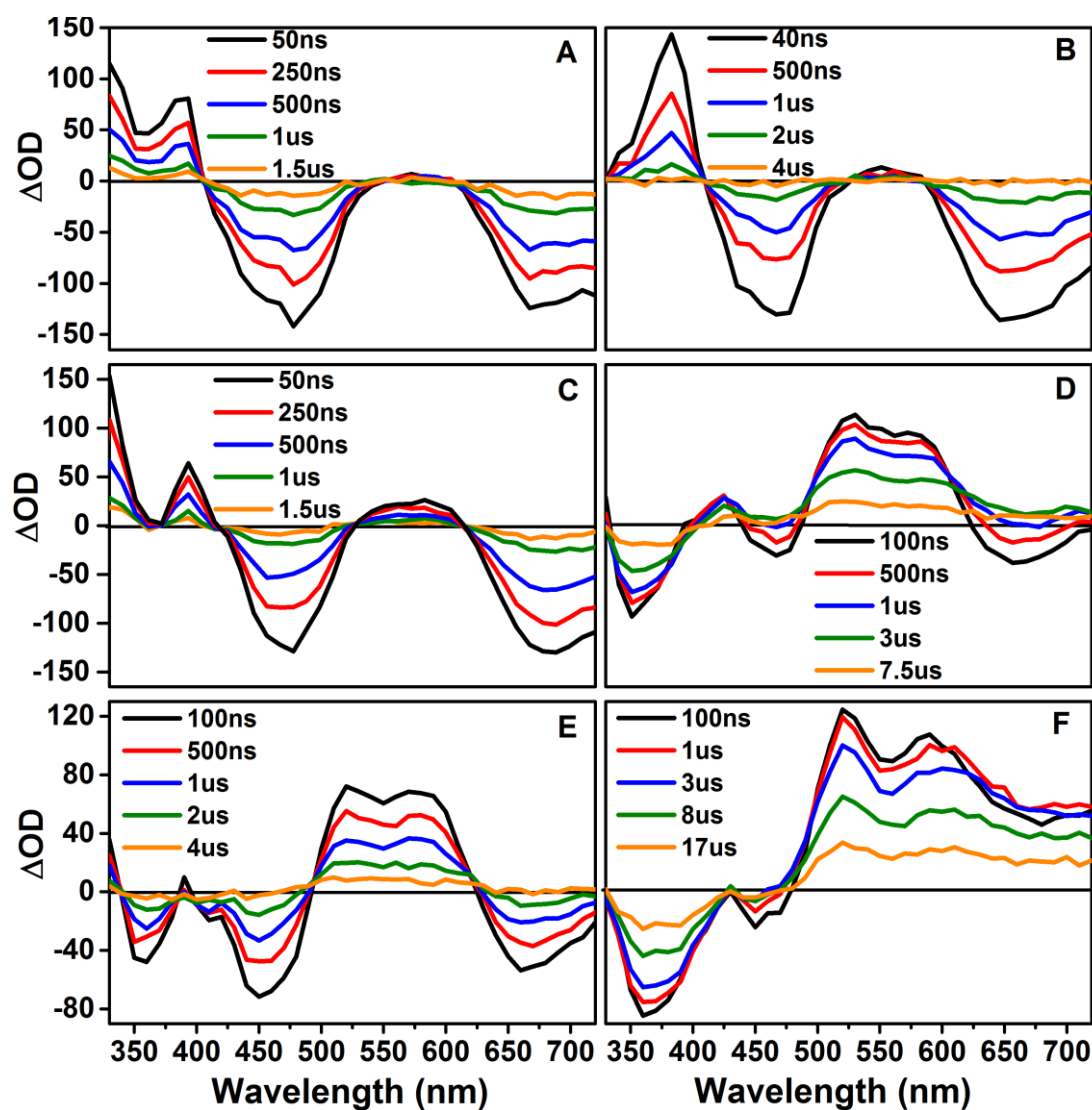
Figure 4.5. Nanosecond transient absorption spectra for each of the chromophores at pH 0 (A, C, and E) and pH 8 (B, D, and F). (A) $[(dcbH_2)_2Ru(bpy)]^{2+}$, (B) $[(dcb)_2Ru(bpy)]^{2-}$, (C) $[(dcbH_2)_2Ru(pyr-ph-bpy)]^{2+}$, (D) $[(dcb)_2Ru(pyr-ph-bpy)]^{2-}$, (E) $[(dcbH_2)_2Ru(pyr-bpy)]^{2+}$, (F) $[(dcb)_2Ru(pyr-bpy)]^{2-}$.

Figure 4.5E shows the transient spectrum of the pyr-bpy complex in acid; the features are similar to the pyr-ph-bpy complex in base. In basic solution (Figure 4.5F), the transient absorption spectrum of the pyr-bpy complex is unique. It has a broad, positive transient absorption from 500 - 700 nm and bleaching between 360 nm and 460 nm. In all cases the lifetimes of the TA signals obtained are comparable to those observed in luminescence. A key aspect of the transient difference decays is that they are cleanly single exponential in all cases; this contrasts the luminescence behavior of the pyr-bpy complex in basic solutions where a double exponential decay is observed. Since transient absorption spectra will reflect the relative concentrations of different species in solution whereas luminescence intensities are a function not only of concentration but also emission efficiency, the short lived component of the luminescence decays observed are believed to be associated with trace impurity emission, likely $[(dcbH_2)_3Ru]^{2+}$. The lifetime of the short component in all of these luminescence decays is independent of the pH and ranges from 700 - 800 ns. The lifetime of $[(dcbH_2)_3Ru]^{2+}$ is also unaffected by pH, with reported lifetime values of 700 ns at pH > 7 and 755 ns at pH 0.[23]

Table 4.1. Luminescence and Transient Absorption Decay lifetimes of the complexes in room temperature aqueous methanol solutions under acidic and basic conditions. Solutions were made with via 1:1 (v:v) combination of MeOH with 0.1M solutions of trichloroacetic acid and sodium acetate. Solutions were deaerated with N_2 for 10 minutes prior to the collection of lifetime data.

Complex	bpy		pyr-bpy		pyr-ph-bpy	
	pH 0	pH 8	pH 0	pH 8	pH 0	pH 8
τ_{em}, µs (λ_{obs}, nm)	0.61 ± 0.01 (668nm)	0.93 ± 0.01 (636nm)	1.9 ± 0.1 (664nm)	17.7 ± 0.1 (637nm)	1.2 ± 0.1 (665nm)	4.7 ± 0.1 (636nm)
τ_{TA}, µs (λ_{obs}, nm)	0.61 ± 0.01 (390nm)	0.94 ± 0.01 (450nm)	1.8 ± 0.1 (360nm)	15 ± 1 (360nm)	0.70 ± 0.05 (390nm)	5.6 ± 0.1 (350nm)
τ_{TA}, µs (λ_{obs}, nm)	0.70 ± 0.02 (660nm)	1.1 ± 0.1 (630nm)	1.7 ± 0.1 (520nm)	15 ± 1 (520nm)	0.91 ± 0.05 (660nm)	5.3 ± 0.1 (520nm)

4.5.4 Ultrafast Time-Resolved Transient Absorption

Since excitation of these complexes with visible light leads to generation of a singlet MLCT state that evolves into the thermally equilibrated state(s), reference tracking the evolution of the these states from inception is certainly desirable. Collected spectra between < 1 ps and 3 ns are shown in Figure 4.6 for the three complexes in acidic and basic solutions following 470 nm excitation with a 100 fs pulse. For $[Ru(dcbH_2)_2(bpy)]^{2+}$ the observed transient spectra in acidic and basic solution (Figures 4.6A and B) include absorption between 350 and 400 nm as well as bleaching between 400 and 500 nm. The spectral features near the end of the ultrafast spectrum (~3000 ps) are similar to those that appear near the beginning of the nanosecond spectrum (~50 ns) with little evidence of dynamics in the earlier time spectra. The pyr-ph-bpy complex at pH 0 (Figure 4.6C) also has spectral features in the 3000 ps spectrum closely resembling the 50 ns spectrum. However, at pH 8 (Figure 4.6D), the initial spectrum acquired 660 (±10) fs following excitation has well defined absorption in the 300-400 nm region and bleaching *only* between 400 and 500 nm; this sharply contrasts the spectrum obtained 100 ns after excitation (*vide supra*). During the time period from 660 fs to 3 ns the spectrum evolves such that the sharp absorption at 380 nm decays, concomitant with loss of the bleach at 460 nm. In addition, a clear isosbestic point is observed at 410 nm, suggesting clean evolution from the initially formed state to another state. Overall, the 3000 ps transient spectrum closely resembles the 100 ns transient spectrum. For the pyr-bpy complex (Figures 4.6E and F), absorption at 660 fs after excitation also contains positive absorption between 350 and 400 nm as well as bleaching between 400 and 500 nm. Following this, changes occur that lead to bleaching between 350 and 380 nm, decreased

MLCT bleaching and increased absorption between 500 and 700 nm. A similar, but more pronounced evolution of the spectral features is observed for this complex in pH 8 solution (Figure 4.6F), resulting in a spectrum after 3 ns that resembles the 100 ns spectrum, with significant bleaching between 300 and 400 nm and strong absorption to the red of 500 nm.
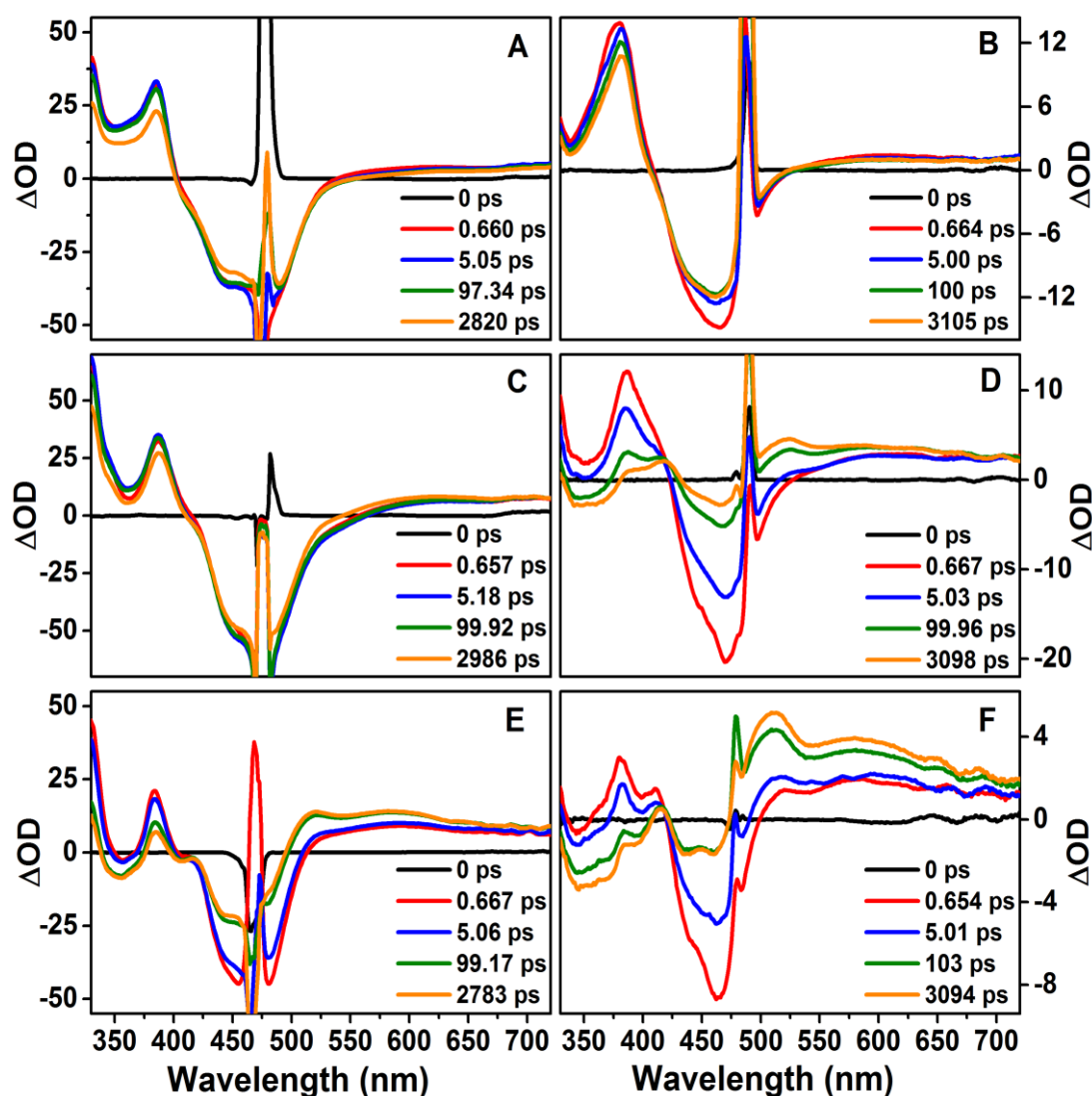
Figure 4.6 Subpicosecond transient absorption spectra for each of the chromophores at pH 0 (A, C, and E) and pH 8 (B, D, and F). (A) $[(dcbH_2)_2Ru(bpy)]^{2+}$, (B) $[(dcb)_2Ru(bpy)]^{2-}$, (C) $[(dcbH_2)_2Ru(pyr-ph-bpy)]^{2+}$, (D) $[(dcb)_2Ru(pyr-ph-bpy)]^{2-}$, (E) $[(dcbH_2)_2Ru(pyr-bpy)]^{2+}$, (F) $[(dcb)_2Ru(pyr-bpy)]^{2-}$.

4.5.5 pH Dependence of MLCT Emission

The ^{3}MLCT excited state of $[(dcbH_2)_2Ru(bpy)]^{2+}$ has two pKa values, each corresponding to the loss of two protons. According to Nazeruddin et al.,[23] at sufficiently low pH, the molecule is fully protonated and the Ru $(d\pi) \rightarrow$ dcbH$_2$ (π^*) ^{3}MLCT state is the lowest energy state. The energy of the MLCT transition to the dcbH$_n$ ligand is raised as the ligand is deprotonated. When the carboxybipyridine is fully deprotonated, the Ru $(d\pi) \rightarrow$ dcb (π^*) ^{3}MLCT state energy has been raised to the point where the state may be higher in energy than the Ru $(d\pi) \rightarrow$ bpy (π^*) ^{3}MLCT transition. Based on the work of Nazeruddin and coworkers,[23] the two pKa values measured for $[(dcbH_2)_2Ru(bpy)]^{2+}$ are 1.8 and 4.5 and can be represented as sequential deprotonation of both of the carboxylated bipyridine ligands as shown in Equations 4.1 and 4.2 below.

$$[(dcbH_2)_2Ru(bpy)]^{2+} \rightleftharpoons [(dcbH)_2Ru(bpy)]^{2+} + 2H^+ \quad K_1 \qquad (4.1)$$

$$[(dcbH)_2Ru(bpy)]^{2+} \rightleftharpoons [(dcb)_2Ru(bpy)]^{2+} + 2H^+ \quad K_2 \qquad (4.2)$$
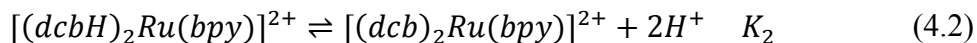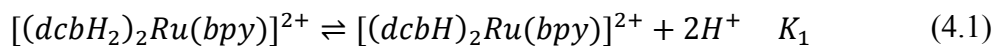
As stated earlier, the implication is that electronic interaction of the two coordinated carboxybipyridine ligands is sufficiently weak that acid dissociation of a carboxylic acid on one ligand does not influence the similar dissociation on the other carboxybipyridyl ligand. As a result, the double deprotonations of Equations 4.1 and 4.2 can be treated as two nearly identical and independent equilibria. Similar behavior is observed for the pyr-bpy and pyr-ph-bpy complexes in aqueous methanol solutions buffered between pH 0 and 8. Figure 4.7 shows the dependence of the emission maximum on pH for $[(dcbH_n)_2Ru(pyr-bpy)]^{(2n-2)}$ (n=0-2). The spectral bandwidth remains relatively constant over the entire pH range, suggesting that the emission spectra reflect the average equilibrated degree of protonation of the complexes. The collected emission maxima can

then be modeled assuming the maximum at any given pH represents the weighted average of the $[Ru(dcbH_2)_2(pyr\text{-}bpy)]^{2+}$ (H_2A), $[Ru(dcbH)_2(pyr\text{-}bpy)]$ (HA) and $[Ru(dcb)_2(pyr\text{-}bpy)]^{2-}$ (A) forms of the complex as given by Equation 4.3.

$$E^{CT} = f_{H2A}E_{H2A} + f_{HA}E_{HA} + f_A E_A \qquad (4.3)$$

The fractions, f, of each of the forms of the acid at any given pH were determined from the K_1 and K_2 values for the two acid dissociations of Equations 4.1 and 4.2 and the emission maxima of each of the three forms of the complex were fitting parameters. Results are shown in Figure 4.7 (solid line and parameters of fit); the two pK values, 2.1 and 4.7, are slightly higher than those determined by Nazeruddin et al. for $[Ru(dcbH_2)_2(bpy)]^{2+}$,[23] but are in generally good agreement given the similarity of the complexes.
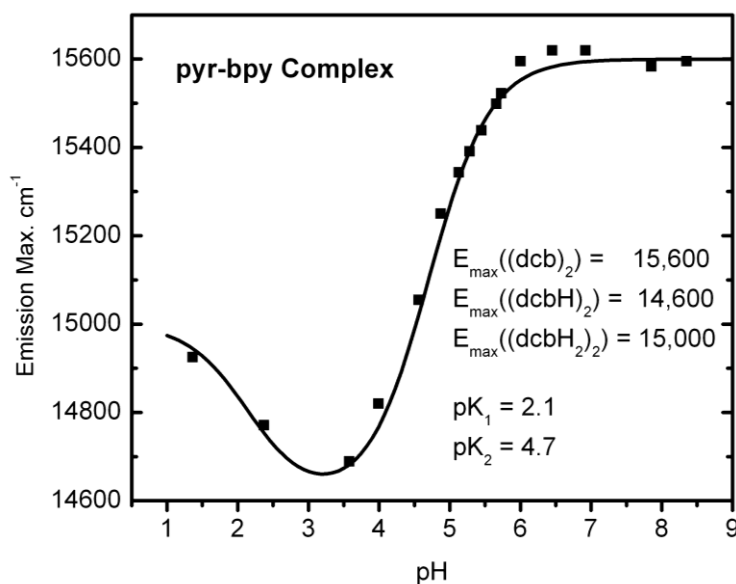
Figure 4.7. Emission maxima of $[(dcbH_n)_2Ru(pyr\text{-}bpy)]^{(2n\text{-}2)}$ (n = 0-2) in 1:1 methanol:water as a function of pH. The solid line represents a fit to Equation 4.3 using the parameters shown in the figure.

The calculated maxima provide approximate values of the emission energy for each form of the complex; these can be used in evaluation of the relative energies of the MLCT and

pyrene localized triplet states (*vide infra*). An interesting observation is that the emission maximum of the partially deprotonated complex is *lower* in energy than the fully protonated complex. This reflects the fact that the initial deprotonation steps will have a significant contributing portion of a mono-deprotonated complex, $[(dcbH_2)(dcbH)Ru(bpy)]^+$; the mono-deprotonated ligand should be a somewhat better σ donor than the fully protonated species and will serve to raise the energy of the dπ orbitals of the Ru, thereby slightly lowering (~ 400 cm^{-1}) the energy of the emission of the remaining Ru (dπ) → dcbH$_2$ (π*) MLCT state. This fourth form of the complex was not used in fitting the pH dependence of the luminescence since good fits were obtained with only the three (H$_2$A, HA and A).

4.5.6 pH Dependence of Transient Spectra

When the complexes are excited at wavelengths to the red of 430 nm, the initial state populated is the ^{1}MLCT state. This state evolves into the thermally equilibrated excited state(s) of the complex from which luminescence or, in this case, reaction with oxygen may occur. At issue is the nature of the lowest excited state. One possibilitiy is complete localization as a Ru (dπ) → dcbH$_2$ (π*) ^{3}MLCT, Ru (dπ) → dcb (π*) ^{3}MLCT, Ru (dπ) → bpy (π*) (or pyr containing bpy (π*)) ^{3}MLCT or pyr π → π* ^{3}IL state. Alternatively the thermally equilibrated state could be a single excited state with contributions from two or more of these states, or an equilibrium mixture of two or more of the states. The transient spectra shown in Figures 4.5 and 4.6 clearly illustrate that there are significant differences in the spectra of the pyrene containing complexes in acidic and basic solution. The ns and fs transient spectra of [Ru(bpy)$_3$]$^{2+}$ have been thoroughly investigated.[30-33] The ns spectrum is characterized by an absorption at 360 nm

attributed to absorption of the bpy anion radical of the [3]MLCT state. This is accompanied by bleaching of the ground state absorbance centered at 454 nm.[34] In the fs spectrum of $[Ru(bpy)_3]^{2+}$ the features characteristic of the thermally equilibrated [3]MLCT state are evident 300 fs following excitation.[15] The $[(dcbH_n)_2Ru(bpy)]^{(2n-2)}$ (n=0-2) series clearly shows the spectral features that can be readily associated with $[Ru(bpy)_3]^{2+}$, in both acidic and basic solutions. In this work, the spectral features appear within less than a ps after excitation for the bpy complex in acidic and basic solution and persist throughout the excited state decay. The absoprtion feature between 300 and 400 nm differs between acidic solutions, where the Ru $(d\pi) \rightarrow dcbH_2 (\pi^*)$ [3]MLCT state is the lowest energy state and solutions above pH 7, where either the Ru $(d\pi) \rightarrow bpy (\pi^*)$ or the Ru $(d\pi) \rightarrow dcb$ (π^*) [3]MLCT state is populated.

Previous investigations of Ru(II) complexes of pyr-bpy and related complexes illustrate significant differences in the ns transient absorption behavior.[5,10,18,20,35] The key difference relative to $[Ru(bpy)_3]^{2+}$ is the appearance of strong transient absorption between 500 and 800 nm. The kinetic behavior of the two pyrene containing complexes clearly shows evolution of the initially formed excited state, an MLCT state by virtue of the excitation wavelength, to what we are presuming to be an equilibrium mixture of a [3]MLCT state with the [3]IL state localized on the pyrene containing ligand. The sequence of events is shown below in Equations 4.4 - 4.6 for the pyr-bpy complex in acidic solution.

$$^1[(dcbH_2)_2Ru(II)(pyrbpy)]^{2+} \xrightarrow{h\nu} {}^1[(dcbH_2)(dcbH_2^-)Ru(II)(pyrbpy)]^{2+} \quad (4.4)$$

$$^1[(dcbH_2)(dcbH_2^-)Ru(II)(pyrbpy)]^{2+} \xrightarrow{isc} {}^3[(dcbH_2)(dcbH_2^-)Ru(II)(pyrbpy)]^{2+} \quad (4.5)$$

$$^3[(dcbH_2)(dcbH_2^-)Ru(II)(pyrbpy)]^{2+} \rightleftharpoons \, ^3[(dcbH_2)_2Ru(II)(\,^3pyrbpy)]^{2+} \quad (4.6)$$
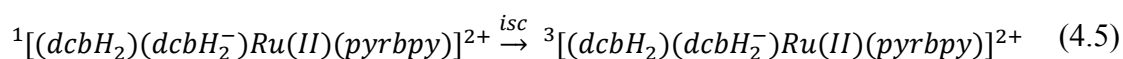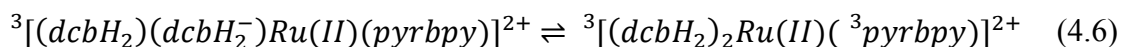
Excitation to the ^{1}MLCT state is followed by intersystem crossing to the ^{3}MLCT state, determined to be <1 ps for a variety of Ru(II) diimine complexes closely related to the systems studied here.[15,33] Energy transfer from the ^{3}MLCT state to the ^{3}IL state, k_{en}, and back energy transfer, k_{-en}, will occur and equilibrium can be established. Rate constants for energy transfer from the ^{3}MLCT to ^{3}IL state are given in Table 4.2. The results are obtained from the temporal evolution of transient spectra on the ps/ns time scale as shown in Figure 4.6 for all the complexes in acidic and basic solution. In each case the energy gap between the ^{3}MLCT and ^{3}IL states is small (< 1000 cm^{-1}; < 0.125 eV) and, as a result, the reverse energy transfer process ($k_{-en,}$ Figure 4.1) should be on the ns or sub-ns time scale. Since the shortest lived excited state of the pyrene containing complexes in any aqueous methanol solution is at least 500 ns and the forward and reverse energy transfer processes are fast relative to this rate of decay, it is safe to assume that the excited states are indeed in equilibrium during relaxation to the ground state.

For the pyr-ph-bpy complex the reaction sequence follows that of Equations 4.4 - 4.6 and Figure 4.1. In acidic solution the ultrafast transient absorption indicates formation of the ^{3}MLCT state in < 1 ps. The spectrum of this state matches that of the complex on the ns to μs time scale. There is, however, a small absorption signal to the red of 500 nm that grows in over the first 1000 ps; the rate constant for this process is determined is 4 x 10^9 s^{-1} (Table 4.2) from fits of the transient rise at 590 nm as well as the decay of the bleach at 450 nm. We have attributed this process to equilibration of the ^{3}MLCT state with the pyr-ph-bpy localized ^{3}IL state via energy transfer. In this case, the transient spectrum obtained on the ns time scale indicates that the position of equilibrium of the

excited state is largely localized on the ^{3}MLCT state, as evidenced by the transient absorption between 350-400 nm as well as a small absorption at wavelengths longer than 500 nm.

In basic solution, the transient spectrum of the pyr-ph-bpy complex exhibits significant changes in bandshape in the first 1000 ps (Figure 4.6D). The features of the initially formed ^{3}MLCT state disappear and are accompanied by the appearance of the ^{3}IL spectrum. The rate constant for this process, 2×10^{10} s^{-1}, is a factor of five faster than the corresponding process in acidic solution. The 100 ns transient spectrum (Figure 4.5D) has the features of the pyrene ^{3}IL spectrum, but also includes emission of the ^{3}MLCT state. Nonetheless, it is clear that, qualitatively, the equilibrium favors the ^{3}IL state at pH 8, consistent with the raising of the ^{3}MLCT state following deprotonation.

In both acidic and basic solution the transient spectrum of the pyr-bpy complex clearly evolves from the ^{3}MLCT to the ^{3}IL spectrum over the first ns. Rate constants for the process are 2×10^{10} s^{-1} at pH 0 and 4×10^{10} s^{-1} at pH 8. Spectra on the μs time scale in acidic solution include features of both states, with bleaching of the MLCT absorption (450 nm) and strong ^{3}IL absorption to the red of 500 nm. At pH 8 the transient absorption spectrum lacks any features of the ^{3}MLCT state (Figures 4.5F, 4.6F).

The key observation for the pyrene containing complexes is that the position of equilibrium changes from an excited state nearly completely localized on the ^{3}MLCT (Ru (dπ) → dcbH$_2$ (π^*)) state to a ^{3}IL (^{3}pyr ($\pi \rightarrow \pi^*$)) state simply by variation of the solution pH from 3 to 6. The relative energies of the states, obtained from analysis of the excited state decays (*vide infra*), are shown in Figure 4.8 for the pyr-ph-bpy complex.

4.5.7 Excited State Equilibria and Decay

Since the excited states of the pyrene containing complexes can be assumed to be in equilibrium, relaxation to the ground state will occur with a rate constant that is the weighted average of the decay rate constants of the ^{3}MLCT, k_{CT}, and the ^{3}IL, $k_{IL,}$ states (Equation 4.7).[36]

$$k_{obs} = f_{CT}(k_{CT}) + f_{IL}(k_{IL}) \qquad (4.7)$$

The excited state lifetime of the ^{3}MLCT state is pH dependent and can be approximated from the lifetime of the parent complex, $[(dcbH_n)_2Ru(bpy)]^{(2n-2)}$ (n=0-2); values used for k_{CT} are given in Table 4.2. The collected transient spectral results indicate that, in acidic solution, the MLCT state is dominant, providing a lower boundary on the energy of the ^{3}IL state (in acid $E_{MCLT} < E_{pyr}$). In basic solution, the ^{3}IL state is the predominant state observed, and here the energy of the observed emission can be used as an upper limit on the pyrene triplet state energy. We note that we cannot collect the reduction potential of dcb at either pH, since the couple lies outside the aqueous electrochemical window. Collectively, the observations bound the free energy for the intramolecular energy transfer (Equation 4.6) to be well below 1000 cm^{-1}, thereby limiting the equilibrium constant at any given pH to be between 0.01 (in acid) and 100 (in base). With this boundary and the observed excited state decays, it is clear that once the decay rate constant of the ^{3}IL state is slower than 10^4 s^{-1} (much faster than that for triplet pyrene),[37] the observed decay rate constant will be completely dominated by the fraction of the ^{3}MLCT state. With this restriction, a decay rate constant of 10^4 s^{-1} was used for the ^{3}IL state of both pyrene containing complexes. The observed rate constant, k_{obs} can be expressed in terms of K_{eq} for the equilibrium expressed in Equation 4.6. This expression

for k_{obs} was included in the exponential decay function and used to fit nanosecond absorption decays (Equation 4.8).

$$\Delta(Abs)_t = \Delta(Abs)_0 \, exp\left[-\left(\left(1-\frac{K_{eq}}{K_{eq}+1}\right)k_{CT}+\left(\frac{K_{eq}}{K_{eq}+1}\right)k_{IL}\right)t\right]+b \qquad (4.8)$$

K_{eq} is the only variable and b is a baseline residual that is nearly zero in all cases. The forward energy transfer rate constants are available from the ultrafast transient data; therefore, back energy transfer rate constants can also be obtained once a value for K_{eq} is determined.

Table 4.2. Kinetic and thermodynamic parameters extracted time-resolved decays and absorption decays.

	pyr-bpy		pyr-phen-bpy	
	pH 0	pH 8	pH 0	pH 8
k_{CT} (MLCT) s^{-1}	1.5×10^6	1.0×10^6	1.5×10^6	1.0×10^6
k_{IL} (IL), s^{-1}	1.0×10^4	1.0×10^4	1.0×10^4	1.0×10^4
k_{en}, s^{-1}	1.6×10^{10}	3.6×10^{10}	4.0×10^9	1.6×10^{10}
K_{EQ}	1.6	16	0.10	4.4
k_{-en}, s^{-1}	1.0×10^{10}	2.3×10^9	4.0×10^{10}	3.6×10^9
ΔG, cm^{-1}	-90	-570	480	-310
E_{IL}, cm^{-1}	14900	15200	15400	15400

The free energies for the energy transfer processes for both the pyr-bpy and the pyr-ph-bpy complexes at pH 0 and pH 8 are determined directly from the equilibrium constants obtained from fits of the transient absorption decays. Given these and the energies of the ^{3}MLCT state at each pH (from the emission spectra of the bpy complex), the energy of the ^{3}IL state can be approximated. The collected values are given in Table 4.2. For the pyr-bpy complex, the energy of the ^{3}IL state obtained using this method differs by 300 cm^{-1} between values obtained in acid and base. The average of the two values is 15050 cm^{-1}. For the pyr-phen-bpy complex the ^{3}IL energy is 15400 cm^{-1} in both determinations.

The results for both chromophores are summarized by Figure 4.8 which estimates, semi-quantitatively, the energy differences between the various states involved at different degrees of protonation. It is assumed that the energy of the ^{3}IL state is unaffected by pH. In acidic solution, the Ru $(d\pi) \rightarrow$ dcbH$_2$ (π^*) ^{3}MLCT state is lowest in energy for the pyr-phen-bpy complex, but the ^{3}IL and ^{3}MLCT (dcbH$_2$) are nearly isoenergetic for the pyr-bpy complex. Upon raising the pH above pH 7, the thermally equilibrated, lowest energy ^{3}MLCT state, either Ru $(d\pi) \rightarrow$ dcb (π^*) or Ru $(d\pi) \rightarrow$ bpy (π^*), lies above the ^{3}IL state by approximately 300 cm^{-1} for the pyr-phen-bpy complex and 600 cm^{-1} for the pyr-bpy complex.

These results were borne out clearly in the nanosecond transient absorption spectra for the complexes (Figure 4.5). In acidic solution, the pyr-bpy complex shows features of the ^{3}IL state, whereas the pyr-phen-bpy complex appears to be dominated by the ^{3}MLCT state. In base, both complexes exhibit spectral features of the ^{3}IL excited state.
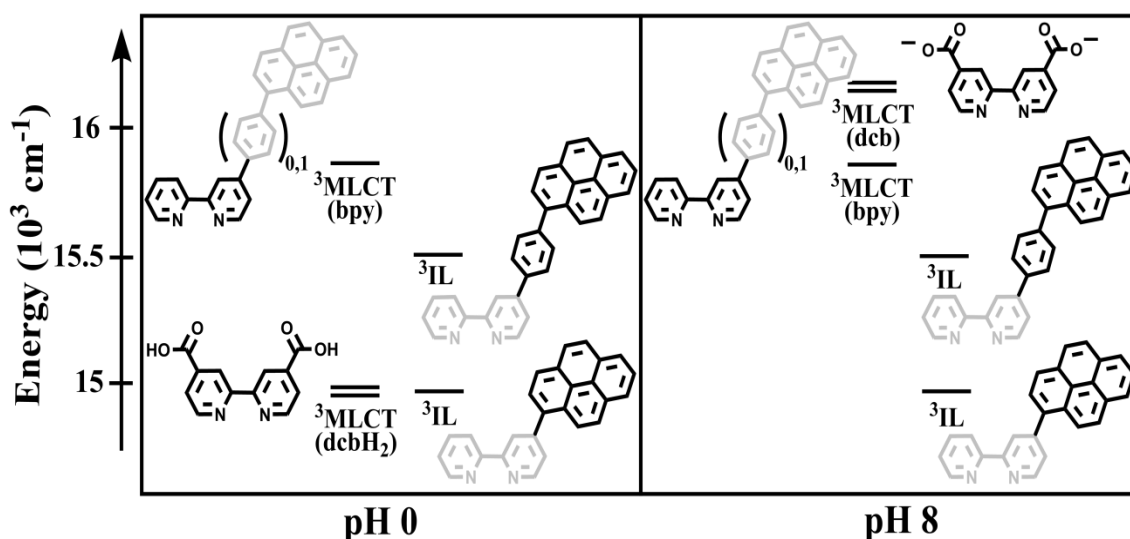
Figure 4.8. Relative energy diagram for compounds containing coupled ^{3}MLCT and aromatic hydrocarbon ^{3}IL ($^3\pi-\pi^*$) states. The relative energies are shown together for both the pyr-bpy and the pyr-ph-bpy complexes.

4.5.8 Oxygen Quenching

Both the luminescence intensity and lifetime of all the complexes are quenched by dissolved oxygen in aqueous methanol. Figure 4.9 illustrates the pH dependence of the degree of quenching of the emission lifetime as a function of dissolved oxygen from aerated solutions for both of the pyrene containing complexes. The pyr-bpy complex has a lifetime quenching ratio in basic aqueous methanol of 27 and the pyr-phen-bpy chromophore has a quenching ratio of 7.5. This figure clearly illustrates that, as the degree of protonation of the carboxybipyridine ligands increases (and the ^{3}MLCT state energy decreases), the degree of the oxygen quenching decreases.
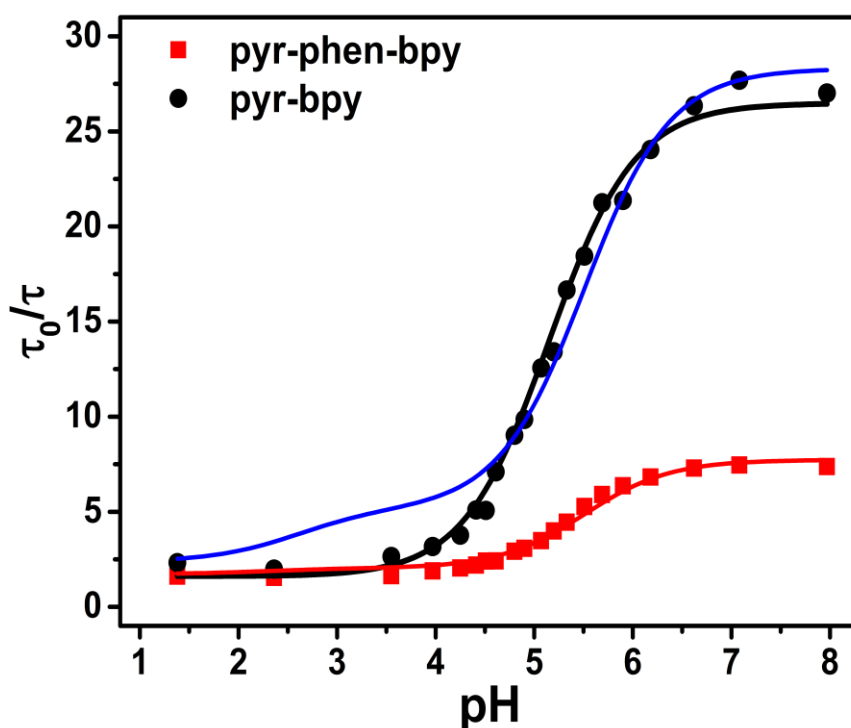
Figure 4.9. Ratio of the deoxygenated to oxygenated excited state lifetime for $[(dcbH_n)_2Ru(pyr-bpy)]^{(2n-2)+}$ (black circle) and $[(dcbH_n)_2Ru(pyr-ph-bpy)]^{(2n-2)+}$ (red square) (n = 0-2) between pH 0 and pH 8. The black and red solid lines represent fits to the data using Equation 4.9. The blue line represents the best fit obtained using the single quenching rate constant for the ^{3}MLCT and ^{3}IL states (see text).

The quenching ratio for $[Ru(dcbH_n)_2(bpy)]^{(2n-2)}$ (n = 0-2) is only weakly pH dependent and is around 2 for acidic and basic solutions. Rate constants for oxygen quenching of the three complexes in neutral aqueous methanol (pH 7) solutions ($[O_2] \sim 6 \times 10^{-4}$ M),[38] measured from luminescence lifetime changes between oxygen free and air saturated solutions, are the same for all of the complexes ($2 \pm 1 \times 10^9$ $M^{-1}s^{-1}$). Thus, the large differences in the magnitude of the quenching shown in Figure 4.9 are the result of differences in the excited state lifetimes of the complexes. The pH dependence for quenching of the two pyrene containing complexes can also be evaluated in relation to the fractional equilibrium occupation of the pyrene localized triplet state. Using the two acid dissociation constants (Equations 4.1 and 4.2, $pK_1 = 2.1$ and $pK_2 = 4.7$), the oxygen concentration in the mixed methanol:water solution and the lifetimes of the respective complexes at pH 0 and pH 8, the lifetime quenching curve can be as given as a modified Stern-Volmer equation (Equation 4.9). The terms k_{acid}, k_{inter} and k_{base} are the inverse excited state lifetimes at pH 0, an intermediate pH, and pH 8, respectively.

$$\frac{\tau_0}{\tau} = 1 + (f_{acid}k_{acid}\tau_{acid} + f_{inter}k_{inter}\tau_{inter} + f_{base}k_{base}\tau_{base})[O_2] \qquad (4.9)$$

Attempts to use one or two fractional lifetime components to fit the pH dependent quenching data resulted in poor data fits. Satisfactory modeling of the data was only achieved when a third component was added to the fit equation. The two component fit is included as the blue line in Figure 4.9. This observation clearly implies that there are variations in the lifetime and bimolecular quenching rate constant for the three forms of the complex.

The implication of these results is that the efficacy of oxygen sensors derived from Ru(II) diimine complexes covalently linked to pyrene (or other aromatic

hydrocarbons with triplet energies close to that of the Ru(II) complex ^{3}MLCT state) is dependent principally on the position of the equilibrium between the ^{3}MLCT state and the ^{3}IL state and the excited state lifetime of the ^{3}IL state. As long as luminescence can be observed from the complex, the limiting lifetime of the excited complex will increase with an increase in the fraction of the ^{3}IL state (Equation 4.6) and a decrease in the excited state decay rate constant of the aromatic hydrocarbon. Given these restrictions, the pyr-bpy complex in basic solution provides very nearly the limiting case oxygen sensing ability $\left(1-\frac{K_{eq}}{K_{eq}+1}\right)k_{CT} < \left(\frac{K_{eq}}{K_{eq}+1}\right)k_{IL}$ and is limited by the decay rate constant of the pyrene triplet.

4.6 Conclusions

The photophysical behavior of two Ru(II) complexes having a covalently linked, non-absorbing pyrene partner for electronic energy transfer were examined. Each complex has carboxybipyridine ligands that allow control of the energy of the emissive ^{3}MLCT state of the complex over the pH range 0 - 8, thereby allowing variation of the energy gap between the ^{3}MLCT state and the pyrene localized ^{3}IL state. The key observation of the work is that energy transfer between the ^{3}MLCT and ^{3}IL states can be controlled by controlling the pH of the system. From analysis of the pH dependence of the emission energy of a model complex, acid dissociation constants for the carboxylate substituents on the bipyridine ligands could be extracted. Further analysis of the luminescence decays of the pyrene complexes and the transient absorption features provided clear evidence that the two excited states are in equilibrium and that relaxation to the ground state is a weighted average of the decays of the ^{3}MLCT and ^{3}IL states. Detailed analysis of the excited state decays at pH 0 and pH 8 allowed determination of

the energy gap between the two states as well as the energy of the spectroscopically silent ^{3}IL state. Oxygen quenching of the complexes occurred with a rate constant of 2 ± 1 x $10^9 \, M^{-1}s^{-1}$ in mixed H_2O:MeOH. The degree of oxygen quenching observed varied over a wide range with changes in pH and reflected the change in the position of the equilibrium between the ^{3}MLCT and ^{3}IL states. Higher fractional occupation of the ^{3}IL state results in a longer excited state lifetime in the absence of oxygen and a higher degree of oxygen quenching. The results are useful in guiding the design of phosphorescent sensors for *in vivo* oxygen sensing in hypoxic environments, where the need to maximize oxygen quenching efficiency is paramount.

CHAPTER 4 REFERENCES

(1) Subotnik, J. E.; Vura-Weis, J.; Sodt, A. J.; Ratner, M. A. *Journal of Physical Chemistry A* **2010***, 114*, 8665-8675.

(2) Vagnini, M. T.; Caleb Rutledge, W.; Wagenknecht, P. S. *Inorg. Chem.* **2010***, 49*, 833-838.

(3) Merkel, P. B.; Dinnocenzo, J. P. *J. Photochem. Photobiol. A.* **2008***, 193*, 110-121.

(4) Demas, J. N. In *Excited state lifetime measurements;* Academic Press: New York, 1983; pp 273.

(5) Simon, J. A.; Curry, S. L.; Schmehl, R. H.; Schatz, T. R.; Piotrowiak, P.; Jin, X.; Thummel, R. P. *J. Am. Chem. Soc.* **1997***, 119*, 11012-11022.

(6) Harriman, A.; Hissler, M.; Khatyr, A.; Ziessel, R. *Chem. Commun. (Cambridge)* **1999**, 735-736.

(7) Sohna Sohna, J.; Carrier, V.; Fages, F.; Amouyal, E. *Inorg. Chem.* **2001***, 40*, 6061-6063.

(8) Gu, J.; Chen, J.; Schmehl, R. H. *J. Am. Chem. Soc.* **2010***, 132*, 7338-7346}.

(9) Tyson, D. S.; Henbest, K. B.; Bialecki, J.; Castellano, F. N. *J. Phys. Chem. A* **2001***, 105*, 8154-8161.

(10) Del Guerzo, A.; Leroy, S.; Fages, F.; Schmehl, R. H. *Inorg. Chem.* **2002***, 41*, 359-366.

(11) Benniston, A. C.; Harriman, A.; Lawrie, D. J.; Mayeux, A. *Phys. Chem. Chem. Phys.* **2004***, 6*, 51-57.

(12) Wang, X. Y.; DelGuerzo, A.; Schmehl, R. H. *J. Photochem. Photobiol., C* **2004***, 5*, 55-77.

(13) Balazs, G. C.; del Guerzo, A.; Schmehl, R. H. *Photochem. Photobiol. Sci.* **2005***, 4*, 89-94.

(14) Ji, S.; Wu, W.; Wu, W.; Guo, H.; Zhao, J. *Angew. Chem. Int. Ed.* **2011***, 50*, 1626-1629.

(15) Yeh, A. T.; Shank, C. V.; McCusker, J. K. *Science* **2000***, 289*, 935-938.

(16) Wallin, S.; Davidsson, J.; Modin, J.; Hammarström, L. *J Phys Chem A* **2005***, 109*, 4697-4704.

(17) Henry, W.; Coates, C. G.; Brady, C.; Ronayne, K. L.; Matousek, P.; Towrie, M.; Botchway, S. W.; Parker, A. W.; Vos, J. G.; Browne, W. R.; McGarvey, J. J. *J Phys Chem A* **2008***, 112*, 4537-4544.

(18) Schmehl, R. *Spectrum (Bowling Green, OH, U. S.)* **2000***, 13*, 17-21.

(19) Tyson, D. S.; Castellano, F. N. *Abstracts of Papers, 220th ACS National Meeting, Washington, DC, United States, August 20-24, 2000,* **2000**, INOR-237.

(20) Tyson, D. S.; Castellano, F. N. *J. Phys. Chem. A* **1999***, 103*, 10955-10960.

(21) Choi, N. W.; Verbridge, S. S.; Williams, R. M.; Chen, J.; Kim, J.; Schmehl, R.; Farnum, C. E.; Zipfel, W. R.; Fischbach, C.; Stroock, A. D. *Biomaterials* **2012***, 33*, 2710-2722.

(22) Giordano, P. J.; Bock, C. R.; Wrighton, M. S.; Interrante, L. V.; Williams, R. F. X. *J. Am. Chem. Soc.* **1977***, 99*, 3187-9.

(23) Nazeeruddin, M. K.; Kalyanasundaram, K. *Inorg. Chem.* **1989***, 28*, 4251-4259.

(24) Cordaro, J. G.; McCusker, J. K.; Bergman, R. G. *Chem. Commun.* **2002**, 1496-1497.

(25) Hoertz, P. G.; Staniszewski, A.; Marton, A.; Higgins, G. T.; Incarvito, C. D.; Rheingold, A. L.; Meyer, G. J. *J. Am. Chem. Soc.* **2006***, 128*, 8234.

(26) Nazeeruddin, M. K.; Zakeeruddin, S. M.; Humphrey-Baker, R.; Jirousek, M.; Liska, P.; Vlachopoulos, N.; Shklover, V.; Fischer, C. H.; Graetzel, M. *Inorg. Chem.* **1999***, 38*, 6298-6302.

(27) Freedman, D. A.; Evju, J. K.; Pomije, M. K.; Mann, K. R. *Inorg. Chem.* **2001***, 40*, 5711-5714.

(28) Chen, J. Ruthenium(II) Pyrene-Bipyridine Complexes: Synthesis, Photophysics, Photochemistry and in Vivo Oxygen Sensing, Tulane University, 2010.

(29) Grusenmeyer, T. A.; Chen, J.; Jin, Y.; Nguyen, J.; Rack, J. J.; Schmehl, R. H. *J. Am. Chem. Soc.* **2012***, 134*, 7497-7506.

(30) Curtright, A. E.; McCusker, J. K. *J. Phys. Chem. A* **1999***, 103*, 7032-7041.

(31) Damrauer, N. H.; Boussie, T. R.; Devenney, M.; McCusker, J. K. *J. Am. Chem. Soc.* **1997***, 119*, 8253-8268.

(32) Damrauer, N. H.; Cerullo, G.; Yeh, A.; McCusker, J. K. *Springer Ser. Chem. Phys.* **1998***, 63*, 627-629.

(33) Damrauer, N. H.; McCusker, J. K. *J. Phys. Chem. A* **1999**, *103*, 8440-8446.

(34) Juris, A.; Balzani, V.; Barigelletti, F.; Campagna, S.; Belser, P.; Von Zelewsky, A. *Coord. Chem. Rev.* **1988**, *84*, 85-277.

(35) Harriman, A.; Khatyr, A.; Ziessel, R. *Dalton Trans.* **2003**, 2061-2068.

(36) Ford, W. E.; Rodgers, M. A. J. *J. Phys. Chem.* **1992**, *96*, 2917-20.

(37) Birks, J. B. *J. Phys. Chem.* **1963**, *67*, 2199-2200.

(38) Korall, P.; Boerje, A.; Norrby, P. O.; Aakermark, B. *Acta Chem. Scand.* **1997**, *51*, 760-766.

APPENDIX A: CHAPTER 2 CRYSTAL INFORMATION
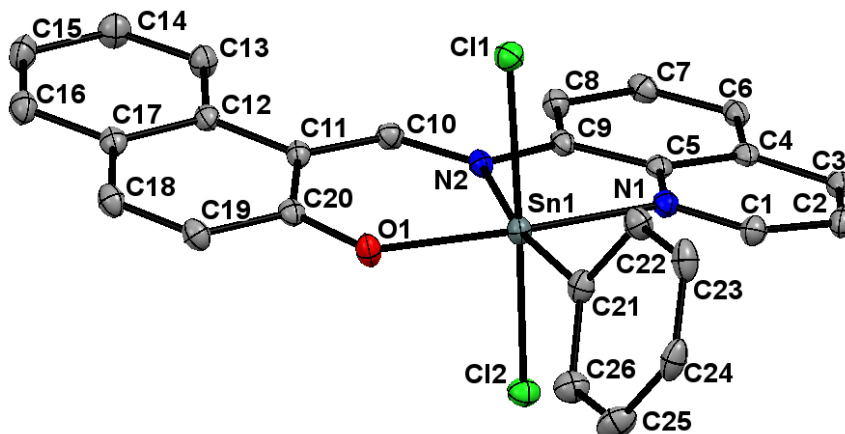
Structure Determination Summary for PhSnLnapCl$_2$

Identification code	RHS008
Empirical formula	C$_{26}$H$_{18}$Cl$_2$N$_2$OSn
Formula weight	564.01 g/mol
Temperature	100(2) K
Wavelength	0.71073 Å
Crystal size	0.100 x 0.160 x 0.160 mm
Crystal habit	orange block
Crystal system	monoclinic
Space group	P2$_1$/c
Unit cell dimensions	a = 12.2999(15) Å α = 90°
	b = 10.4788(13) Å β = 90.753(2)°
	c = 17.361(2) Å γ = 90°
Volume	2237.4(5) Å^3
Density (calculated)	1.674 g/cm^3
Absorption coefficient	1.403 mm^{-1}
F(000)	1120
θ range for data collection	2.27 to 28.95°
Limiting Indices	-16< h< 16, -14< k< 14, -23< l< 23
Reflections collected	38292
Independent reflections	5774 [R(int) = 0.0561]
Completeness to θ = 28.95°	97.6%
Absorption correction	multi-scan
Max. and min. transmission	0.8724 and 0.7162
Structure solution technique	direct methods
Refinement method	Full-matrix least-squares on F2
Data / restraints / parameters	5774 / 0 / 289
Goodness-of-fit on F2	1.047
Final R indices	4873 data; I>2σ(I) R1 = 0.0288, wR2 = 0.0639
	all data R1 = 0.0393, wR2 = 0.0696
Absolute Structure Parameter	0.004
Largest diff. peak and hole	1.079 and -0.781 eÅ^{-3}

Table S1. Atomic coordinates and equivalent isotropic atomic displacement parameters (Å^2) for PhSnLnapCl$_2$. U(eq) is defined as one third of the trace of the orthogonalized U$_{ij}$ tensor.

Atom	x/a	y/b	z/c	U(eq)
Sn1	0.739021(12)	0.781903(15)	0.586934(9)	0.01260(5)
Cl1	0.82040(5)	0.66407(6)	0.47897(3)	0.01742(12)
Cl2	0.63294(5)	0.91273(6)	0.67792(3)	0.01770(12)
O1	0.82860(14)	0.94117(16)	0.56322(10)	0.0171(4)
N1	0.59580(16)	0.65118(19)	0.59114(11)	0.0139(4)
N2	0.62625(15)	0.85236(19)	0.49751(11)	0.0130(4)
C1	0.58468(19)	0.5578(2)	0.64201(13)	0.0153(5)
C2	0.4886(2)	0.4871(2)	0.64777(14)	0.0171(5)
C3	0.4031(2)	0.5144(2)	0.59893(14)	0.0160(5)
C4	0.41265(19)	0.6129(2)	0.54400(13)	0.0137(4)
C5	0.51182(19)	0.6819(2)	0.54251(13)	0.0130(4)
C6	0.32888(19)	0.6459(2)	0.49095(13)	0.0151(5)
C7	0.3442(2)	0.7445(2)	0.44069(14)	0.0159(5)
C8	0.4414(2)	0.8160(2)	0.44092(14)	0.0157(5)
C9	0.52575(19)	0.7863(2)	0.49095(13)	0.0131(4)
C10	0.65020(19)	0.9429(2)	0.44834(13)	0.0146(5)
C11	0.74256(19)	0.0238(2)	0.44738(13)	0.0131(4)
C12	0.74773(19)	0.1203(2)	0.38667(13)	0.0135(4)
C13	0.6692(2)	0.1343(2)	0.32672(14)	0.0177(5)
C14	0.6776(2)	0.2284(3)	0.27221(15)	0.0203(5)
C15	0.7648(2)	0.3139(2)	0.27297(15)	0.0210(5)
C16	0.8426(2)	0.3035(2)	0.33006(15)	0.0191(5)
C17	0.83516(19)	0.2091(2)	0.38761(14)	0.0149(5)
C18	0.91447(19)	0.2032(2)	0.44778(14)	0.0168(5)
C19	0.90937(19)	0.1142(2)	0.50410(14)	0.0162(5)
C20	0.82478(19)	0.0220(2)	0.50544(13)	0.0134(4)
C21	0.83370(19)	0.6849(2)	0.67355(14)	0.0160(5)
C22	0.8700(2)	0.5609(2)	0.65977(15)	0.0183(5)
C23	0.9245(2)	0.4926(2)	0.71733(16)	0.0219(5)
C24	0.9457(2)	0.5485(3)	0.78816(15)	0.0220(5)
C25	0.9106(2)	0.6719(3)	0.80206(15)	0.0239(6)
C26	0.8535(2)	0.7397(3)	0.74557(15)	0.0201(5)

Table S2. Bond Lengths (Å) for PhSnLnapCl$_2$.

Bond	Length	Bond	Length
Sn1-O1	2.0447(17)	Sn1-C21	2.146(2)
Sn1-N2	2.1960(19)	Sn1-N1	2.234(2)
Sn1-Cl1	2.4676(6)	Sn1-Cl2	2.4761(6)
O1-C20	1.313(3)	N1-C1	1.326(3)
N1-C5	1.364(3)	N2-C10	1.312(3)
N2-C9	1.420(3)	C1-C2	1.399(3)
C1-H1	0.95	C2-C3	1.373(3)
C2-H2	0.95	C3-C4	1.411(3)
C3-H3	0.95	C4-C6	1.416(3)
C4-C5	1.419(3)	C5-C9	1.425(3)
C6-C7	1.367(3)	C6-H6	0.95
C7-C8	1.411(3)	C7-H7	0.95
C8-C9	1.380(3)	C8-H8	0.95
C10-C11	1.418(3)	C10-H10	0.95
C11-C20	1.419(3)	C11-C12	1.462(3)
C12-C13	1.418(3)	C12-C17	1.422(3)
C13-C14	1.372(3)	C13-H13	0.95
C14-C15	1.397(4)	C14-H14	0.95
C15-C16	1.373(4)	C15-H15	0.95
C16-C17	1.410(3)	C16-H16	0.95
C17-C18	1.421(3)	C18-C19	1.353(3)
C18-H18	0.95	C19-C20	1.420(3)
C19-H19	0.95	C21-C26	1.394(3)
C21-C22	1.396(3)	C22-C23	1.393(3)
C22-H22	0.95	C23-C24	1.384(4)
C23-H23	0.95	C24-C25	1.385(4)
C24-H24	0.95	C25-C26	1.394(4)
C25-H25	0.95	C26-H26	0.95

Table S3. Bond Angles (degrees) for PhSnLnapCl$_2$.

Atoms	Angle	Atoms	Angle
O1-Sn1-C21	103.82(8)	O1-Sn1-N2	85.43(7)
C21-Sn1-N2	170.59(8)	O1-Sn1-N1	159.15(7)
C21-Sn1-N1	96.17(8)	N2-Sn1-N1	74.82(7)
O1-Sn1-Cl1	91.75(5)	C21-Sn1-Cl1	94.21(7)
N2-Sn1-Cl1	83.68(5)	N1-Sn1-Cl1	92.63(5)
O1-Sn1-Cl2	88.08(5)	C21-Sn1-Cl2	95.80(7)
N2-Sn1-Cl2	86.08(5)	N1-Sn1-Cl2	84.04(5)
Cl1-Sn1-Cl2	169.74(2)	C20-O1-Sn1	131.77(15)
C1-N1-C5	120.2(2)	C1-N1-Sn1	124.23(16)
C5-N1-Sn1	115.22(15)	C10-N2-C9	120.2(2)
C10-N2-Sn1	123.91(16)	C9-N2-Sn1	115.71(15)
N1-C1-C2	122.2(2)	N1-C1-H1	118.9
C2-C1-H1	118.9	C3-C2-C1	119.1(2)
C3-C2-H2	120.5	C1-C2-H2	120.5
C2-C3-C4	120.0(2)	C2-C3-H3	120.0
C4-C3-H3	120.0	C3-C4-C6	123.5(2)
C3-C4-C5	117.7(2)	C6-C4-C5	118.8(2)
N1-C5-C4	120.8(2)	N1-C5-C9	118.3(2)
C4-C5-C9	120.9(2)	C7-C6-C4	119.6(2)
C7-C6-H6	120.2	C4-C6-H6	120.2
C6-C7-C8	121.6(2)	C6-C7-H7	119.2
C8-C7-H7	119.2	C9-C8-C7	120.8(2)
C9-C8-H8	119.6	C7-C8-H8	119.6
C8-C9-N2	125.9(2)	C8-C9-C5	118.2(2)
N2-C9-C5	115.8(2)	N2-C10-C11	128.8(2)
N2-C10-H10	115.6	C11-C10-H10	115.6
C10-C11-C20	123.2(2)	C10-C11-C12	117.7(2)
C20-C11-C12	119.0(2)	C13-C12-C17	116.6(2)
C13-C12-C11	124.4(2)	C17-C12-C11	118.9(2)
C14-C13-C12	121.6(2)	C14-C13-H13	119.2
C12-C13-H13	119.2	C13-C14-C15	121.3(2)
C13-C14-H14	119.4	C15-C14-H14	119.4
C16-C15-C14	118.9(2)	C16-C15-H15	120.6
C14-C15-H15	120.6	C15-C16-C17	121.1(2)
C15-C16-H16	119.4	C17-C16-H16	119.4

Table S3. Bond Angles (degrees) for PhSnLnapCl$_2$.

Atoms	Angle
C16-C17-C18	120.1(2)
C18-C17-C12	119.4(2)
C19-C18-H18	119.2
C18-C19-C20	121.4(2)
C20-C19-H19	119.3
O1-C20-C19	115.6(2)
C26-C21-C22	119.0(2)
C22-C21-Sn1	119.54(17)
C23-C22-H22	119.8
C24-C23-C22	120.2(2)
C22-C23-H23	119.9
C23-C24-H24	120.2
C24-C25-C26	120.6(2)
C26-C25-H25	119.7
C25-C26-H26	119.9
C16-C17-C12	120.5(2)
C19-C18-C17	121.5(2)
C17-C18-H18	119.2
C18-C19-H19	119.3
O1-C20-C11	124.7(2)
C11-C20-C19	119.6(2)
C26-C21-Sn1	121.32(19)
C23-C22-C21	120.5(2)
C21-C22-H22	119.8
C24-C23-H23	119.9
C23-C24-C25	119.6(2)
C25-C24-H24	120.2
C24-C25-H25	119.7
C25-C26-C21	120.1(2)
C21-C26-H26	119.9

Table S4. Anisotropic atomic displacement parameters ($\mathring{A}^2$) for PhSnLnapCl$_2$. The anisotropic atomic displacement factor exponent takes the form: $-2\pi^2[\,h^2\,a^{*2}\,U_{11} + ... + 2\,h\,k\,a^*\,b^*\,U_{12}]$.

Atom	U$_{11}$	U$_{22}$	U$_{33}$	U$_{23}$	U$_{13}$	U$_{12}$
Sn1	0.01185(8)	0.01161(8)	0.01433(8)	0.00139(6)	-0.00075(6)	-0.00096(6)
Cl1	0.0161(3)	0.0185(3)	0.0176(3)	-0.0016(2)	0.0016(2)	-0.0008(2)
Cl2	0.0184(3)	0.0167(3)	0.0180(3)	-0.0017(2)	0.0010(2)	0.0025(2)
O1	0.0181(8)	0.0138(8)	0.0192(8)	0.0030(7)	-0.0032(7)	-0.0040(7)
N1	0.0132(9)	0.0129(9)	0.0155(9)	-0.0003(8)	0.0019(7)	-0.0006(8)
N2	0.0115(9)	0.0119(9)	0.0157(9)	-0.0001(7)	0.0003(7)	-0.0015(8)
C1	0.0156(11)	0.0143(11)	0.0159(11)	0.0018(9)	0.0002(9)	0.0002(9)
C2	0.0191(12)	0.0139(11)	0.0182(12)	0.0028(9)	0.0034(9)	-0.0009(10)
C3	0.0157(11)	0.0139(11)	0.0187(11)	-0.0017(9)	0.0053(9)	-0.0039(9)
C4	0.0145(11)	0.0118(11)	0.0149(11)	-0.0032(9)	0.0039(8)	-0.0004(9)
C5	0.0134(11)	0.0113(10)	0.0144(10)	-0.0026(8)	0.0029(8)	0.0006(9)
C6	0.0125(11)	0.0138(11)	0.0189(11)	-0.0041(9)	0.0032(9)	-0.0027(9)
C7	0.0132(11)	0.0158(11)	0.0188(11)	-0.0028(9)	-0.0008(9)	0.0001(9)
C8	0.0156(11)	0.0133(11)	0.0183(11)	0.0006(9)	0.0007(9)	-0.0002(9)
C9	0.0122(10)	0.0112(11)	0.0161(11)	-0.0020(9)	0.0022(8)	-0.0005(9)
C10	0.0161(11)	0.0142(11)	0.0135(10)	-0.0002(9)	-0.0012(9)	0.0005(9)
C11	0.0128(10)	0.0106(10)	0.0159(11)	0.0006(8)	0.0019(8)	-0.0005(9)
C12	0.0127(11)	0.0125(11)	0.0154(10)	-0.0009(9)	0.0027(8)	-0.0005(9)
C13	0.0170(12)	0.0169(12)	0.0192(12)	0.0018(9)	-0.0015(9)	-0.0024(10)
C14	0.0188(12)	0.0219(13)	0.0200(12)	0.0029(10)	-0.0037(10)	-0.0006(10)
C15	0.0241(13)	0.0169(12)	0.0219(12)	0.0064(10)	0.0033(10)	-0.0009(10)
C16	0.0172(12)	0.0174(12)	0.0228(12)	0.0018(10)	0.0041(10)	-0.0024(10)
C17	0.0129(11)	0.0132(11)	0.0185(11)	-0.0006(9)	0.0023(9)	0.0006(9)
C18	0.0128(11)	0.0145(11)	0.0230(12)	-0.0003(9)	0.0004(9)	-0.0010(9)
C19	0.0135(11)	0.0145(11)	0.0204(12)	-0.0006(9)	-0.0021(9)	-0.0003(9)
C20	0.0125(10)	0.0116(11)	0.0163(11)	-0.0010(9)	0.0017(8)	0.0011(9)
C21	0.0119(11)	0.0184(12)	0.0177(11)	0.0035(9)	-0.0011(9)	-0.0012(9)
C22	0.0167(12)	0.0172(12)	0.0209(12)	-0.0003(10)	-0.0018(9)	-0.0015(10)
C23	0.0182(12)	0.0162(12)	0.0314(14)	0.0076(11)	-0.0013(10)	-0.0007(10)
C24	0.0182(12)	0.0256(14)	0.0220(12)	0.0123(11)	-0.0013(10)	-0.0023(10)
C25	0.0226(13)	0.0325(15)	0.0165(12)	0.0015(11)	-0.0022(10)	0.0024(12)
C26	0.0194(12)	0.0214(13)	0.0194(12)	-0.0003(10)	0.0000(10)	0.0028(10)

Table S5. Hydrogen atomic coordinates and isotropic atomic displacement parameters (Å^2) for PhSnLnapCl$_2$.

Atom	x/a	y/b	z/c	U(eq)
H1	0.6439	0.5383	0.6757	0.018
H2	0.4827	0.4210	0.6850	0.02
H3	0.3375	0.4671	0.6021	0.019
H6	0.2624	0.5998	0.4903	0.018
H7	0.2881	0.7654	0.4048	0.019
H8	0.4489	0.8854	0.4062	0.019
H10	0.5987	0.9559	0.4079	0.018
H13	0.6093	1.0771	0.3243	0.021
H14	0.6231	1.2356	0.2332	0.024
H15	0.7701	1.3782	0.2346	0.025
H16	0.9024	1.3608	0.3308	0.023
H18	0.9724	1.2631	0.4485	0.02
H19	0.9636	1.1134	0.5436	0.019
H22	0.8575	0.5228	0.6108	0.022
H23	0.9472	0.4074	0.7079	0.026
H24	0.9841	0.5025	0.8270	0.026
H25	0.9256	0.7106	0.8505	0.029
H26	0.8280	0.8233	0.7561	0.024
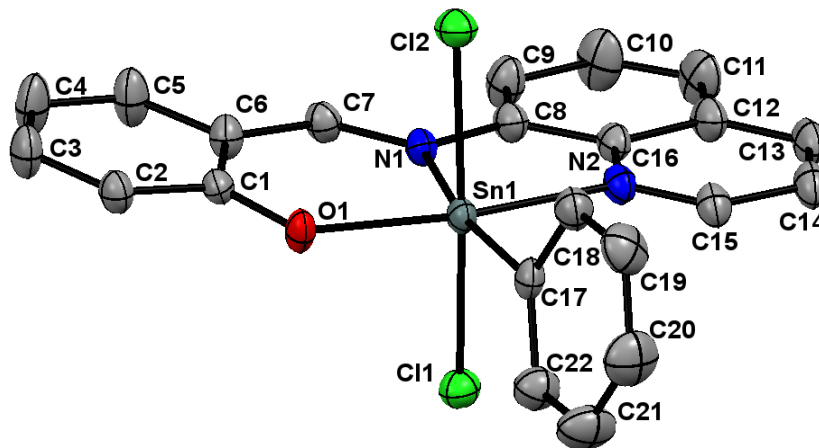
Structure Determination Summary for PhSnLsalCl$_2$

Identification code	RHS013
Empirical formula	$C_{22}H_{16}Cl_2N_2OSn$
Formula weight	513.96
Temperature	150(2) K
Wavelength	0.71073 Å
Crystal size	0.040 x 0.150 x 0.170 mm
Crystal habit	yellow plate
Crystal system	monoclinic
Space group	C2/c
Unit cell dimensions	a = 23.5629(5) Å α = 90°
	b = 11.2171(2) Å β = 90.4150(10)°
	c = 16.9265(3) Å γ = 90°
Volume	4473.68(15) Å^3
Density (calculated)	1.526 g/cm^3
Absorption coefficient	1.395 mm^{-1}
F(000)	2032
θ range for data collection	2.34 to 26.37°
Limiting Indices	-29< h< 29, -14< k< 14, -21< l< 21
Reflections collected	36088
Independent reflections	4583 [R(int) = 0.0491]
Completeness to θ = 26.37°	100.0%
Absorption correction	multi-scan
Max. and min. transmission	0.9460 and 0.7970
Refinement method	Full-matrix least-squares on F2
Data / restraints / parameters	4583 / 89 / 253
Goodness-of-fit on F2	1.047
Final R indices	4027 data; I>2σ(I) R1 = 0.0243, wR2 = 0.0623
	all data R1 = 0.0286, wR2 = 0.0643
Absolute Structure Parameter	0.001
Largest diff. peak and hole	0.689 and -0.756 eÅ^{-3}

Table S6. Atomic coordinates and equivalent isotropic atomic displacement parameters (Å^2) for PhSnLsalCl$_2$. U(eq) is defined as one third of the trace of the orthogonalized U$_{ij}$ tensor.

Atom	x	y	z	U(eq)
Sn1	0.13813(2)	0.49123(2)	0.04356(2)	0.01925(6)
Cl1	0.23219(2)	0.54587(5)	0.99034(3)	0.02810(13)
Cl2	0.05159(2)	0.39135(5)	0.08671(3)	0.02818(13)
O1	0.17495(7)	0.46426(14)	0.15125(9)	0.0251(3)
N1	0.16473(7)	0.30706(16)	0.01317(10)	0.0213(4)
N2	0.11068(8)	0.46387(18)	0.91851(11)	0.0224(4)
C1	0.19115(9)	0.3639(2)	0.18598(12)	0.0210(4)
C2	0.20338(10)	0.3694(2)	0.26767(13)	0.0254(5)
C3	0.22246(11)	0.2704(2)	0.30767(14)	0.0339(6)
C4	0.23071(12)	0.1622(2)	0.26877(15)	0.0412(7)
C5	0.21838(12)	0.1541(2)	0.18949(14)	0.0368(6)
C6	0.19786(10)	0.2541(2)	0.14643(13)	0.0251(5)
C7	0.18582(9)	0.2327(2)	0.06496(13)	0.0244(5)
C8	0.15244(9)	0.2701(2)	0.93457(13)	0.0247(5)
C9	0.16617(12)	0.1622(2)	0.90186(14)	0.0346(6)
C10	0.15123(13)	0.1355(3)	0.82315(15)	0.0442(7)
C11	0.12294(13)	0.2166(2)	0.77687(15)	0.0407(7)
C12	0.10822(10)	0.3283(2)	0.80762(13)	0.0296(5)
C13	0.07967(10)	0.4180(2)	0.76398(13)	0.0312(5)
C14	0.06857(10)	0.5251(2)	0.79712(14)	0.0307(5)
C15	0.08461(9)	0.5456(2)	0.87557(13)	0.0267(5)
C16	0.12362(9)	0.3555(2)	0.88677(12)	0.0234(5)
C17	0.10655(10)	0.6706(2)	0.05245(12)	0.0231(5)
C18	0.04851(10)	0.6907(2)	0.06122(14)	0.0293(5)
C19	0.02723(11)	0.8063(2)	0.06154(16)	0.0389(6)
C20	0.06346(13)	0.9022(3)	0.05368(18)	0.0450(7)
C21	0.12093(12)	0.8828(2)	0.04590(18)	0.0449(7)
C22	0.14254(10)	0.7679(2)	0.04451(14)	0.0327(6)

Table S7. Bond Lengths (Å) for PhSnLsalCl$_2$.

Bond	Length	Bond	Length
Sn1-O1	2.0357(15)	Sn1-C17	2.151(2)
Sn1-N1	2.2204(18)	Sn1-N2	2.2300(18)
Sn1-Cl2	2.4430(6)	Sn1-Cl1	2.4755(6)
O1-C1	1.325(3)	N1-C7	1.306(3)
N1-C8	1.421(3)	N2-C15	1.319(3)
N2-C16	1.364(3)	C1-C6	1.411(3)
C1-C2	1.412(3)	C2-C3	1.374(3)
C2-H2	0.95	C3-C4	1.395(3)
C3-H3	0.95	C4-C5	1.374(3)
C4-H4	0.95	C5-C6	1.421(3)
C5-H5	0.95	C6-C7	1.426(3)
C7-H7	0.95	C8-C9	1.371(3)
C8-C16	1.424(3)	C9-C10	1.408(3)
C9-H9	0.95	C10-C11	1.370(4)
C10-H10	0.95	C11-C12	1.402(4)
C11-H11	0.95	C12-C13	1.415(3)
C12-C16	1.419(3)	C13-C14	1.352(4)
C13-H13	0.95	C14-C15	1.397(3)
C14-H14	0.95	C15-H15	0.95
C17-C22	1.389(3)	C17-C18	1.395(3)
C18-C19	1.391(3)	C18-H18	0.95
C19-C20	1.381(4)	C19-H19	0.95
C20-C21	1.379(4)	C20-H20	0.95
C21-C22	1.385(4)	C21-H21	0.95
C22-H22	0.95		

Table S8. Bond Angles (degrees) for PhSnLsalCl$_2$.

Atoms	Angle	Atoms	Angle
O1-Sn1-C17	102.82(7)	O1-Sn1-N1	87.13(6)
C17-Sn1-N1	170.05(7)	O1-Sn1-N2	161.49(7)
C17-Sn1-N2	95.57(7)	N1-Sn1-N2	74.48(7)
O1-Sn1-Cl2	90.88(5)	C17-Sn1-Cl2	96.79(6)
N1-Sn1-Cl2	83.12(5)	N2-Sn1-Cl2	89.06(5)
O1-Sn1-Cl1	89.18(5)	C17-Sn1-Cl1	96.02(6)
N1-Sn1-Cl1	83.75(5)	N2-Sn1-Cl1	86.73(5)
Cl2-Sn1-Cl1	166.85(2)	C1-O1-Sn1	130.04(14)
C7-N1-C8	121.05(19)	C7-N1-Sn1	123.08(14)
C8-N1-Sn1	115.62(14)	C15-N2-C16	120.45(19)
C15-N2-Sn1	123.92(16)	C16-N2-Sn1	115.61(14)
O1-C1-C6	124.33(19)	O1-C1-C2	117.0(2)
C6-C1-C2	118.7(2)	C3-C2-C1	120.8(2)
C3-C2-H2	119.6	C1-C2-H2	119.6
C2-C3-C4	121.1(2)	C2-C3-H3	119.4
C4-C3-H3	119.4	C5-C4-C3	119.3(2)
C5-C4-H4	120.4	C3-C4-H4	120.4
C4-C5-C6	121.2(2)	C4-C5-H5	119.4
C6-C5-H5	119.4	C1-C6-C5	119.00(19)
C1-C6-C7	125.7(2)	C5-C6-C7	115.3(2)
N1-C7-C6	127.8(2)	N1-C7-H7	116.1
C6-C7-H7	116.1	C9-C8-N1	126.1(2)
C9-C8-C16	118.6(2)	N1-C8-C16	115.38(19)
C8-C9-C10	120.8(2)	C8-C9-H9	119.6
C10-C9-H9	119.6	C11-C10-C9	121.2(2)
C11-C10-H10	119.4	C9-C10-H10	119.4
C10-C11-C12	120.1(2)	C10-C11-H11	119.9
C12-C11-H11	119.9	C11-C12-C13	124.0(2)
C11-C12-C16	118.7(2)	C13-C12-C16	117.2(2)
C14-C13-C12	120.5(2)	C14-C13-H13	119.8
C12-C13-H13	119.8	C13-C14-C15	119.3(2)
C13-C14-H14	120.4	C15-C14-H14	120.4
N2-C15-C14	122.1(2)	N2-C15-H15	119.0
C14-C15-H15	119.0	N2-C16-C12	120.5(2)
N2-C16-C8	118.89(19)	C12-C16-C8	120.6(2)

Table S8. Bond Angles (degrees) for PhSnLsalCl$_2$.

Atoms	Angle	Atoms	Angle
C22-C17-C18	118.9(2)	C22-C17-Sn1	121.09(17)
C18-C17-Sn1	119.88(17)	C19-C18-C17	120.3(2)
C19-C18-H18	119.9	C17-C18-H18	119.9
C20-C19-C18	120.2(2)	C20-C19-H19	119.9
C18-C19-H19	119.9	C21-C20-C19	119.6(3)
C21-C20-H20	120.2	C19-C20-H20	120.2
C20-C21-C22	120.7(3)	C20-C21-H21	119.7
C22-C21-H21	119.7	C21-C22-C17	120.3(2)
C21-C22-H22	119.9	C17-C22-H22	119.9

Table S9. Anisotropic atomic displacement parameters (Å^2) for PhSnLsalCl$_2$. The anisotropic atomic displacement factor exponent takes the form: $-2\pi^2[\,h^2\,a^{*2}\,U_{11} + ... + 2\,h\,k\,a^*\,b^*\,U_{12}]$.

Atom	U$_{11}$	U$_{22}$	U$_{33}$	U$_{23}$	U$_{13}$	U$_{12}$
Sn1	0.02225(10)	0.02140(10)	0.01404(9)	0.00008(5)	-0.00289(6)	-0.00033(6)
Cl1	0.0248(3)	0.0284(3)	0.0311(3)	0.0041(2)	0.0017(2)	-0.0001(2)
Cl2	0.0272(3)	0.0315(3)	0.0259(3)	-0.0009(2)	0.0017(2)	-0.0057(2)
O1	0.0365(9)	0.0215(8)	0.0170(8)	0.0002(6)	-0.0085(7)	0.0010(7)
N1	0.0240(10)	0.0241(10)	0.0157(9)	-0.0003(7)	-0.0025(7)	-0.0011(8)
N2	0.0231(10)	0.0284(10)	0.0156(9)	-0.0014(8)	-0.0011(7)	0.0007(8)
C1	0.0190(11)	0.0249(12)	0.0189(11)	0.0018(9)	-0.0035(8)	-0.0005(9)
C2	0.0291(12)	0.0268(12)	0.0201(11)	-0.0023(9)	-0.0046(9)	0.0013(9)
C3	0.0445(15)	0.0365(14)	0.0205(12)	0.0001(10)	-0.0106(11)	0.0066(12)
C4	0.0640(19)	0.0299(14)	0.0294(14)	0.0030(11)	-0.0146(13)	0.0146(13)
C5	0.0539(17)	0.0283(13)	0.0279(13)	-0.0031(10)	-0.0136(12)	0.0129(12)
C6	0.0283(12)	0.0266(12)	0.0204(11)	0.0007(9)	-0.0045(9)	0.0046(9)
C7	0.0272(12)	0.0234(12)	0.0227(11)	-0.0031(9)	-0.0032(9)	0.0007(9)
C8	0.0279(12)	0.0281(12)	0.0180(11)	-0.0020(9)	-0.0015(9)	-0.0027(9)
C9	0.0516(16)	0.0302(13)	0.0221(12)	-0.0023(10)	-0.0052(11)	0.0032(12)
C10	0.072(2)	0.0342(15)	0.0266(13)	-0.0122(11)	-0.0059(13)	0.0061(14)
C11	0.0615(18)	0.0404(16)	0.0200(12)	-0.0088(11)	-0.0066(12)	-0.0023(13)
C12	0.0343(14)	0.0374(14)	0.0170(11)	-0.0020(10)	-0.0027(10)	-0.0044(11)
C13	0.0319(13)	0.0473(16)	0.0145(11)	0.0003(10)	-0.0044(9)	-0.0031(11)
C14	0.0278(13)	0.0442(15)	0.0199(12)	0.0033(10)	-0.0037(10)	0.0027(11)
C15	0.0236(12)	0.0359(13)	0.0205(11)	0.0002(10)	-0.0021(9)	0.0042(10)
C16	0.0247(12)	0.0302(12)	0.0152(10)	-0.0008(9)	-0.0002(9)	-0.0017(9)
C17	0.0285(12)	0.0253(12)	0.0156(10)	0.0020(9)	-0.0042(9)	0.0024(9)
C18	0.0312(13)	0.0302(13)	0.0263(12)	0.0010(10)	-0.0045(10)	0.0003(10)
C19	0.0297(13)	0.0377(15)	0.0493(16)	0.0009(12)	-0.0055(12)	0.0094(11)
C20	0.0488(17)	0.0289(15)	0.0575(18)	0.0028(13)	0.0007(14)	0.0108(12)
C21	0.0422(16)	0.0261(14)	0.066(2)	0.0040(13)	0.0030(14)	-0.0016(12)
C22	0.0328(14)	0.0277(13)	0.0377(15)	0.0001(10)	0.0004(11)	0.0005(10)

Table S10. Hydrogen atomic coordinates and isotropic atomic displacement parameters (Å^2) for PhSnLsalCl$_2$.

Atom	x	y	z	U(eq)
H2	0.1984	0.4423	0.2953	0.03
H3	0.2302	0.2758	0.3627	0.041
H4	0.2447	0.0948	0.2968	0.049
H5	0.2237	0.0803	0.1630	0.044
H7	0.1942	0.1549	0.0461	0.029
H9	0.1860	0.1047	-0.0673	0.042
H10	0.1609	0.0600	-0.1983	0.053
H11	0.1133	0.1970	-0.2762	0.049
H13	0.0682	0.4029	-0.2890	0.037
H14	0.0501	0.5857	-0.2326	0.037
H15	0.0765	0.6208	-0.1013	0.032
H18	0.0234	0.6250	0.0670	0.035
H19	-0.0124	0.8193	0.0672	0.047
H20	0.0489	0.9812	0.0536	0.054
H21	0.1460	0.9488	0.0414	0.054
H22	0.1821	0.7557	0.0381	0.039
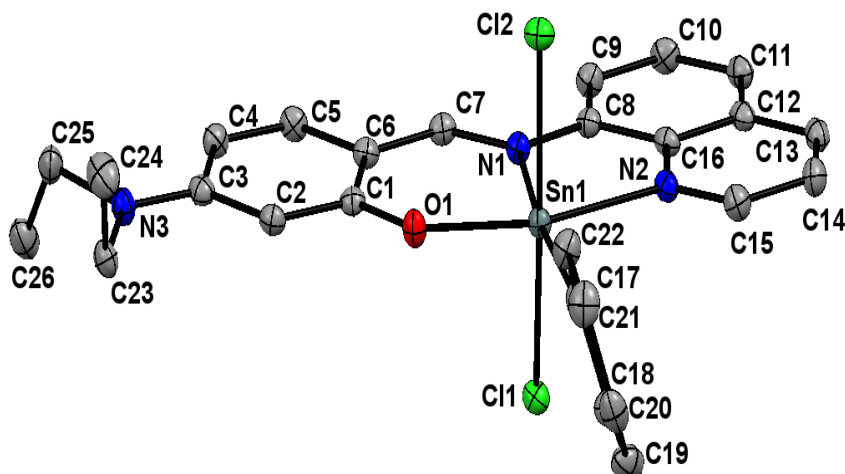
Structure Determination Summary for PhSnLdeaCl$_2$

Identification code	RHS015
Empirical formula	C$_{27}$H$_{27}$Cl$_4$N$_3$OSn
Formula weight	670.00
Temperature	100(2) K
Wavelength	1.54178 Å
Crystal size	0.050 x 0.160 x 0.260 mm
Crystal habit	orange slab
Crystal system	triclinic
Space group	P$\bar{1}$
Unit cell dimensions	a = 9.4970(6) Å α = 79.475(2)°
	b = 11.2897(7) Å β = 85.523(2)°
	c = 12.8081(8) Å γ = 89.2860(10)°
Volume	1346.04(15) Å^3
Density (calculated)	1.653 g/cm^3
Absorption coefficient	11.415 mm^{-1}
F(000)	672
θ range for data collection	3.52 to 69.78°
Limiting Indices	-11< h< 11, -13< k< 13, -14< l< 15
Reflections collected	19798
Independent reflections	4970 [R(int) = 0.0326]
Completeness to θ = 69.78°	97.5%
Absorption correction	numerical
Max. and min. transmission	0.5990 and 0.1550
Refinement method	Full-matrix least-squares on F2
Data / restraints / parameters	4970 / 0 / 327
Goodness-of-fit on F2	1.067
Final R indices	4858 data; I>2σ(I) R1 = 0.0191, wR2 = 0.0469
	all data R1 = 0.0197, wR2 = 0.0473
Absolute Structure Parameter	0.001
Largest diff. peak and hole	0.390 and -0.506 eÅ^{-3}

Table S11. Atomic coordinates and equivalent isotropic atomic displacement parameters ($\mathring{A}^2$) for PhSnLdeaCl$_2$. U(eq) is defined as one third of the trace of the orthogonalized U$_{ij}$ tensor.

Atom	x	y	z	U(eq)
Sn1	0.22174(2)	0.26637(2)	0.16442(2)	0.01319(5)
Cl1	0.05907(4)	0.12366(4)	0.28838(3)	0.01725(9)
Cl2	0.34202(4)	0.42009(4)	0.02522(3)	0.01865(9)
O1	0.19252(13)	0.39355(11)	0.25810(10)	0.0171(3)
N1	0.02824(15)	0.32596(13)	0.09202(12)	0.0142(3)
N2	0.20388(15)	0.15576(13)	0.03740(12)	0.0153(3)
N3	0.99544(16)	0.70236(14)	0.42920(12)	0.0185(3)
C1	0.08671(18)	0.46974(15)	0.26709(14)	0.0145(3)
C2	0.09348(18)	0.54250(15)	0.34272(14)	0.0156(4)
C3	0.98836(19)	0.63004(16)	0.35667(14)	0.0167(4)
C4	0.87288(19)	0.64037(16)	0.28980(15)	0.0183(4)
C5	0.86617(19)	0.56849(16)	0.21666(15)	0.0176(4)
C6	0.97014(18)	0.47970(15)	0.20110(14)	0.0153(3)
C7	0.94870(18)	0.41333(15)	0.12180(14)	0.0156(4)
C8	0.98742(18)	0.26492(15)	0.01279(14)	0.0151(3)
C9	0.86486(19)	0.28334(16)	0.96037(15)	0.0178(4)
C10	0.8382(2)	0.21805(17)	0.88058(15)	0.0196(4)
C11	0.93102(19)	0.13416(16)	0.85119(14)	0.0180(4)
C12	0.05730(19)	0.11172(16)	0.90271(14)	0.0166(4)
C13	0.16044(19)	0.02815(16)	0.87705(14)	0.0181(4)
C14	0.2810(2)	0.01160(16)	0.93038(15)	0.0196(4)
C15	0.29899(19)	0.07712(16)	0.01145(15)	0.0183(4)
C16	0.08449(18)	0.17629(15)	0.98395(14)	0.0150(3)
C17	0.41093(18)	0.18583(16)	0.22643(14)	0.0167(4)
C18	0.4075(2)	0.07168(17)	0.29070(16)	0.0216(4)
C19	0.5275(2)	0.02358(18)	0.33873(16)	0.0249(4)
C20	0.6518(2)	0.08901(18)	0.32355(15)	0.0231(4)
C21	0.6580(2)	0.20126(18)	0.25847(17)	0.0245(4)
C22	0.5386(2)	0.24948(17)	0.20943(16)	0.0207(4)
C23	0.1094(2)	0.69365(17)	0.50109(15)	0.0197(4)
C24	0.2363(2)	0.7715(2)	0.45170(18)	0.0298(5)
C25	0.8937(2)	0.80164(17)	0.43482(16)	0.0224(4)
C26	0.7540(2)	0.76076(19)	0.49632(16)	0.0273(4)
C27	0.4696(2)	0.58039(19)	0.23618(17)	0.0274(4)

Table S11. Atomic coordinates and equivalent isotropic atomic displacement parameters (Å^2) for PhSnLdeaCl$_2$. U(eq) is defined as one third of the trace of the orthogonalized U$_{ij}$ tensor.

Atom	x	y	z	U(eq)
Cl3	0.52199(5)	0.73394(4)	0.21411(4)	0.02848(11)
Cl4	0.50258(6)	0.50607(5)	0.36530(4)	0.03529(12)

Table S12. Bond Lengths (Å) for PhSnLdeaCl$_2$.

Bond	Length	Bond	Length
Sn1-O1	2.0361(12)	Sn1-C17	2.1457(18)
Sn1-N1	2.1673(15)	Sn1-N2	2.2417(15)
Sn1-Cl2	2.4692(4)	Sn1-Cl1	2.4995(4)
O1-C1	1.326(2)	N1-C7	1.328(2)
N1-C8	1.407(2)	N2-C15	1.325(2)
N2-C16	1.366(2)	N3-C3	1.350(2)
N3-C23	1.466(2)	N3-C25	1.479(2)
C1-C2	1.385(3)	C1-C6	1.435(3)
C2-C3	1.420(2)	C2-H2	0.95
C3-C4	1.434(3)	C4-C5	1.352(3)
C4-H4	0.95	C5-C6	1.427(2)
C5-H5	0.95	C6-C7	1.396(3)
C7-H7	0.95	C8-C9	1.383(3)
C8-C16	1.431(2)	C9-C10	1.404(3)
C9-H9	0.95	C10-C11	1.369(3)
C10-H10	0.95	C11-C12	1.412(3)
C11-H11	0.95	C12-C13	1.413(3)
C12-C16	1.416(3)	C13-C14	1.372(3)
C13-H13	0.95	C14-C15	1.402(3)
C14-H14	0.95	C15-H15	0.95
C17-C18	1.396(3)	C17-C22	1.399(3)
C18-C19	1.394(3)	C18-H18	0.95
C19-C20	1.382(3)	C19-H19	0.95
C20-C21	1.383(3)	C20-H20	0.95
C21-C22	1.396(3)	C21-H21	0.95
C22-H22	0.95	C23-C24	1.526(3)
C23-H23A	0.99	C23-H23B	0.99
C24-H24A	0.98	C24-H24B	0.98
C24-H24C	0.98	C25-C26	1.521(3)
C25-H25A	0.99	C25-H25B	0.99
C26-H26A	0.98	C26-H26B	0.98
C26-H26C	0.98	C27-Cl4	1.762(2)
C27-Cl3	1.776(2)	C27-H27A	0.99
C27-H27B	0.99		

Table S13. Bond Angles (degrees) for PhSnLdeaCl$_2$.

Atoms	Angle	Atoms	Angle
O1-Sn1-C17	98.63(6)	O1-Sn1-N1	88.96(5)
C17-Sn1-N1	172.14(6)	O1-Sn1-N2	163.55(5)
C17-Sn1-N2	97.61(6)	N1-Sn1-N2	74.91(5)
O1-Sn1-Cl2	88.76(4)	C17-Sn1-Cl2	95.93(5)
N1-Sn1-Cl2	86.23(4)	N2-Sn1-Cl2	87.02(4)
O1-Sn1-Cl1	91.32(4)	C17-Sn1-Cl1	94.70(5)
N1-Sn1-Cl1	83.02(4)	N2-Sn1-Cl1	89.90(4)
Cl2-Sn1-Cl1	169.243(15)	C1-O1-Sn1	130.48(11)
C7-N1-C8	120.75(15)	C7-N1-Sn1	122.57(12)
C8-N1-Sn1	116.66(11)	C15-N2-C16	120.16(16)
C15-N2-Sn1	125.24(12)	C16-N2-Sn1	114.60(11)
C3-N3-C23	122.48(15)	C3-N3-C25	121.38(16)
C23-N3-C25	115.97(15)	O1-C1-C2	117.13(16)
O1-C1-C6	122.55(16)	C2-C1-C6	120.31(16)
C1-C2-C3	121.85(17)	C1-C2-H2	119.1
C3-C2-H2	119.1	N3-C3-C2	122.11(17)
N3-C3-C4	120.31(16)	C2-C3-C4	117.57(16)
C5-C4-C3	120.35(17)	C5-C4-H4	119.8
C3-C4-H4	119.8	C4-C5-C6	123.24(17)
C4-C5-H5	118.4	C6-C5-H5	118.4
C7-C6-C5	116.33(16)	C7-C6-C1	126.99(16)
C5-C6-C1	116.67(16)	N1-C7-C6	128.33(17)
N1-C7-H7	115.8	C6-C7-H7	115.8
C9-C8-N1	126.47(16)	C9-C8-C16	117.78(16)
N1-C8-C16	115.75(15)	C8-C9-C10	120.82(17)
C8-C9-H9	119.6	C10-C9-H9	119.6
C11-C10-C9	122.02(17)	C11-C10-H10	119.0
C9-C10-H10	119.0	C10-C11-C12	119.29(17)
C10-C11-H11	120.4	C12-C11-H11	120.4
C11-C12-C13	123.49(17)	C11-C12-C16	119.11(17)
C13-C12-C16	117.40(17)	C14-C13-C12	120.15(17)
C14-C13-H13	119.9	C12-C13-H13	119.9
C13-C14-C15	119.11(17)	C13-C14-H14	120.4
C15-C14-H14	120.4	N2-C15-C14	122.04(17)
N2-C15-H15	119.0	C14-C15-H15	119.0

Table S13. Bond Angles (degrees) for PhSnLdeaCl$_2$.

Atoms	Angle	Atoms	Angle
N2-C16-C12	121.11(16)	N2-C16-C8	117.91(16)
C12-C16-C8	120.98(16)	C18-C17-C22	118.33(17)
C18-C17-Sn1	120.68(13)	C22-C17-Sn1	120.85(13)
C19-C18-C17	120.80(18)	C19-C18-H18	119.6
C17-C18-H18	119.6	C20-C19-C18	120.16(18)
C20-C19-H19	119.9	C18-C19-H19	119.9
C19-C20-C21	119.87(18)	C19-C20-H20	120.1
C21-C20-H20	120.1	C20-C21-C22	120.23(18)
C20-C21-H21	119.9	C22-C21-H21	119.9
C21-C22-C17	120.57(18)	C21-C22-H22	119.7
C17-C22-H22	119.7	N3-C23-C24	112.02(16)
N3-C23-H23A	109.2	C24-C23-H23A	109.2
N3-C23-H23B	109.2	C24-C23-H23B	109.2
H23A-C23-H23B	107.9	C23-C24-H24A	109.5
C23-C24-H24B	109.5	H24A-C24-H24B	109.5
C23-C24-H24C	109.5	H24A-C24-H24C	109.5
H24B-C24-H24C	109.5	N3-C25-C26	113.49(16)
N3-C25-H25A	108.9	C26-C25-H25A	108.9
N3-C25-H25B	108.9	C26-C25-H25B	108.9
H25A-C25-H25B	107.7	C25-C26-H26A	109.5
C25-C26-H26B	109.5	H26A-C26-H26B	109.5
C25-C26-H26C	109.5	H26A-C26-H26C	109.5
H26B-C26-H26C	109.5	Cl4-C27-Cl3	111.39(12)
Cl4-C27-H27A	109.4	Cl3-C27-H27A	109.4
Cl4-C27-H27B	109.4	Cl3-C27-H27B	109.4
H27A-C27-H27B	108.0		

Table S14. Anisotropic atomic displacement parameters (Å^2) for PhSnLdeaCl$_2$. The anisotropic atomic displacement factor exponent takes the form: $-2\pi^2[\,h^2\,a^{*2}\,U_{11} + ... + 2\,h\,k\,a^*\,b^*\,U_{12}]$.

Atom	U$_{11}$	U$_{22}$	U$_{33}$	U$_{23}$	U$_{13}$	U$_{12}$
Sn1	0.01112(7)	0.01553(7)	0.01380(7)	-0.00385(4)	-0.00372(4)	0.00060(4)
Cl1	0.0151(2)	0.0202(2)	0.0166(2)	-0.00351(16)	-0.00175(15)	-0.00176(15)
Cl2	0.0164(2)	0.0211(2)	0.0178(2)	-0.00071(16)	-0.00358(16)	-0.00302(16)
O1	0.0147(6)	0.0203(6)	0.0187(7)	-0.0080(5)	-0.0062(5)	0.0037(5)
N1	0.0123(7)	0.0156(7)	0.0153(7)	-0.0036(6)	-0.0034(6)	-0.0004(5)
N2	0.0150(7)	0.0172(7)	0.0143(8)	-0.0035(6)	-0.0026(6)	-0.0016(6)
N3	0.0183(8)	0.0212(8)	0.0175(8)	-0.0071(6)	-0.0038(6)	0.0028(6)
C1	0.0127(8)	0.0150(8)	0.0154(9)	-0.0013(6)	-0.0011(7)	-0.0018(6)
C2	0.0140(8)	0.0180(9)	0.0152(9)	-0.0025(7)	-0.0040(7)	-0.0001(7)
C3	0.0162(9)	0.0178(9)	0.0158(9)	-0.0023(7)	-0.0005(7)	-0.0024(7)
C4	0.0160(9)	0.0206(9)	0.0183(9)	-0.0036(7)	-0.0019(7)	0.0028(7)
C5	0.0138(8)	0.0217(9)	0.0178(9)	-0.0039(7)	-0.0046(7)	0.0006(7)
C6	0.0133(8)	0.0170(8)	0.0154(9)	-0.0018(7)	-0.0016(7)	-0.0005(6)
C7	0.0116(8)	0.0175(8)	0.0174(9)	-0.0015(7)	-0.0033(7)	-0.0001(6)
C8	0.0150(8)	0.0156(8)	0.0147(9)	-0.0020(7)	-0.0020(7)	-0.0021(6)
C9	0.0159(9)	0.0188(9)	0.0192(9)	-0.0038(7)	-0.0050(7)	0.0008(7)
C10	0.0177(9)	0.0220(9)	0.0202(10)	-0.0034(7)	-0.0087(7)	-0.0002(7)
C11	0.0210(9)	0.0189(9)	0.0152(9)	-0.0039(7)	-0.0053(7)	-0.0038(7)
C12	0.0181(9)	0.0175(9)	0.0138(9)	-0.0018(7)	-0.0009(7)	-0.0040(7)
C13	0.0204(9)	0.0186(9)	0.0160(9)	-0.0050(7)	-0.0001(7)	-0.0035(7)
C14	0.0185(9)	0.0205(9)	0.0209(10)	-0.0069(7)	-0.0006(7)	0.0013(7)
C15	0.0151(9)	0.0217(9)	0.0188(9)	-0.0050(7)	-0.0031(7)	0.0007(7)
C16	0.0142(8)	0.0174(8)	0.0133(9)	-0.0015(7)	-0.0027(7)	-0.0027(7)
C17	0.0123(8)	0.0229(9)	0.0168(9)	-0.0079(7)	-0.0037(7)	0.0035(7)
C18	0.0171(9)	0.0238(10)	0.0229(10)	-0.0018(8)	-0.0019(7)	0.0008(7)
C19	0.0232(10)	0.0269(10)	0.0227(10)	0.0005(8)	-0.0036(8)	0.0062(8)
C20	0.0183(9)	0.0335(11)	0.0199(10)	-0.0093(8)	-0.0076(7)	0.0094(8)
C21	0.0153(9)	0.0298(10)	0.0308(11)	-0.0099(8)	-0.0068(8)	-0.0005(8)
C22	0.0174(9)	0.0208(9)	0.0252(10)	-0.0057(7)	-0.0054(7)	0.0009(7)
C23	0.0211(9)	0.0234(9)	0.0162(9)	-0.0074(7)	-0.0032(7)	-0.0002(7)
C24	0.0264(11)	0.0355(12)	0.0292(12)	-0.0102(9)	-0.0010(9)	-0.0094(9)
C25	0.0277(10)	0.0204(9)	0.0205(10)	-0.0072(7)	-0.0046(8)	0.0059(8)
C26	0.0285(11)	0.0335(11)	0.0202(10)	-0.0061(8)	-0.0028(8)	0.0106(9)
C27	0.0268(11)	0.0308(11)	0.0249(11)	-0.0059(8)	-0.0013(8)	-0.0084(8)

Table S14. Anisotropic atomic displacement parameters ($\mathring{A}^2$) for PhSnLdeaCl$_2$. The anisotropic atomic displacement factor exponent takes the form: $-2\pi^2[\, h^2\, a^{*2}\, U_{11} + ... + 2\, h\, k\, a^*\, b^*\, U_{12}]$.

Atom	U$_{11}$	U$_{22}$	U$_{33}$	U$_{23}$	U$_{13}$	U$_{12}$
Cl3	0.0191(2)	0.0289(2)	0.0375(3)	-0.0042(2)	-0.00676(19)	-0.00139(18)
Cl4	0.0330(3)	0.0394(3)	0.0315(3)	0.0011(2)	-0.0072(2)	-0.0054(2)

Table S15. Hydrogen atomic coordinates and isotropic atomic displacement parameters ($\mathring{A}^2$) for PhSnLdeaCl$_2$.

Atom	x	y	z	U(eq)
H2	0.1706	0.5336	0.3865	0.019
H4	-0.1993	0.6980	0.2969	0.022
H5	-0.2116	0.5775	0.1735	0.021
H7	-0.1333	0.4332	0.0843	0.019
H9	-0.2021	0.3409	-0.0214	0.021
H10	-0.2469	0.2325	-0.1541	0.024
H11	-0.0893	0.0915	-0.2033	0.022
H13	0.1463	-0.0166	-0.1773	0.022
H14	0.3513	-0.0435	-0.0874	0.024
H15	0.3820	0.0647	0.0489	0.022
H18	0.3224	0.0262	0.3019	0.026
H19	0.5238	-0.0544	0.3820	0.03
H20	0.7328	0.0569	0.3577	0.028
H21	0.7438	0.2457	0.2471	0.029
H22	0.5440	0.3262	0.1641	0.025
H23A	0.1397	0.6086	0.5189	0.024
H23B	0.0734	0.7194	0.5681	0.024
H24A	0.2726	0.7461	0.3855	0.045
H24B	0.3105	0.7622	0.5017	0.045
H24C	0.2075	0.8561	0.4362	0.045
H25A	-0.1248	0.8408	0.3615	0.027
H25B	-0.0632	0.8626	0.4691	0.027
H26A	-0.2945	0.7072	0.4585	0.041
H26B	-0.3053	0.8312	0.5024	0.041
H26C	-0.2283	0.7175	0.5676	0.041
H27A	0.3676	0.5756	0.2265	0.033
H27B	0.5219	0.5395	0.1830	0.033
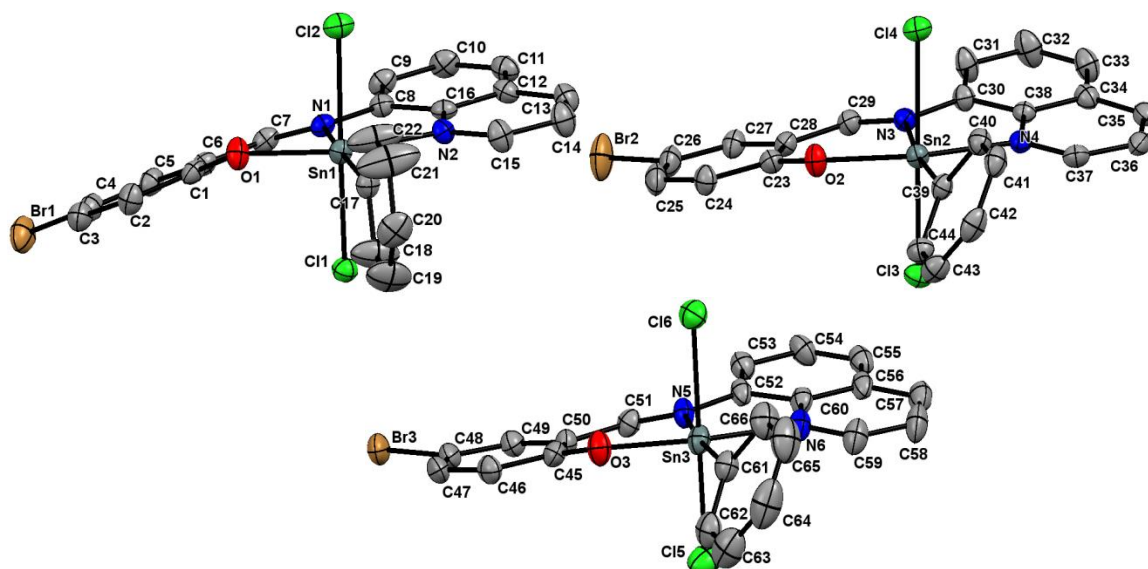
Structure Determination Summary for PhSnLBrCl$_2$

Identification code	RHS012
Empirical formula	C$_{22}$H$_{15}$BrCl$_2$N$_2$OSn
Formula weight	592.86
Temperature	150(2) K
Wavelength	0.71073 Å
Crystal size	0.110 x 0.150 x 0.180 mm
Crystal habit	orange block
Crystal system	monoclinic
Space group	P2$_1$/n
Unit cell dimensions	a = 23.2013(8) Å α = 90°
	b = 10.8280(4) Å β = 98.767(2)°
	c = 28.3103(9) Å γ = 90°
Volume	7029.1(4) Å^3
Density (calculated)	1.681 g/cm^3
Absorption coefficient	3.039 mm^{-1}
F(000)	3456
θ range for data collection	1.78 to 30.51°
Limiting Indices	-33< h< 33, -15< k< 15, -40< l< 40
Reflections collected	129329
Independent reflections	21467 [R(int) = 0.0693]
Completeness to θ = 30.51°	100.0%
Absorption correction	multi-scan
Max. and min. transmission	0.7310 and 0.6110
Refinement method	Full-matrix least-squares on F2
Data / restraints / parameters	21467 / 276 / 784
Goodness-of-fit on F2	1.054
Final R indices	15701 data; I>2σ(I) R1 = 0.0389, wR2 = 0.0772
	all data R1 = 0.0609, wR2 = 0.0832
Absolute Structure Parameter	0.003
Largest diff. peak and hole	1.844 and -1.895 eÅ^{-3}

Table S16. Atomic coordinates and equivalent isotropic atomic displacement parameters (Å^2) for PhSnLBrCl$_2$. U(eq) is defined as one third of the trace of the orthogonalized U$_{ij}$ tensor.

Atom	x	y	z	U(eq)
Sn1	0.90014(2)	0.93797(2)	0.08707(2)	0.02048(5)
Br1	0.97713(2)	0.46781(3)	0.91182(2)	0.04164(9)
Cl1	0.93745(3)	0.74540(6)	0.12762(3)	0.02624(15)
Cl2	0.88639(3)	0.13520(7)	0.04350(3)	0.02887(16)
O1	0.86753(8)	0.84713(19)	0.02599(7)	0.0277(5)
N1	0.98575(10)	0.9262(2)	0.06065(8)	0.0214(5)
N2	0.96238(10)	0.0444(2)	0.13964(8)	0.0220(5)
C1	0.89453(13)	0.7641(3)	0.00253(10)	0.0237(6)
C2	0.86010(13)	0.6752(3)	0.97539(11)	0.0299(7)
C3	0.88373(14)	0.5890(3)	0.94817(11)	0.0312(7)
C4	0.94373(14)	0.5896(3)	0.94760(10)	0.0297(7)
C5	0.97915(13)	0.6741(3)	0.97382(10)	0.0261(6)
C6	0.95552(12)	0.7631(3)	0.00216(10)	0.0232(6)
C7	0.99622(12)	0.8437(3)	0.02936(10)	0.0224(6)
C8	0.03176(12)	0.9960(3)	0.08712(10)	0.0214(6)
C9	0.08661(13)	0.0107(3)	0.07572(11)	0.0275(6)
C10	0.12872(13)	0.0829(3)	0.10497(11)	0.0303(7)
C11	0.11626(13)	0.1395(3)	0.14528(11)	0.0290(7)
C12	0.06002(12)	0.1286(3)	0.15774(11)	0.0250(6)
C13	0.04332(14)	0.1839(3)	0.19886(11)	0.0308(7)
C14	0.98778(14)	0.1701(3)	0.20839(12)	0.0351(8)
C15	0.94807(13)	0.0994(3)	0.17779(11)	0.0308(7)
C16	0.01775(12)	0.0562(2)	0.12849(10)	0.0210(6)
C17	0.82359(12)	0.9452(3)	0.12095(10)	0.0253(6)
C18	0.81113(17)	0.8502(4)	0.15029(15)	0.0546(11)
C19	0.76010(17)	0.8504(4)	0.17025(15)	0.0535(11)
C20	0.72109(14)	0.9433(4)	0.16098(12)	0.0404(8)
C21	0.73326(19)	0.0377(5)	0.13230(18)	0.0789(17)
C22	0.78438(17)	0.0387(4)	0.11265(16)	0.0614(13)
Sn2	0.27333(2)	0.53352(2)	0.18423(2)	0.02103(5)
Br2	0.33675(2)	0.68156(4)	0.93581(2)	0.05057(11)
Cl3	0.25164(3)	0.33521(7)	0.14202(3)	0.02789(16)
Cl4	0.31620(3)	0.72390(6)	0.22218(3)	0.02754(15)
O2	0.24332(9)	0.62543(19)	0.12204(7)	0.0283(5)

Table S16. Atomic coordinates and equivalent isotropic atomic displacement parameters (Å^2) for PhSnLBrCl$_2$. U(eq) is defined as one third of the trace of the orthogonalized U$_{ij}$ tensor.

Atom	x	y	z	U(eq)
N3	0.35830(10)	0.5220(2)	0.15796(8)	0.0220(5)
N4	0.33239(10)	0.4297(2)	0.24030(8)	0.0215(5)
C23	0.26531(12)	0.6311(3)	0.08166(10)	0.0246(6)
C24	0.22976(13)	0.6783(3)	0.04072(11)	0.0282(7)
C25	0.25023(15)	0.6924(3)	0.99808(11)	0.0336(7)
C26	0.30708(14)	0.6578(3)	0.99413(11)	0.0312(7)
C27	0.34301(14)	0.6096(3)	0.03237(10)	0.0266(6)
C28	0.32319(13)	0.5944(3)	0.07683(10)	0.0235(6)
C29	0.36579(13)	0.5471(3)	0.11440(10)	0.0240(6)
C30	0.40508(12)	0.4744(3)	0.19087(10)	0.0240(6)
C31	0.46270(13)	0.4747(3)	0.18517(11)	0.0322(7)
C32	0.50480(14)	0.4189(3)	0.21933(12)	0.0393(8)
C33	0.49037(14)	0.3637(3)	0.25914(11)	0.0331(7)
C34	0.43223(13)	0.3653(3)	0.26789(10)	0.0252(6)
C35	0.41312(13)	0.3135(3)	0.30851(10)	0.0265(6)
C36	0.35592(13)	0.3211(3)	0.31435(11)	0.0270(6)
C37	0.31654(13)	0.3811(3)	0.27947(10)	0.0252(6)
C38	0.38924(12)	0.4229(2)	0.23360(10)	0.0202(6)
C39	0.19694(12)	0.5379(2)	0.21789(10)	0.0225(6)
C40	0.19888(13)	0.5935(3)	0.26302(10)	0.0264(6)
C41	0.14971(14)	0.5966(3)	0.28499(11)	0.0291(7)
C42	0.09740(14)	0.5481(3)	0.26220(12)	0.0325(7)
C43	0.09489(13)	0.4964(3)	0.21739(12)	0.0314(7)
C44	0.14470(13)	0.4895(3)	0.19566(11)	0.0273(6)
Sn3	0.45239(2)	0.26569(2)	0.90894(2)	0.02735(5)
Br3	0.75101(2)	0.97420(3)	0.97097(2)	0.03829(9)
Cl5	0.42406(4)	0.04628(7)	0.90045(3)	0.0449(2)
Cl6	0.48718(4)	0.47172(7)	0.93425(3)	0.03524(18)
O3	0.52888(9)	0.2277(2)	0.88497(8)	0.0340(5)
N5	0.49548(10)	0.2057(2)	0.98006(9)	0.0262(5)
N6	0.38451(11)	0.2815(2)	0.95679(10)	0.0302(6)
C45	0.57408(13)	0.1617(3)	0.90465(11)	0.0272(6)
C46	0.61759(13)	0.1353(3)	0.87652(11)	0.0305(7)
C47	0.66898(14)	0.0779(3)	0.89552(12)	0.0321(7)

Table S16. Atomic coordinates and equivalent isotropic atomic displacement parameters (Å^2) for PhSnLBrCl$_2$. U(eq) is defined as one third of the trace of the orthogonalized U$_{ij}$ tensor.

Atom	x	y	z	U(eq)
C48	0.67824(13)	0.0421(3)	0.94367(12)	0.0297(7)
C49	0.63568(13)	0.0608(3)	0.97153(12)	0.0293(7)
C50	0.58299(12)	0.1210(3)	0.95310(11)	0.0255(6)
C51	0.54401(13)	0.1443(3)	0.98719(11)	0.0272(6)
C52	0.46269(13)	0.2236(3)	0.01805(11)	0.0266(6)
C53	0.48276(14)	0.2069(3)	0.06575(11)	0.0307(7)
C54	0.44494(15)	0.2214(3)	0.09997(12)	0.0346(7)
C55	0.38831(14)	0.2540(3)	0.08702(12)	0.0323(7)
C56	0.36620(13)	0.2758(3)	0.03849(12)	0.0289(7)
C57	0.30786(14)	0.3103(3)	0.02205(13)	0.0361(8)
C58	0.28955(14)	0.3263(3)	0.97434(14)	0.0419(9)
C59	0.32899(14)	0.3124(3)	0.94236(13)	0.0376(8)
C60	0.40389(13)	0.2623(3)	0.00411(11)	0.0268(6)
C61	0.40079(13)	0.3248(3)	0.84371(11)	0.0310(7)
C62	0.39186(15)	0.2473(3)	0.80428(12)	0.0379(8)
C63	0.35685(17)	0.2841(4)	0.76273(13)	0.0502(10)
C64	0.33017(16)	0.3967(5)	0.75977(14)	0.0564(11)
C65	0.33806(17)	0.4759(4)	0.79878(16)	0.0547(11)
C66	0.37406(15)	0.4403(3)	0.84061(14)	0.0431(9)

Table S17. Bond Lengths (Å) for PhSnLBrCl$_2$.

Bond	Length	Bond	Length
Sn1-O1	2.0326(19)	Sn1-C17	2.144(3)
Sn1-N2	2.230(2)	Sn1-N1	2.230(2)
Sn1-Cl2	2.4626(7)	Sn1-Cl1	2.4723(7)
Br1-C4	1.899(3)	O1-C1	1.330(3)
N1-C7	1.306(3)	N1-C8	1.424(3)
N2-C15	1.320(4)	N2-C16	1.375(3)
C1-C2	1.402(4)	C1-C6	1.417(4)
C2-C3	1.377(4)	C2-H2	0.95
C3-C4	1.395(4)	C3-H3	0.95
C4-C5	1.370(4)	C5-C6	1.417(4)
C5-H5	0.95	C6-C7	1.423(4)
C7-H7	0.95	C8-C9	1.369(4)
C8-C16	1.421(4)	C9-C10	1.416(4)
C9-H9	0.95	C10-C11	1.364(4)
C10-H10	0.95	C11-C12	1.408(4)
C11-H11	0.95	C12-C13	1.415(4)
C12-C16	1.419(4)	C13-C14	1.364(4)
C13-H13	0.95	C14-C15	1.393(4)
C14-H14	0.95	C15-H15	0.95
C17-C22	1.358(4)	C17-C18	1.380(4)
C18-C19	1.387(5)	C18-H18	0.95
C19-C20	1.352(5)	C19-H19	0.95
C20-C21	1.361(5)	C20-H20	0.95
C21-C22	1.385(5)	C21-H21	0.95
C22-H22	0.95	Sn2-O2	2.0497(19)
Sn2-C39	2.137(3)	Sn2-N3	2.214(2)
Sn2-N4	2.236(2)	Sn2-Cl4	2.4631(7)
Sn2-Cl3	2.4717(7)	Br2-C26	1.900(3)
O2-C23	1.322(3)	N3-C29	1.300(4)
N3-C30	1.416(3)	N4-C37	1.329(3)
N4-C38	1.363(3)	C23-C24	1.412(4)
C23-C28	1.427(4)	C24-C25	1.372(4)
C24-H24	0.95	C25-C26	1.392(4)
C25-H25	0.95	C26-C27	1.365(4)
C27-C28	1.414(4)	C27-H27	0.95

Table S17. Bond Lengths (Å) for PhSnLBrCl$_2$.

Bond	Length	Bond	Length
C28-C29	1.432(4)	C29-H29	0.95
C30-C31	1.371(4)	C30-C38	1.430(4)
C31-C32	1.402(4)	C31-H31	0.95
C32-C33	1.362(4)	C32-H32	0.95
C33-C34	1.408(4)	C33-H33	0.95
C34-C35	1.410(4)	C34-C38	1.425(4)
C35-C36	1.365(4)	C35-H35	0.95
C36-C37	1.399(4)	C36-H36	0.95
C37-H37	0.95	C39-C44	1.381(4)
C39-C40	1.407(4)	C40-C41	1.381(4)
C40-H40	0.95	C41-C42	1.388(4)
C41-H41	0.95	C42-C43	1.380(4)
C42-H42	0.95	C43-C44	1.392(4)
C43-H43	0.95	C44-H44	0.95
Sn3-O3	2.036(2)	Sn3-C61	2.140(3)
Sn3-N5	2.205(2)	Sn3-N6	2.235(2)
Sn3-Cl6	2.4425(8)	Sn3-Cl5	2.4669(9)
Br3-C48	1.895(3)	O3-C45	1.320(3)
N5-C51	1.296(4)	N5-C52	1.422(4)
N6-C59	1.333(4)	N6-C60	1.363(4)
C45-C46	1.407(4)	C45-C50	1.425(4)
C46-C47	1.379(4)	C46-H46	0.95
C47-C48	1.402(4)	C47-H47	0.95
C48-C49	1.369(4)	C49-C50	1.413(4)
C49-H49	0.95	C50-C51	1.442(4)
C51-H51	0.95	C52-C53	1.372(4)
C52-C60	1.424(4)	C53-C54	1.412(4)
C53-H53	0.95	C54-C55	1.356(4)
C54-H54	0.95	C55-C56	1.411(4)
C55-H55	0.95	C56-C60	1.412(4)
C56-C57	1.413(4)	C57-C58	1.364(5)
C57-H57	0.95	C58-C59	1.390(4)
C58-H58	0.95	C59-H59	0.95
C61-C62	1.386(4)	C61-C66	1.392(4)
C62-C63	1.382(5)	C62-H62	0.95

Table S17. Bond Lengths (Å) for PhSnLBrCl$_2$.

Bond	Length	Bond	Length
C63-C64	1.364(6)	C63-H63	0.95
C64-C65	1.388(6)	C64-H64	0.95
C65-C66	1.395(5)	C65-H65	0.95
C66-H66	0.95		

Table S18. Bond Angles (degrees) for PhSnLBrCl$_2$.

Atoms	Angle	Atoms	Angle
O1-Sn1-C17	99.89(9)	O1-Sn1-N2	159.56(8)
C17-Sn1-N2	100.31(10)	O1-Sn1-N1	85.53(8)
C17-Sn1-N1	173.05(10)	N2-Sn1-N1	74.58(8)
O1-Sn1-Cl2	89.45(6)	C17-Sn1-Cl2	98.03(8)
N2-Sn1-Cl2	84.69(6)	N1-Sn1-Cl2	86.31(6)
O1-Sn1-Cl1	92.61(6)	C17-Sn1-Cl1	94.48(8)
N2-Sn1-Cl1	88.89(6)	N1-Sn1-Cl1	80.84(6)
Cl2-Sn1-Cl1	166.78(2)	C1-O1-Sn1	127.55(17)
C7-N1-C8	121.2(2)	C7-N1-Sn1	122.26(19)
C8-N1-Sn1	115.31(17)	C15-N2-C16	120.4(2)
C15-N2-Sn1	124.2(2)	C16-N2-Sn1	115.33(18)
O1-C1-C2	117.7(3)	O1-C1-C6	123.8(3)
C2-C1-C6	118.5(3)	C3-C2-C1	122.0(3)
C3-C2-H2	119.0	C1-C2-H2	119.0
C2-C3-C4	119.1(3)	C2-C3-H3	120.4
C4-C3-H3	120.4	C5-C4-C3	120.9(3)
C5-C4-Br1	119.5(2)	C3-C4-Br1	119.5(2)
C4-C5-C6	120.6(3)	C4-C5-H5	119.7
C6-C5-H5	119.7	C1-C6-C5	118.8(3)
C1-C6-C7	124.9(3)	C5-C6-C7	116.2(3)
N1-C7-C6	127.6(3)	N1-C7-H7	116.2
C6-C7-H7	116.2	C9-C8-C16	118.6(3)
C9-C8-N1	125.9(3)	C16-C8-N1	115.5(2)
C8-C9-C10	120.7(3)	C8-C9-H9	119.7
C10-C9-H9	119.7	C11-C10-C9	121.4(3)
C11-C10-H10	119.3	C9-C10-H10	119.3
C10-C11-C12	119.7(3)	C10-C11-H11	120.2
C12-C11-H11	120.2	C11-C12-C13	123.5(3)
C11-C12-C16	119.0(3)	C13-C12-C16	117.5(3)
C14-C13-C12	120.1(3)	C14-C13-H13	119.9
C12-C13-H13	119.9	C13-C14-C15	119.5(3)
C13-C14-H14	120.3	C15-C14-H14	120.3
N2-C15-C14	122.1(3)	N2-C15-H15	118.9
C14-C15-H15	118.9	N2-C16-C12	120.3(3)
N2-C16-C8	119.0(2)	C12-C16-C8	120.7(3)

Table S18. Bond Angles (degrees) for PhSnLBrCl$_2$.

Atoms	Angle	Atoms	Angle
C22-C17-C18	117.6(3)	C22-C17-Sn1	121.9(2)
C18-C17-Sn1	120.4(2)	C17-C18-C19	121.0(3)
C17-C18-H18	119.5	C19-C18-H18	119.5
C20-C19-C18	120.6(3)	C20-C19-H19	119.7
C18-C19-H19	119.7	C19-C20-C21	118.7(3)
C19-C20-H20	120.6	C21-C20-H20	120.6
C20-C21-C22	120.9(4)	C20-C21-H21	119.5
C22-C21-H21	119.5	C17-C22-C21	121.1(3)
C17-C22-H22	119.4	C21-C22-H22	119.4
O2-Sn2-C39	100.13(9)	O2-Sn2-N3	86.68(8)
C39-Sn2-N3	172.99(9)	O2-Sn2-N4	160.95(8)
C39-Sn2-N4	98.91(9)	N3-Sn2-N4	74.30(8)
O2-Sn2-Cl4	91.72(6)	C39-Sn2-Cl4	95.40(8)
N3-Sn2-Cl4	82.69(6)	N4-Sn2-Cl4	87.04(6)
O2-Sn2-Cl3	89.37(6)	C39-Sn2-Cl3	96.50(8)
N3-Sn2-Cl3	85.11(6)	N4-Sn2-Cl3	87.93(6)
Cl4-Sn2-Cl3	167.66(2)	C23-O2-Sn2	129.77(18)
C29-N3-C30	120.0(2)	C29-N3-Sn2	124.16(19)
C30-N3-Sn2	115.60(18)	C37-N4-C38	119.4(2)
C37-N4-Sn2	125.03(19)	C38-N4-Sn2	115.45(17)
O2-C23-C24	118.2(3)	O2-C23-C28	124.2(3)
C24-C23-C28	117.6(3)	C25-C24-C23	121.7(3)
C25-C24-H24	119.1	C23-C24-H24	119.1
C24-C25-C26	120.0(3)	C24-C25-H25	120.0
C26-C25-H25	120.0	C27-C26-C25	120.7(3)
C27-C26-Br2	118.8(2)	C25-C26-Br2	120.4(2)
C26-C27-C28	120.5(3)	C26-C27-H27	119.7
C28-C27-H27	119.7	C27-C28-C23	119.4(3)
C27-C28-C29	114.9(3)	C23-C28-C29	125.6(3)
N3-C29-C28	127.0(3)	N3-C29-H29	116.5
C28-C29-H29	116.5	C31-C30-N3	125.8(3)
C31-C30-C38	118.8(3)	N3-C30-C38	115.4(2)
C30-C31-C32	120.5(3)	C30-C31-H31	119.8
C32-C31-H31	119.8	C33-C32-C31	121.8(3)
C33-C32-H32	119.1	C31-C32-H32	119.1

Table S18. Bond Angles (degrees) for PhSnLBrCl$_2$.

Atoms	Angle	Atoms	Angle
C32-C33-C34	120.2(3)	C32-C33-H33	119.9
C34-C33-H33	119.9	C33-C34-C35	124.6(3)
C33-C34-C38	118.4(3)	C35-C34-C38	117.1(3)
C36-C35-C34	120.5(3)	C36-C35-H35	119.8
C34-C35-H35	119.8	C35-C36-C37	119.0(3)
C35-C36-H36	120.5	C37-C36-H36	120.5
N4-C37-C36	122.6(3)	N4-C37-H37	118.7
C36-C37-H37	118.7	N4-C38-C34	121.4(2)
N4-C38-C30	118.4(2)	C34-C38-C30	120.2(3)
C44-C39-C40	118.7(3)	C44-C39-Sn2	121.2(2)
C40-C39-Sn2	120.0(2)	C41-C40-C39	120.4(3)
C41-C40-H40	119.8	C39-C40-H40	119.8
C40-C41-C42	120.4(3)	C40-C41-H41	119.8
C42-C41-H41	119.8	C43-C42-C41	119.5(3)
C43-C42-H42	120.3	C41-C42-H42	120.3
C42-C43-C44	120.5(3)	C42-C43-H43	119.8
C44-C43-H43	119.8	C39-C44-C43	120.6(3)
C39-C44-H44	119.7	C43-C44-H44	119.7
O3-Sn3-C61	100.03(10)	O3-Sn3-N5	87.00(9)
C61-Sn3-N5	172.89(10)	O3-Sn3-N6	161.43(9)
C61-Sn3-N6	98.45(11)	N5-Sn3-N6	74.49(9)
O3-Sn3-Cl6	90.96(7)	C61-Sn3-Cl6	95.52(9)
N5-Sn3-Cl6	85.28(7)	N6-Sn3-Cl6	89.07(7)
O3-Sn3-Cl5	90.32(7)	C61-Sn3-Cl5	95.65(9)
N5-Sn3-Cl5	83.23(7)	N6-Sn3-Cl5	86.06(7)
Cl6-Sn3-Cl5	168.36(3)	C45-O3-Sn3	130.20(19)
C51-N5-C52	120.3(3)	C51-N5-Sn3	123.7(2)
C52-N5-Sn3	115.45(18)	C59-N6-C60	119.9(3)
C59-N6-Sn3	124.8(2)	C60-N6-Sn3	115.27(19)
O3-C45-C46	117.6(3)	O3-C45-C50	124.3(3)
C46-C45-C50	118.1(3)	C47-C46-C45	121.5(3)
C47-C46-H46	119.2	C45-C46-H46	119.2
C46-C47-C48	119.9(3)	C46-C47-H47	120.0
C48-C47-H47	120.0	C49-C48-C47	120.1(3)
C49-C48-Br3	119.9(2)	C47-C48-Br3	119.9(2)

Table S18. Bond Angles (degrees) for PhSnLBrCl$_2$.

Atoms	Angle	Atoms	Angle
C48-C49-C50	121.0(3)	C48-C49-H49	119.5
C50-C49-H49	119.5	C49-C50-C45	119.2(3)
C49-C50-C51	115.4(3)	C45-C50-C51	125.2(3)
N5-C51-C50	127.1(3)	N5-C51-H51	116.4
C50-C51-H51	116.4	C53-C52-N5	125.9(3)
C53-C52-C60	118.6(3)	N5-C52-C60	115.5(3)
C52-C53-C54	120.5(3)	C52-C53-H53	119.7
C54-C53-H53	119.7	C55-C54-C53	121.4(3)
C55-C54-H54	119.3	C53-C54-H54	119.3
C54-C55-C56	120.0(3)	C54-C55-H55	120.0
C56-C55-H55	120.0	C55-C56-C60	118.9(3)
C55-C56-C57	123.5(3)	C60-C56-C57	117.6(3)
C58-C57-C56	119.9(3)	C58-C57-H57	120.1
C56-C57-H57	120.1	C57-C58-C59	119.7(3)
C57-C58-H58	120.2	C59-C58-H58	120.2
N6-C59-C58	121.9(3)	N6-C59-H59	119.0
C58-C59-H59	119.0	N6-C60-C56	121.1(3)
N6-C60-C52	118.4(3)	C56-C60-C52	120.5(3)
C62-C61-C66	118.8(3)	C62-C61-Sn3	120.6(2)
C66-C61-Sn3	120.5(3)	C63-C62-C61	120.5(4)
C63-C62-H62	119.8	C61-C62-H62	119.8
C64-C63-C62	120.8(4)	C64-C63-H63	119.6
C62-C63-H63	119.6	C63-C64-C65	120.0(4)
C63-C64-H64	120.0	C65-C64-H64	120.0
C64-C65-C66	119.6(4)	C64-C65-H65	120.2
C66-C65-H65	120.2	C61-C66-C65	120.3(4)
C61-C66-H66	119.8	C65-C66-H66	119.8

Table S19. Anisotropic atomic displacement parameters (Å^2) for PhSnLBrCl$_2$. The anisotropic atomic displacement factor exponent takes the form: $-2\pi^2[\, h^2\, a^{*2}\, U_{11} + ... + 2\, h\, k\, a^*\, b^*\, U_{12}]$.

Atom	U$_{11}$	U$_{22}$	U$_{33}$	U$_{23}$	U$_{13}$	U$_{12}$
Sn1	0.01695(9)	0.02441(10)	0.02085(10)	-0.00135(8)	0.00533(7)	0.00091(7)
Br1	0.0498(2)	0.0428(2)	0.03191(18)	-0.01183(15)	0.00463(16)	0.01571(16)
Cl1	0.0277(4)	0.0237(3)	0.0274(4)	0.0008(3)	0.0046(3)	0.0014(3)
Cl2	0.0267(4)	0.0295(4)	0.0322(4)	0.0060(3)	0.0102(3)	0.0054(3)
O1	0.0206(10)	0.0352(12)	0.0271(11)	-0.0090(9)	0.0026(8)	0.0064(9)
N1	0.0200(12)	0.0238(12)	0.0213(12)	0.0020(9)	0.0059(9)	0.0019(9)
N2	0.0209(12)	0.0218(12)	0.0239(12)	-0.0021(10)	0.0052(10)	0.0018(9)
C1	0.0259(15)	0.0285(15)	0.0172(14)	0.0018(11)	0.0051(11)	0.0045(12)
C2	0.0238(15)	0.0398(18)	0.0262(16)	-0.0037(13)	0.0042(12)	-0.0022(13)
C3	0.0349(17)	0.0328(17)	0.0258(16)	-0.0034(13)	0.0041(13)	-0.0009(14)
C4	0.0384(18)	0.0295(16)	0.0216(15)	-0.0024(12)	0.0060(13)	0.0094(13)
C5	0.0267(15)	0.0308(16)	0.0216(15)	-0.0011(12)	0.0066(12)	0.0066(12)
C6	0.0221(14)	0.0281(15)	0.0203(14)	0.0026(11)	0.0059(11)	0.0024(11)
C7	0.0163(13)	0.0303(15)	0.0213(14)	0.0040(11)	0.0052(11)	0.0038(11)
C8	0.0180(13)	0.0230(14)	0.0231(14)	0.0021(11)	0.0028(11)	0.0013(11)
C9	0.0225(15)	0.0353(17)	0.0256(16)	0.0032(13)	0.0065(12)	0.0012(13)
C10	0.0207(15)	0.0375(18)	0.0339(18)	0.0028(14)	0.0075(13)	-0.0040(13)
C11	0.0231(15)	0.0268(16)	0.0362(18)	0.0021(13)	0.0013(13)	-0.0030(12)
C12	0.0237(15)	0.0201(14)	0.0311(16)	0.0011(12)	0.0032(12)	0.0000(11)
C13	0.0316(17)	0.0250(15)	0.0349(18)	-0.0074(13)	0.0016(14)	-0.0010(13)
C14	0.0311(17)	0.0378(19)	0.0375(19)	-0.0132(15)	0.0085(14)	-0.0006(14)
C15	0.0244(16)	0.0332(17)	0.0362(18)	-0.0096(14)	0.0092(13)	0.0005(13)
C16	0.0186(13)	0.0200(14)	0.0246(14)	0.0049(11)	0.0042(11)	0.0017(11)
C17	0.0214(14)	0.0306(16)	0.0247(15)	-0.0043(12)	0.0059(12)	-0.0012(12)
C18	0.051(2)	0.045(2)	0.078(3)	0.022(2)	0.041(2)	0.0130(18)
C19	0.049(2)	0.051(2)	0.069(3)	0.014(2)	0.035(2)	-0.0022(19)
C20	0.0239(17)	0.060(2)	0.041(2)	0.0040(17)	0.0150(15)	-0.0020(16)
C21	0.050(3)	0.094(4)	0.104(4)	0.059(3)	0.048(3)	0.046(2)
C22	0.042(2)	0.069(3)	0.082(3)	0.047(2)	0.039(2)	0.028(2)
Sn2	0.01900(10)	0.02364(10)	0.02071(10)	0.00043(8)	0.00383(7)	0.00070(7)
Br2	0.0650(3)	0.0610(3)	0.02898(19)	0.01672(17)	0.01784(18)	0.0198(2)
Cl3	0.0258(4)	0.0301(4)	0.0283(4)	-0.0070(3)	0.0057(3)	-0.0030(3)
Cl4	0.0254(4)	0.0239(3)	0.0338(4)	-0.0031(3)	0.0061(3)	-0.0015(3)
O2	0.0262(11)	0.0362(12)	0.0234(11)	0.0059(9)	0.0063(9)	0.0074(9)

Table S19. Anisotropic atomic displacement parameters (Å^2) for PhSnLBrCl$_2$. The anisotropic atomic displacement factor exponent takes the form: $-2\pi^2[\,h^2\,a^{*2}\,U_{11} + ... + 2\,h\,k\,a^*\,b^*\,U_{12}]$.

Atom	U_{11}	U_{22}	U_{33}	U_{23}	U_{13}	U_{12}
N3	0.0202(12)	0.0225(12)	0.0230(12)	0.0005(10)	0.0028(9)	0.0001(9)
N4	0.0237(12)	0.0201(11)	0.0207(12)	-0.0007(9)	0.0035(10)	-0.0001(9)
C23	0.0246(15)	0.0246(15)	0.0243(15)	0.0014(12)	0.0025(12)	-0.0023(12)
C24	0.0247(15)	0.0305(16)	0.0285(16)	0.0055(13)	0.0015(12)	0.0061(13)
C25	0.045(2)	0.0299(17)	0.0242(16)	0.0070(13)	0.0001(14)	0.0068(14)
C26	0.0416(19)	0.0303(17)	0.0226(15)	0.0062(13)	0.0073(13)	0.0021(14)
C27	0.0318(16)	0.0251(15)	0.0240(15)	0.0030(12)	0.0075(12)	0.0041(12)
C28	0.0266(15)	0.0209(14)	0.0231(14)	0.0028(11)	0.0036(12)	-0.0019(11)
C29	0.0229(15)	0.0232(15)	0.0261(15)	0.0002(12)	0.0041(12)	0.0009(11)
C30	0.0216(14)	0.0258(15)	0.0242(15)	0.0014(12)	0.0024(11)	0.0032(12)
C31	0.0246(16)	0.051(2)	0.0215(15)	0.0052(14)	0.0054(12)	0.0052(14)
C32	0.0222(16)	0.061(2)	0.0347(19)	0.0039(17)	0.0035(14)	0.0086(15)
C33	0.0277(16)	0.0435(19)	0.0274(17)	0.0012(14)	0.0013(13)	0.0092(14)
C34	0.0260(15)	0.0243(15)	0.0243(15)	-0.0028(12)	0.0008(12)	0.0034(12)
C35	0.0327(16)	0.0222(14)	0.0231(15)	-0.0005(12)	-0.0011(12)	0.0002(12)
C36	0.0366(17)	0.0208(14)	0.0234(15)	0.0016(12)	0.0040(13)	-0.0033(13)
C37	0.0234(15)	0.0234(15)	0.0290(16)	-0.0018(12)	0.0042(12)	-0.0040(12)
C38	0.0196(13)	0.0196(13)	0.0215(14)	-0.0021(11)	0.0034(11)	0.0001(11)
C39	0.0217(14)	0.0218(14)	0.0248(15)	0.0037(11)	0.0063(11)	0.0028(11)
C40	0.0298(16)	0.0242(15)	0.0255(15)	0.0016(12)	0.0050(12)	0.0025(12)
C41	0.0389(18)	0.0281(16)	0.0220(15)	0.0030(12)	0.0101(13)	0.0060(13)
C42	0.0300(17)	0.0336(18)	0.0387(18)	0.0100(14)	0.0205(14)	0.0048(13)
C43	0.0215(15)	0.0302(16)	0.0428(19)	0.0053(14)	0.0061(14)	-0.0005(13)
C44	0.0257(15)	0.0255(15)	0.0310(17)	-0.0016(13)	0.0053(13)	-0.0002(12)
Sn3	0.02471(11)	0.02871(11)	0.02968(11)	0.00694(9)	0.00751(9)	0.00167(8)
Br3	0.02470(17)	0.03775(19)	0.0535(2)	-0.00579(16)	0.00948(15)	0.00538(14)
Cl5	0.0448(5)	0.0294(4)	0.0571(6)	0.0090(4)	-0.0032(4)	-0.0028(4)
Cl6	0.0393(5)	0.0325(4)	0.0358(4)	0.0021(3)	0.0117(4)	-0.0039(3)
O3	0.0313(12)	0.0426(13)	0.0301(12)	0.0078(10)	0.0111(10)	0.0060(10)
N5	0.0236(13)	0.0281(13)	0.0289(13)	0.0070(11)	0.0098(10)	0.0044(10)
N6	0.0244(13)	0.0305(14)	0.0372(15)	0.0089(12)	0.0100(11)	0.0030(11)
C45	0.0221(15)	0.0288(16)	0.0316(16)	-0.0030(13)	0.0070(12)	-0.0039(12)
C46	0.0340(17)	0.0334(17)	0.0267(16)	-0.0024(13)	0.0131(13)	-0.0021(13)
C47	0.0286(17)	0.0322(17)	0.0380(18)	-0.0103(14)	0.0135(14)	-0.0001(13)

Table S19. Anisotropic atomic displacement parameters (Å^2) for PhSnLBrCl$_2$. The anisotropic atomic displacement factor exponent takes the form: $-2\pi^2[\, h^2\, a^{*2}\, U_{11} + ... + 2\, h\, k\, a^*\, b^*\, U_{12}]$.

Atom	U$_{11}$	U$_{22}$	U$_{33}$	U$_{23}$	U$_{13}$	U$_{12}$
C48	0.0235(15)	0.0246(16)	0.0421(19)	-0.0070(13)	0.0087(13)	0.0025(12)
C49	0.0267(16)	0.0271(16)	0.0347(17)	-0.0015(13)	0.0063(13)	0.0016(12)
C50	0.0214(14)	0.0270(15)	0.0291(16)	-0.0009(12)	0.0071(12)	0.0011(12)
C51	0.0259(15)	0.0308(16)	0.0258(15)	0.0040(13)	0.0066(12)	-0.0027(12)
C52	0.0266(15)	0.0221(14)	0.0342(16)	0.0037(13)	0.0144(13)	0.0013(12)
C53	0.0331(17)	0.0268(16)	0.0342(17)	0.0019(13)	0.0119(14)	0.0037(13)
C54	0.0419(19)	0.0357(18)	0.0288(17)	-0.0010(14)	0.0135(14)	0.0067(15)
C55	0.0373(18)	0.0247(16)	0.0393(18)	0.0030(14)	0.0194(15)	0.0028(13)
C56	0.0268(15)	0.0232(15)	0.0402(18)	0.0036(13)	0.0168(13)	-0.0011(12)
C57	0.0295(17)	0.0343(18)	0.048(2)	0.0037(16)	0.0177(15)	-0.0007(14)
C58	0.0242(17)	0.048(2)	0.056(2)	0.0126(18)	0.0157(16)	0.0062(15)
C59	0.0265(17)	0.043(2)	0.045(2)	0.0115(16)	0.0092(15)	0.0032(14)
C60	0.0247(15)	0.0228(15)	0.0346(17)	0.0045(13)	0.0105(13)	-0.0007(12)
C61	0.0261(16)	0.0349(17)	0.0327(17)	0.0045(14)	0.0071(13)	0.0000(13)
C62	0.0361(19)	0.049(2)	0.0314(18)	0.0053(15)	0.0141(15)	-0.0012(16)
C63	0.047(2)	0.076(3)	0.0275(19)	0.0054(19)	0.0058(16)	-0.010(2)
C64	0.037(2)	0.095(3)	0.036(2)	0.028(2)	0.0010(17)	0.001(2)
C65	0.042(2)	0.060(3)	0.062(3)	0.023(2)	0.011(2)	0.0173(19)
C66	0.041(2)	0.044(2)	0.045(2)	0.0111(17)	0.0079(17)	0.0071(16)

Table S20. Hydrogen atomic coordinates and isotropic atomic displacement parameters ($\mathring{A}^2$) for PhSnLBrCl$_2$.

Atom	x	y	z	U(eq)
H2	0.8192	0.6745	-0.0242	0.036
H3	0.8595	0.5299	-0.0700	0.037
H5	1.0199	0.6730	-0.0270	0.031
H7	1.0356	0.8368	0.0242	0.027
H9	1.0965	0.9722	0.0479	0.033
H10	1.1665	1.0921	0.0963	0.036
H11	1.1454	1.1860	0.1648	0.035
H13	1.0708	1.2307	0.2199	0.037
H14	0.9763	1.2084	0.2357	0.042
H15	0.9094	1.0906	0.1846	0.037
H18	0.8379	0.7838	0.1569	0.066
H19	0.7525	0.7846	0.1906	0.064
H20	0.6858	0.9427	0.1742	0.048
H21	0.7063	1.1037	0.1257	0.095
H22	0.7922	1.1060	0.0930	0.074
H24	0.1906	0.7008	0.0428	0.034
H25	0.2256	0.7258	-0.0288	0.04
H27	0.3816	0.5861	0.0291	0.032
H29	0.4036	0.5323	0.1067	0.029
H31	0.4742	0.5130	0.1579	0.039
H32	0.5445	0.4196	0.2146	0.047
H33	0.5196	0.3240	0.2811	0.04
H35	0.4403	0.2731	0.3320	0.032
H36	0.3430	0.2861	0.3417	0.032
H37	0.2769	0.3873	0.2840	0.03
H40	0.2342	0.6291	0.2785	0.032
H41	0.1517	0.6321	0.3159	0.035
H42	0.0636	0.5505	0.2773	0.039
H43	0.0589	0.4653	0.2013	0.038
H44	0.1428	0.4511	0.1653	0.033
H46	0.6114	0.1575	0.8437	0.037
H47	0.6981	0.0627	0.8760	0.038
H49	0.6417	0.0330	1.0037	0.035
H51	0.5551	0.1110	1.0183	0.033

Table S20. Hydrogen atomic coordinates and isotropic atomic displacement parameters (Å^2) for PhSnLBrCl$_2$.

Atom	x	y	z	U(eq)
H53	0.5224	0.1853	1.0758	0.037
H54	0.4595	0.2080	1.1328	0.042
H55	0.3635	0.2622	1.1106	0.039
H57	0.2814	0.3223	1.0442	0.043
H58	0.2501	0.3468	0.9630	0.05
H59	0.3160	0.3253	0.9093	0.045
H62	0.4099	0.1684	0.8058	0.046
H63	0.3513	0.2303	0.7359	0.06
H64	0.3062	0.4209	0.7310	0.068
H65	0.3191	0.5539	0.7970	0.066
H66	0.3804	0.4951	0.8671	0.052

APPENDIX B: CHAPTER 3 CRYSTAL INFORMATION
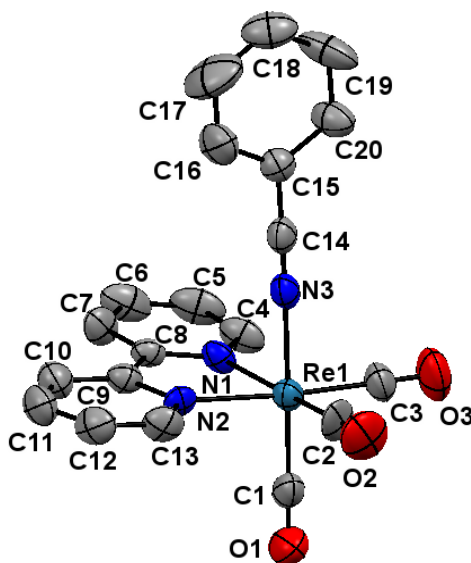
Structure Determination Summary for fac-[Re(bpy)(CO)$_3$BN](BArF$_{24}$)

Identification code	JPD515_0m
Empirical formula	C$_{52}$H$_{25}$BF$_{24}$N$_3$O$_3$Re
Formula weight	1392.76
Temperature	150(2) K
Wavelength	0.71073 Å
Crystal system	orthorhombic
Space group	Pna2$_1$
Unit cell dimensions	a = 16.8751(18) Å α = 90°
	b = 16.1125(18) Å β = 90°
	c = 19.776(2) Å γ = 90°
Volume	5377.2(10) Å^3
Density (calculated	1.720 g/cm^3
Absorption coefficient	2.389 mm^{-1}
F(000)	2712
Crystal size	0.25 x 0.17 x 0.13 mm
θ range for data collection	1.75 to 28.02°
Limiting indices	-22 < h < 22, -21 < k < 21, -25 < l < 26
Reflections collected	88513
Independent reflections	12892 (R$_{int}$ = 0.0489)
Completeness to θ = 28.02°	99.6 %
Absorption correction	Semi-empirical from equivalents
Max. and min. transmission	0.7497 and 0.6018
Refinement method	Full-matrix least-squares on F^2
Data / restraints / parameters	12892 / 404 / 837
Goodness-of-fit on F^2	1.090
Final R indices [I>2σ(I)]	R1 = 0.0597, wR2 = 0.1459
R indices (all data)	R1 = 0.0811, wR2 = 0.1601
Absolute structure parameter	0.003(14)
Largest diff. peak and hole	4.471 and -1.367 e·Å^{-3}

Table S21. Atomic coordinates (x 10^4) and equivalent isotropic displacement parameters [$\mathring{A}^2$ x 10^3] for fac-[Re(bpy)(CO)$_3$BN](BArF$_{24}$). U(eq) is defined as one third of the trace of the orthogonalized U$_{ij}$ tensor.

Atom	x	y	z	U(eq)
Re(1)	7(1)	5562(1)	8044(1)	42(1)
F(1A)	906(16)	3560(19)	4810(18)	70(4)
F(2A)	1992(18)	4230(20)	4830(20)	67(3)
F(3A)	1200(30)	4170(20)	5709(13)	97(6)
F(1B)	763(5)	3670(8)	5070(10)	70(4)
F(2B)	1869(7)	4070(8)	4655(7)	67(3)
F(3B)	1607(15)	4338(7)	5672(6)	97(6)
F(4A)	4338(4)	2864(6)	5705(9)	140(7)
F(5A)	4259(4)	1772(8)	6245(5)	103(4)
F(6A)	4257(6)	1711(13)	5193(7)	181(9)
F(4B)	4341(19)	2500(30)	5193(16)	140(7)
F(5B)	4306(18)	2470(30)	6256(14)	103(4)
F(6B)	4250(20)	1368(12)	5730(30)	181(9)
F(7A)	-700(20)	2653(13)	8120(30)	96(7)
F(8A)	-943(18)	1390(20)	8406(14)	79(5)
F(9A)	-1183(17)	1790(30)	7394(14)	128(7)
F(7B)	-633(15)	2540(14)	8299(18)	96(7)
F(8B)	-1101(15)	1315(12)	8248(16)	79(5)
F(9B)	-1118(13)	2050(30)	7365(9)	128(7)
F(10A)	2757(7)	1819(12)	8338(7)	130(6)
F(11A)	2432(7)	616(5)	8674(6)	76(3)
F(12A)	1906(7)	1627(9)	9147(4)	88(3)
F(10B)	2540(30)	2090(20)	8510(30)	130(6)
F(11B)	2720(20)	810(30)	8470(20)	76(3)
F(12B)	1910(30)	1320(40)	9179(8)	88(3)
F(13A)	3790(20)	-650(30)	4790(30)	83(5)
F(14A)	2750(20)	-1070(40)	4248(12)	97(4)
F(15A)	3470(40)	-1942(17)	4780(30)	115(5)
F(13B)	3559(13)	-492(7)	4598(11)	83(5)
F(14B)	2701(7)	-1349(16)	4283(6)	97(4)
F(15B)	3705(13)	-1782(12)	4855(8)	115(5)
F(16A)	2620(8)	-1685(8)	7700(5)	96(4)
F(17A)	1559(6)	-2136(6)	7400(5)	85(3)
F(18A)	2435(8)	-2785(5)	6975(6)	94(4)

Table S21. Atomic coordinates (x 10^4) and equivalent isotropic displacement parameters [$\mathring{A}^2$ x 10^3] for fac-[Re(bpy)(CO)$_3$BN](BArF$_{24}$). U(eq) is defined as one third of the trace of the orthogonalized U$_{ij}$ tensor.

Atom	x	y	z	U(eq)
F(16B)	2229(18)	-1658(19)	7755(8)	96(4)
F(17B)	1921(17)	-2714(11)	7116(13)	85(3)
F(18B)	3068(8)	-2292(14)	7202(13)	94(4)
F(19A)	-580(40)	190(20)	3484(19)	113(5)
F(20A)	356(19)	1040(40)	3590(20)	140(6)
F(21A)	-810(30)	1400(30)	3810(20)	110(5)
F(19B)	-949(7)	524(8)	3566(6)	113(5)
F(20B)	267(9)	506(11)	3507(5)	140(6)
F(21B)	-273(11)	1591(5)	3807(5)	110(5)
F(22A)	-1192(7)	-1266(8)	6280(11)	142(9)
F(23A)	-2035(6)	-811(13)	5518(6)	130(6)
F(24A)	-1842(8)	-133(7)	6370(7)	100(4)
F(22B)	-1496(12)	-1386(8)	5681(13)	142(9)
F(23B)	-2148(6)	-256(13)	5875(13)	130(6)
F(24B)	-1311(13)	-750(14)	6588(6)	100(4)
O(1)	-386(6)	4627(5)	9352(5)	78(2)
O(2)	-1492(5)	4882(6)	7367(6)	96(3)
O(3)	-929(5)	7062(5)	8585(6)	94(3)
N(1)	1187(4)	5941(4)	8357(4)	41(2)
N(2)	795(4)	4596(4)	7677(4)	38(1)
N(3)	300(4)	6185(5)	7140(4)	47(2)
C(1)	-239(6)	4972(6)	8877(6)	56(2)
C(2)	-943(5)	5152(7)	7629(7)	65(3)
C(3)	-590(6)	6499(6)	8377(6)	60(3)
C(4)	1353(7)	6640(6)	8702(5)	58(3)
C(5)	2112(9)	6897(7)	8842(6)	71(3)
C(6)	2729(7)	6398(7)	8651(6)	69(3)
C(7)	2575(5)	5673(6)	8309(5)	55(2)
C(8)	1798(5)	5462(5)	8165(4)	38(2)
C(9)	1592(5)	4689(5)	7792(4)	42(2)
C(10)	2130(6)	4119(6)	7581(5)	55(2)
C(11)	1850(7)	3409(6)	7222(6)	61(3)
C(12)	1069(7)	3346(6)	7106(5)	59(3)
C(13)	561(6)	3920(6)	7333(5)	52(2)

Table S21. Atomic coordinates (x 10^4) and equivalent isotropic displacement parameters [Å^2 x 10^3] for fac-[Re(bpy)(CO)$_3$BN](BArF$_{24}$). U(eq) is defined as one third of the trace of the orthogonalized U$_{ij}$ tensor.

Atom	x	y	z	U(eq)
C(14)	465(5)	6504(6)	6644(5)	48(2)
C(15)	684(6)	6913(6)	6028(5)	44(2)
C(16)	1151(8)	6506(7)	5581(7)	74(3)
C(17)	1365(11)	6881(12)	4976(8)	109(6)
C(18)	1112(9)	7702(9)	4858(6)	75(4)
C(19)	656(11)	8119(8)	5314(7)	89(5)
C(20)	427(8)	7719(6)	5902(6)	63(3)
C(21)	1809(4)	1517(4)	5824(4)	31(2)
C(22)	1472(4)	2256(4)	5590(4)	35(2)
C(23)	1922(5)	2955(4)	5420(4)	37(2)
C(24)	2750(5)	2926(5)	5469(4)	40(2)
C(25)	3086(5)	2207(5)	5692(4)	40(2)
C(26)	2642(4)	1525(5)	5868(4)	35(2)
C(27)	1536(4)	3730(5)	5205(4)	55(2)
C(28)	3952(5)	2142(5)	5710(4)	59(3)
C(29)	1063(4)	1001(5)	6872(5)	39(2)
C(30)	309(5)	1285(5)	7070(5)	46(2)
C(31)	166(4)	1582(6)	7709(5)	51(2)
C(32)	738(5)	1597(6)	8204(5)	55(3)
C(33)	1497(4)	1339(5)	8020(6)	44(2)
C(34)	1645(4)	1053(5)	7385(4)	37(2)
C(35)	-650(6)	1863(5)	7899(4)	85(5)
C(36)	2130(5)	1374(5)	8529(4)	57(2)
C(37)	1816(4)	-129(5)	6084(4)	37(2)
C(38)	2274(5)	-318(5)	5511(5)	45(2)
C(39)	2707(5)	-1036(5)	5453(5)	48(2)
C(40)	2736(6)	-1600(5)	5995(6)	58(3)
C(41)	2293(6)	-1428(5)	6561(5)	50(2)
C(42)	1838(5)	-695(5)	6607(5)	40(2)
C(43)	3170(5)	-1170(4)	4817(6)	73(3)
C(44)	2306(6)	-1998(5)	7142(5)	74(3)
C(45)	500(4)	527(4)	5653(5)	35(2)
C(46)	442(4)	736(5)	4978(5)	44(2)
C(47)	-237(4)	531(4)	4598(5)	41(2)

Table S21. Atomic coordinates (x 10^4) and equivalent isotropic displacement parameters [$Å^2$ x 10^3] for fac-[Re(bpy)(CO)$_3$BN](BArF$_{24}$). U(eq) is defined as one third of the trace of the orthogonalized U_{ij} tensor.

Atom	x	y	z	U(eq)
C(48)	-878(5)	87(5)	4912(6)	53(2)
C(49)	-805(5)	-143(5)	5577(6)	55(3)
C(50)	-123(4)	63(5)	5940(6)	47(2)
C(51)	-299(6)	770(5)	3908(6)	66(3)
C(52)	-1434(4)	-608(5)	5928(5)	73(4)
B(1)	1286(5)	732(5)	6117(5)	36(2)

Table S22. Bond Lengths (Å) for fac-[Re(bpy)(CO)$_3$BN](BArF$_{24}$). Symmetry transformations used to generate equivalent atoms:

Bond	Length	Bond	Length
Re(1)-C(2)	1.919(9)	F(20A)-C(51)	1.342(9)
Re(1)-C(3)	1.933(10)	F(21A)-C(51)	1.349(9)
Re(1)-C(1)	1.947(12)	F(19B)-C(51)	1.348(6)
Re(1)-N(3)	2.109(8)	F(20B)-C(51)	1.312(17)
Re(1)-N(2)	2.171(7)	F(21B)-C(51)	1.339(7)
Re(1)-N(1)	2.172(7)	F(22A)-C(52)	1.332(8)
F(1A)-C(27)	1.348(8)	F(23A)-C(52)	1.339(7)
F(2A)-C(27)	1.336(8)	F(24A)-C(52)	1.350(8)
F(3A)-C(27)	1.343(8)	F(22B)-C(52)	1.349(8)
F(1B)-C(27)	1.335(7)	F(23B)-C(52)	1.335(8)
F(2B)-C(27)	1.341(7)	F(24B)-C(52)	1.341(8)
F(3B)-C(27)	1.351(7)	O(1)-C(1)	1.119(12)
F(4A)-C(28)	1.333(7)	O(2)-C(2)	1.147(12)
F(5A)-C(28)	1.321(7)	O(3)-C(3)	1.149(12)
F(6A)-C(28)	1.337(8)	N(1)-C(8)	1.343(11)
F(4B)-C(28)	1.342(8)	N(1)-C(4)	1.347(11)
F(5B)-C(28)	1.344(9)	N(2)-C(13)	1.343(11)
F(6B)-C(28)	1.343(9)	N(2)-C(9)	1.372(11)
F(7A)-C(35)	1.346(8)	N(3)-C(14)	1.141(12)
F(8A)-C(35)	1.353(8)	C(4)-C(5)	1.374(16)
F(9A)-C(35)	1.350(9)	C(4)-H(4)	0.95
F(7B)-C(35)	1.348(8)	C(5)-C(6)	1.369(18)
F(8B)-C(35)	1.355(8)	C(5)-H(5)	0.95
F(9B)-C(35)	1.352(8)	C(6)-C(7)	1.375(15)
F(10A)-C(36)	1.332(7)	C(6)-H(6)	0.95
F(11A)-C(36)	1.353(7)	C(7)-C(8)	1.385(11)
F(12A)-C(36)	1.343(7)	C(7)-H(7)	0.95
F(10B)-C(36)	1.350(8)	C(8)-C(9)	1.488(11)
F(11B)-C(36)	1.346(8)	C(9)-C(10)	1.358(13)
F(12B)-C(36)	1.343(9)	C(10)-C(11)	1.428(15)
F(13A)-C(43)	1.345(9)	C(10)-H(10)	0.95
F(14A)-C(43)	1.344(9)	C(11)-C(12)	1.343(15)
F(15A)-C(43)	1.347(8)	C(11)-H(11)	0.95
F(13B)-C(43)	1.347(8)	C(12)-C(13)	1.339(14)

Table S22. Bond Lengths (Å) for fac-[Re(bpy)(CO)$_3$BN](BArF$_{24}$). Symmetry transformations used to generate equivalent atoms:

Bond	Length	Bond	Length
F(14B)-C(43)	1.351(8)	C(12)-H(12)	0.95
F(15B)-C(43)	1.340(8)	C(13)-H(13)	0.95
F(16A)-C(44)	1.325(8)	C(14)-C(15)	1.434(14)
F(17A)-C(44)	1.377(8)	C(15)-C(16)	1.353(15)
F(18A)-C(44)	1.329(7)	C(15)-C(20)	1.391(14)
F(16B)-C(44)	1.337(8)	C(16)-C(17)	1.388(19)
F(17B)-C(44)	1.325(8)	C(16)-H(16)	0.95
F(18B)-C(44)	1.375(8)	C(17)-C(18)	1.41(2)
F(19A)-C(51)	1.343(9)	C(17)-H(17)	0.95
C(18)-C(19)	1.36(2)	C(45)-B(1)	1.645(11)
C(18)-H(18)	0.95	C(46)-C(47)	1.409(10)
C(19)-C(20)	1.386(16)	C(46)-H(46)	0.95
C(19)-H(19)	0.95	C(47)-C(51)	1.422(15)
C(20)-H(20)	0.95	C(47)-C(48)	1.437(13)
C(21)-C(22)	1.398(10)	C(48)-C(49)	1.373(15)
C(21)-C(26)	1.409(9)	C(48)-H(48)	0.95
C(21)-B(1)	1.649(11)	C(49)-C(50)	1.396(12)
C(22)-C(23)	1.399(10)	C(49)-C(52)	1.472(12)
C(22)-H(22)	0.95	C(50)-H(50)	0.95
C(23)-C(24)	1.401(11)	C(33)-C(36)	1.470(13)
C(23)-C(27)	1.471(10)	C(34)-H(34)	0.95
C(24)-C(25)	1.363(11)	C(37)-C(42)	1.379(12)
C(24)-H(24)	0.95	C(37)-C(38)	1.405(12)
C(25)-C(26)	1.374(11)	C(37)-B(1)	1.652(11)
C(25)-C(28)	1.467(11)	C(38)-C(39)	1.373(11)
C(26)-H(26)	0.95	C(38)-H(38)	0.95
C(29)-C(30)	1.407(10)	C(39)-C(40)	1.406(14)
C(29)-C(34)	1.414(11)	C(39)-C(43)	1.497(14)
C(29)-B(1)	1.600(14)	C(40)-C(41)	1.375(15)
C(30)-C(31)	1.373(14)	C(40)-H(40)	0.95
C(30)-H(30)	0.95	C(41)-C(42)	1.411(11)
C(31)-C(32)	1.374(14)	C(41)-C(44)	1.471(13)
C(31)-C(35)	1.498(13)	C(42)-H(42)	0.95
C(32)-C(33)	1.394(11)	C(45)-C(46)	1.381(13)

Table S22. Bond Lengths (Å) for fac-[Re(bpy)(CO)$_3$BN](BArF$_{24}$). Symmetry transformations used to generate equivalent atoms:

Bond	Length	Bond	Length
C(32)-H(32)	0.95	C(45)-C(50)	1.410(11)
C(33)-C(34)	1.361(14)		

Table S23. Bond Angles (degrees) for fac-[Re(bpy)(CO)$_3$BN](BArF$_{24}$). Symmetry transformations used to generate equivalent atoms:

Atoms	Angle	Atoms	Angle
C(2)-Re(1)-C(3)	88.8(5)	C(9)-C(10)-C(11)	118.2(10)
C(2)-Re(1)-C(1)	90.8(5)	C(9)-C(10)-H(10)	120.9
C(3)-Re(1)-C(1)	88.9(4)	C(11)-C(10)-H(10)	120.9
C(2)-Re(1)-N(3)	89.9(4)	C(12)-C(11)-C(10)	118.1(9)
C(3)-Re(1)-N(3)	92.2(4)	C(12)-C(11)-H(11)	120.9
C(1)-Re(1)-N(3)	178.6(3)	C(10)-C(11)-H(11)	120.9
C(2)-Re(1)-N(2)	97.0(4)	C(13)-C(12)-C(11)	121.2(10)
C(3)-Re(1)-N(2)	173.6(4)	C(13)-C(12)-H(12)	119.4
C(1)-Re(1)-N(2)	93.7(3)	C(11)-C(12)-H(12)	119.4
N(3)-Re(1)-N(2)	85.1(3)	C(12)-C(13)-N(2)	122.8(9)
C(2)-Re(1)-N(1)	170.0(4)	C(12)-C(13)-H(13)	118.6
C(3)-Re(1)-N(1)	99.3(4)	N(2)-C(13)-H(13)	118.6
C(1)-Re(1)-N(1)	95.2(4)	N(3)-C(14)-C(15)	178.9(11)
N(3)-Re(1)-N(1)	83.9(3)	C(16)-C(15)-C(20)	121.2(10)
N(2)-Re(1)-N(1)	74.7(2)	C(16)-C(15)-C(14)	118.8(9)
C(8)-N(1)-C(4)	117.7(8)	C(20)-C(15)-C(14)	120.0(9)
C(8)-N(1)-Re(1)	117.5(5)	C(15)-C(16)-C(17)	120.2(12)
C(4)-N(1)-Re(1)	124.8(7)	C(15)-C(16)-H(16)	119.9
C(13)-N(2)-C(9)	117.4(8)	C(17)-C(16)-H(16)	119.9
C(13)-N(2)-Re(1)	124.8(6)	C(16)-C(17)-C(18)	118.2(13)
C(9)-N(2)-Re(1)	117.8(5)	C(16)-C(17)-H(17)	120.9
C(14)-N(3)-Re(1)	178.3(8)	C(18)-C(17)-H(17)	120.9
O(1)-C(1)-Re(1)	179.2(12)	C(19)-C(18)-C(17)	121.6(12)
O(2)-C(2)-Re(1)	177.0(11)	C(19)-C(18)-H(18)	119.2
O(3)-C(3)-Re(1)	178.2(11)	C(17)-C(18)-H(18)	119.2
N(1)-C(4)-C(5)	123.2(11)	C(18)-C(19)-C(20)	118.9(12)
N(1)-C(4)-H(4)	118.4	C(18)-C(19)-H(19)	120.5
C(5)-C(4)-H(4)	118.4	C(20)-C(19)-H(19)	120.5
C(6)-C(5)-C(4)	118.5(10)	C(19)-C(20)-C(15)	119.8(11)
C(6)-C(5)-H(5)	120.7	C(19)-C(20)-H(20)	120.1
C(4)-C(5)-H(5)	120.7	C(15)-C(20)-H(20)	120.1
C(5)-C(6)-C(7)	119.4(10)	C(22)-C(21)-C(26)	114.7(6)
C(5)-C(6)-H(6)	120.3	C(22)-C(21)-B(1)	123.6(6)
C(7)-C(6)-H(6)	120.3	C(26)-C(21)-B(1)	121.3(6)

Table S23. Bond Angles (degrees) for fac-[Re(bpy)(CO)$_3$BN](BArF$_{24}$). Symmetry transformations used to generate equivalent atoms:

Atoms	Angle	Atoms	Angle
C(6)-C(7)-C(8)	119.3(10)	C(21)-C(22)-C(23)	123.0(7)
C(6)-C(7)-H(7)	120.4	C(21)-C(22)-H(22)	118.5
C(8)-C(7)-H(7)	120.4	C(23)-C(22)-H(22)	118.5
N(1)-C(8)-C(7)	121.9(8)	C(22)-C(23)-C(24)	119.8(7)
N(1)-C(8)-C(9)	116.2(7)	C(22)-C(23)-C(27)	120.8(7)
C(7)-C(8)-C(9)	122.0(8)	C(24)-C(23)-C(27)	119.4(7)
C(10)-C(9)-N(2)	122.1(8)	C(25)-C(24)-C(23)	117.7(7)
C(10)-C(9)-C(8)	124.1(8)	C(25)-C(24)-H(24)	121.1
N(2)-C(9)-C(8)	113.8(8)	C(23)-C(24)-H(24)	121.1
C(24)-C(25)-C(26)	122.4(7)	F(6B)-C(28)-C(25)	115.9(17)
C(24)-C(25)-C(28)	118.8(7)	F(5B)-C(28)-C(25)	115.7(15)
C(26)-C(25)-C(28)	118.7(7)	C(30)-C(29)-C(34)	114.2(8)
C(25)-C(26)-C(21)	122.4(7)	C(30)-C(29)-B(1)	124.1(8)
C(25)-C(26)-H(26)	118.8	C(34)-C(29)-B(1)	121.4(7)
C(21)-C(26)-H(26)	118.8	C(31)-C(30)-C(29)	121.9(8)
F(1B)-C(27)-F(2A)	119.8(17)	C(31)-C(30)-H(30)	119.1
F(1B)-C(27)-F(2B)	106.1(8)	C(29)-C(30)-H(30)	119.1
F(1B)-C(27)-F(3A)	77.3(17)	C(30)-C(31)-C(32)	122.5(8)
F(2A)-C(27)-F(3A)	109.2(18)	C(30)-C(31)-C(35)	119.8(8)
F(2B)-C(27)-F(3A)	124.2(18)	C(32)-C(31)-C(35)	117.5(9)
F(2A)-C(27)-F(1A)	105.0(17)	C(31)-C(32)-C(33)	117.0(9)
F(2B)-C(27)-F(1A)	86.7(16)	C(31)-C(32)-H(32)	121.5
F(3A)-C(27)-F(1A)	102.0(16)	C(33)-C(32)-H(32)	121.5
F(1B)-C(27)-F(3B)	106.1(9)	C(34)-C(33)-C(32)	120.8(9)
F(2A)-C(27)-F(3B)	83.4(18)	C(34)-C(33)-C(36)	120.7(7)
F(2B)-C(27)-F(3B)	102.8(8)	C(32)-C(33)-C(36)	118.5(9)
F(1A)-C(27)-F(3B)	127.9(15)	C(33)-C(34)-C(29)	123.6(7)
F(1B)-C(27)-C(23)	115.4(7)	C(33)-C(34)-H(34)	118.2
F(2A)-C(27)-C(23)	114.6(16)	C(29)-C(34)-H(34)	118.2
F(2B)-C(27)-C(23)	113.2(8)	F(7A)-C(35)-F(9A)	106.0(18)
F(3A)-C(27)-C(23)	114.6(15)	F(7B)-C(35)-F(9A)	121(3)
F(1A)-C(27)-C(23)	110.2(14)	F(7A)-C(35)-F(9B)	91(3)
F(3B)-C(27)-C(23)	112.2(8)	F(7B)-C(35)-F(9B)	107.1(14)
F(5A)-C(28)-F(4A)	102.0(8)	F(7A)-C(35)-F(8A)	106.0(18)

Table S23. Bond Angles (degrees) for fac-[Re(bpy)(CO)$_3$BN](BArF$_{24}$). Symmetry transformations used to generate equivalent atoms:

Atoms	Angle	Atoms	Angle
F(5A)-C(28)-F(6A)	103.1(10)	F(7B)-C(35)-F(8A)	92(2)
F(4A)-C(28)-F(6A)	105.2(11)	F(9A)-C(35)-F(8A)	105.1(17)
F(5A)-C(28)-F(4B)	127.7(18)	F(9B)-C(35)-F(8A)	119(2)
F(4A)-C(28)-F(4B)	52(2)	F(7A)-C(35)-F(8B)	115(3)
F(6A)-C(28)-F(4B)	57(2)	F(7B)-C(35)-F(8B)	104.0(12)
F(5A)-C(28)-F(6B)	54(2)	F(9A)-C(35)-F(8B)	87(2)
F(4A)-C(28)-F(6B)	129.0(19)	F(9B)-C(35)-F(8B)	102.3(14)
F(6A)-C(28)-F(6B)	53(2)	F(7A)-C(35)-C(31)	114.7(17)
F(4B)-C(28)-F(6B)	103.5(19)	F(7B)-C(35)-C(31)	111.9(13)
F(5A)-C(28)-F(5B)	50.1(19)	F(9A)-C(35)-C(31)	113.7(18)
F(4A)-C(28)-F(5B)	56.2(19)	F(9B)-C(35)-C(31)	114.0(13)
F(6A)-C(28)-F(5B)	130.4(17)	F(8A)-C(35)-C(31)	110.5(15)
F(4B)-C(28)-F(5B)	103.2(18)	F(8B)-C(35)-C(31)	116.6(13)
F(6B)-C(28)-F(5B)	100.3(18)	F(10A)-C(36)-F(12B)	122(2)
F(5A)-C(28)-C(25)	116.2(7)	F(10A)-C(36)-F(12A)	108.5(9)
F(4A)-C(28)-C(25)	115.1(7)	F(10A)-C(36)-F(11B)	76(2)
F(6A)-C(28)-C(25)	113.7(7)	F(12B)-C(36)-F(11B)	104.1(19)
F(4B)-C(28)-C(25)	116.1(16)	F(12A)-C(36)-F(11B)	119(2)
F(12B)-C(36)-F(10B)	102.9(19)	F(15B)-C(43)-C(39)	114.3(10)
F(12A)-C(36)-F(10B)	85(3)	F(14A)-C(43)-C(39)	114.2(19)
F(11B)-C(36)-F(10B)	101.6(19)	F(13A)-C(43)-C(39)	111.0(17)
F(10A)-C(36)-F(11A)	104.3(9)	F(13B)-C(43)-C(39)	114.0(8)
F(12B)-C(36)-F(11A)	81(2)	F(15A)-C(43)-C(39)	112.3(19)
F(12A)-C(36)-F(11A)	100.7(8)	F(14B)-C(43)-C(39)	112.5(9)
F(10B)-C(36)-F(11A)	126(2)	F(16A)-C(44)-F(17B)	124.0(15)
F(10A)-C(36)-C(33)	113.9(8)	F(16A)-C(44)-F(18A)	120.3(10)
F(12B)-C(36)-C(33)	116.7(19)	F(17B)-C(44)-F(16B)	110.1(17)
F(12A)-C(36)-C(33)	115.5(9)	F(18A)-C(44)-F(16B)	129.2(17)
F(11B)-C(36)-C(33)	116.8(16)	F(16A)-C(44)-F(18B)	71.5(13)
F(10B)-C(36)-C(33)	112.7(19)	F(17B)-C(44)-F(18B)	99.3(14)
F(11A)-C(36)-C(33)	112.6(7)	F(18A)-C(44)-F(18B)	62.6(12)
C(42)-C(37)-C(38)	116.6(7)	F(16B)-C(44)-F(18B)	98.8(15)
C(42)-C(37)-B(1)	122.7(7)	F(16A)-C(44)-F(17A)	96.8(9)
C(38)-C(37)-B(1)	120.7(7)	F(17B)-C(44)-F(17A)	55.0(14)

Table S23. Bond Angles (degrees) for fac-[Re(bpy)(CO)$_3$BN](BArF$_{24}$). Symmetry transformations used to generate equivalent atoms:

Atoms	Angle	Atoms	Angle
C(39)-C(38)-C(37)	122.8(9)	F(18A)-C(44)-F(17A)	95.1(9)
C(39)-C(38)-H(38)	118.6	F(16B)-C(44)-F(17A)	69.0(14)
C(37)-C(38)-H(38)	118.6	F(18B)-C(44)-F(17A)	140.1(13)
C(38)-C(39)-C(40)	120.0(9)	F(16A)-C(44)-C(41)	114.8(8)
C(38)-C(39)-C(43)	118.0(8)	F(17B)-C(44)-C(41)	120.5(12)
C(40)-C(39)-C(43)	121.9(8)	F(18A)-C(44)-C(41)	113.9(8)
C(41)-C(40)-C(39)	118.1(8)	F(16B)-C(44)-C(41)	116.8(15)
C(41)-C(40)-H(40)	121	F(18B)-C(44)-C(41)	107.3(12)
C(39)-C(40)-H(40)	121	F(17A)-C(44)-C(41)	112.1(8)
C(40)-C(41)-C(42)	121.2(8)	C(46)-C(45)-C(50)	117.7(7)
C(40)-C(41)-C(44)	120.1(8)	C(46)-C(45)-B(1)	123.3(6)
C(42)-C(41)-C(44)	118.6(9)	C(50)-C(45)-B(1)	118.9(8)
C(37)-C(42)-C(41)	121.2(8)	C(45)-C(46)-C(47)	121.0(7)
C(37)-C(42)-H(42)	119.4	C(45)-C(46)-H(46)	119.5
C(41)-C(42)-H(42)	119.4	C(47)-C(46)-H(46)	119.5
F(15B)-C(43)-F(14A)	119(3)	C(46)-C(47)-C(51)	120.5(8)
F(15B)-C(43)-F(13A)	86(2)	C(46)-C(47)-C(48)	120.0(9)
F(14A)-C(43)-F(13A)	107.9(19)	C(51)-C(47)-C(48)	119.5(7)
F(15B)-C(43)-F(13B)	106.7(9)	C(49)-C(48)-C(47)	118.7(8)
F(14A)-C(43)-F(13B)	84(2)	C(49)-C(48)-H(48)	120.7
F(14A)-C(43)-F(15A)	105(2)	C(47)-C(48)-H(48)	120.7
F(13A)-C(43)-F(15A)	106(2)	C(48)-C(49)-C(50)	120.1(9)
F(13B)-C(43)-F(15A)	123(2)	C(48)-C(49)-C(52)	121.6(8)
F(15B)-C(43)-F(14B)	106.3(10)	C(50)-C(49)-C(52)	118.3(10)
F(13A)-C(43)-F(14B)	124(2)	C(49)-C(50)-C(45)	122.4(10)
F(13B)-C(43)-F(14B)	101.9(10)	C(49)-C(50)-H(50)	118.8
F(15A)-C(43)-F(14B)	89(3)	C(45)-C(50)-H(50)	118.8
F(20B)-C(51)-F(21B)	101.9(11)	C(45)-B(1)-C(37)	104.3(6)
F(21B)-C(51)-F(20A)	65(3)	C(21)-B(1)-C(37)	109.9(6)
F(20B)-C(51)-F(19A)	69(3)	F(23A)-C(52)-F(24B)	131.7(13)
F(21B)-C(51)-F(19A)	128(2)	F(22A)-C(52)-F(22B)	58.2(13)
F(20A)-C(51)-F(19A)	103(2)	F(23B)-C(52)-F(22B)	107.3(12)
F(20B)-C(51)-F(19B)	101.1(11)	F(23A)-C(52)-F(22B)	59.7(12)
F(21B)-C(51)-F(19B)	104.0(9)	F(24B)-C(52)-F(22B)	101.8(14)

Table S23. Bond Angles (degrees) for fac-[Re(bpy)(CO)$_3$BN](BArF$_{24}$). Symmetry transformations used to generate equivalent atoms:

Atoms	Angle	Atoms	Angle
F(20A)-C(51)-F(19B)	122(2)	F(22A)-C(52)-F(24A)	105.6(12)
F(20B)-C(51)-F(21A)	128(2)	F(23B)-C(52)-F(24A)	49.5(11)
F(20A)-C(51)-F(21A)	103(2)	F(23A)-C(52)-F(24A)	98.3(10)
F(19A)-C(51)-F(21A)	102(2)	F(24B)-C(52)-F(24A)	63.0(12)
F(19B)-C(51)-F(21A)	68(3)	F(22B)-C(52)-F(24A)	136.2(12)
F(20B)-C(51)-C(47)	116.1(9)	F(22A)-C(52)-C(49)	115.4(8)
F(21B)-C(51)-C(47)	114.1(9)	F(23B)-C(52)-C(49)	113.4(11)
F(20A)-C(51)-C(47)	118(2)	F(23A)-C(52)-C(49)	112.7(9)
F(19A)-C(51)-C(47)	115.8(19)	F(24B)-C(52)-C(49)	115.7(10)
F(19B)-C(51)-C(47)	117.5(9)	F(22B)-C(52)-C(49)	111.0(11)
F(21A)-C(51)-C(47)	113.2(18)	F(24A)-C(52)-C(49)	112.6(8)
F(22A)-C(52)-F(23B)	131.0(13)	C(29)-B(1)-C(45)	112.7(6)
F(22A)-C(52)-F(23A)	110.7(11)	C(29)-B(1)-C(21)	104.2(6)
F(23B)-C(52)-F(23A)	51.2(11)	C(45)-B(1)-C(21)	112.8(7)
F(22A)-C(52)-F(24B)	46.2(11)	C(29)-B(1)-C(37)	113.1(7)
F(23B)-C(52)-F(24B)	106.8(14)		

Table S24. Anisotropic displacement parameters ($\mathring{A}^2$ x 10^3) for fac-[Re(bpy)(CO)$_3$BN](BArF$_{24}$). The anisotropic displacement factor exponent takes the form: $-2\pi^2[(ha^*)^2U^{11} + ... + 2hka^*b^*U^{12}]$.

Atom	U_{11}	U_{22}	U_{33}	U_{23}	U_{13}	U_{12}
Re(1)	36(1)	33(1)	57(1)	2(1)	0(1)	-1(1)
F(1A)	25(3)	47(4)	137(11)	36(6)	9(5)	10(3)
F(2A)	37(4)	56(6)	109(7)	40(6)	-7(5)	-3(4)
F(3A)	157(17)	30(5)	104(6)	-10(4)	-41(8)	19(7)
F(1B)	25(3)	47(4)	137(11)	36(6)	9(5)	10(3)
F(2B)	37(4)	56(6)	109(7)	40(6)	-7(5)	-3(4)
F(3B)	157(17)	30(5)	104(6)	-10(4)	-41(8)	19(7)
F(4A)	28(3)	83(7)	307(19)	80(9)	-41(7)	-38(4)
F(5A)	33(3)	137(10)	140(8)	80(7)	-14(4)	-4(5)
F(6A)	37(5)	370(30)	132(11)	-99(14)	-8(6)	47(9)
F(4B)	28(3)	83(7)	307(19)	80(9)	-41(7)	-38(4)
F(5B)	33(3)	137(10)	140(8)	80(7)	-14(4)	-4(5)
F(6B)	37(5)	370(30)	132(11)	-99(14)	-8(6)	47(9)
F(7A)	54(5)	65(6)	169(17)	-1(9)	42(8)	17(5)
F(8A)	22(7)	102(6)	112(11)	-40(7)	18(7)	-32(5)
F(9A)	41(5)	210(20)	128(7)	-7(9)	26(5)	40(8)
F(7B)	54(5)	65(6)	169(17)	-1(9)	42(8)	17(5)
F(8B)	22(7)	102(6)	112(11)	-40(7)	18(7)	-32(5)
F(9B)	41(5)	210(20)	128(7)	-7(9)	26(5)	40(8)
F(10A)	86(8)	206(13)	97(8)	57(8)	-35(6)	-104(9)
F(11A)	45(6)	91(6)	93(7)	8(5)	-13(5)	-9(4)
F(12A)	99(6)	102(10)	63(4)	-16(5)	-6(4)	-12(6)
F(10B)	86(8)	206(13)	97(8)	57(8)	-35(6)	-104(9)
F(11B)	45(6)	91(6)	93(7)	8(5)	-13(5)	-9(4)
F(12B)	99(6)	102(10)	63(4)	-16(5)	-6(4)	-12(6)
F(13A)	78(9)	58(5)	113(9)	10(5)	38(8)	19(5)
F(14A)	106(7)	107(12)	79(5)	-13(6)	30(5)	2(7)
F(15A)	124(11)	86(7)	135(8)	0(6)	42(8)	68(8)
F(13B)	78(9)	58(5)	113(9)	10(5)	38(8)	19(5)
F(14B)	106(7)	107(12)	79(5)	-13(6)	30(5)	2(7)
F(15B)	124(11)	86(7)	135(8)	0(6)	42(8)	68(8)
F(16A)	110(11)	88(6)	88(6)	32(5)	-49(7)	-42(8)
F(17A)	113(8)	59(5)	82(6)	29(5)	-10(6)	-10(5)
F(18A)	121(10)	44(5)	117(9)	31(5)	25(7)	27(5)

Table S24. Anisotropic displacement parameters (Å^2 x 10^3) for fac-[Re(bpy)(CO)$_3$BN](BArF$_{24}$). The anisotropic displacement factor exponent takes the form: $-2\pi^2[(ha^*)^2U^{11} + ... + 2hka^*b^*U^{12}]$.

Atom	U$_{11}$	U$_{22}$	U$_{33}$	U$_{23}$	U$_{13}$	U$_{12}$
F(16B)	110(11)	88(6)	88(6)	32(5)	-49(7)	-42(8)
F(17B)	113(8)	59(5)	82(6)	29(5)	-10(6)	-10(5)
F(18B)	121(10)	44(5)	117(9)	31(5)	25(7)	27(5)
F(19A)	111(10)	112(9)	116(7)	34(6)	-70(7)	-59(7)
F(20A)	186(12)	180(16)	53(5)	-7(7)	-12(6)	74(11)
F(21A)	191(14)	47(5)	92(6)	12(4)	-33(7)	-21(6)
F(19B)	111(10)	112(9)	116(7)	34(6)	-70(7)	-59(7)
F(20B)	186(12)	180(16)	53(5)	-7(7)	-12(6)	74(11)
F(21B)	191(14)	47(5)	92(6)	12(4)	-33(7)	-21(6)
F(22A)	46(7)	59(6)	320(30)	71(12)	10(9)	-20(5)
F(23A)	41(5)	229(19)	120(11)	-45(10)	8(6)	-76(9)
F(24A)	111(10)	78(8)	110(9)	-10(7)	34(8)	-57(7)
F(22B)	46(7)	59(6)	320(30)	71(12)	10(9)	-20(5)
F(23B)	41(5)	229(19)	120(11)	-45(10)	8(6)	-76(9)
F(24B)	111(10)	78(8)	110(9)	-10(7)	34(8)	-57(7)
O(1)	80(6)	73(5)	80(6)	13(5)	29(5)	15(5)
O(2)	42(4)	92(6)	154(9)	9(6)	-14(5)	-26(4)
O(3)	69(5)	51(5)	161(9)	-8(5)	3(6)	21(4)
N(1)	47(4)	25(3)	51(4)	-3(3)	-8(3)	-2(3)
N(2)	28(3)	36(3)	50(4)	-1(3)	-1(3)	-10(3)
N(3)	33(3)	41(4)	67(5)	4(4)	-5(3)	5(3)
C(1)	47(5)	40(5)	81(7)	2(5)	18(5)	5(4)
C(2)	14(3)	63(6)	119(9)	9(6)	-3(4)	-10(4)
C(3)	48(5)	44(5)	87(7)	7(5)	2(5)	13(4)
C(4)	81(7)	32(4)	59(6)	-6(4)	-10(5)	-10(4)
C(5)	106(10)	41(6)	67(7)	-4(5)	-17(7)	-28(6)
C(6)	69(7)	59(6)	80(8)	13(6)	-35(6)	-27(6)
C(7)	30(4)	51(5)	83(7)	6(4)	-15(4)	-8(4)
C(8)	36(4)	34(4)	45(6)	5(3)	-5(3)	-8(3)
C(9)	45(4)	34(4)	46(4)	1(3)	-2(3)	-7(3)
C(10)	53(6)	48(5)	63(6)	2(4)	-4(5)	5(4)
C(11)	68(7)	41(5)	75(7)	-5(5)	9(5)	14(5)
C(12)	75(7)	40(5)	63(6)	-14(4)	12(5)	-4(5)
C(13)	52(5)	41(5)	63(6)	-8(4)	-4(4)	-17(4)

Table S24. Anisotropic displacement parameters ($\mathring{A}^2$ x 10^3) for fac-[Re(bpy)(CO)$_3$BN](BArF$_{24}$). The anisotropic displacement factor exponent takes the form: $-2\pi^2[(ha^*)^2U^{11} + ... + 2hka^*b^*U^{12}]$.

Atom	U_{11}	U_{22}	U_{33}	U_{23}	U_{13}	U_{12}
C(14)	32(4)	47(5)	66(6)	1(4)	-1(4)	5(4)
C(15)	42(5)	42(5)	48(5)	-3(4)	-5(4)	-4(4)
C(16)	89(9)	40(5)	92(9)	-4(6)	18(7)	13(5)
C(17)	128(14)	119(13)	81(9)	-17(9)	57(10)	-16(11)
C(18)	96(10)	81(9)	49(6)	0(6)	1(6)	-30(7)
C(19)	159(15)	40(6)	68(8)	12(5)	-16(9)	-6(8)
C(20)	90(8)	42(5)	57(6)	-1(4)	8(6)	3(5)
C(21)	11(3)	35(4)	47(4)	-3(3)	1(3)	-3(2)
C(22)	25(3)	24(3)	56(5)	-4(3)	-3(3)	-2(3)
C(23)	37(4)	22(3)	51(5)	0(3)	-3(3)	3(3)
C(24)	33(4)	31(4)	54(5)	5(3)	-4(3)	-10(3)
C(25)	29(4)	36(4)	55(5)	5(3)	1(3)	-2(3)
C(26)	21(3)	32(4)	53(5)	4(3)	-4(3)	2(3)
C(27)	50(5)	30(4)	84(7)	10(4)	-12(5)	-2(4)
C(28)	31(4)	65(6)	82(7)	23(6)	-8(4)	-10(4)
C(29)	19(3)	30(4)	68(5)	4(4)	1(3)	-4(3)
C(30)	20(3)	39(4)	77(6)	1(4)	6(4)	-11(3)
C(31)	19(4)	52(5)	83(7)	-2(5)	12(4)	-7(3)
C(32)	42(5)	51(5)	72(8)	-2(4)	22(4)	6(4)
C(33)	31(3)	45(4)	57(4)	5(5)	0(5)	-9(3)
C(34)	22(3)	29(4)	59(5)	-2(3)	2(3)	-4(3)
C(35)	56(7)	90(9)	109(13)	-21(8)	28(8)	-1(6)
C(36)	50(6)	73(7)	49(5)	-5(5)	-6(4)	-7(5)
C(37)	25(3)	31(4)	55(5)	-1(3)	-2(3)	-3(3)
C(38)	41(4)	29(3)	67(6)	3(4)	5(4)	0(3)
C(39)	38(4)	27(4)	79(6)	-6(4)	2(4)	3(3)
C(40)	59(6)	28(4)	87(8)	-1(4)	-12(5)	12(4)
C(41)	66(6)	25(4)	60(6)	2(4)	-11(5)	3(4)
C(42)	36(4)	29(4)	55(5)	-1(3)	1(3)	-2(3)
C(43)	69(7)	37(5)	111(10)	-15(6)	23(7)	5(5)
C(44)	86(9)	56(7)	79(8)	15(6)	-5(7)	29(6)
C(45)	7(3)	21(3)	77(6)	-9(3)	-6(3)	-2(2)
C(46)	14(3)	32(4)	85(6)	-7(4)	-10(3)	-20(3)
C(47)	8(3)	22(3)	94(7)	-11(4)	-13(3)	1(2)

Table S24. Anisotropic displacement parameters ($\mathring{A}^2$ x 10^3) for fac-[Re(bpy)(CO)$_3$BN](BArF$_{24}$). The anisotropic displacement factor exponent takes the form: $-2\pi^2[(ha^*)^2U^{11} + ... + 2hka^*b^*U^{12}]$.

Atom	U$_{11}$	U$_{22}$	U$_{33}$	U$_{23}$	U$_{13}$	U$_{12}$
C(48)	29(4)	39(5)	92(8)	-3(5)	-15(4)	-1(3)
C(49)	28(4)	38(5)	97(8)	-4(5)	-5(5)	-9(3)
C(50)	27(4)	28(4)	85(7)	-1(4)	-1(4)	-9(3)
C(51)	63(7)	50(6)	86(8)	-13(6)	-11(6)	-23(5)
C(52)	17(4)	50(6)	152(12)	-4(6)	-5(5)	-22(4)
B(1)	19(3)	30(4)	60(6)	6(4)	1(3)	-5(3)

Table S25. Hydrogen coordinates (x 10^4) and isotropic displacement parameters (Å^2 x 10^3 for fac-[Re(bpy)(CO)$_3$BN](BArF$_{24}$).

Atom	x	y	z	U(eq)
H(4)	924	6972	8857	69
H(5)	2206	7408	9067	86
H(6)	3259	6552	8753	83
H(7)	2998	5320	8174	66
H(10)	2679	4191	7671	65
H(11)	2206	2993	7069	74
H(12)	872	2885	6858	71
H(13)	12	3847	7246	62
H(16)	1332	5962	5683	89
H(17)	1674	6591	4651	131
H(18)	1263	7971	4450	91
H(19)	498	8676	5229	107
H(20)	95	7994	6219	75
H(22)	913	2285	5545	42
H(24)	3067	3392	5351	47
H(26)	2907	1042	6025	42
H(30)	-113	1270	6753	55
H(32)	622	1775	8651	66
H(34)	2169	878	7280	44
H(38)	2284	68	5148	55
H(40)	3053	-2086	5970	69
H(42)	1541	-590	7006	48
H(46)	867	1022	4765	53
H(48)	-1343	-45	4663	64
H(50)	-78	-116	6396	56
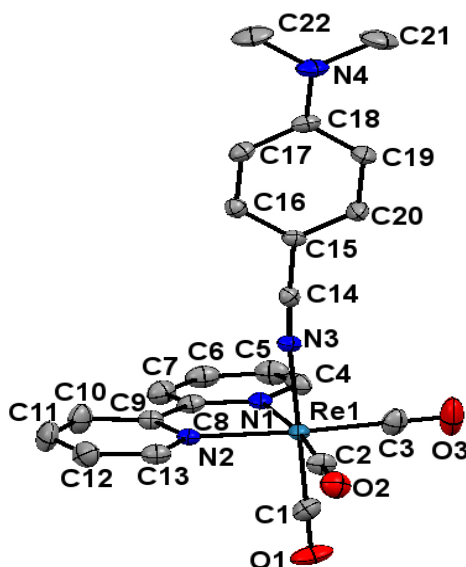
Structure Determination Summary for fac-[Re(bpy)(CO)₃4DMABN](BArF₂₄)

Identification code	RHS010
Empirical formula	$C_{54}H_{30}BF_{24}N_4O_3Re$
Formula weight	1435.83 g/mol
Temperature	100(2) K
Wavelength	0.71073 Å
Crystal size	0.140 x 0.200 x 0.210 mm
Crystal habit	yellow Block
Crystal system	monoclinic
Space group	$P2_1/c$
Unit cell dimensions	a = 13.6239(12) Å α = 90°
	b = 15.1205(14) Å β = 94.9290(10)°
	c = 28.362(3) Å γ = 90°
Volume	5821.0(9) Å³
Density (calculated)	1.638 g/cm³
Absorption coefficient	2.210 mm⁻¹
F(000)	2808
θ range for data collection	1.97 to 28.66°
Limiting Indices	-18< h< 18, -20< k< 20, -38< l< 38
Reflections collected	100194
Independent reflections	14808 [R(int) = 0.0610]
Completeness to θ = 28.66°	98.7%
Absorption correction	multi-scan
Max. and min. transmission	0.7931 and 0.5644
Structure solution technique	direct methods
Refinement method	Full-matrix least-squares on F2
Data / restraints / parameters	14808 / 144 / 786
Goodness-of-fit on F2	1.112
Final R indices	12423 data; I>2σ(I) R1 = 0.0457, wR2 = 0.1033
	all data R1 = 0.0552, wR2 = 0.1071
Absolute Structure Parameter	0.001
Largest diff. peak and hole	4.971 and -2.345 eÅ⁻³

Table S26. Atomic coordinates and equivalent isotropic atomic displacement parameters (Å^2) for fac-[Re(bpy)(CO)$_3$4DMABN](BArF$_{24}$). U(eq) is defined as one third of the trace of the orthogonalized U$_{ij}$ tensor.

Atom	x	y	z	U(eq)
Re1	0.425928(11)	0.767457(11)	0.806519(5)	0.01943(5)
O1	0.6419(2)	0.7673(2)	0.84616(16)	0.0455(10)
O2	0.4360(3)	0.9700(2)	0.79903(12)	0.0372(8)
O3	0.5015(4)	0.7517(3)	0.70816(15)	0.0552(12)
N1	0.4198(2)	0.6276(2)	0.82224(12)	0.0223(7)
N2	0.3701(2)	0.7606(2)	0.87576(12)	0.0186(6)
N3	0.2756(3)	0.7581(2)	0.77880(12)	0.0209(7)
N4	0.8264(3)	0.7538(3)	0.65892(15)	0.0321(9)
C1	0.5611(3)	0.7688(3)	0.83162(17)	0.0291(9)
C2	0.4296(3)	0.8955(3)	0.80159(15)	0.0241(9)
C3	0.4724(4)	0.7583(3)	0.74494(18)	0.0316(10)
C4	0.4482(3)	0.5622(3)	0.79409(16)	0.0271(9)
C5	0.4557(4)	0.4764(3)	0.80847(19)	0.0348(11)
C6	0.4315(4)	0.4538(3)	0.85284(19)	0.0342(11)
C7	0.3997(3)	0.5195(3)	0.88206(18)	0.0316(10)
C8	0.3933(3)	0.6063(3)	0.86588(16)	0.0247(9)
C9	0.3590(3)	0.6795(3)	0.89463(14)	0.0216(8)
C10	0.3188(4)	0.6693(3)	0.93755(18)	0.0361(11)
C11	0.2914(4)	0.7425(4)	0.96202(19)	0.0396(12)
C12	0.3045(4)	0.8252(3)	0.94326(17)	0.0336(10)
C13	0.3438(3)	0.8319(3)	0.90022(16)	0.0264(9)
C14	0.1973(3)	0.7566(3)	0.76065(14)	0.0194(8)
C15	0.1022(3)	0.7552(2)	0.73555(14)	0.0189(8)
C16	0.0158(3)	0.7536(3)	0.75912(15)	0.0218(8)
C17	0.9252(3)	0.7530(3)	0.73405(16)	0.0247(9)
C18	0.9161(3)	0.7540(3)	0.68419(16)	0.0232(9)
C19	0.0036(3)	0.7560(3)	0.66095(16)	0.0287(10)
C20	0.0944(3)	0.7564(3)	0.68630(15)	0.0270(9)
C21	0.8193(4)	0.7545(4)	0.6074(2)	0.0456(14)
C22	0.7369(4)	0.7516(4)	0.6831(2)	0.0458(14)
B1	0.9113(3)	0.7541(3)	0.91443(15)	0.0147(8)
F1	0.6980(2)	0.0100(2)	0.82931(11)	0.0506(9)
F2	0.7214(2)	0.9329(2)	0.76841(11)	0.0466(8)
F3	0.7817(2)	0.0625(2)	0.77499(12)	0.0491(8)

Table S26. Atomic coordinates and equivalent isotropic atomic displacement parameters (Å^2) for fac-[Re(bpy)(CO)$_3$4DMABN](BArF$_{24}$). U(eq) is defined as one third of the trace of the orthogonalized U_{ij} tensor.

Atom	x	y	z	U(eq)
F4	0.19364(19)	0.92198(18)	0.82711(10)	0.0347(6)
F5	0.1340(2)	0.05010(19)	0.80929(13)	0.0460(8)
F6	0.1725(2)	0.0145(2)	0.88194(12)	0.0488(8)
F7	0.1437(3)	0.9722(2)	0.01855(13)	0.0690(12)
F8	0.1827(3)	0.9059(2)	0.08487(15)	0.0747(13)
F9	0.0390(3)	0.9550(2)	0.06707(13)	0.0574(10)
F10	0.1754(3)	0.5888(2)	0.08407(15)	0.0837(15)
F11	0.0301(3)	0.5446(2)	0.06583(14)	0.0625(10)
F12	0.1355(3)	0.5246(2)	0.01733(13)	0.0658(11)
F13	0.6931(2)	0.4950(3)	0.83088(12)	0.0563(9)
F14	0.7709(2)	0.4503(2)	0.77341(12)	0.0487(8)
F15	0.7072(2)	0.5790(2)	0.77193(12)	0.0537(9)
F16	0.1241(2)	0.45911(19)	0.80491(12)	0.0414(7)
F17	0.1636(2)	0.4887(2)	0.87836(11)	0.0432(7)
F18	0.18596(19)	0.58574(18)	0.82545(10)	0.0313(6)
F19	0.6561(3)	0.9641(3)	0.0088(3)	0.122(2)
F20	0.6179(5)	0.9731(4)	0.9389(3)	0.156(3)
F21	0.5202(2)	0.9115(2)	0.98175(15)	0.0583(10)
F22	0.5335(3)	0.5958(3)	0.9945(2)	0.0893(16)
F23	0.6174(4)	0.5321(3)	0.94444(16)	0.0780(13)
F24	0.6762(3)	0.5462(3)	0.01419(15)	0.0673(11)
C23	0.9266(3)	0.8402(2)	0.88103(13)	0.0155(7)
C24	0.8468(3)	0.8789(3)	0.85404(14)	0.0190(8)
C25	0.8574(3)	0.9514(3)	0.82444(14)	0.0208(8)
C26	0.9495(3)	0.9869(3)	0.81924(14)	0.0211(8)
C27	0.0302(3)	0.9484(3)	0.84426(14)	0.0198(8)
C28	0.0189(3)	0.8762(2)	0.87421(13)	0.0171(7)
C29	0.7656(3)	0.9896(3)	0.79925(15)	0.0272(9)
C30	0.1312(3)	0.9840(3)	0.84037(17)	0.0274(9)
C31	0.9911(3)	0.7516(2)	0.96123(13)	0.0160(7)
C32	0.0237(3)	0.8287(3)	0.98446(13)	0.0184(7)
C33	0.0834(3)	0.8276(3)	0.02687(14)	0.0210(8)
C34	0.1123(3)	0.7481(2)	0.04834(13)	0.0196(8)
C35	0.0804(3)	0.6708(3)	0.02621(14)	0.0215(8)

Table S26. Atomic coordinates and equivalent isotropic atomic displacement parameters ($\mathring{A}^2$) for fac-[Re(bpy)(CO)$_3$4DMABN](BArF$_{24}$). U(eq) is defined as one third of the trace of the orthogonalized U_{ij} tensor.

Atom	x	y	z	U(eq)
C36	0.0208(3)	0.6726(3)	0.98360(13)	0.0190(8)
C37	0.1136(4)	0.9135(3)	0.04949(17)	0.0326(10)
C38	0.1076(4)	0.5838(3)	0.04834(16)	0.0344(11)
C39	0.9218(3)	0.6677(2)	0.88043(13)	0.0154(7)
C40	0.8402(3)	0.6302(2)	0.85424(13)	0.0179(7)
C41	0.8491(3)	0.5580(3)	0.82425(14)	0.0202(8)
C42	0.9401(3)	0.5210(3)	0.81787(14)	0.0196(8)
C43	0.0220(3)	0.5592(3)	0.84229(14)	0.0186(8)
C44	0.0130(3)	0.6308(2)	0.87274(13)	0.0159(7)
C45	0.7560(3)	0.5203(3)	0.79998(16)	0.0268(9)
C46	0.1226(3)	0.5228(3)	0.83742(16)	0.0256(9)
C47	0.8036(3)	0.7547(2)	0.93710(13)	0.0166(7)
C48	0.7546(3)	0.8327(3)	0.94685(15)	0.0239(8)
C49	0.6629(3)	0.8325(3)	0.96566(17)	0.0293(10)
C50	0.6181(4)	0.7541(3)	0.97650(17)	0.0302(10)
C51	0.6671(3)	0.6763(3)	0.96873(16)	0.0260(9)
C52	0.7584(3)	0.6763(3)	0.94984(14)	0.0217(8)
C53	0.6130(5)	0.9185(4)	0.9728(3)	0.061(2)
C54	0.6227(4)	0.5897(4)	0.9807(2)	0.0400(12)

Table S27. Bond Lengths (Å) for fac-[Re(bpy)(CO)$_3$4DMABN](BArF$_{24}$).

Bond	Length	Bond	Length
Re1-C3	1.913(5)	Re1-C1	1.916(5)
Re1-C2	1.942(4)	Re1-N3	2.134(3)
Re1-N1	2.164(4)	Re1-N2	2.169(3)
O1-C1	1.143(6)	O2-C2	1.132(5)
O3-C3	1.151(6)	N1-C4	1.348(5)
N1-C8	1.358(6)	N2-C13	1.347(5)
N2-C9	1.352(5)	N3-C14	1.145(5)
N4-C18	1.362(5)	N4-C22	1.450(7)
N4-C21	1.455(7)	C4-C5	1.362(7)
C4-H4	0.95	C5-C6	1.371(7)
C5-H5	0.95	C6-C7	1.387(7)
C6-H6	0.95	C7-C8	1.390(6)
C7-H7	0.95	C8-C9	1.475(6)
C9-C10	1.385(6)	C10-C11	1.375(7)
C10-H10	0.95	C11-C12	1.377(7)
C11-H11	0.95	C12-C13	1.379(6)
C12-H12	0.95	C13-H13	0.95
C14-C15	1.423(5)	C15-C20	1.392(6)
C15-C16	1.403(6)	C16-C17	1.371(6)
C16-H16	0.95	C17-C18	1.409(6)
C17-H17	0.95	C18-C19	1.412(6)
C19-C20	1.376(6)	C19-H19	0.95
C20-H20	0.95	C21-H21A	0.98
C21-H21B	0.98	C21-H21C	0.98
C22-H22A	0.98	C22-H22B	0.98
C22-H22C	0.98	B1-C23	1.634(5)
B1-C39	1.637(5)	B1-C31	1.642(6)
B1-C47	1.652(6)	F1-C29	1.343(6)
F2-C29	1.331(5)	F3-C29	1.327(5)
F4-C30	1.341(5)	F5-C30	1.335(5)
F6-C30	1.343(6)	F7-C37	1.337(6)
F8-C37	1.321(5)	F9-C37	1.327(6)
F10-C38	1.313(5)	F11-C38	1.343(6)
F12-C38	1.332(6)	F13-C45	1.333(6)
F14-C45	1.325(5)	F15-C45	1.331(5)

Table S27. Bond Lengths (Å) for fac-[Re(bpy)(CO)$_3$4DMABN](BArF$_{24}$).

Bond	Length	Bond	Length
F16-C46	1.334(5)	F17-C46	1.347(5)
F18-C46	1.348(5)	F19-C53	1.326(9)
F20-C53	1.275(9)	F21-C53	1.314(6)
F22-C54	1.312(6)	F23-C54	1.344(7)
F24-C54	1.323(6)	C23-C28	1.400(5)
C23-C24	1.402(5)	C24-C25	1.397(5)
C24-H24	0.95	C25-C26	1.384(6)
C25-C29	1.502(6)	C26-C27	1.384(6)
C26-H26	0.95	C27-C28	1.400(5)
C27-C30	1.491(6)	C28-H28	0.95
C31-C32	1.393(5)	C31-C36	1.396(5)
C32-C33	1.393(5)	C32-H32	0.95
C33-C34	1.389(6)	C33-C37	1.491(6)
C34-C35	1.379(6)	C34-H34	0.95
C35-C36	1.397(5)	C35-C38	1.491(6)
C36-H36	0.95	C39-C44	1.397(5)
C39-C40	1.402(5)	C40-C41	1.396(5)
C40-H40	0.95	C41-C42	1.386(6)
C41-C45	1.502(6)	C42-C43	1.388(6)
C42-H42	0.95	C43-C44	1.397(5)
C43-C46	1.494(6)	C44-H44	0.95
C47-C48	1.394(5)	C47-C52	1.397(5)
C48-C49	1.400(6)	C48-H48	0.95
C49-C50	1.380(6)	C49-C53	1.489(7)
C50-C51	1.378(6)	C50-H50	0.95
C51-C52	1.396(6)	C51-C54	1.494(6)
C52-H52	0.95		

Table S28. Bond Angles (degrees) for fac-[Re(bpy)(CO)$_3$4DMABN](BArF$_{24}$).

Atoms	Angle	Atoms	Angle
C3-Re1-C1	87.5(2)	C3-Re1-C2	89.64(19)
C1-Re1-C2	89.23(19)	C3-Re1-N3	92.37(19)
C1-Re1-N3	176.78(17)	C2-Re1-N3	93.99(16)
C3-Re1-N1	98.00(17)	C1-Re1-N1	89.21(16)
C2-Re1-N1	172.13(16)	N3-Re1-N1	87.61(13)
C3-Re1-N2	173.03(16)	C1-Re1-N2	93.71(17)
C2-Re1-N2	97.22(16)	N3-Re1-N2	86.00(13)
N1-Re1-N2	75.18(13)	C4-N1-C8	118.6(4)
C4-N1-Re1	125.2(3)	C8-N1-Re1	115.9(3)
C13-N2-C9	118.6(4)	C13-N2-Re1	123.9(3)
C9-N2-Re1	117.5(3)	C14-N3-Re1	174.3(3)
C18-N4-C22	120.2(4)	C18-N4-C21	120.5(4)
C22-N4-C21	119.3(4)	O1-C1-Re1	178.2(4)
O2-C2-Re1	177.1(4)	O3-C3-Re1	178.8(5)
N1-C4-C5	122.7(4)	N1-C4-H4	118.7
C5-C4-H4	118.7	C4-C5-C6	119.6(4)
C4-C5-H5	120.2	C6-C5-H5	120.2
C5-C6-C7	118.8(4)	C5-C6-H6	120.6
C7-C6-H6	120.6	C6-C7-C8	119.5(5)
C6-C7-H7	120.2	C8-C7-H7	120.2
N1-C8-C7	120.7(4)	N1-C8-C9	116.6(4)
C7-C8-C9	122.7(4)	N2-C9-C10	121.1(4)
N2-C9-C8	114.2(4)	C10-C9-C8	124.7(4)
C11-C10-C9	119.9(4)	C11-C10-H10	120.1
C9-C10-H10	120.1	C10-C11-C12	119.1(5)
C10-C11-H11	120.5	C12-C11-H11	120.5
C11-C12-C13	118.8(4)	C11-C12-H12	120.6
C13-C12-H12	120.6	N2-C13-C12	122.5(4)
N2-C13-H13	118.7	C12-C13-H13	118.7
N3-C14-C15	176.7(4)	C20-C15-C16	118.9(4)
C20-C15-C14	119.3(4)	C16-C15-C14	121.8(4)
C17-C16-C15	120.5(4)	C17-C16-H16	119.7
C15-C16-H16	119.7	C16-C17-C18	121.2(4)
C16-C17-H17	119.4	C18-C17-H17	119.4
N4-C18-C17	121.7(4)	N4-C18-C19	120.6(4)

Table S28. Bond Angles (degrees) for fac-[Re(bpy)(CO)$_3$4DMABN](BArF$_{24}$).

Atoms	Angle	Atoms	Angle
C17-C18-C19	117.6(4)	C20-C19-C18	120.9(4)
C20-C19-H19	119.6	C18-C19-H19	119.6
C19-C20-C15	120.8(4)	C19-C20-H20	119.6
C15-C20-H20	119.6	N4-C21-H21A	109.5
N4-C21-H21B	109.5	H21A-C21-H21B	109.5
N4-C21-H21C	109.5	H21A-C21-H21C	109.5
H21B-C21-H21C	109.5	N4-C22-H22A	109.5
N4-C22-H22B	109.5	H22A-C22-H22B	109.5
N4-C22-H22C	109.5	H22A-C22-H22C	109.5
H22B-C22-H22C	109.5	C23-B1-C39	105.8(3)
C23-B1-C31	112.2(3)	C39-B1-C31	111.9(3)
C23-B1-C47	112.5(3)	C39-B1-C47	111.0(3)
C31-B1-C47	103.5(3)	C28-C23-C24	115.2(3)
C28-C23-B1	123.4(3)	C24-C23-B1	121.2(3)
C25-C24-C23	122.7(4)	C25-C24-H24	118.7
C23-C24-H24	118.7	C26-C25-C24	120.7(4)
C26-C25-C29	121.7(4)	C24-C25-C29	117.5(4)
C25-C26-C27	118.0(4)	C25-C26-H26	121.0
C27-C26-H26	121.0	C26-C27-C28	121.0(4)
C26-C27-C30	120.5(4)	C28-C27-C30	118.5(4)
C23-C28-C27	122.3(4)	C23-C28-H28	118.9
C27-C28-H28	118.9	F3-C29-F2	106.3(4)
F3-C29-F1	106.9(4)	F2-C29-F1	105.6(4)
F3-C29-C25	113.5(4)	F2-C29-C25	112.1(4)
F1-C29-C25	112.0(4)	F5-C30-F4	106.5(4)
F5-C30-F6	106.8(4)	F4-C30-F6	105.0(4)
F5-C30-C27	113.4(4)	F4-C30-C27	112.3(4)
F6-C30-C27	112.2(4)	C32-C31-C36	115.7(4)
C32-C31-B1	121.7(3)	C36-C31-B1	122.2(3)
C31-C32-C33	122.4(4)	C31-C32-H32	118.8
C33-C32-H32	118.8	C34-C33-C32	120.8(4)
C34-C33-C37	120.5(4)	C32-C33-C37	118.6(4)
C35-C34-C33	117.9(4)	C35-C34-H34	121.1
C33-C34-H34	121.1	C34-C35-C36	121.0(4)
C34-C35-C38	119.9(4)	C36-C35-C38	119.1(4)

Table S28. Bond Angles (degrees) for fac-[Re(bpy)(CO)$_3$4DMABN](BArF$_{24}$).

Atoms	Angle	Atoms	Angle
C31-C36-C35	122.2(4)	C31-C36-H36	118.9
C35-C36-H36	118.9	F8-C37-F9	105.9(4)
F8-C37-F7	108.5(5)	F9-C37-F7	102.8(4)
F8-C37-C33	113.7(4)	F9-C37-C33	112.5(4)
F7-C37-C33	112.6(4)	F10-C38-F12	109.1(5)
F10-C38-F11	105.3(4)	F12-C38-F11	103.0(4)
F10-C38-C35	114.0(4)	F12-C38-C35	112.9(4)
F11-C38-C35	111.7(4)	C44-C39-C40	115.5(3)
C44-C39-B1	122.3(3)	C40-C39-B1	122.0(3)
C41-C40-C39	122.2(4)	C41-C40-H40	118.9
C39-C40-H40	118.9	C42-C41-C40	121.3(4)
C42-C41-C45	121.1(4)	C40-C41-C45	117.6(4)
C41-C42-C43	117.2(4)	C41-C42-H42	121.4
C43-C42-H42	121.4	C42-C43-C44	121.4(4)
C42-C43-C46	120.4(4)	C44-C43-C46	118.2(4)
C43-C44-C39	122.2(3)	C43-C44-H44	118.9
C39-C44-H44	118.9	F14-C45-F15	106.6(4)
F14-C45-F13	106.5(4)	F15-C45-F13	105.5(4)
F14-C45-C41	113.5(4)	F15-C45-C41	112.3(4)
F13-C45-C41	111.9(4)	F16-C46-F17	106.8(4)
F16-C46-F18	106.7(3)	F17-C46-F18	105.1(4)
F16-C46-C43	113.5(4)	F17-C46-C43	112.1(4)
F18-C46-C43	112.0(3)	C48-C47-C52	115.9(4)
C48-C47-B1	122.6(3)	C52-C47-B1	121.5(3)
C47-C48-C49	122.2(4)	C47-C48-H48	118.9
C49-C48-H48	118.9	C50-C49-C48	120.8(4)
C50-C49-C53	120.3(4)	C48-C49-C53	118.9(4)
C51-C50-C49	117.9(4)	C51-C50-H50	121.1
C49-C50-H50	121.1	C50-C51-C52	121.4(4)
C50-C51-C54	120.0(4)	C52-C51-C54	118.6(4)
C51-C52-C47	121.7(4)	C51-C52-H52	119.1
C47-C52-H52	119.1	F20-C53-F21	108.2(7)
F20-C53-F19	101.3(6)	F21-C53-F19	105.3(5)
F20-C53-C49	114.1(5)	F21-C53-C49	114.4(5)
F19-C53-C49	112.5(6)	F22-C54-F24	106.7(5)

Table S28. Bond Angles (degrees) for fac-[Re(bpy)(CO)$_3$4DMABN](BArF$_{24}$).

Atoms	Angle	Atoms	Angle
F22-C54-F23	106.5(5)	F24-C54-F23	102.5(5)
F22-C54-C51	114.2(4)	F24-C54-C51	113.0(5)
F23-C54-C51	113.0(4)		

Table S29. Anisotropic atomic displacement parameters (Å^2) for fac-[Re(bpy)(CO)$_3$4DMABN](BArF$_{24}$).. The anisotropic atomic displacement factor exponent takes the form: $-2\pi^2[\,h^2\,a^{*2}\,U_{11} + ... + 2\,h\,k\,a^*\,b^*\,U_{12}]$.

Atom	U_{11}	U_{22}	U_{33}	U_{23}	U_{13}	U_{12}
Re1	0.01459(8)	0.02477(9)	0.01858(8)	0.00110(6)	-0.00065(5)	-0.00097(6)
O1	0.0173(16)	0.041(2)	0.076(3)	0.0038(19)	-0.0096(17)	-0.0024(15)
O2	0.041(2)	0.033(2)	0.0371(19)	0.0065(15)	-0.0014(15)	0.0002(15)
O3	0.086(3)	0.044(2)	0.040(2)	-0.0045(17)	0.035(2)	-0.010(2)
N1	0.0157(16)	0.0288(19)	0.0215(16)	0.0002(14)	-0.0024(13)	-0.0003(14)
N2	0.0162(15)	0.0198(16)	0.0193(15)	-0.0011(13)	-0.0017(12)	-0.0010(13)
N3	0.0185(16)	0.0220(17)	0.0212(16)	-0.0002(13)	-0.0031(13)	-0.0011(13)
N4	0.0209(19)	0.033(2)	0.040(2)	0.0033(17)	-0.0096(16)	-0.0024(15)
C1	0.024(2)	0.025(2)	0.038(2)	0.0006(19)	0.0049(18)	-0.0016(18)
C2	0.029(2)	0.0093(17)	0.033(2)	0.0024(16)	-0.0026(17)	0.0005(16)
C3	0.039(3)	0.023(2)	0.034(2)	0.0009(18)	0.011(2)	-0.0030(19)
C4	0.026(2)	0.031(2)	0.025(2)	-0.0083(18)	0.0012(17)	0.0043(18)
C5	0.034(2)	0.024(2)	0.046(3)	-0.011(2)	0.000(2)	0.0051(19)
C6	0.031(2)	0.023(2)	0.048(3)	0.001(2)	-0.004(2)	-0.0010(19)
C7	0.031(2)	0.028(2)	0.036(2)	0.0044(19)	0.0016(19)	-0.0003(19)
C8	0.0198(19)	0.022(2)	0.032(2)	-0.0002(17)	-0.0010(17)	0.0003(16)
C9	0.0207(19)	0.0192(19)	0.0245(19)	-0.0006(15)	-0.0004(15)	0.0012(15)
C10	0.045(3)	0.030(2)	0.035(3)	0.007(2)	0.013(2)	-0.003(2)
C11	0.046(3)	0.042(3)	0.034(3)	-0.002(2)	0.022(2)	-0.001(2)
C12	0.035(3)	0.033(3)	0.034(2)	-0.012(2)	0.010(2)	0.001(2)
C13	0.024(2)	0.022(2)	0.033(2)	-0.0012(17)	-0.0022(17)	0.0005(17)
C14	0.023(2)	0.0162(19)	0.0188(18)	0.0019(14)	0.0008(15)	0.0006(15)
C15	0.0185(18)	0.0160(19)	0.0215(18)	-0.0005(14)	-0.0022(15)	-0.0011(14)
C16	0.024(2)	0.021(2)	0.0198(19)	0.0008(15)	0.0014(16)	-0.0001(15)
C17	0.0175(19)	0.026(2)	0.031(2)	0.0019(17)	0.0020(16)	-0.0001(15)
C18	0.0175(19)	0.018(2)	0.034(2)	0.0019(16)	-0.0036(16)	-0.0014(14)
C19	0.022(2)	0.042(3)	0.021(2)	0.0011(18)	-0.0041(16)	-0.0025(18)
C20	0.019(2)	0.041(3)	0.021(2)	0.0014(17)	0.0023(16)	-0.0009(17)
C21	0.038(3)	0.052(3)	0.042(3)	0.003(2)	-0.023(2)	-0.006(2)
C22	0.016(2)	0.049(3)	0.070(4)	-0.003(3)	-0.007(2)	0.002(2)
B1	0.0178(19)	0.0086(19)	0.0174(19)	0.0002(14)	0.0003(15)	0.0003(14)
F1	0.0379(17)	0.075(2)	0.0385(16)	0.0110(16)	-0.0002(13)	0.0279(16)
F2	0.0443(17)	0.0446(18)	0.0460(17)	-0.0012(14)	-0.0247(14)	0.0011(14)
F3	0.0436(17)	0.0391(17)	0.062(2)	0.0298(15)	-0.0129(15)	0.0015(14)

Table S29. Anisotropic atomic displacement parameters (Å^2) for fac-[Re(bpy)(CO)$_3$4DMABN](BArF$_{24}$).. The anisotropic atomic displacement factor exponent takes the form: $-2\pi^2[\,h^2\,a^{*2}\,U_{11} + ... + 2\,h\,k\,a^*\,b^*\,U_{12}]$.

Atom	U_{11}	U_{22}	U_{33}	U_{23}	U_{13}	U_{12}
F4	0.0263(13)	0.0315(14)	0.0479(16)	0.0075(12)	0.0127(12)	0.0072(11)
F5	0.0320(15)	0.0310(15)	0.077(2)	0.0290(15)	0.0171(15)	0.0011(12)
F6	0.0349(16)	0.058(2)	0.0543(19)	-0.0181(16)	0.0066(14)	-0.0233(15)
F7	0.109(3)	0.044(2)	0.054(2)	-0.0159(16)	0.007(2)	-0.046(2)
F8	0.085(3)	0.0435(19)	0.084(3)	-0.0311(19)	-0.061(2)	0.0154(18)
F9	0.069(2)	0.0379(18)	0.064(2)	-0.0313(16)	0.0000(18)	0.0122(16)
F10	0.110(3)	0.042(2)	0.086(3)	0.0284(19)	-0.070(2)	-0.013(2)
F11	0.082(3)	0.0374(18)	0.069(2)	0.0300(17)	0.014(2)	-0.0060(18)
F12	0.105(3)	0.0399(19)	0.053(2)	0.0146(16)	0.011(2)	0.041(2)
F13	0.0383(17)	0.085(3)	0.0450(18)	-0.0115(17)	0.0001(14)	-0.0311(17)
F14	0.0391(17)	0.0409(17)	0.063(2)	-0.0327(15)	-0.0123(15)	-0.0014(14)
F15	0.0519(19)	0.0415(18)	0.060(2)	-0.0016(15)	-0.0371(16)	0.0005(15)
F16	0.0306(14)	0.0313(15)	0.064(2)	-0.0232(14)	0.0163(14)	-0.0003(12)
F17	0.0301(14)	0.0501(18)	0.0498(17)	0.0170(14)	0.0060(13)	0.0186(13)
F18	0.0233(13)	0.0299(14)	0.0416(15)	-0.0038(12)	0.0086(11)	-0.0053(11)
F19	0.054(2)	0.077(3)	0.237(6)	-0.105(4)	0.025(3)	-0.008(2)
F20	0.188(5)	0.081(3)	0.221(6)	0.073(4)	0.141(5)	0.096(4)
F21	0.0317(16)	0.0437(19)	0.101(3)	-0.0225(19)	0.0137(17)	0.0074(14)
F22	0.051(2)	0.052(2)	0.174(4)	0.042(3)	0.061(3)	0.0065(18)
F23	0.098(3)	0.051(2)	0.085(3)	-0.001(2)	0.011(2)	-0.044(2)
F24	0.063(2)	0.057(2)	0.083(3)	0.046(2)	0.011(2)	0.0008(18)
C23	0.0207(18)	0.0097(16)	0.0158(16)	-0.0038(13)	0.0000(14)	0.0017(14)
C24	0.0199(18)	0.0157(18)	0.0208(18)	-0.0007(14)	-0.0018(15)	-0.0025(15)
C25	0.026(2)	0.0176(19)	0.0181(18)	0.0015(15)	-0.0043(15)	0.0021(16)
C26	0.030(2)	0.0138(18)	0.0197(18)	0.0034(15)	0.0040(16)	0.0013(16)
C27	0.024(2)	0.0144(18)	0.0214(18)	-0.0030(15)	0.0065(15)	-0.0004(15)
C28	0.0195(18)	0.0113(17)	0.0200(18)	-0.0034(14)	-0.0003(14)	0.0044(14)
C29	0.031(2)	0.024(2)	0.026(2)	0.0086(17)	-0.0035(18)	0.0015(18)
C30	0.026(2)	0.021(2)	0.037(2)	0.0064(18)	0.0072(18)	0.0019(17)
C31	0.0212(18)	0.0107(18)	0.0160(17)	-0.0004(13)	0.0002(14)	0.0005(13)
C32	0.0224(19)	0.0128(17)	0.0199(18)	0.0004(14)	-0.0001(15)	0.0020(14)
C33	0.024(2)	0.0198(19)	0.0192(18)	-0.0064(15)	0.0028(15)	-0.0009(16)
C34	0.025(2)	0.020(2)	0.0133(16)	0.0037(14)	0.0013(15)	-0.0007(15)
C35	0.028(2)	0.0183(19)	0.0184(18)	0.0053(15)	0.0007(16)	0.0008(16)

Table S29. Anisotropic atomic displacement parameters (Å^2) for fac-[Re(bpy)(CO)$_3$4DMABN](BArF$_{24}$).. The anisotropic atomic displacement factor exponent takes the form: $-2\pi^2[\, h^2\, a^{*2}\, U_{11} + ... + 2\, h\, k\, a^*\, b^*\, U_{12}]$.

Atom	U_{11}	U_{22}	U_{33}	U_{23}	U_{13}	U_{12}
C36	0.0245(19)	0.0124(17)	0.0198(18)	-0.0010(14)	0.0003(15)	-0.0030(15)
C37	0.041(3)	0.026(2)	0.029(2)	-0.0111(19)	-0.009(2)	0.001(2)
C38	0.050(3)	0.024(2)	0.026(2)	0.0081(18)	-0.012(2)	-0.001(2)
C39	0.0218(18)	0.0091(16)	0.0152(16)	0.0025(13)	0.0003(14)	-0.0005(14)
C40	0.0195(18)	0.0138(17)	0.0200(18)	0.0001(14)	-0.0013(14)	0.0023(14)
C41	0.0221(19)	0.0183(19)	0.0194(18)	-0.0023(15)	-0.0030(15)	-0.0014(15)
C42	0.027(2)	0.0126(17)	0.0189(18)	-0.0044(14)	0.0013(15)	0.0004(15)
C43	0.0206(19)	0.0141(18)	0.0218(18)	0.0002(14)	0.0056(15)	0.0011(14)
C44	0.0170(17)	0.0113(17)	0.0193(17)	0.0026(14)	0.0003(14)	-0.0033(14)
C45	0.028(2)	0.023(2)	0.028(2)	-0.0064(17)	-0.0048(17)	-0.0020(17)
C46	0.027(2)	0.019(2)	0.031(2)	-0.0028(17)	0.0075(18)	-0.0003(17)
C47	0.0214(19)	0.0115(17)	0.0164(17)	-0.0013(13)	-0.0008(14)	0.0006(14)
C48	0.027(2)	0.0168(19)	0.029(2)	-0.0030(16)	0.0056(17)	-0.0039(16)
C49	0.028(2)	0.025(2)	0.037(2)	-0.0070(19)	0.0107(19)	0.0034(18)
C50	0.026(2)	0.033(3)	0.033(2)	-0.0008(19)	0.0111(19)	0.0003(18)
C51	0.024(2)	0.025(2)	0.030(2)	0.0075(17)	0.0031(17)	-0.0024(17)
C52	0.023(2)	0.0177(19)	0.0248(19)	0.0052(15)	0.0035(16)	0.0016(15)
C53	0.053(4)	0.026(3)	0.111(6)	-0.006(3)	0.050(4)	0.004(3)
C54	0.033(3)	0.033(3)	0.056(3)	0.016(2)	0.016(2)	0.000(2)

Table S30. Hydrogen atomic coordinates and isotropic atomic displacement parameters ($Å^2$) for fac-[Re(bpy)(CO)$_3$4DMABN](BArF$_{24}$).

Atom	x	y	z	U(eq)
H4	0.4635	0.5766	0.7630	0.033
H5	0.4777	0.4324	0.7879	0.042
H6	0.4365	0.3942	0.8634	0.041
H7	0.3824	0.5054	0.9129	0.038
H10	0.3103	0.6118	0.9501	0.043
H11	0.2637	0.7361	0.9915	0.047
H12	0.2868	0.8767	0.9597	0.04
H13	0.3528	0.8890	0.8873	0.032
H16	0.0202	0.7528	0.7927	0.026
H17	-0.1325	0.7519	0.7506	0.03
H19	-0.0002	0.7570	0.6273	0.034
H20	0.1524	0.7576	0.6700	0.032
H21A	-0.1426	0.8042	0.5964	0.068
H21B	-0.2499	0.7607	0.5952	0.068
H21C	-0.1544	0.6989	0.5959	0.068
H22A	-0.2633	0.6985	0.7029	0.069
H22B	-0.3204	0.7507	0.6597	0.069
H22C	-0.2661	0.8043	0.7031	0.069
H24	0.7829	0.8548	0.8560	0.023
H26	0.9571	1.0362	0.7991	0.025
H28	1.0759	0.8507	0.8905	0.02
H32	1.0044	0.8842	0.9709	0.022
H34	1.1528	0.7470	1.0773	0.024
H36	0.9997	0.6182	0.9694	0.023
H40	0.7768	0.6548	0.8570	0.022
H42	0.9461	0.4717	0.7976	0.024
H44	1.0709	0.6551	0.8888	0.019
H48	0.7844	0.8877	0.9405	0.029
H50	0.5555	0.7537	0.9889	0.036
H52	0.7906	0.6216	0.9455	0.026
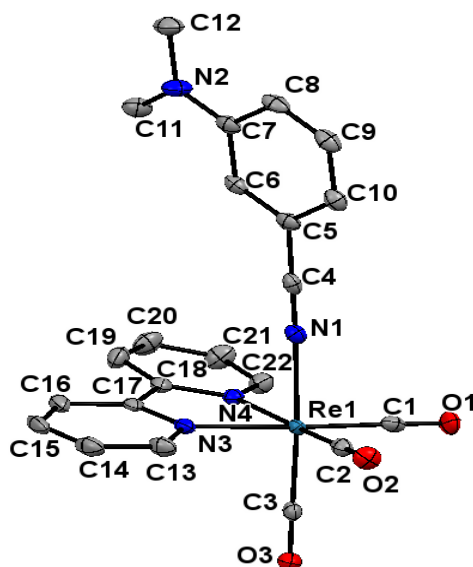
Structure Determination Summary for fac-[Re(bpy)(CO)$_3$3DMABN](BArF$_{24}$)

Identification code	RHS-011
Empirical formula	$C_{54}H_{30}BF_{24}N_4O_3Re$
Formula weight	1435.83
Temperature	293(2) K
Wavelength	1.54178 Å
Crystal size	0.110 x 0.152 x 0.240 mm
Crystal habit	clear yellow Block
Crystal system	triclinic
Space group	P$\bar{1}$
Unit cell dimensions	a = 12.2427(3) Å α = 84.7050(10)°
	b = 14.2659(3) Å β = 74.4170(10)°
	c = 16.2785(4) Å γ = 76.9680(10)°
Volume	2666.53(11) Å^3
Density (calculated)	1.788 g/cm^3
Absorption coefficient	5.676 mm^{-1}
F(000)	1404
θ range for data collection	2.82 to 69.84°
Limiting indices	-14< h< 14, -17< k< 17, -19< l< 18
Reflections collected	45801
Independent reflections	9758 [R(int) = 0.1010]
Completeness to θ = 69.84^o	96.9%
Absorption correction	multi-scan
Structure solution technique	direct methods
Refinement method	Full-matrix least-squares on F2
Data / restraints / parameters	9758 / 0 / 786
Goodness-of-fit on F2	1.072
Final R indices	9609 data; I>2σ(I) R1 = 0.0250, wR2 = 0.0633
	all data R1 = 0.0255, wR2 = 0.0639
Absolute structure parameter	0.004
Largest diff. peak and hole	1.182 and -1.380 eÅ^{-3}

Table S31. Atomic coordinates and equivalent isotropic atomic displacement parameters (Å^2) for fac-[Re(bpy)(CO)$_3$3DMABN](BArF$_{24}$). U(eq) is defined as one third of the trace of the orthogonalized U_{ij} tensor.

Atom	x	y	z	U(eq)
Re1	0.899575(7)	0.781097(6)	0.152607(5)	0.01325(5)
O1	0.93413(16)	0.86362(14)	0.96813(11)	0.0252(4)
O2	0.77960(16)	0.63149(13)	0.10910(12)	0.0254(4)
O3	0.66758(15)	0.92827(14)	0.19878(11)	0.0241(4)
N1	0.06200(17)	0.68233(15)	0.12731(12)	0.0179(4)
N2	0.52495(18)	0.50864(16)	0.17689(15)	0.0263(5)
N3	0.88732(16)	0.73305(15)	0.28463(12)	0.0171(4)
N4	0.99591(16)	0.86632(14)	0.19838(12)	0.0159(4)
C1	0.9219(2)	0.83140(17)	0.03660(15)	0.0186(5)
C2	0.8231(2)	0.68879(17)	0.12417(15)	0.0181(5)
C3	0.7543(2)	0.87333(18)	0.18170(14)	0.0180(5)
C4	0.1499(2)	0.62899(18)	0.11647(14)	0.0180(5)
C5	0.2572(2)	0.55927(17)	0.10354(15)	0.0185(5)
C6	0.3402(2)	0.57061(17)	0.14407(15)	0.0187(5)
C7	0.4431(2)	0.50027(17)	0.13622(15)	0.0199(5)
C8	0.4579(2)	0.42068(17)	0.08554(16)	0.0225(5)
C9	0.3751(2)	0.41266(18)	0.04477(16)	0.0235(5)
C10	0.2733(2)	0.48095(18)	0.05258(15)	0.0210(5)
C11	0.5161(2)	0.59709(19)	0.21708(17)	0.0259(5)
C12	0.6296(2)	0.4342(2)	0.16953(18)	0.0291(6)
C13	0.8220(2)	0.67071(19)	0.32716(17)	0.0237(5)
C14	0.8143(2)	0.6440(2)	0.41194(17)	0.0293(6)
C15	0.8760(2)	0.6825(2)	0.45471(15)	0.0274(6)
C16	0.9432(2)	0.74656(19)	0.41236(15)	0.0237(5)
C17	0.94800(19)	0.77099(17)	0.32692(14)	0.0172(5)
C18	0.0141(2)	0.84130(17)	0.27724(15)	0.0179(5)
C19	0.0872(2)	0.88119(19)	0.30782(17)	0.0252(5)
C20	0.1412(2)	0.9506(2)	0.25894(19)	0.0296(6)
C21	0.1205(2)	0.9784(2)	0.17968(18)	0.0281(6)
C22	0.0480(2)	0.93451(18)	0.15168(16)	0.0218(5)
B1	0.3337(2)	0.19919(18)	0.28757(15)	0.0122(5)
C23	0.42619(19)	0.18013(15)	0.19338(13)	0.0125(4)
C24	0.39574(19)	0.16174(15)	0.12033(14)	0.0137(4)
C25	0.4765(2)	0.14407(16)	0.04173(14)	0.0156(4)

Table S31. Atomic coordinates and equivalent isotropic atomic displacement parameters (Å^2) for fac-[Re(bpy)(CO)$_3$3DMABN](BArF$_{24}$). U(eq) is defined as one third of the trace of the orthogonalized U_{ij} tensor.

Atom	x	y	z	U(eq)
C26	0.5924(2)	0.14310(16)	0.03240(14)	0.0168(4)
C27	0.62635(19)	0.15756(16)	0.10479(14)	0.0161(4)
C28	0.4363(2)	0.12753(17)	0.96628(15)	0.0186(5)
C29	0.7524(2)	0.15285(19)	0.09574(16)	0.0215(5)
C30	0.35000(19)	0.29585(16)	0.32757(13)	0.0132(4)
C31	0.44620(19)	0.29647(16)	0.35885(14)	0.0150(4)
C32	0.4627(2)	0.38009(17)	0.38826(14)	0.0168(4)
C33	0.3806(2)	0.46546(17)	0.39231(14)	0.0169(4)
C34	0.28268(19)	0.46562(16)	0.36486(14)	0.0149(4)
C35	0.26883(19)	0.38353(16)	0.33217(13)	0.0141(4)
C36	0.5698(2)	0.37677(19)	0.41700(17)	0.0238(5)
C37	0.1868(2)	0.55331(17)	0.37617(15)	0.0185(5)
C38	0.19809(19)	0.21722(16)	0.28152(14)	0.0133(4)
C39	0.15659(19)	0.27859(16)	0.21875(14)	0.0150(4)
C40	0.0409(2)	0.29734(17)	0.21648(14)	0.0166(4)
C41	0.9596(2)	0.25681(17)	0.27742(15)	0.0182(5)
C42	0.9980(2)	0.19743(17)	0.34095(14)	0.0169(4)
C43	0.11403(19)	0.17768(16)	0.34285(14)	0.0151(4)
C44	0.0026(2)	0.3653(2)	0.14863(17)	0.0239(5)
C45	0.9111(2)	0.1571(2)	0.41042(16)	0.0245(5)
C46	0.35837(17)	0.10301(16)	0.34909(14)	0.0124(4)
C47	0.38915(18)	0.01057(16)	0.31601(14)	0.0135(4)
C48	0.39582(19)	0.92770(16)	0.36814(14)	0.0155(4)
C49	0.37405(19)	0.93323(17)	0.45640(14)	0.0157(4)
C50	0.34614(18)	0.02371(17)	0.49022(14)	0.0141(4)
C51	0.33829(18)	0.10686(16)	0.43797(14)	0.0135(4)
C52	0.4247(2)	0.82970(17)	0.33127(15)	0.0196(5)
C53	0.3180(2)	0.03289(17)	0.58525(14)	0.0161(4)
C54	0.54514(19)	0.17552(16)	0.18282(14)	0.0145(4)
F1	0.34328(13)	0.08692(12)	0.98801(9)	0.0269(3)
F2	0.40584(15)	0.21008(11)	0.92295(9)	0.0291(3)
F3	0.51903(13)	0.07005(11)	0.90981(9)	0.0252(3)
F4	0.81877(13)	0.06830(12)	0.06624(12)	0.0362(4)
F5	0.79280(15)	0.21952(14)	0.03946(13)	0.0442(5)

Table S31. Atomic coordinates and equivalent isotropic atomic displacement parameters
(Å^2) for fac-[Re(bpy)(CO)$_3$3DMABN](BArF$_{24}$). U(eq) is defined as one third of the
trace of the orthogonalized U$_{ij}$ tensor.

Atom	x	y	z	U(eq)
F6	0.77651(14)	0.16599(18)	0.16814(11)	0.0465(5)
F7	0.59901(15)	0.46214(13)	0.41088(13)	0.0404(4)
F8	0.66275(16)	0.31952(18)	0.36984(18)	0.0670(8)
F9	0.5588(2)	0.34778(18)	0.49781(13)	0.0571(6)
F10	0.22440(14)	0.63578(11)	0.36255(13)	0.0362(4)
F11	0.11754(14)	0.55542(12)	0.45552(10)	0.0361(4)
F12	0.11818(14)	0.55794(11)	0.32359(10)	0.0302(3)
F13	0.89999(14)	0.35806(16)	0.13930(12)	0.0463(5)
F14	0.99442(17)	0.45744(12)	0.16508(11)	0.0405(4)
F15	0.07744(13)	0.35072(12)	0.07166(9)	0.0285(3)
F16	0.82043(12)	0.14618(12)	0.38530(10)	0.0278(3)
F17	0.86772(16)	0.21574(17)	0.47744(10)	0.0457(5)
F18	0.95669(14)	0.07167(15)	0.44149(13)	0.0502(6)
F19	0.4219(2)	0.83341(12)	0.24968(10)	0.0499(6)
F20	0.34876(15)	0.77625(12)	0.37196(10)	0.0329(4)
F21	0.52789(15)	0.77891(13)	0.33619(16)	0.0501(5)
F22	0.37292(12)	0.95706(11)	0.62419(8)	0.0242(3)
F23	0.20385(12)	0.04043(10)	0.62209(8)	0.0217(3)
F24	0.34451(13)	0.11196(11)	0.60680(9)	0.0242(3)

Table S32. Bond Lengths (Å) for fac-[Re(bpy)(CO)$_3$3DMABN](BArF$_{24}$).

Bond	Length	Bond	Length
Re1-C1	1.928(2)	Re1-C3	1.930(2)
Re1-C2	1.930(3)	Re1-N1	2.124(2)
Re1-N4	2.170(2)	Re1-N3	2.1708(19)
O1-C1	1.150(3)	O2-C2	1.147(3)
O3-C3	1.151(3)	N1-C4	1.149(3)
N2-C7	1.372(3)	N2-C11	1.444(4)
N2-C12	1.453(3)	N3-C13	1.348(3)
N3-C17	1.358(3)	N4-C22	1.347(3)
N4-C18	1.363(3)	C4-C5	1.435(3)
C5-C6	1.396(4)	C5-C10	1.400(3)
C6-C7	1.406(3)	C6-H6	0.93
C7-C8	1.415(4)	C8-C9	1.381(4)
C8-H8	0.93	C9-C10	1.381(4)
C9-H9	0.93	C10-H10	0.93
C11-H11A	0.96	C11-H11B	0.96
C11-H11C	0.96	C12-H12A	0.96
C12-H12B	0.96	C12-H12C	0.96
C13-C14	1.381(4)	C13-H13	0.93
C14-C15	1.378(4)	C14-H14	0.93
C15-C16	1.380(4)	C15-H15	0.93
C16-C17	1.391(3)	C16-H16	0.93
C17-C18	1.476(3)	C18-C19	1.376(4)
C19-C20	1.385(4)	C19-H19	0.93
C20-C21	1.386(4)	C20-H20	0.93
C21-C22	1.381(4)	C21-H21	0.93
C22-H22	0.93	B1-C46	1.643(3)
B1-C23	1.647(3)	B1-C38	1.649(3)
B1-C30	1.651(3)	C23-C24	1.401(3)
C23-C54	1.407(3)	C24-C25	1.395(3)
C24-H24	0.93	C25-C26	1.383(3)
C25-C28	1.496(3)	C26-C27	1.396(3)
C26-H26	0.93	C27-C54	1.391(3)
C27-C29	1.497(3)	C28-F1	1.342(3)
C28-F3	1.344(3)	C28-F2	1.347(3)
C29-F6	1.328(3)	C29-F5	1.340(3)

Table S32. Bond Lengths (Å) for fac-[Re(bpy)(CO)₃3DMABN](BArF₂₄).

Bond	Length	Bond	Length
C29-F4	1.342(3)	C30-C35	1.405(3)
C30-C31	1.405(3)	C31-C32	1.400(3)
C31-H31	0.93	C32-C33	1.387(3)
C32-C36	1.497(3)	C33-C34	1.387(3)
C33-H33	0.93	C34-C35	1.392(3)
C34-C37	1.497(3)	C35-H35	0.93
C36-F9	1.322(3)	C36-F7	1.332(3)
C36-F8	1.333(3)	C37-F10	1.337(3)
C37-F12	1.339(3)	C37-F11	1.340(3)
C38-C43	1.407(3)	C38-C39	1.408(3)
C39-C40	1.390(3)	C39-H39	0.93
C40-C41	1.390(3)	C40-C44	1.502(3)
C41-C42	1.389(3)	C41-H41	0.93
C42-C43	1.393(3)	C42-C45	1.500(3)
C43-H43	0.93	C44-F13	1.332(3)
C44-F15	1.341(3)	C44-F14	1.342(3)
C45-F16	1.326(3)	C45-F18	1.335(3)
C45-F17	1.353(3)	C46-C47	1.403(3)
C46-C51	1.405(3)	C47-C48	1.390(3)
C47-H47	0.93	C48-C49	1.395(3)
C48-C52	1.503(3)	C49-C50	1.385(3)
C49-H49	0.93	C50-C51	1.395(3)
C50-C53	1.503(3)	C51-H51	0.93
C52-F21	1.325(3)	C52-F19	1.334(3)
C52-F20	1.335(3)	C53-F22	1.341(3)
C53-F24	1.342(3)	C53-F23	1.349(3)
C54-H54	0.93		

Table S33. Bond Angles (degrees) for fac-[Re(bpy)(CO)$_3$3DMABN](BArF$_{24}$).

Atoms	Angle	Atoms	Angle
C1-Re1-C3	88.53(9)	C1-Re1-C2	88.77(10)
C3-Re1-C2	90.77(10)	C1-Re1-N1	93.86(9)
C3-Re1-N1	176.41(8)	C2-Re1-N1	91.97(9)
C1-Re1-N4	98.97(9)	C3-Re1-N4	94.71(9)
C2-Re1-N4	170.62(8)	N1-Re1-N4	82.27(8)
C1-Re1-N3	173.99(9)	C3-Re1-N3	92.76(8)
C2-Re1-N3	97.08(9)	N1-Re1-N3	84.60(7)
N4-Re1-N3	75.09(8)	C4-N1-Re1	177.68(19)
C7-N2-C11	120.3(2)	C7-N2-C12	120.2(2)
C11-N2-C12	119.0(2)	C13-N3-C17	118.6(2)
C13-N3-Re1	124.58(18)	C17-N3-Re1	116.80(15)
C22-N4-C18	118.2(2)	C22-N4-Re1	124.87(16)
C18-N4-Re1	116.54(16)	O1-C1-Re1	178.3(2)
O2-C2-Re1	177.5(2)	O3-C3-Re1	179.7(2)
N1-C4-C5	177.7(3)	C6-C5-C10	122.4(2)
C6-C5-C4	118.9(2)	C10-C5-C4	118.7(2)
C5-C6-C7	119.8(2)	C5-C6-H6	120.1
C7-C6-H6	120.1	N2-C7-C6	120.9(2)
N2-C7-C8	121.7(2)	C6-C7-C8	117.3(2)
C9-C8-C7	121.4(2)	C9-C8-H8	119.3
C7-C8-H8	119.3	C8-C9-C10	121.7(2)
C8-C9-H9	119.1	C10-C9-H9	119.1
C9-C10-C5	117.3(2)	C9-C10-H10	121.4
C5-C10-H10	121.4	N2-C11-H11A	109.5
N2-C11-H11B	109.5	H11A-C11-H11B	109.5
N2-C11-H11C	109.5	H11A-C11-H11C	109.5
H11B-C11-H11C	109.5	N2-C12-H12A	109.5
N2-C12-H12B	109.5	H12A-C12-H12B	109.5
N2-C12-H12C	109.5	H12A-C12-H12C	109.5
H12B-C12-H12C	109.5	N3-C13-C14	122.7(3)
N3-C13-H13	118.6	C14-C13-H13	118.6
C15-C14-C13	118.6(3)	C15-C14-H14	120.7
C13-C14-H14	120.7	C14-C15-C16	119.6(2)
C14-C15-H15	120.2	C16-C15-H15	120.2
C15-C16-C17	119.5(3)	C15-C16-H16	120.2

Table S33. Bond Angles (degrees) for fac-[Re(bpy)(CO)₃3DMABN](BArF₂₄).

Atoms	Angle	Atoms	Angle
C17-C16-H16	120.2	N3-C17-C16	121.0(2)
N3-C17-C18	115.6(2)	C16-C17-C18	123.4(2)
N4-C18-C19	121.5(2)	N4-C18-C17	115.1(2)
C19-C18-C17	123.3(2)	C18-C19-C20	119.7(2)
C18-C19-H19	120.1	C20-C19-H19	120.1
C19-C20-C21	119.1(3)	C19-C20-H20	120.5
C21-C20-H20	120.5	C22-C21-C20	118.6(2)
C22-C21-H21	120.7	C20-C21-H21	120.7
N4-C22-C21	122.8(2)	N4-C22-H22	118.6
C21-C22-H22	118.6	C46-B1-C23	108.08(17)
C46-B1-C38	108.08(17)	C23-B1-C38	111.87(18)
C46-B1-C30	111.53(18)	C23-B1-C30	109.38(17)
C38-B1-C30	107.93(17)	C24-C23-C54	115.19(19)
C24-C23-B1	123.90(19)	C54-C23-B1	120.8(2)
C25-C24-C23	122.6(2)	C25-C24-H24	118.7
C23-C24-H24	118.7	C26-C25-C24	121.1(2)
C26-C25-C28	119.7(2)	C24-C25-C28	119.2(2)
C25-C26-C27	117.8(2)	C25-C26-H26	121.1
C27-C26-H26	121.1	C54-C27-C26	120.8(2)
C54-C27-C29	121.2(2)	C26-C27-C29	118.0(2)
F1-C28-F3	106.9(2)	F1-C28-F2	106.2(2)
F3-C28-F2	106.15(18)	F1-C28-C25	112.71(19)
F3-C28-C25	112.3(2)	F2-C28-C25	112.2(2)
F6-C29-F5	106.3(2)	F6-C29-F4	106.9(2)
F5-C29-F4	105.16(19)	F6-C29-C27	113.62(19)
F5-C29-C27	112.0(2)	F4-C29-C27	112.3(2)
C35-C30-C31	115.3(2)	C35-C30-B1	122.2(2)
C31-C30-B1	122.45(19)	C32-C31-C30	122.1(2)
C32-C31-H31	119.0	C30-C31-H31	119.0
C33-C32-C31	121.1(2)	C33-C32-C36	119.6(2)
C31-C32-C36	119.3(2)	C34-C33-C32	117.8(2)
C34-C33-H33	121.1	C32-C33-H33	121.1
C33-C34-C35	121.0(2)	C33-C34-C37	119.4(2)
C35-C34-C37	119.4(2)	C34-C35-C30	122.6(2)
C34-C35-H35	118.7	C30-C35-H35	118.7

Table S33. Bond Angles (degrees) for fac-[Re(bpy)(CO)$_3$3DMABN](BArF$_{24}$).

Atoms	Angle	Atoms	Angle
F9-C36-F7	105.5(2)	F9-C36-F8	108.1(3)
F7-C36-F8	104.6(2)	F9-C36-C32	112.6(2)
F7-C36-C32	113.1(2)	F8-C36-C32	112.3(2)
F10-C37-F12	105.7(2)	F10-C37-F11	106.7(2)
F12-C37-F11	106.20(19)	F10-C37-C34	113.44(19)
F12-C37-C34	113.12(19)	F11-C37-C34	111.16(19)
C43-C38-C39	115.4(2)	C43-C38-B1	121.92(19)
C39-C38-B1	122.53(19)	C40-C39-C38	122.3(2)
C40-C39-H39	118.8	C38-C39-H39	118.8
C41-C40-C39	121.2(2)	C41-C40-C44	119.5(2)
C39-C40-C44	119.3(2)	C42-C41-C40	117.5(2)
C42-C41-H41	121.2	C40-C41-H41	121.2
C41-C42-C43	121.4(2)	C41-C42-C45	118.8(2)
C43-C42-C45	119.8(2)	C42-C43-C38	122.1(2)
C42-C43-H43	118.9	C38-C43-H43	118.9
F13-C44-F15	106.3(2)	F13-C44-F14	107.2(2)
F15-C44-F14	105.5(2)	F13-C44-C40	113.0(2)
F15-C44-C40	112.4(2)	F14-C44-C40	111.9(2)
F16-C45-F18	107.2(2)	F16-C45-F17	105.9(2)
F18-C45-F17	106.3(2)	F16-C45-C42	112.9(2)
F18-C45-C42	112.6(2)	F17-C45-C42	111.4(2)
C47-C46-C51	116.0(2)	C47-C46-B1	120.83(19)
C51-C46-B1	122.86(19)	C48-C47-C46	122.1(2)
C48-C47-H47	118.9	C46-C47-H47	118.9
C47-C48-C49	120.9(2)	C47-C48-C52	121.0(2)
C49-C48-C52	118.1(2)	C50-C49-C48	117.9(2)
C50-C49-H49	121.0	C48-C49-H49	121.0
C49-C50-C51	121.1(2)	C49-C50-C53	119.5(2)
C51-C50-C53	119.2(2)	C50-C51-C46	121.9(2)
C50-C51-H51	119.0	C46-C51-H51	119.0
F21-C52-F19	107.4(2)	F21-C52-F20	105.7(2)
F19-C52-F20	105.3(2)	F21-C52-C48	113.4(2)
F19-C52-C48	112.7(2)	F20-C52-C48	111.69(19)
F22-C53-F24	107.41(19)	F22-C53-F23	106.11(18)
F24-C53-F23	105.48(18)	F22-C53-C50	112.93(19)

Table S33. Bond Angles (degrees) for fac-[Re(bpy)(CO)$_3$3DMABN](BArF$_{24}$).

Atoms	Angle	Atoms	Angle
F24-C53-C50	112.40(18)	F23-C53-C50	112.00(19)
C27-C54-C23	122.6(2)	C27-C54-H54	118.7
C23-C54-H54	118.7		

Table S34. Anisotropic atomic displacement parameters ($\mathring{A}^2$) for fac-[Re(bpy)(CO)$_3$3DMABN](BArF$_{24}$).. The anisotropic atomic displacement factor exponent takes the form: $-2\pi^2[\,h^2\,a^{*2}\,U_{11} + ... + 2\,h\,k\,a^*\,b^*\,U_{12}]$.

Atom	U_{11}	U_{22}	U_{33}	U_{23}	U_{13}	U_{12}
Re1	0.01169(6)	0.01592(6)	0.01093(6)	0.00034(4)	-0.00089(4)	-0.00317(4)
O1	0.0258(9)	0.0330(10)	0.0148(8)	0.0073(7)	-0.0032(7)	-0.0074(8)
O2	0.0246(9)	0.0247(9)	0.0292(9)	-0.0034(7)	-0.0056(7)	-0.0107(7)
O3	0.0199(9)	0.0288(10)	0.0196(8)	-0.0029(7)	-0.0043(7)	0.0028(7)
N1	0.0186(10)	0.0186(10)	0.0152(9)	-0.0002(8)	-0.0014(7)	-0.0050(8)
N2	0.0178(10)	0.0244(11)	0.0328(12)	-0.0049(9)	-0.0043(9)	0.0029(9)
N3	0.0139(9)	0.0187(10)	0.0145(9)	0.0007(7)	-0.0001(7)	0.0001(7)
N4	0.0139(9)	0.0152(9)	0.0170(9)	0.0000(7)	-0.0035(7)	-0.0007(7)
C1	0.0122(11)	0.0202(11)	0.0225(12)	-0.0047(10)	-0.0017(9)	-0.0029(9)
C2	0.0182(11)	0.0174(11)	0.0161(11)	0.0017(9)	-0.0023(9)	-0.0018(9)
C3	0.0202(12)	0.0214(12)	0.0122(10)	0.0009(9)	-0.0039(9)	-0.0050(10)
C4	0.0214(13)	0.0203(12)	0.0120(10)	-0.0011(9)	0.0000(9)	-0.0086(10)
C5	0.0173(11)	0.0174(11)	0.0170(11)	0.0010(9)	0.0022(9)	-0.0042(9)
C6	0.0197(11)	0.0159(11)	0.0166(11)	-0.0027(9)	0.0022(9)	-0.0030(9)
C7	0.0178(11)	0.0195(12)	0.0181(11)	0.0010(9)	0.0024(9)	-0.0044(9)
C8	0.0236(12)	0.0127(11)	0.0229(12)	0.0008(9)	0.0035(9)	0.0014(9)
C9	0.0292(13)	0.0166(11)	0.0209(12)	-0.0028(9)	0.0021(10)	-0.0063(10)
C10	0.0237(12)	0.0204(12)	0.0182(11)	-0.0015(9)	-0.0006(9)	-0.0088(10)
C11	0.0204(12)	0.0262(13)	0.0296(13)	-0.0016(11)	-0.0035(10)	-0.0051(10)
C12	0.0193(12)	0.0299(14)	0.0308(14)	0.0026(11)	-0.0025(10)	0.0035(10)
C13	0.0194(12)	0.0244(13)	0.0230(12)	0.0034(10)	0.0013(9)	-0.0055(10)
C14	0.0213(13)	0.0323(14)	0.0243(13)	0.0083(11)	0.0035(10)	-0.0003(11)
C15	0.0253(13)	0.0314(14)	0.0127(11)	0.0037(10)	0.0033(9)	0.0084(10)
C16	0.0235(12)	0.0264(13)	0.0150(11)	-0.0034(10)	-0.0031(9)	0.0066(10)
C17	0.0135(11)	0.0179(11)	0.0142(10)	-0.0021(9)	-0.0004(8)	0.0057(8)
C18	0.0164(11)	0.0181(11)	0.0164(11)	-0.0040(9)	-0.0035(9)	0.0024(9)
C19	0.0276(13)	0.0274(13)	0.0228(12)	-0.0025(10)	-0.0128(10)	-0.0019(10)
C20	0.0282(14)	0.0291(14)	0.0392(15)	-0.0018(12)	-0.0181(12)	-0.0096(11)
C21	0.0290(14)	0.0243(13)	0.0354(14)	0.0049(11)	-0.0129(11)	-0.0110(11)
C22	0.0209(12)	0.0218(12)	0.0235(12)	0.0042(10)	-0.0067(9)	-0.0069(9)
B1	0.0091(11)	0.0134(11)	0.0121(11)	-0.0020(9)	-0.0001(8)	-0.0010(8)
C23	0.0136(10)	0.0094(10)	0.0116(10)	-0.0005(8)	0.0001(8)	-0.0005(8)
C24	0.0114(10)	0.0126(10)	0.0156(10)	-0.0007(8)	-0.0022(8)	-0.0010(8)
C25	0.0190(11)	0.0130(10)	0.0127(10)	-0.0010(8)	-0.0025(8)	-0.0009(8)

Table S34. Anisotropic atomic displacement parameters (Å^2) for fac-[Re(bpy)(CO)$_3$3DMABN](BArF$_{24}$).. The anisotropic atomic displacement factor exponent takes the form: $-2\pi^2[\,h^2\,a^{*2}\,U_{11} + ... + 2\,h\,k\,a^*\,b^*\,U_{12}]$.

Atom	U_{11}	U_{22}	U_{33}	U_{23}	U_{13}	U_{12}
C26	0.0166(11)	0.0156(11)	0.0139(10)	-0.0015(8)	0.0022(8)	-0.0011(8)
C27	0.0141(11)	0.0149(10)	0.0171(11)	-0.0015(8)	-0.0004(8)	-0.0023(8)
C28	0.0218(12)	0.0167(11)	0.0145(11)	-0.0029(9)	-0.0021(9)	-0.0001(9)
C29	0.0140(11)	0.0257(13)	0.0212(12)	-0.0045(10)	0.0022(9)	-0.0030(9)
C30	0.0115(10)	0.0155(10)	0.0098(9)	-0.0001(8)	0.0018(8)	-0.0028(8)
C31	0.0132(10)	0.0156(11)	0.0138(10)	-0.0011(8)	-0.0008(8)	-0.0007(8)
C32	0.0162(11)	0.0199(11)	0.0134(10)	-0.0031(9)	-0.0018(8)	-0.0035(9)
C33	0.0186(11)	0.0163(11)	0.0147(10)	-0.0035(8)	-0.0010(8)	-0.0038(9)
C34	0.0136(10)	0.0147(11)	0.0130(10)	0.0005(8)	0.0011(8)	-0.0017(8)
C35	0.0116(10)	0.0156(11)	0.0133(10)	-0.0007(8)	-0.0004(8)	-0.0027(8)
C36	0.0228(13)	0.0226(12)	0.0292(13)	-0.0078(10)	-0.0116(10)	-0.0026(10)
C37	0.0168(11)	0.0156(11)	0.0210(11)	-0.0029(9)	-0.0020(9)	-0.0017(9)
C38	0.0119(10)	0.0135(10)	0.0127(10)	-0.0044(8)	-0.0002(8)	-0.0010(8)
C39	0.0114(10)	0.0154(10)	0.0155(10)	-0.0014(8)	0.0024(8)	-0.0038(8)
C40	0.0140(11)	0.0180(11)	0.0161(11)	-0.0006(9)	-0.0029(8)	-0.0010(8)
C41	0.0113(10)	0.0225(12)	0.0191(11)	-0.0007(9)	-0.0021(8)	-0.0020(9)
C42	0.0137(11)	0.0202(11)	0.0155(11)	-0.0010(9)	-0.0003(8)	-0.0050(9)
C43	0.0151(11)	0.0161(11)	0.0127(10)	-0.0013(8)	-0.0014(8)	-0.0030(8)
C44	0.0148(11)	0.0284(13)	0.0258(13)	0.0066(10)	-0.0043(9)	-0.0033(10)
C45	0.0141(11)	0.0355(14)	0.0229(12)	0.0065(11)	-0.0037(9)	-0.0078(10)
C46	0.0064(9)	0.0150(10)	0.0144(10)	-0.0013(8)	-0.0004(7)	-0.0019(8)
C47	0.0110(10)	0.0157(11)	0.0118(10)	-0.0027(8)	0.0009(8)	-0.0027(8)
C48	0.0123(10)	0.0154(11)	0.0168(11)	-0.0026(9)	0.0002(8)	-0.0026(8)
C49	0.0125(10)	0.0162(11)	0.0153(10)	0.0034(8)	0.0003(8)	-0.0031(8)
C50	0.0082(10)	0.0190(11)	0.0131(10)	0.0002(8)	0.0004(8)	-0.0027(8)
C51	0.0092(10)	0.0143(10)	0.0146(10)	-0.0027(8)	0.0000(8)	-0.0004(8)
C52	0.0221(12)	0.0169(11)	0.0165(11)	-0.0004(9)	0.0016(9)	-0.0054(9)
C53	0.0144(11)	0.0167(11)	0.0145(11)	-0.0005(8)	-0.0007(8)	-0.0014(8)
C54	0.0138(11)	0.0140(10)	0.0140(10)	-0.0007(8)	-0.0011(8)	-0.0023(8)
F1	0.0286(8)	0.0353(8)	0.0207(7)	-0.0051(6)	-0.0076(6)	-0.0115(6)
F2	0.0455(9)	0.0198(7)	0.0223(7)	0.0006(6)	-0.0163(7)	0.0013(6)
F3	0.0305(8)	0.0250(7)	0.0156(7)	-0.0076(6)	-0.0027(6)	0.0023(6)
F4	0.0147(7)	0.0324(9)	0.0553(11)	-0.0126(8)	-0.0004(7)	0.0019(6)
F5	0.0226(8)	0.0457(10)	0.0610(12)	0.0185(9)	-0.0031(8)	-0.0180(7)

Table S34. Anisotropic atomic displacement parameters (Å^2) for fac-[Re(bpy)(CO)$_3$3DMABN](BArF$_{24}$).. The anisotropic atomic displacement factor exponent takes the form: $-2\pi^2[\,h^2\,a^{*2}\,U_{11} + ... + 2\,h\,k\,a^*\,b^*\,U_{12}]$.

Atom	U_{11}	U_{22}	U_{33}	U_{23}	U_{13}	U_{12}
F6	0.0168(8)	0.0946(16)	0.0309(9)	-0.0203(9)	-0.0030(6)	-0.0138(9)
F7	0.0323(9)	0.0370(9)	0.0639(12)	0.0062(8)	-0.0268(8)	-0.0172(7)
F8	0.0233(9)	0.0772(16)	0.1064(19)	-0.0654(15)	-0.0304(10)	0.0194(9)
F9	0.0674(14)	0.0824(16)	0.0459(11)	0.0279(11)	-0.0422(10)	-0.0442(12)
F10	0.0254(8)	0.0134(7)	0.0669(12)	-0.0047(7)	-0.0071(8)	-0.0025(6)
F11	0.0307(8)	0.0369(9)	0.0221(7)	-0.0006(7)	0.0064(6)	0.0149(7)
F12	0.0292(8)	0.0244(8)	0.0369(8)	-0.0107(6)	-0.0174(7)	0.0094(6)
F13	0.0202(8)	0.0726(14)	0.0497(10)	0.0355(10)	-0.0201(7)	-0.0187(8)
F14	0.0539(11)	0.0228(8)	0.0374(9)	0.0059(7)	-0.0123(8)	0.0048(7)
F15	0.0273(8)	0.0382(9)	0.0187(7)	0.0078(6)	-0.0058(6)	-0.0078(7)
F16	0.0173(7)	0.0362(9)	0.0316(8)	0.0079(7)	-0.0048(6)	-0.0147(6)
F17	0.0353(10)	0.0819(14)	0.0201(8)	-0.0118(8)	0.0102(7)	-0.0297(10)
F18	0.0203(8)	0.0594(12)	0.0608(12)	0.0439(10)	-0.0063(8)	-0.0107(8)
F19	0.1080(17)	0.0194(8)	0.0169(8)	-0.0049(6)	-0.0078(9)	-0.0103(9)
F20	0.0400(9)	0.0249(8)	0.0330(8)	-0.0068(7)	0.0044(7)	-0.0193(7)
F21	0.0264(9)	0.0243(9)	0.0996(16)	-0.0280(10)	-0.0166(10)	0.0057(7)
F22	0.0249(7)	0.0267(7)	0.0151(6)	0.0021(6)	-0.0046(5)	0.0051(6)
F23	0.0154(7)	0.0260(7)	0.0176(6)	-0.0020(5)	0.0045(5)	-0.0017(5)
F24	0.0320(8)	0.0267(7)	0.0157(6)	-0.0029(6)	-0.0045(6)	-0.0112(6)

Table S35. Hydrogen atomic coordinates and isotropic atomic displacement parameters (Å^2) for fac-[Re(bpy)(CO)$_3$3DMABN](BArF$_{24}$).

Atom	x	y	z	U(eq)
H6	0.3275	0.6245	0.1762	0.022
H8	0.5248	0.3727	0.0796	0.027
H9	0.3883	0.3599	0.0112	0.028
H10	0.2178	0.4751	0.0251	0.025
H11A	0.5131	0.6496	0.1758	0.039
H11B	0.5824	0.5922	0.2392	0.039
H11C	0.4468	0.6083	0.2629	0.039
H12A	0.6090	0.3734	0.1887	0.044
H12B	0.6753	0.4495	0.2040	0.044
H12C	0.6737	0.4306	0.1110	0.044
H13	-0.2195	0.6446	0.2982	0.028
H14	-0.2317	0.6010	0.4396	0.035
H15	-0.1275	0.6654	0.5118	0.033
H16	-0.0151	0.7732	0.4407	0.028
H19	0.1003	0.8616	0.3611	0.03
H20	0.1906	0.9782	0.2790	0.036
H21	0.1548	1.0256	0.1460	0.034
H22	0.0347	0.9528	0.0983	0.026
H24	0.3186	0.1613	0.1244	0.016
H26	0.6460	0.1332	-0.0203	0.02
H31	0.5007	0.2395	0.3600	0.018
H33	0.3909	0.5208	0.4128	0.02
H35	0.2033	0.3868	0.3126	0.017
H39	0.2084	0.3076	0.1773	0.018
H41	-0.1176	0.2690	0.2757	0.022
H43	0.1367	0.1370	0.3861	0.018
H47	0.4056	0.0045	0.2573	0.016
H49	0.3782	-0.1221	0.4914	0.019
H51	0.3192	0.1666	0.4627	0.016
H54	0.5705	0.1848	0.2299	0.017